
Politecnico di Milano
Dipartimento di Energia
Doctoral Programme in
Energy and Nuclear Science and Technology

---

# Advanced materials for novel laser–driven ion acceleration schemes

Doctoral Dissertation of:
**Irene Prencipe**

Supervisor:
**Dr. Matteo Passoni**

Tutor:
**Prof. Carlo E. Bottani**

The Chair of the Doctoral Program:
**Prof. Carlo E. Bottani**

Year 2015 – Cycle XXVII

*a Stefano*

# Abstract

Among the secondary sources of radiation produced by the interaction of ultra–short (10s fs) ultra–intense ($10^{18} - 10^{21}$ W/cm$^2$) laser pulses with matter, large interest has been devoted to laser-generated ion beams. The great potential of this technique for scientific and technological applications (as, for example, production of radioisotopes for medical diagnostics, material irradiation and in a more distant future cancer hadrontherapy and fast ignition of targets for inertial fusion) is related to the possibility of producing multi–MeV/nucleon protons and ions with a high degree of laminarity and low emittance exploiting an experimental apparatus relatively compact and cheap compared to common acceleration systems. A possible strategy to enhance the acceleration performances in view of specific applications is to obtain a better control of the laser–matter interaction phase through the adoption of advanced target configurations. In this PhD thesis, multilayer targets were investigated with the aim of exploiting the presence of a near–critical density layer to optimize the laser–target coupling. Therefore, this thesis had a twofold goal. Firstly, advanced material science techniques were developed and optimized for the production and characterization of ultra–low density carbon foams for nano–engineered targets. The second part of my PhD activities was devoted to laser–driven ion acceleration experiments performed in external laser facilities to investigate the potential of novel target configurations.

# Premessa

Tra le sorgenti secondarie di radiazione prodotte nell'interazione di impulsi laser ultra–brevi (10s fs) e ultra–intensi ($10^{18} - 10^{21}$ W/cm$^2$) con la materia, particolare interesse è stato suscitato da fasci di ioni prodotti da impulsi laser. Il notevole potenziale di questa tecnica per applicazioni scientifiche e tecnologiche (tra cui, ad esempio, la produzione di isotopi per diagnostica medica, l'irraggiamento di materiali e, in un futuro più lontano, l'adroterapia oncologica e l'ignizione rapida di bersagli per fusione inerziale) è legato alla possibilità di produrre protoni e ioni con energie di diversi MeV/nucleone, un elevato grado di laminarità e emittanza ridotta con un apparato sperimentale relativamente compatto ed economico rispetto alle tecniche di accelerazione convenzionali. Una possibile strategia per migliorare le performances di accelerazione in vista di possibili applicazioni consiste nel perseguire un miglior controllo della fase di interazione tra laser e materia attraverso l'utilizzo di bersagli innovativi. In particolare, in questa tesi di dottorato, sono stati studiati target multistrato al fine di sfruttare la presenza di uno strato con densità circa critica per ottimizzare l'accoppiamento tra laser e bersaglio. Questa tesi ha avuto un duplice obiettivo. In primo luogo, sono state sviluppate e ottimizzate tecniche avanzate di scienza dei materiali per la produzione e caratterizzazione di nanoschiume di carbonio a bassa densità per target nano–ingegnerizzati. La seconda parte delle mie attività di dottorato è stata dedicata ad esperimenti di accelerazione di ioni indotta da impulsi laser, eseguiti in laser facilities esterne volti ad investigare il potenziale di bersagli innovativi.

# Contents

# Introduction

In the last decades, impressive advancements in laser technology led to the production of laser pulses with intensity in excess of $10^{18}$ W/cm$^2$ and triggered a growing interest in the investigation of the interaction of ultra–intense laser pulses with matter. A large number of experiments were performed to explore laser–matter interaction in the high intensity regime and the generation of accelerated ions was observed due to the expansion of the plasma produced by the incident pulse [1]. However, the broad angular distribution and relatively low energies (in the 100 keV/nucleon range) of ions emitted from laser–irradiated surfaces made them scarcely appealing for applications. As a consequence, the potential of ion acceleration driven by ultra–intense ultra–short laser pulses for scientific and technological applications went almost unnoticed until 2000, when the emission of collimated ion beams orthogonal to the non–irradiated surface of thin solid foils with energies up to several tens of MeV/nucleon was observed for the first time in three independent experiments [2–4].

The emission of accelerated protons and ions produced by the interaction of ultra–intense ultra–short laser pulses with matter can be due to different physical phenomena depending on the experimental conditions. The so–called Target Normal Sheath Acceleration (TNSA) is currently the most investigated acceleration mechanism [5]. The acceleration process in the TNSA scheme is due to the generation of fast electrons in the interaction between the incident laser pulse and the plasma produced on the target surface by the pulse itself. As fast electrons propagate beyond the non–illuminated surface of the target, they produce a quasi–static sheath field at the vacuum–solid interface, which in turn accelerates light ions adsorbed on the rear target surface.

Laser–driven ion beams may be very appealing for applications due to their peculiar properties [6–8]. The ions have a broad energy spectrum and cut–off energy of several tens of MeV/nucleon. The ion bunches are short (ps) compared to other acceleration techniques, have fs synchronization with the laser pulse and contain $10^{11} - 10^{12}$ ions/bunch. The effective source size is quite small, around 10 $\mu$m, and the degree of laminarity is high, resulting in extremely low transversal and longitudinal emittance values (0.004 mm mrad and $< 10^4$ eV s, respectively).

Thus, for protons up to 10 MeV, the beam transversal emittance is two orders of magnitude better than typical Radio Frequency (RF) wave–based accelerators and the ion current (per single bunch) is substantially higher (kA range) [9]. Finally, the characteristic acceleration gradients of laser–driven ion sources (MeV/$\mu$m) are extremely high compared to acceleration gradients produced by conventional RF accelerators (MeV/m), which is potentially very promising for the development of compact table–top acceleration systems.
The high sensitivity of protons to electric and magnetic fields and to areal density gradients, the high laminarity and the small size of the ion source have been employed so far to develop high space resolution plasma diagnostics and proton radiography. The ultra–short bunch duration and the intrinsic energy dispersion of ion beams accelerated by laser pulses allow to achieve an extraordinary time resolution (ps), providing a unique diagnostic tool to probe fast dynamics in plasmas. Another current application of laser-driven ion sources is the isochoric heating of solid–density matter on ultra–short time scales, which allows the production and investigation of warm dense matter states of great interest for material science and astrophysics.
In addition to the above mentioned, a number of applications requiring enhanced acceleration performances have been proposed and explored so far. The possibility of employing laser–driven ion acceleration for oncological hadrontherapy and for the fast ignition of inertial confinement fusion targets has been widely investigated in literature. However, these foreseen applications require energy up to several hundreds of MeV per nucleon, much higher than the maximum energy of particle beams currently produced by laser–driven acceleration, and monochromatic energy spectra are required for ion–driven fast ignition. Moreover, as well as radiotherapy, several industrial applications, related for example to material science for material processing, characterization and irradiation and to the production of isotopes for medical diagnostic techniques, require high average ion current, that is high repetition rates.
Thus, great effort is being devoted worldwide to the enhancement of the acceleration performances in terms of maximum ion energy, control of ion spectral and angular properties, efficiency and repetition rate of the acceleration process. Different strategies have been adopted to this aim. A detailed insight of the laser–ion acceleration physics in a variety of experimental conditions has been pursued through both theoretical and numerical studies. Moreover, the development of advanced laser systems and the realization of international mega–facilities, for example in the frame of the Extreme Light Infrastructure (ELI) and Helmholtz International Beamline for Extreme Fields (HIBEF) pan European projects, have recently allowed the production of ultra–short laser pulses (10s fs) with super–high intensity (above $10^{20}$ W/cm$^2$) and power up to 10 PW, giving access to new laser–plasma interaction regimes and acceleration mechanisms. Finally, a considerable effort is being devoted to the development of advanced target configurations. This approach exploits the peculiar properties of novel nano–engineered materials to achieve an optimal control of the laser–matter interaction phase, and, as a consequence, to increase laser–ions energy conversion efficiency, thus leading to an enhancement of the acceleration performances, for example in terms of ion en-

ergy and number of accelerated particles. In addition, the better target–coupling achieved with advanced materials allows to achieve interesting acceleration performances also in the moderate intensity regime, thus reducing the cost and the complexity of the development of ultra–high power laser systems.

## PhD thesis: motivations and goals

The main goal of my PhD thesis was to explore novel and enhanced ion acceleration mechanisms through the design, production and employment of engineered nanostructured targets. In this frame, the possibility of enhancing the efficiency of the TNSA scheme, both in terms of number and maximum energy of accelerated ions, by enhancing laser absorption and fast electron production through suitable target design was investigated. Two target configurations were considered in this thesis: foam–based and grating targets.
The most part of my PhD activities was devoted to investigate the possibility of employing multilayer targets composed by a thin solid aluminium foil with a low–density layer (carbon foam) on the directly illuminated target surface with the aim of exploiting the enhanced laser absorption in ultra–low density materials [10–12]. According to recent numerical studies [13, 14], in this configuration the presence of a foam layer should lead to enhanced acceleration performances provided that the film properties satisfy specific requirements. In particular, the foam density should be around the so–called plasma critical density, above which the propagation of laser radiation in the plasma produced by the pulse itself on the target irradiated surface is forbidden in the low amplitude limit, where non–linear and relativistic effects can be neglected. For plasmas in this density regime and high intensity laser pulses, both volume and surface laser absorption mechanisms can take place, as well as additional absorption phenomena, thus an enhancement in the production of relativistically hot electrons should be expected for foam–attached solid foils. For near–infrared laser pulses ($0.8 - 1\,\mu$m) and fully ionized carbon, the critical density corresponds to extremely low mass density values in the $3 - 6\,\mathrm{mg/cm^3}$ range.
Due to the extremely low density required for foam–attached targets, their production and characterization are not straightforward and require advanced material science techniques. Therefore, a crucial objective of this thesis work was the development of suitable techniques for the production and the characterization of foams–attached multilayer targets for laser–driven ion acceleration experiments to be performed in external laser facilities. The approach proposed by Zani et al. [15] for the production of carbon foams by Pulsed Laser Deposition (PLD) was here further improved and optimized through an extensive study on the role of process parameters such as the process duration, the deposition geometry and the substrate rotational and translational movement, in order to achieve a reliable and reproducible process for the production of variable density carbon foams (down to a few $\mathrm{mg/cm^3}$) in a wide thickness range (from a few $\mu$m to 100 $\mu$m), with satisfactory substrate coverage and uniformity and good adhesion to a solid substrate. Reproducibility was addressed for several deposition conditions to enhance the technique reliability. Issues related to the characterization of ultra–low

density porous films were addressed and an innovative technique for thin film density evaluation based on Energy Dispersive X–ray Spectroscopy (EDS) proposed in [16] was further developed, validated for nanostructured thin films with density ranging from the density of solid to a few mg/cm$^3$ and a large variety of compositions and morphologies and employed for carbon foam density evaluation. Several procedural and theoretical aspects related to this technique were considered to enhance the technique reliability, to simplify the measurement procedures and to adapt the technique to new measurement configurations.
The techniques developed for the production and characterization of low density carbon films were exploited for the production of foam–based multilayer targets, whose application in laser driven ion acceleration experiments was one of the main objectives of this work. Two acceleration experiments on foam–attached targets were performed in external laser facilities. A first experiment was performed at the Laboratoire Interactions Dynamique et Lasers (LIDyL, France) to provide a proof of concept of the acceleration performance enhancement of the foam–based multilayer target configuration at moderate intensities (from $5 \times 10^{16}$ W/cm$^2$ to $5 \times 10^{19}$ W/cm$^2$). A second experiment was performed at the PW laser facility of the Gwangju Institute of Science and Technology (GIST, South Korea) to investigate the effect of the target properties (i.e. foam thickness and density) and the laser parameters (pulse intensity and polarization) on the acceleration mechanisms at high intensity (from $7 \times 10^{19}$ W/cm$^2$ to about $5 \times 10^{20}$ W/cm$^2$).
The goals of my PhD research activities on nanostructured targets for ion acceleration also included the participation to an experimental campaign, performed at the LIDyL facility, on grating targets with periodically modulated rear surface. This experiment was aimed at the investigation of the effect of the resonant excitation of electromagnetic surface waves by ultra–intense laser pulses incident with a resonance angle on a modulated surface with a periodic groove on the acceleration mechanism.

## PhD thesis: structure

Hereinafter a brief description of the thesis structure is provided.
The main body of the thesis is divided into three parts. Part I is dedicated to the presentation of the basic concepts and the state of the art for laser–driven ion acceleration, with particular attention to novel target designs, and advanced techniques for the production and the characterization of low density materials. Parts II and III correspond to the two principal activities of my PhD research. In part II, the development of techniques for the production and characterization of low density carbon foams is discussed. In part III, laser–driven ion acceleration experiments performed on foam–attached and grating targets are illustrated. Finally, the main conclusions and the future perspectives of the research activities performed in my PhD are discussed in Chapter 6.

**Part I: Basic concepts and state of the art**

**Chapter 1: An introduction to laser–driven ion acceleration**

In Chapter 1, a review of the basic physical aspects related to laser–driven ion acceleration is provided, with particular attention to the laser–matter interaction in the relativistic regime and to the associated laser–driven acceleration mechanisms. The most interesting applications of laser–driven ion sources are briefly illustrated along with issues related to the role of advanced targets for enhanced acceleration regimes.

**Chapter 2: Production and characterization of low density thin films**

In Chapter 2, a general introduction to the techniques adopted during my PhD activities for the production and the characterization of low–density films is provided. More in particular, the main issues related to the production of carbon foams by Pulsed Laser Deposition (PLD) and the application of Energy Dispersive X–Ray Spectroscopy (EDS) to nanostructured film density evaluation are discussed, due to their relevance in my thesis work.

**Part II: Carbon foam production and characterization**

**Chapter 3: Production of foam–based targets**

In Chapter 3, advancements in the production of low density carbon foams for multilayer targets are discussed with particular attention to the control of foam properties (thickness, density and uniformity) and to process reproducibility. Technical solutions adopted for the manufacturing, transport and irradiation of foam based targets in acceleration experiments are illustrated along with possible target configurations for the adoption of foam–based targets in high repetition rate experiments.

**Chapter 4: Energy Dispersive X-ray Spectroscopy for thin film density evaluation**

In Chapter 4, an extensive experimental validation campaign on EDS based methods for nanostructured film density evaluation is illustrated. The main experimental issues to be considered to achieve reliable results are discussed and a model for the X–ray generation distribution in depth for multilayer samples is proposed. Novel measurement geometries allowing an extension of the technique applicability to free–standing films and a simplification of the data acquisition process are introduced.

**Part III: Laser–driven ion acceleration experiments with advanced targets**

**Chapter 5: Laser–driven ion acceleration experiments on advanced targets**

In Chapter 5, the laser–driven ion acceleration experiments performed on advanced targets during my PhD activities are discussed: a proof of principle experiment performed on foam–attached targets at moderate intensity at the LIDyL facility (France); an extensive investigation performed at GIST (South

Korea) on the role of foam–based target properties and laser parameters at high intensity; an experimental study on the role of high field plasmonics in the acceleration process with grating targets performed at the LIDyL facility.

**Chapter 6: Conclusions and future perspectives**
In Chapter 6, the main conclusions on my PhD research activities are drawn and the future perspectives of this thesis work are illustrated.

## Publications and presentations in international conferences

The original contents of this PhD thesis led to the publication of the following peer–reviewed papers, ordered by year.

- M. Passoni, A. Zani, A. Sgattoni, D. Dellasega, A. Macchi, I. Prencipe, V. Floquet, P. Martin, T. V. Lysekina and T. Ceccotti, Energetic ions at moderate laser intensities using foam–based multi–layered targets. *Plasma Physics and Controlled Fusion*, **56** 045001

- I. Prencipe, D. Dellasega and M. Passoni, Advancements in the production and characterization of carbon foams for laser driven ion acceleration. *Journal of Physics: Conference Series* (in press)

- I. Prencipe, D. Dellasega, A. Zani, D. Rizzo, M. Passoni, Energy dispersive X–ray spectroscopy for nanostructured thin film density evaluation. *Science and Technology of Advanced Materials* (in press)

- M. Passoni, I. Prencipe, D. Dellasega, A. Sgattoni, L. Fedeli, A. Macchi, I. W. Choi, K. A., I. J. Kim, A. K. Janulewicz, H. W. Lee, J. H. Sung, S. K. Lee, C. H. Nam, (in preparation)

I presented the results illustrated in this PhD thesis in several international conferences, ordered by year.

- I. Prencipe, A. Zani, D. Dellasega, V. Russo, T. Ceccotti, V. Floquet, A. Sgattoni, A. Macchi M. Passoni. Ultra–intense laser-driven ion acceleration with multi-layered targets. 40th EPS Conference on Plasma Physics, Espoo, Finland, 1–5 July 2013. Poster and Proceeding.

- I. Prencipe, A. Zani, D. Dellasega, V. Russo, T. Ceccotti, V. Floquet, A. Sgattoni, A. Macchi M. Passoni. Ultra–intense laser-driven ion acceleration with multi-layered targets. International School of Quantum Electronics, 54th Course: Atoms and Plasmas in Super–Intense Laser Fields, Erice, Italy, 21–31 July 2013. Poster.

- I. Prencipe, A. Zani, D. Dellasega, V. Russo, T. Ceccotti, V. Floquet, A. Sgattoni, A. Macchi M. Passoni. Production of low–density targets for laser driven ion acceleration. Targetry for laser–driven proton (ion) accelerator sources, Garching, Germany, 9–11 October 2013. Oral Presentation.

- I. Prencipe, D. Dellasega, M. Passoni, Production and characterization of carbon foams for laser driven ion acceleration. 5th Target Fabrication Workshop, St. Andrews, United Kingdom, 6–11 July 2014. Oral Presentation.

# Part I

# Basic concepts and state of the art

# 1

# An introduction to laser–driven ion acceleration

In this chapter, an introduction to the fundamental concepts related to laser–driven ion acceleration is presented. In Section 1.1, the main interaction mechanisms between laser radiation and matter in the relativistic regime are briefly illustrated. This is a crucial phase of the laser–driven ion acceleration process and involves complex physical phenomena, such as the ionization of the irradiated target, the consequent formation of a plasma and the absorption of the incoming pulse energy by plasma electrons. In Section 1.2, the main laser–driven ion acceleration mechanisms and the current applications of laser–driven ion sources are illustrated, as well as the most interesting foreseen applications requiring enhanced acceleration performances. Finally, in Section 1.3, some of the most interesting advanced target configurations proposed so far in literature and the target concepts considered in this thesis are described.

## 1.1 Interaction of ultra–intense laser pulses with matter

In the last 30 years, the advent of ultra–short pulse generators and solid state amplifiers, as well as the introduction of the Chirped Pulse Amplification (CPA) technique, has allowed to achieve the production of laser pulses with focused intensities higher than $10^{18}\,\mathrm{W/cm^2}$ also in relatively small–scale laser facilities [17]. This impressive advancement in laser technology and the consequent widespread availability of ultra–intense laser systems made possible the investigation of laser–plasma interaction in the relativistic regime and opened up new prospectives for the application of laser science in many fields, among which plasma, nuclear and high energy physics, material science, astrophysics and cosmology.
Between the 1960s and 1985, the development of ultra–high intensity laser systems was damped by the impossibility of amplifying laser pulses in the picosecond and femtosecond regime, due to unwanted non–linearities and optics damage caused by the high intensity values in the amplifying materials. Thus, the production of *high* intensity pulses (up to $10^{15}\,\mathrm{W/cm^2}$) could only be achieved in expensive large–size laser systems with low repetition rates using low energy density storage

amplifiers (i.e. dyes and excimer amplifiers). In fact, in general, direct amplification of ultra–short laser pulses is not possible in high energy density storage materials such as solid state amplifiers. In these materials the high pulse intensities ($TW/cm^2$), corresponding to the high pulse fluence required for energy extraction, are well above the material damage threshold ($GW/cm^2$). In addition, such high intensities can produce unwanted non–linearities as the distortion of the laser wavefront or a filamentation of the laser beam [18].
The introduction of CPA in 1985 removed this bottleneck [19–21]. Instead of being directly amplified, in CPA systems the ultra–short pulse is stretched in time by a $10^4$ factor before the amplification stage by introducing a frequency chirp onto the laser pulse with a dispersive grating. Then the stretched pulse is amplified in solid state amplifiers, avoiding super–high peak intensity and consequent non–linear effects, and re–compressed to its original duration by the inverse dispersive process. The development of CPA allowed to increase immediately by a $10^5 - 10^6$ factor the intensity of pulses produced in existing facilities. However, it became widespread only in the 1990s, when the advent of solid state active materials and new mode–locking techniques, such as the Kerr–lens mode–locking in Ti:sapphire crystals [22], made possible the production of ultra–short laser pulses with reliable, relatively simple and user–friendly laser systems also in small–scale facilities.
In the most recent femtosecond petawatt–class laser systems, the introduction of ultra–short pulse generators, solid state amplifiers and the Chirped Pulse Amplification (CPA) technique has allowed to achieve the production of laser pulses with focused intensities up to $10^{21} - 10^{22}\,W/cm^2$, suitable for the investigation of relativistic interaction mechanisms between matter and electromagnetic radiation in different intensity regimes.
The interaction of an ultra–intense laser pulse with a target is a crucial phase of laser–driven ion acceleration and a very complex process, in which the dominant effects depend on many factors, among which the intensity, frequency and polarization of the incoming electromagnetic radiation, the spatial and temporal quality of the laser pulse, the properties of the target material and the interaction geometry (i.e. the incidence angle). An exhaustive dissertation on this topic is beyond the purpose of this introduction and can be found in [23–26]. Hereinafter, the main mechanisms of interaction between ultra–short ultra–intense laser pulses and matter are illustrated to provide the tools for a better understanding of the physical system considered in this thesis.
Since the intensity required for target ionization is generally in the $10^{12}-10^{14}\,W/cm^2$ range, the first effect of the incidence of an ultra–intense laser pulse on a target is the ionization of the illuminated surface and the formation of a plasma, whose properties depend on both the laser parameters and the target properties. In particular, the target ionization is due to fast electron collisions and to multi-photon and field ionization processes, as the energy of a single photon is not sufficient to produce direct ionization. In general, many factors (among which the amplification of spontaneous emission in the laser oscillator and the incomplete pulse recompression) contribute to the reduction of the pulse temporal quality introducing prepulse radiation emission with duration from the picosecond to the

nanosecond regime and intensity high enough to ionize the target surface (i.e $10^6$ orders of magnitude lower than the main pulse). Thus, the main pulse interacts with the non–uniform expanding plasma produced on the directly irradiated surface of the target by the laser prepulse. Many techniques for the enhancement of the pulse contrast ratio (the pulse peak to prepulse intensity ratio $I_{pulse}/I_{prepulse}$) have been developed, allowing to produce pulses with good temporal quality (contrast up to $10^{12}$) [27]. In high contrast configuration, the target surface is ionized by the main pulse in a few laser cycles, so that the rear part of the pulse interacts with the plasma produced by the front of the pulse itself and the target superficial structure is preserved until the incidence of the main pulse. In this case, the plasma has a sharp density gradient, since the plasma expansion can be neglected on the ultra–short timescale of the pulse–target interaction.
However, for both high and low contrast configurations, the main pulse interacts with a plasma, an ionized medium whose dynamics is dominated by collective electromagnetic interactions, since each charged particle is strongly influenced by an average field produced by all the other particles and, in addition, by external electromagnetic fields, while the interactions between neighbouring particles are less important than the autoconsistent electromagnetic field and can be considered as collisions. The optical response of a plasma is determined by the motion of free electrons, while the response of ionic populations is affected by collective plasma fields on longer characteristic timescales.
In the non–relativistic regime, the dispersion relation of a wave with frequency $\omega$ and wave vector $\mathbf{k}$ in a plasma is $k^2c^2 = (\omega_p - \omega)$, where $\omega_p = (4\pi e^2 n_e/m_e)^{1/2}$ is the so–called *plasma frequency* ($e$ elementary charge, $n_e$ number density of plasma electrons and $m_e$ electron mass). This represents a cut–off frequency for the propagation of electromagnetic waves, since for $\omega < \omega_p$ the wave vector is not a real number ($k^2 < 0$) and the wave propagation is forbidden in the plasma. This is evident in the case of a plane wave $\mathbf{E}(\mathbf{r}, t) = \mathbf{E}_0 e^{i\mathbf{k}\cdot\mathbf{r}}$: for $\omega < \omega_p$, the imaginary part of the wave vector introduces a damping factor, $e^{-kz}$, where $z$ is the space coordinate along the wave propagation direction. Thus the electric field is exponentially evanescent on a characteristic length, so–called *skin depth*, $L = c(\omega_p^2 - \omega^2)^{1/2}$, which represents the maximum penetration depth of the electromagnetic wave in the plasma.
The cut–off condition $\omega < \omega_p$ can be also expressed in terms of the plasma electron density $n_e$ and a cut–off density, so called *critical density*, can be defined as

$$n_c = \frac{m_e \omega^2}{4\pi e^2} \,. \tag{1.1}$$

Thus, two distinct laser–matter interaction regimes exist depending on plasma density:

$n_e > n_c$ *overdense–dense* plasma, in which the propagation of electromagnetic waves is forbidden;

$n_e < n_c$ *under–dense* plasma, transparent for incoming electromagnetic waves.

In addition, for ultra–intense radiation ($I > 10^{18}\,\mathrm{W/cm^2}$), a new critical density definition is required to take into account relativistic effects:

$$n_c = \gamma \frac{m_e \omega^2}{4\pi e^2}\,, \tag{1.2}$$

where $\gamma = (1 - v^2/c^2)^{-1/2}$ is the well–known *Lorentz factor*. Since $\gamma < 1$, the critical density decreases in the relativistic regime, thus the propagation of ultra–intense laser radiation is actually allowed also in classically over–dense plasmas. This effect is known as *relativistic induced transparency*. In addition, the physical description of laser–plasma interaction is further complicated by a number of strongly non–linear effects which arise in the relativistic regime.
The following paragraphs provide a brief introduction of the main laser–plasma interaction mechanisms in the relativistic regime for both under–dense and over–dense plasmas and for plasmas with density around the critical density, in the so–called *near–critical* regime.

### 1.1.1 Under–dense regime

In the under–dense regime, typical of the interaction of an intense pulse on a gas jet target, the propagation of an ultra–intense plasma is allowed, but it is strongly affected by non–linear effects, such as the dependence of the plasma refractive index on the wave amplitude, which can generate a distortion in the pulse temporal and spatial profile. For example, a pulse with a Gaussian intensity profile in the transversal plane interacts with a medium whose refractive index is higher along the pulse propagation axis, where the electromagnetic field intensity is maximum, and decreases in the outer region. Thus, the plasma acts as a converging lens for the laser pulse and a *relativistic self–focusing* occurs if this effect is dominant with respect with the natural beam diffraction [28, 29]. For pulses with slightly modulated wave amplitude in the transverse direction, this effect can result in a beam filamentation [18].
In addition, a laser pulse, having a finite extension in both space and time, exerts a so–called *ponderomotive* force on plasma charged species. The ponderomotive force is a non–linear force acting on charged particles subject to an inhomogeneous oscillating electromagnetic field, it scales as squared particle charge and inverse particle mass, thus it mainly affects electrons, while its effect on ions is negligible. The action of this force during the propagation of a laser pulse in an under–dense plasma results in the expulsion of electrons from the high intensity region, leading to a further enhancement of the refractive index along the laser beam axis and producing a *self–channeling* effect which contributes to the pulse self–focusing.
The ponderomotive force plays a key role in the interaction between ultra–intense laser radiation and under–dense plasma. As as the pulse propagates in the plasma, the ponderomotive force due to the intensity time profile at the target front accelerates electrons in the laser propagation direction. Moreover, the ponderomotive force produces an electron depleted region in the pulse wake, as sketched in Figure 1.1. As a consequence, the collective forces due to the charge separation produce plasma oscillations known as *wake waves* [30, 31]. These are electrostatic waves with $\omega = \omega_p$, whose wavevector depends on the oscillation amplitude as well as

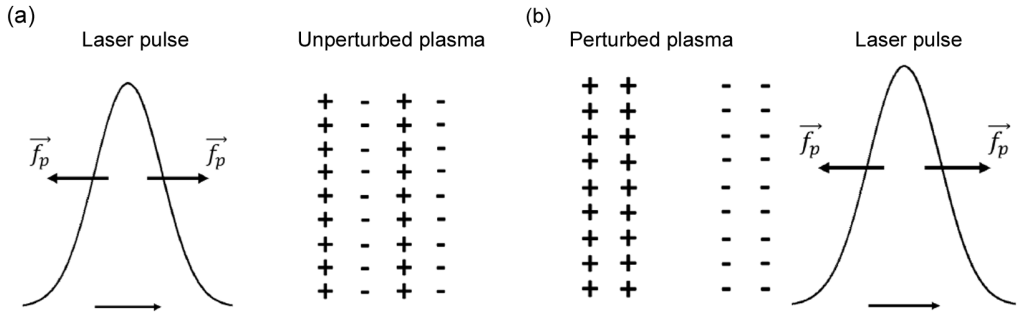


**Figure 1.1:** *Schematic view of the non–linear effect of the ponderomotive force $\vec{f}_p$ on a plasma slab: (a) unperturbed plasma before the interaction, (b) formation of the charge separation after the interaction. From [16].*

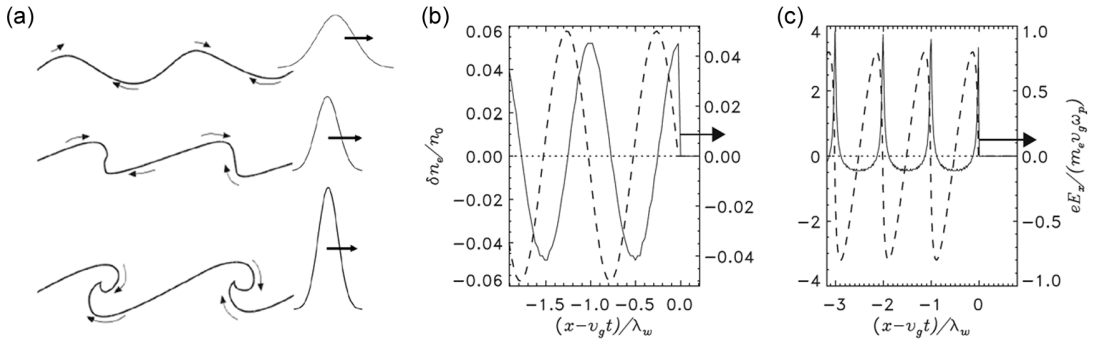


**Figure 1.2:** *Schematic representation of the wakefield generation (a) (from the top) in the weakly non linear case, for relativistic intensity and in the wavebreaking condition, from [16]. Sheet model simulation of electron density and electric field in the wake of a pulse propagating in underdense plasma in the weekly non–linear (b) and relativistic case (c), from [26]*

the wavelength and the phase velocity. The resonant ponderomotive excitation of wake waves is most effective when the laser pulse duration is half the period of the plasma oscillations, i.e. if the plasma oscillation wavelength is twice the laser pulse length. In this frame, an additional effect can occur if the maximum value of the electic field is higher than the so–called *relativistic wavebreaking limit*, also known as the *Akhiezer and Polovin limit* [32]. As the wakefield approaches the wavebreaking limit, the electric field acquires a sawtooth shape and the electron density appears as a sequence of narrow peaks (Figure 1.2). When the limit is reached, the periodic wave structure is lost and an effective energy transfer from the pulse to plasma electrons occurs, leading to the production of high energy electron bunches [33].

### 1.1.2 Over–dense regime

In general, the incidence of an ultra–intense pulse on a solid target produces an over–dense plasma, whose density gradient at the vacuum–plasma interface is strongly dependent on the interaction conditions. If the density gradient at the

plasma boundary is steep, the propagation of electromagnetic waves is limited to the skin layer and the energy transfer occurs at the vacuum–plasma interface, while for gentle gradients the laser radiation can propagate until it reaches the critical surface for which $n_e \simeq n_c$, thus the interaction occurs in the near–critical region of the plasma. In both cases, the laser pulse incidence leads to the production of high energy (*hot*) electrons which provide the most efficient energy transport to the over–dense plasma region where the pulse propagation is forbidden.

The dominant interaction mechanisms leading to the production of hot electrons in over–dense plasmas strongly depend on the intensity of the incoming laser pulse. For non–relativistic intensity values, in the range between $10^{12}\,\mathrm{W/cm^2}$ and $10^{17}\,\mathrm{W/cm^2}$, the dominant processes are *inverse Bremsstrahlung absorption* [23, 34] and *resonance absorption* [23]. This interaction regime is typical of the first phase of the interaction, in which the prepulse or the pulse front interact with the solid target.

Inverse Bremsstrahlung absorption is a collisional absorption mechanism: the energy transfer from the laser pulse to plasma electrons occurs in the collisions of electrons with other plasma particles (ions). However, in general, the efficiency of collisional processes decreases strongly with increasing intensity, thus efficient energy absorption in the high intensity regime only occurs via collisionless mechanisms.

The necessary condition for an efficient transfer of pulse energy to plasma electrons in collisionless mechanisms is the presence, along the density gradient direction, of an oscillating component of the Lorentz force due to the incoming laser pulse, the reflected radiation and the plasma self–generated electromagnetic fields

$$\mathbf{F}_L = -e(\mathbf{E} + \frac{1}{c}\mathbf{v} \times \mathbf{B})\,, \tag{1.3}$$

with $\mathbf{E}$ electric field, $\mathbf{B}$ magnetic field and $\mathbf{v}$ velocity of the particle on which the force is exerted. Since the direction of the electric and magnetic components of the Lorentz force is determined by the pulse polarization, this property has an important role in determining the dominant interaction mechanism. The pulse polarization defines the direction of oscillation of the electric field vector in the plane orthogonal to the propagation direction. If the electric field vector direction is constant during the oscillation, the pulse has *linear polarization*. Depending on the direction of oscillation of the electric field respect to the incidence plane (i.e. the plane containing the wave vector and the target normal), two cases of interest in the interaction of the ultra–intense laser pulses with an over–dense plasma: p–polarization, when $\mathbf{E}$ is parallel to the incidence plane, and s–polarization, when $\mathbf{E}$ is orthogonal to the incidence plane. In the case of a linearly polarized electromagnetic wave, the electric field vector can be decomposed into two components oscillating in phase with the same amplitude. If, on the contrary, the two components have $\pi/2$ a phase shift, the point of the resulting electric field describes a circle in the transverse plane and the electromagnetic wave has *circular polarization*.

In the non–relativistic regime, the non–collisional absorption of an incident laser pulse is due to resonant absorption. This mechanism is based on the production

of plasma oscillations at frequency $\omega$ in the near–critical plasma region and on the consequent efficient wave absorption and generation of relativistic electrons. The production of density perturbations leading to the excitation of plasma electrostatic modes is driven by the electric field component along the density gradient direction, thus (for plane targets) oblique incidence and p–polarization are required. However, for oblique incident waves, the reflection of the incoming pulse takes place for $n < n_c$ and the electromagnetic field of the incident wave is evanescent in the near–critical region, thus an optimal incidence angle exists. Moreover, plasma density must be approximately constant over the oscillation amplitude (gentle plasma density gradients) and the pulse intensity should not be high enough to cause plasma oscillation breaking.
In the relativistic interaction regime ($I > 10^{18}\,\mathrm{W/cm^2}$), other absorption mechanisms become dominant: *vacuum heating*, also known as *Brunel effect* or *not–so–resonant absorption* [35], and *relativistic $J \times B$ heating* [36].
In the vacuum heating model, the electrons are extracted from the plasma at the vacuum–solid interface by the p component of the electric field and accelerated to a velocity of the order of the oscillation velocity in the electric field in vacuum $eE/m\omega$. After half an oscillation in the vacuum, the electrons re–enter the over–dense plasma, where the electric field is evanescent. In this region electrons are no more subject to the electric field, thus the energy transfer is not reversible. Due to the oscillations of the driving force, hot electrons are produced in bunches with frequency equal to the electromagnetic wave frequency. The efficiency of this process is maximum for high laser intensity and sharp density gradients, typical of plasmas produced by high contrast pulses, for which the interaction time scale is too short for plasma hydrodynamic expansion. As in the case of resonant absorption, laser pulses with p–polarization and oblique incidence of the laser pulse are required to have a non–null driving force for electron acceleration.
For s polarization or normal incidence the vacuum heating effect is strongly suppressed and the relativistic $J \times B$ heating becomes dominant. In the relativistic regime, the magnetic term of the Lorentz force drives non–linear electron oscillations along the density gradient. The electron acceleration mechanism is similar to vacuum heating with a different driving force. In this case, the electron bunches are produced with frequency $2\omega$, which is the dominant frequency of the magnetic component of the Lorentz force.
Another effect which can contribute to the absorption of the incident laser radiation is the excitation of surface electron waves, so–called *surface plasmons*, at the steep surface of an over–dense plasma. Surface plasmons are fluctuations of the electron density propagating along the interaction surface. These electron waves are strongly localized at the vacuum–plasma interface: their electromagnetic field is maximum at the surface and exponentially evanescent along the direction perpendicular to the target surface [26].
Resonant surface waves (with wavevector $\mathbf{k}_{sp}$) can be excited by a laser pulse with frequency $\omega$ and wavevector $\mathbf{k}$ if the phase matching condition $k_y = k_{sp}$ is satisfied (where $k_y = k\sin(\theta)$ is the component of $\mathbf{k}$ in the plasma surface plane and $\theta$ is the incidence angle). The dispersion relation of surface plasmons can be calculated imposing boundary conditions for the electromagnetic field at the

vacuum–plasma interface

$$k_{sp}^2 c^2 = \frac{1 - \omega_p^2/\omega^2}{2 - \omega_p^2/\omega^2} \,. \tag{1.4}$$

Thus, the condition for the wave propagation is $1 < \omega_p/\omega < \sqrt{(2)}$, while for $\omega_p/\sqrt{2} < \omega < \omega_p$ $k_{sp}$ is imaginary and the wave propagation is forbidden. However, the upper branch describes the propagation of high frequency electromagnetic waves in a plasma, thus only the branch with $\omega < \omega_p/\sqrt{(2)}$ is of interest for plasmons. In the latter case, $k_{sp} > \omega/c$ and the phase matching condition

$$k_{sp} = \frac{\omega}{c} \sin(\theta) \tag{1.5}$$

has no solutions for $\omega < \omega_p$, thus in principle it's not possible to achieve a phase matching between the incoming electromagnetic radiation and a surface plasmon (since the plasmon phase velocity is lower than $c$). This limitation can be overcome if surface nanostructures are introduced as pulse–plasmon couplers. In particular, in presence of a periodic surface modulation the phase matching condition is modified due to the surface periodicity and becomes

$$k(\omega) \sin\theta = k_{sp}(\omega) + n\frac{2\pi}{d} \,, \tag{1.6}$$

where $d$ is the grating period and $n$ is an integer number. For given grating properties (i.e. period), equation (1.6) can be interpreted as a condition on the pulse incidence angle: phase matching between the incoming pulse and the surface plasmon can be achieved if the incidence angle is around the resonance angle $\theta_{res}$ defined by the relation

$$\sin(\theta_{res}) + \frac{\lambda}{d} = \left(\frac{1 - n_e/n_c}{2 - n_e/n_c}\right)^{1/2} \,, \tag{1.7}$$

where $\lambda$ is the wavelength of the incoming pulse. This theoretical description, however, does not take into account the non–linear effects which become dominant in the relativistic intensity regime: a detailed non–linear theory of surface plasmons is not available. The results of a few numerical studies performed to investigate relativistic surface plasmons on modulated surfaces (and their effect on laser–driven ion acceleration processes) will be discussed in Section 1.3.3.

### 1.1.3 Near–critical regime

Near–critical plasma represents a boundary regime between under–dense plasma, transparent for incoming laser radiation, and over–dense plasma, in which the propagation of electromagnetic waves is forbidden, at least if non–linear and relativistic effects can be neglected. For near–infrared wavelength laser radiation ($\sim 1\,\mu$m), the critical density corresponds to mass densities of a few mg/cm$^3$, an intermediate value between the density of solid and gas jet targets. The production of porous targets in this density range (*foams*), however, is experimentally challenging, thus the near–critical interaction regime has not been extensively investigated.

The interest of this interaction regime is related to the high laser absorption fraction and hot electron production efficiency characterizing near–critical plasma [11, 12, 37]. This effect can be explained considering the efficiency scaling of absorption mechanisms in over–dense and under–dense plasma. In the latter regime, the interaction volume is extended to the plasma region affected by the pulse propagation and the laser–plasma energy transfer efficiency is enhanced for increasing plasma density. This is the case, for example, of electrons accelerated via wavebreaking, whose maximum energy scales as $\sqrt{n_e}$. In the case of over–dense plasma, the interaction volume thickness is given by the skin layer and scales as $\sqrt{n_c/n_e}$. As a consequence, for decreasing density the interaction region in which absorption mechanisms can occur is larger and the laser absorption is enhanced. Hence, in both interaction regimes laser absorption and hot electron production are favoured for plasma density values approaching the critical value. In addition, in the boundary region, a superimposition of interaction mechanisms typical of under–dense and over–dense plasma can take place. Thus, in near–critical plasma an optimal coupling between the incoming laser pulse and plasma electrons can be achieved.
The propagation of an ultra–intense pulse in the near–critical plasma can also lead to the formation of structures, such as channels [38, 39] and magnetic vortices [40–43], which can have an important role in laser–driven ion acceleration. In particular, the formation of channel structures is mainly due to the action of the ponderomotive force exerted by the propagating pulse on plasma electrons. The ponderomotive force expels electrons from the maximum intensity region (i.e. the region surrounding the pulse propagation axis) leaving a ionic channel. This soliton structure is stable as long as the electrostatic force due to the charge separation balances the laser ponderomotive force. However, after a time interval comparable with the typical ionic dynamics timescales, the ponderomotive force produces bubbles of ion depletion in which oscillating electromagnetic fields are trapped [39].
According to recent numerical and experimental studies on electron heating and channel formation in the near–critical (and slightly over–critical) regime an enhancement of both the channel length and the electron momentum can be observed as the target density approaches the critical density, as illustrated in Figures 1.3 and 1.4, respectively, [44]. In addition, PIC simulations showed an almost linear dependence of the momentum of accelerated electrons and the channel length from the pulse normalized vector potential ($a_0 = eA_0/m_ec^2$, where $A_0$ is the amplitude of the vector potential associated to the electromagnetic field) and a reduction in the electron heating efficiency for out–of–plane polarization (i.e. s–polarization) with respect to the case of p–polarized pulses, due to the lower laser absorption at the channel surface.

## 1.2 Laser–driven ion sources

In general, laser–plasma interaction in the relativistic regime involves a number of complex interrelated effects leading to the emission of secondary radiation, which is strongly dependent on the properties of both target and laser pulse (see Figure

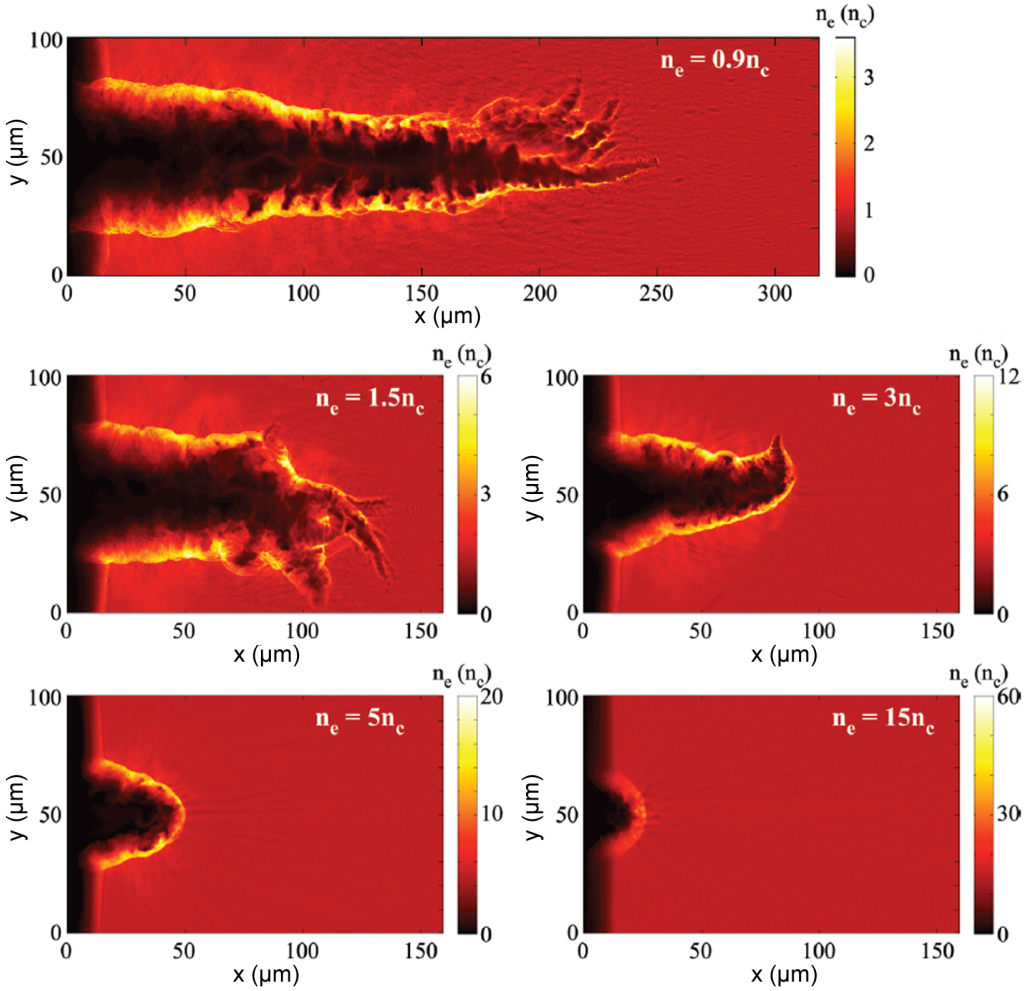


**Figure 1.3:** *Simulated electron density spatial distribution produced by a p–polarized laser pulse ($a_0 = 6$) channelling in plasmas with different density values. From [44].*

1.5). As mentioned in the previous section, the incoming laser pulse interacts directly with plasma electrons due to their low inertia leading to the production of high energy electrons. In addition, the emission of X–rays is generally observed due to a number of effects, among which bremstrahlung and de–excitation of atoms and ions, and high–order optical harmonics can be generated due to non–linear optic effects [45, 46].
The emission of ions as secondary radiation was observed in several laser–plasma interaction experiments performed in the 1980s and 1990s on different kinds of targets, among which solid foils [47], gas jets [48,49] and clusters [50,51]. However, laser–driven ion sources attracted little interest before 2000 due to the scarcely appealing properties of emitted ions, among which moderate energy ($\sim$ 100 keV/nucleon) and broad angular distribution.
In 2000, the observation of high energy ion beams with good collimation produced in the interaction of high intensity laser pulses and thin solid foils raised a new interest in laser–driven ion sources both in fundamental research and in view of possible applications [2–4]. In the last 15 years, an extraordinary number of

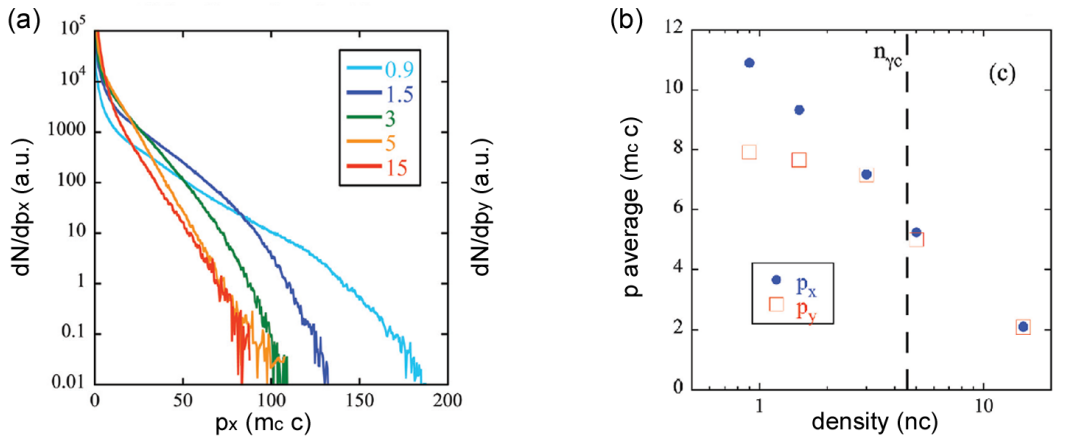


**Figure 1.4:** *Results of PIC simulations on pulse channelling in low density plasmas. (a) Longitudinal momentum spectra of electrons for different density values with $a_0 = 6$ and p–polarization. (b) Corresponding average longitudinal and transverse momentum values plotted as a function of plasma density. From [44].*

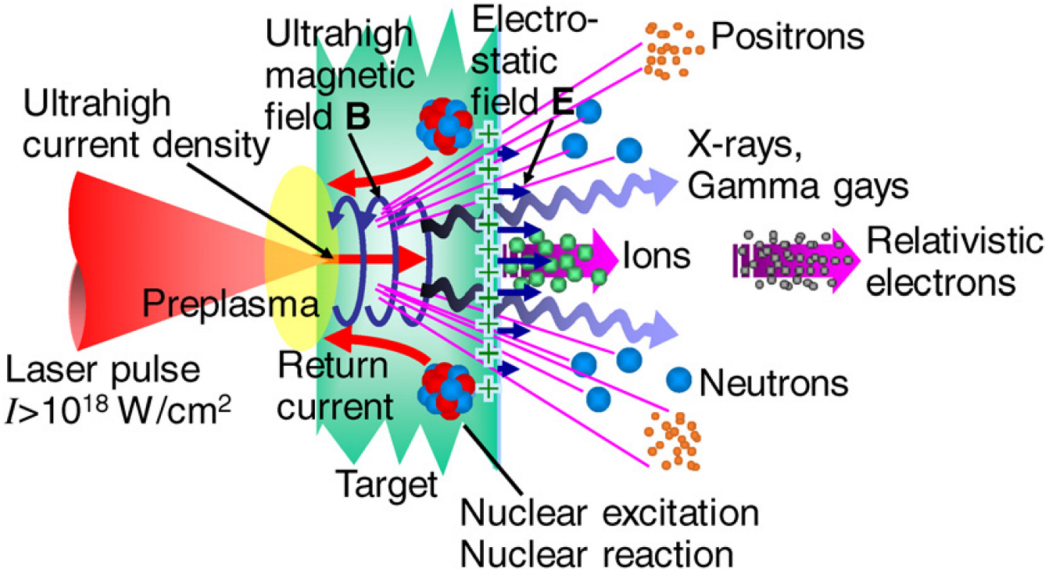


**Figure 1.5:** *Schematic representation of secondary radiation emission in the interaction of an intense laser pulse with a solid foil. From [7].*

numerical, theoretical and experimental studies have been performed to investigate the physical mechanisms leading to ion emission, the role of the interaction conditions and the possibility of achieving a better control of the properties of accelerated ions.

Due to the long typical timescale of the ion response to external fields, the plasma ions don't interact directly with ultra–short pulses, but their dynamics is strongly affected by slowly varying electromagnetic fields produced in the plasma by the high energy electrons generated in laser–plasma interaction. The emission of ions in laser–plasma interaction can be the result of different possible physical processes. The expansion of the plasma produced on the target's front surface, for

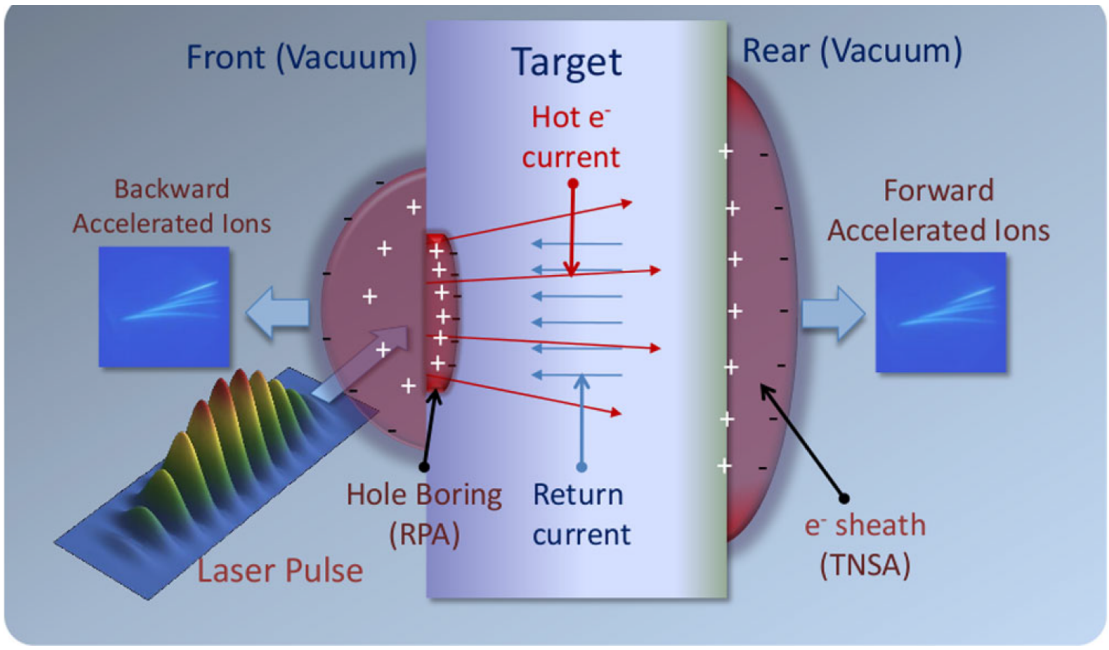


**Figure 1.6:** *Schematic representation of some of the possible ion acceleration mechanisms produced by the interaction of an intense laser pulse with a thin solid foil. From [8].*

example, leads to the almost isotropic emission of ions with relatively low energy (plasma blowoff [52]). In addition, in the interaction of an ultra–intense pulse with a solid target, the laser radiation pressure acting on both electrons and ions at the front target surface can in specific conditions produce beams of accelerated ions. Another possible ion emission mechanism is related to the formation of shock waves due to the propagation of accelerated electrons in a target, together with the laser ponderomotive force produced by a pulse propagating in low density targets. Moreover, hot electrons propagating in a target produces intense magnetic fields which can affect strongly the dynamics of ions in a plasma. For thin targets, hot electrons can reach the target rear surface and escape in vacuum producing a charge separation and, as a consequence, an electric field acting on ions on the rear target surface. Thus, due to the complexity of the laser–matter interaction dynamics in the relativistic regime, different acceleration schemes can take place depending on the properties of both target and pulse (sketched in Figure 1.6) and on the interaction conditions and many effects should be taken into account in the investigation of laser–driven ion sources.

In this section, the main laser–driven ion acceleration mechanisms are reviewed (Subsection 1.2.1). In Subsection 1.2.2, some of the most interesting applications of the technique are illustrated.

### 1.2.1 Acceleration mechanisms

#### Target Normal Sheath Acceleration

As mentioned before, in 2000 the observation of high energy ions collimated along the target normal direction in the interaction of ultra–intense laser pulses with

thin solid foils was reported in three independent papers [2–4]. In these experiments, Al, Au and plastic (CH) targets with thickness in the 1-125 $\mu$m range were irradiated with laser intensity from $3 \times 10^{18}\,\mathrm{W/cm^2}$ to $3 \times 10^{20}\,\mathrm{W/cm^2}$. The predominant component of the accelerated ions detected in these experiments was due to proton emission even for metallic targets with no hydrogen content, due to the presence of hydrogen containing contaminants on the target surfaces, such as hydrocarbons or water vapour [47]. Accelerated proton bunches containing from $10^9$ to $2 \times 10^{13}$ protons were observed. Accelerated protons had broad energy spectra with a spectral cut–off at high energy. The maximum cut–off energy achieved (58 MeV) was observed irradiating a 100 $\mu$m thick CH target with pulse intensity $3 \times 10^{20}\,\mathrm{W/cm^2}$ and normal incidence. The proton angular distribution was peaked along the target normal (independently from the laser incidence angle) and the beam divergence was lower for protons having higher energy.
These observations gave rise to a discussion about the mechanisms responsible for the acceleration process and, in particular, about the region from which the accelerated ions were emitted. According to E. L. Clark *et al.* [2] and Maksimchuk *et al.* [3], ions were produced at the front surface of the target, where the laser–plasma interaction occurs, then the ions propagate through the solid foil and escape the target from the rear surface. This hypothesis was rejected when acceleration experiments performed by Snavely *et al.* [4] and Hatchett *et al.* [53] on wedge targets showed that ions were emitted along the direction orthogonal to the rear target surface, suggesting that ions were emitted from the rear target surface.
In general, the experimental results mentioned before are not compatible with a ponderomotive acceleration process at the target front surface for a number of reasons [53]: ions are emitted along the rear target surface; the estimated size of the ion emission region is much larger than the laser focal spot, the number of contaminant protons in the focal spot area is much lower than the number of protons detected in experiments (and the prepulse would blow them off before the main pulse incidence).
On the contrary, the experimental results are compatible with the presence of a sheath electrostatic accelerating field generated by relativistic electrons expanding beyond the target rear surface. According to a simple electrostatic picture of this process, proposed by S. P. Hatchett *et al.*, only a small fraction of the hot electrons produced in laser–plasma interaction can escape the Coulomb potential, while the rest would propagate back and forth in the target while transversally drifting. As a consequence, an electron sheath is formed at the target surfaces, generating a charge separation on a space scale comparable with the Debye length

$$\lambda_D = \left( \frac{T_e}{4\pi e^2 n_e} \right)^{1/2} , \tag{1.8}$$

where $T_e$ is the electron temperature in MeV. A rough evaluation of the accelerating field produced by the electron sheath at the rear target surface was achieved using a simple one–dimensional capacitor model

$$E_{acc} = \frac{T_e}{e\lambda_D} . \tag{1.9}$$

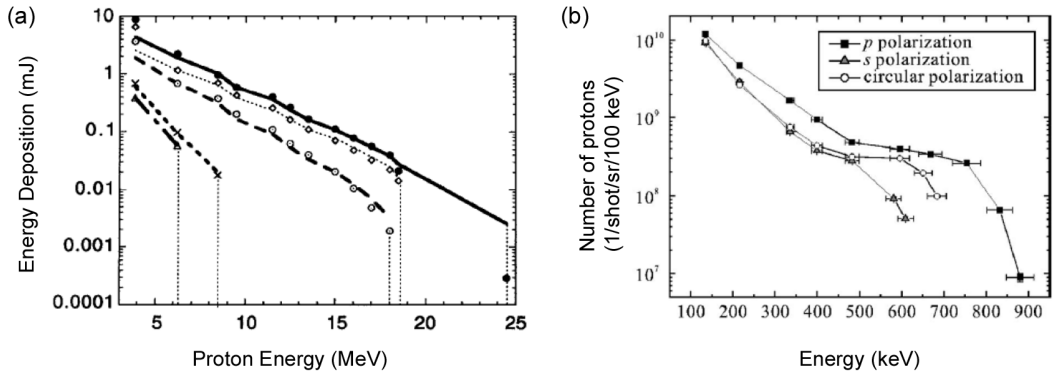


**Figure 1.7:** *Typical TNSA proton spectra (a) showing an exponential decrease and a sharp cut–off, from [55], and (b) with a plateau superimposed to the exponential spectrum and a sharp cut–off, from [56].*

This electrostatic field corresponds to a few MeV/$\mu$m and acts on the ions at the target rear surface for a few picoseconds. The accelerating field action is most effective on protons adsorbed on the target surface as contaminants, due to their low mass. On the contrary, the emission of accelerated ions from the front surface is strongly inhibited by the plasma expansion, since the presence of a gentle gradient in the ion density reduces the charge separation between target ions and electron sheath at the vacuum–plasma interface. Many experimental results confirmed this picture: for example, Mackinnon *et al.* observed that the acceleration process is strongly inhibited in presence of a preformed plasma on the rear surface [54]. In 2001, S. C. Wilks *et al.* expanded this simple electrostatic picture of the acceleration process and introduced the expression Target Normal Sheath Acceleration (TNSA), currently used to indicate this acceleration scheme [5].
This simple picture is coherent with the main properties of accelerated ions. For instance, the evolution of the electron sheath distribution during the acceleration results in broad exponential ion energy spectra with a sharp cut–off. In a few cases, the presence of a plateau can be observed due to the production of a two–temperature electron population in the pulse–target interaction. Figure 1.7 shows typical proton spectra for the two cases mentioned [55, 56]. In addition, the spatial distribution of electron in the sheath at the rear target surface plays a crucial role in the angular distribution of accelerated ions and the sharp cut–off observed in the ion angular distribution is coherent with a Gaussian electron transverse distribution. The properties of the electron sheath are strongly affected by the electron transport in the target: while good collimation is observed for conductive targets, in insulators the formation of electron filaments leads to proton density inhomogeneities in the beam transversal direction [57]. The direct experimental evidence of the Gaussian shape of the accelerating electron sheath was provided by Romagnani *et al.* using TNSA produced protons as probe beam to study the evolution of the system [58], as shown in Figure 1.8. Finally, the accelerated particles have a high degree of laminarity (i.e. a strong correlation between the point in the surface where the particle is emitted and its angle of emission). The degree of laminarity can be expressed in terms of *transverse emittance* [59]. This quan-

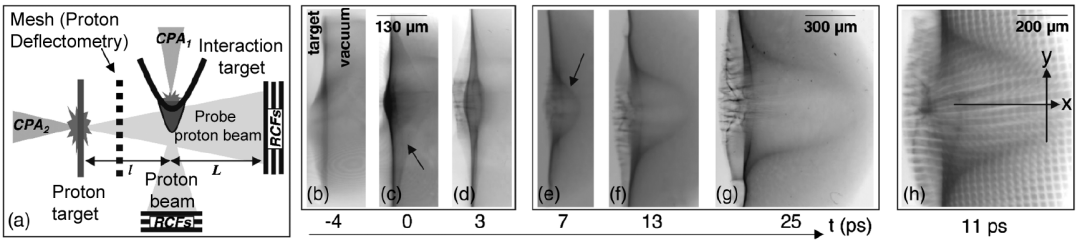


**Figure 1.8:** *Proton probing of the expanding sheath at the rear target surface of a thin solid foil irradiated with an intense laser pulse: (a) experimental setup; (b)–(g) temporal series of images produced by the deflection of TNSA probe protons; (h) deflectometry image (mesh placed between the probe source and the sheath to measure proton deflection). From [58].*

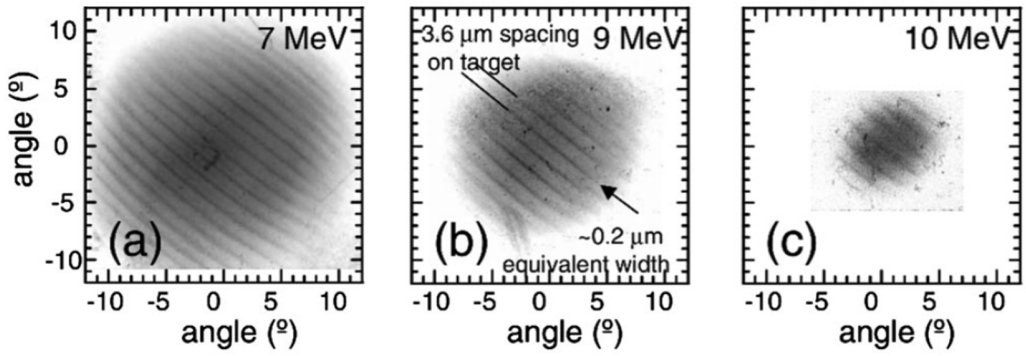


**Figure 1.9:** *Transverse emittance evaluation: modulation in the proton distribution due to rear target surface microstructuring, shown for (a) 7 MeV, (b) 9 MeV and (c) 10 MeV protons. From [9].*

tity describes the effective phase volume of the beam distribution, i.e the volume of the ellipsoid enclosing the region occupied by the particle distribution in the $r - r'$ space (where $r$ is the distance from the beam propagation axis and $r'$ is the angle between the single particle propagation direction and the beam axis). This quantity has been evaluated, for example, by studying the projection of meshes placed close to the target rear surface on the path of accelerated ions [60–62], achieving transversal emittance values below $0.1\pi$ mm mrad . However, these methods don't allow to accurately reconstruct the transverse phase space because the ion beam can be slightly deflected by the object and, in addition, ions don't propagate ballistically close to the target. A more accurate method for transverse emittance evaluation exploits the modulation of the transverse distribution of accelerated ions due to a suitable modulation of the rear target surface (see Figure 1.9) [9,63]. This modulation is superimposed to the divergence of the propagating ion beam and allows to reconstruct the transverse phase space and to evaluate the transverse emittance, which for protons up to 10 Mev is about 0.004 mm mrad, two orders of magnitude better than values achieved for typical radio–frequency accelerators. Moreover, results reported in [9] show that the proton transverse emittance does not increase significantly if electrons propagating with the proton beam are removed after 1 cm of beam propagation.

A large number of theoretical and numerical studies has been dedicated to the de-

velopment of an appropriate model for TNSA, in order to achieve a deeper insight into the acceleration process and to provide theoretically grounded scaling laws for the properties of accelerated ions. In addition, large effort has been devoted to experimental parametric investigations to better understand the effect of the target and pulse properties on the acceleration process and to validate theoretical models.
In general, analytical models for TNSA consider the production of hot electrons as a boundary condition and focus mainly on the acceleration process taking place at the rear surface, while Particle In Cell (PIC) simulations give a more complete picture of both the laser–plasma interaction and the sheath acceleration phases. TNSA is the result of phenomena which take place on very different timescales. Thus, the whole process can be subdivided into three main phases. In the first, hot electrons produced in laser–plasma interaction expand in the target and form a sheath at the its rear surface. The characteristic timescale of electron dynamics is $10^{-15}$ s. In this phase ions can be considered fixed, since their dynamics is much slower ($10^{-12}$ s). In the second phase, on the sub–ps timescale, light ions present on the rear surface as contaminants begin to be affected by the sheath electric field, which in this phase can be considered electrostatic as the first accelerated protons don't affect the electron sheath. In the third phase, in the ps regime, the sheath field is reduced by the accelerated ions, the hot electron energy is progressively depleted and electron and target ions expand together as a quasi–neutral plasma. Depending on the timescale considered in the description, three possible classes of TNSA models have been proposed. *Quasi–static models* describe the acceleration process neglecting heavy ion dynamics: accelerated ions are considered as probe charges which don't affect the sheath field [64, 65]. These models describe the sub–picosecond acceleration phase and provide reliable scaling laws for the maximum energy of accelerated ions. On longer timescales quasi–static descriptions are no longer valid, since the dynamics of heavy ions cannot be neglected. So–called *fluid models* describe the ion acceleration process as the isotermal expansion of a of a quasi–neutral plasma [66, 67]. A third class of models, the so–called *hybrid models* combine characteristics of fluid and quasi–static descriptions [68, 69]. These models refer to the same timescale of the quasi–static models, for example by considering light ions as probe particles, but they take into account the effect of accelerated ions on the electrostatic fields, for example considering the isothermal expansion of heavy ions.
The effect of the laser parameters and target properties on the acceleration process has been extensively studied and particular attention has been devoted to the effect of the experimental configuration on the maximum energy of accelerated protons and ions. Databases of published results have been used to infer scaling laws for the maximum ion energy with pulse parameters [6, 70]. According to Borghesi *et al.* [6], different scaling laws can be achieved for maximum proton energy as a function of laser irradiance ($I\lambda$) considering in different pulse duration regimes: for $\tau_L > 100$ fs, the maximum proton energy scales as $(I\lambda^2)^{1/2}$ (even though parametric measurements by Robson *et al.* [71] suggest a slower scaling), while for ultra–short pulses (tens of fs) the maximum proton energy increases linearly with laser irradiance, as shown in Figure 1.10. The systematic collection

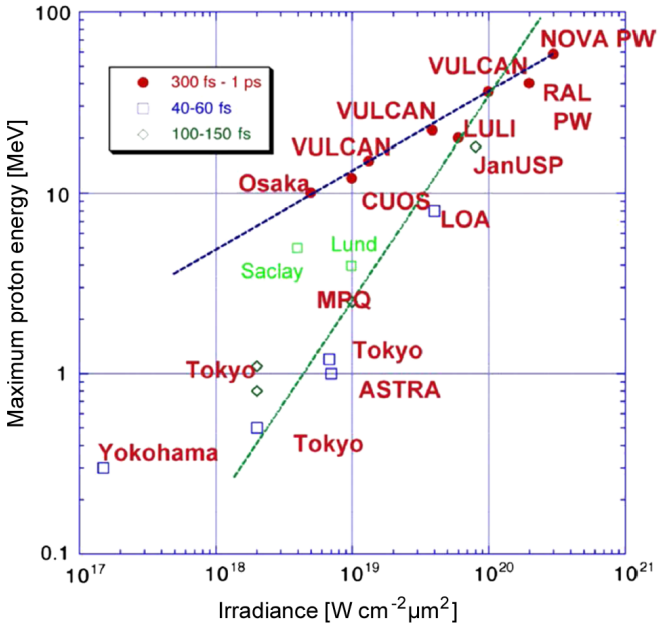


**Figure 1.10:** *Maximum proton energy produced in the interaction of intense laser pulses with solid foils. From [6].*

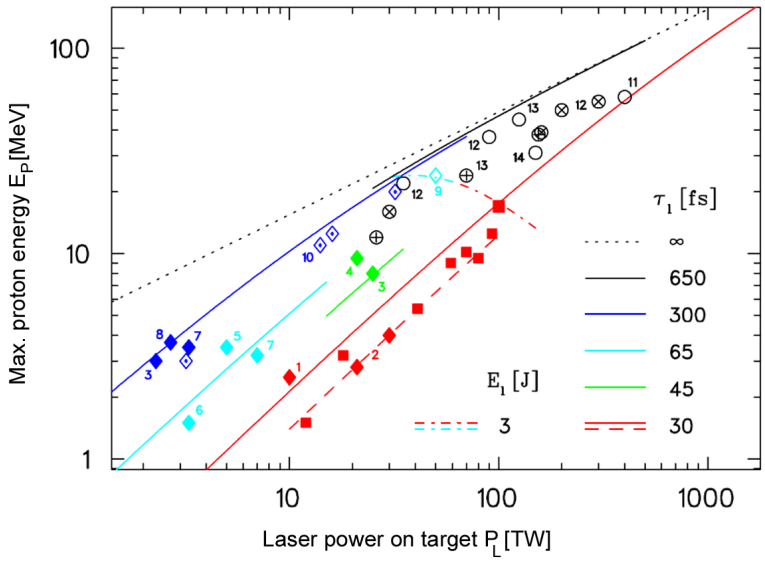


**Figure 1.11:** *Scaling of the maximum proton energy with the laser power for different interaction conditions (for details see [75] and references therein). From [75].*

of published experimental results has been often exploited to validate theoretical models [72–74]: Figure 1.11 shows the experimental scaling of the maximum proton energy with laser power in different pulse duration regimes fitted using a scaling of the quasi–static model proposed by Schreiber *et al.* [65]. The role of the single scaling parameters in the acceleration process has been studied in experimental parametric studies [70, 71, 76, 77]. These experiments are performed in

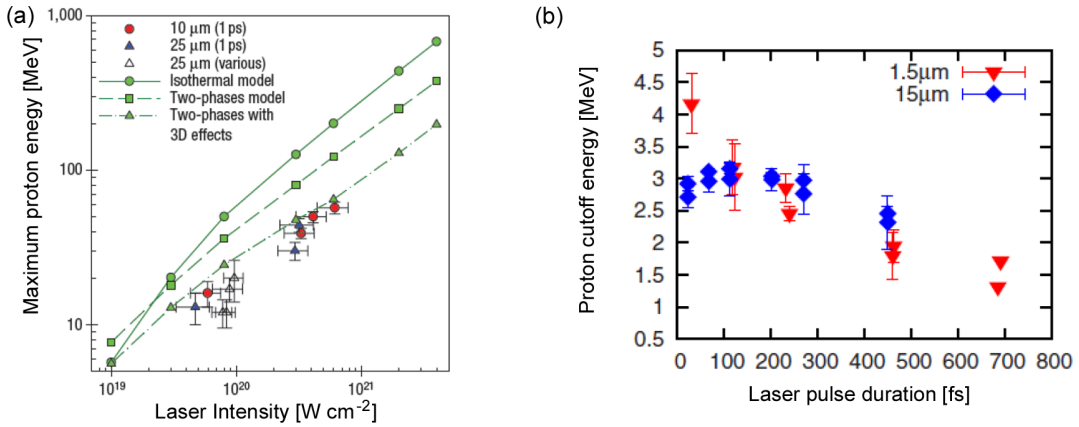


**Figure 1.12:** *Results of parametric studied: dependence of maximum proton energy on (a) laser intensity (with constant pulse duration and varying pulse energy), from [71], and (b) pulse duration (at fixed laser energy) from [76].*

controlled conditions and the laser parameters are varied one at a time. In Figure 1.11, the scaling of maximum proton energy with the pulse energy at constant $\tau_L$ is shown [75]. Conversely, Figure 1.12 represents the effect of the pulse duration on maximum proton energy for constant pulse energy.

Moreover, the acceleration performances are also influenced by laser polarization, which strongly affect the laser–plasma interaction mechanisms (as seen in Section 1.1.2). In general, linear p–polarization enhances the production of hot electrons with respect to s–polarization, while circular polarization attenuates the oscillating component of the ponderomotive force, resulting in a reduction of the energy transfer from the incoming pulse to target electrons.
Finally, the target geometry, density and composition play a fundamental role in the acceleration process. For example, the first parametric study on the effect of target thickness on the electron dynamics and the formation of the electron sheath in TNSA was performed in 2002 by Mackinnon *et al.* [55]: targets with thickness in the 3–100 $\mu$m range were irradiated with 100 fs pulses with intensity above $10^{20}\,\mathrm{W/cm^2}$. As a result an increase of maximum proton energy was observed for thin targets, due to enhanced density of MeV electrons at the rear surface of thin targets. The effect of targets properties on the TNSA process has been extensively investigated [55, 70, 76] and will be discussed in detail in Section 1.3.

#### Other acceleration schemes

The TNSA scheme discussed in the previous subsection describes the dominant ion acceleration mechanism driven by the incidence of ultra–intense laser pulses on micrometric targets. However, TNSA can be suppressed in particular conditions, for example if the production of hot electrons is inhibited, so that other acceleration mechanisms become dominant. For example, for circular polarization and normal incidence, the oscillating component of the $\mathbf{v} \times \mathbf{B}$ force vanishes and the generation of hot electron bunches at $2\omega$ is suppressed. In this case, the only effective acceleration mechanisms are related to the direct effect of the radiation

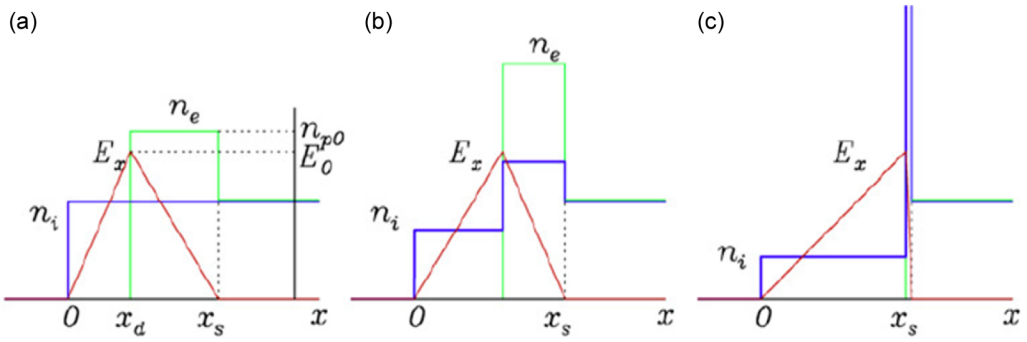


**Figure 1.13:** *One–dimensional sketch of the hole–boring RPA mechanism phases. From [79].*

pressure, i.e. the pressure exerted by the incoming laser beam on a surface due to the transfer of momentum to a non–trasparent medium, as an over–dense plasma. The effect of radiation pressure becomes dominant with respect to TNSA also for linearly polarized laser pulses with ultra–high intensity values ($> 10^{22}\,\mathrm{W/cm^2}$). In these conditions, the steady component of the $\mathbf{v} \times \mathbf{B}$ force acts on the target electrons pushing them inwards and leaving a depleted layer, thus the charge separation generates an electrostatic field which balances exactly the ponderomotive force [78]. This effect can result in different acceleration mechanisms, depending on the experimental conditions.

The so–called Hole Boring (HB) Radiation Pressure Acceleration (RPA) mechanism takes place for targets much thicker than the skin layer [79]. In this case, the radiation pressure produces a parabolic deformation and penetrates into the target, resulting in the generation of an electrostatic field and, as a consequence, to the acceleration of the ions in the compression layer. A simple one–dimensional sketch of the process is shown in Figure 1.13. As the plasma surface recedes at velocity $v_{HB}$, ions are dragged by the field due to electron displacement and form a sharp density spike. This leads to an hydrodynamic break of the electron equilibrium and to the injection of a bunch of ions with velocity $2v_{HB}$ in the solid. This process is repeated as long as the laser pulse is on, leading to a pulsed acceleration mechanism. The maximum energy per nucleon for accelerated ions can be calculated by equating the radiation pressure and the plasma momentum flux

$$\mathcal{E}_{max} = 2m_p c^2 \frac{\Pi}{1 + 2\Pi^{1/2}}\,, \tag{1.10}$$

where $\Pi = I/\rho c$ is the *pistoning parameter* [80]. Thus, the maximum energy of ions produced via hole boring RPA can be enhanced by considering slightly overcritical targets, while the process is not so effective for solid targets. Experimental proof of this acceleration mechanism was provided by Palmer *et al.* [81], who achieved protons with energy up to 1.2 MeV, narrow energy spread and energy scaling with $I/n_e$ using a $H_2$ gas jet target and 10 $\mu$m wavelength pulses with $\sim 6 \times 10^{15}\,\mathrm{W/cm^2}$ intensity and circular polarization. Experimental evidence of hole boring acceleration in solid targets is less clear since the mechanism is much less effective for high density plasma, but results compatible with a hole boring RPA mechanism are reported in the literature [82–84].

In particular experimental conditions, the radiation pressure of an intense laser–

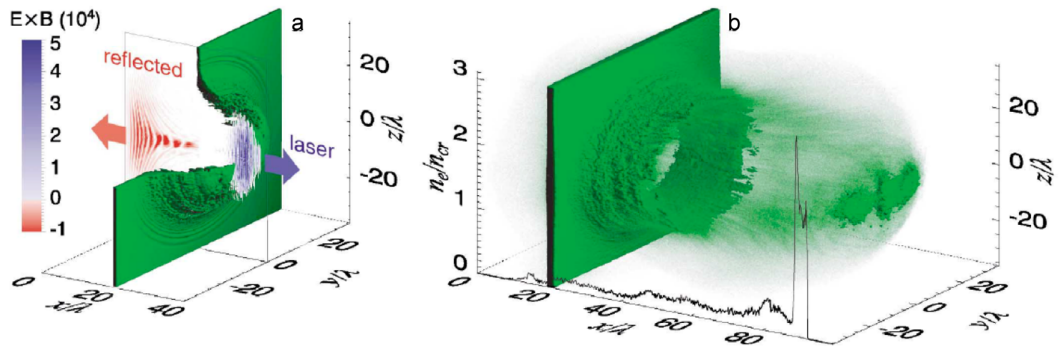


**Figure 1.14:** *Three–dimensional rendering of PIC simulation results for laser–driven ion acceleration in the light sail regime. From [91].*

pulse interacting with an over–dense target can act as a piston and drive collisionless electrostatic shocks in the plasma, with propagation velocity $v_{shock} \simeq v_{HB}$. The front of the shock wave can reflect target ions at $2v_{shock}$ as the shock propagates in the target bulk, leading to a volume acceleration mechanism known as Collisionless Shock Acceleration (CSA) [85,86]. The condition for ion reflection by the shock front is $\sqrt{a_0} > n_e/n_c$ ($a_0 = eA_0/m_ec^2$ is the pulse normalized potential, with $A_0$ amplitude of the vector potential associated to the electromagnetic field). In addition, the maximum ion energy is enhanced for decreasing target density, thus the CSA mechanism is favoured for slightly over–dense targets. However, this mechanism could be inhibited by circular polarization due to the existence of a general condition on the Mach number ($M = v_{HB}/c_s$, where $c_s$ is the acoustic wave propagation velocity in the plasma) for the onset of electrostatic shocks ($M < 6.5$) [87]. As a consequence, CSA is generally observed in combination with TNSA, producing a plateau in the TNSA ion spectrum, as reported for example by Zepf *et al.* [88].

If the target thickness is lower than the plasma skin layer, ions can be accelerated through the so–called Light Sail (LS) RPA mechanism. In this case, the target hole boring is complete, thus the target ions are accelerated as a whole before the end of the laser pulse and can receive a further boost by radiation pressure (see Figure 1.14). A rough scaling for ion energy in the light sail regime can be achieved by describing the process as the acceleration of a flat perfectly reflecting mirror by the radiation pressure of a planar wave [89, 90]

$$\mathcal{E} = m_p c^2 \frac{\mathcal{F}^2}{2(\mathcal{F}+1)} \tag{1.11}$$

where $\mathcal{F}$ is the total laser fluence. The light sail acceleration mechanism is characterized by high laser–ion beam conversion efficiency and by the possibility of reaching very high ion energy. PIC simulations performed by Esirkepov *et al.* [91] for extremely high intensity values ($> 10^{23}\,\mathrm{W/cm^2}$) and proton slab target with thickness $\sim \lambda$ and density $49n_c$ show a good agreement with the simple light sail model. According to simulation results, the target ions are coherently accelerated as a whole to energies around 1.5 GeV.

However, the intensity regime simulated by Esirkepov *et al.* are not experimen-

tally achievable with current laser systems, thus the experimental evidence of the light sail regime has been achieved by exploiting circularly polarized laser pulses, which allowed an optimum coupling between laser pulse and ultra–thin targets and the production of narrow ion spectra [92–94]. Other experimental results compatible with the light sail acceleration scheme can be found in literature: Kar *et al.* reported the observation of narrow energy spectra for light ions, with peak energies up to 10 MeV/nucleon scaling as squared pulse fluence in high contrast experiments with 800 fs $3 \times 10^{20}\,\mathrm{W/cm^2}$ pulses and 100 nm metallic targets [95]; Henig *et al.* reported the observation of strong electron heating suppression and of a broad peak around 30 MeV in the experimental energy spectrum of $C^{6+}$ ions produced with circularly polarized 45 fs, $5 \times 10^{19}\,\mathrm{W/cm^2}$ pulses on a few nm DLC foils in ultra–high contrast configuration, while effective electron heating and typical TNSA spectra had been observed for linearly polarized pulses in the very same experimental conditions [96]. In general, according to PIC simulations [91,97], the effect of radiation pressure becomes competitive with TNSA for intensity above $10^{22}$ also for linear polarization. However, as mentioned before, this Radiation Pressure Dominant (RPD) regime is not experimental available. Moreover, according to theoretical studies, a number of non–linear effects must be taken into account, such as for example Rayleigh–Taylor like instabilities of the target [98] and the effects of radiation friction [99].

The light sail acceleration regime requires non–transparent ultra–thin targets to achieve an effective transfer of momentum from the incoming electromagnetic radiation to the target ions. Thus, the onset of a relativistic transparency regime for high intensities limits the laser amplitude for which light sail RPA can be observed. In this case, the effective volumetric heating of the target electrons produces stronger electrostatic fields, resulting in a more efficient ion acceleration if the relativistic transparency onset occurs in correspondence with the pulse peak, as reported for example by Henig *et al.* for $C^{6+}$ ions accelerated by irradiating 10–50 nm thick foils with 700 fs $7-9\times10^{19}\,\mathrm{W/cm^2}$ pulses [100]. According to Yin *et al.*, the acceleration mechanism observed in this case involves an early TNSA stage and an enhanced TNSA stage, in which all the target electrons are converted into hot electrons. A third stage, so–called Break Out Afterburner (BOA), follows in which the relativistic transparency onset allows the pulse penetration to the rear target surface and the production of a forward directed electron beam (see Figure 1.15. The acceleration process is due to the a relativistic Buneman instability that rapidly converts the electron energy into ion energy [101]. The BOA mechanism is believed to be responsible for the observation of 160 MeV protons from sub–micrometric $CH_2$ foils irradiated with 550 fs pulses with intensity up to $2 \times 10^{21}\,\mathrm{W/cm^2}$ reported by Heghelich and Jung *et al.* [102]. This is the highest proton energy ever reached by laser–driven ion acceleration, being about three times the previous proton energy record achieved for laser–driven proton sources, and falls in range of proton energies required for cancer hadrontherapy.

The last acceleration mechanism considered in this section is the so–called magnetic vortex acceleration. This process can occur when an intense laser pulse interacts with a near–critical target forming a channel due to relativistic self–focusing. The vortical motion of electrons due to the acceleration of electrons

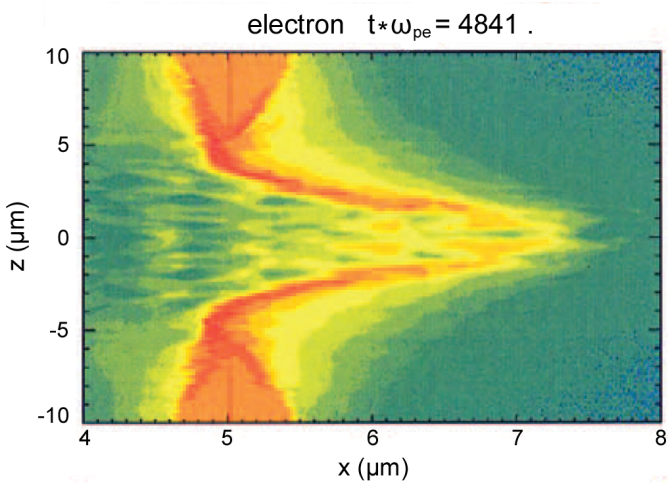


**Figure 1.15:** *Simulated electron density during the break–our afterburner phase of laser–driven ion acceleration with ultra–thin foils (initial position $x = 5\,\mu m$). From [101].*

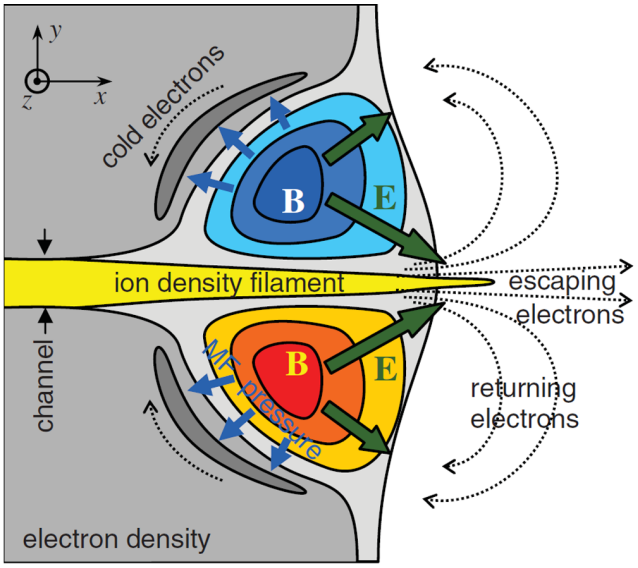


**Figure 1.16:** *Schematic view of the magnetic vortex acceleration mechanism. From [11].*

in the channel and to the background electrons flow compensating the hot electron propagation produces a toroidal quasi–static magnetic field with magnitude exceeding 100 MG (see Figure 1.16). In general, for gentle density gradients, magnetic vortices with a lifetime comparable with the characteristic timescale of ion response (sub–ps) propagate along the channel axis direction. The expulsion of electrons from the magnetized regions due to magnetic pressure results in the production of positively charged regions and an electrostatic sheath in front of the rear target surface. This long–living charge separation leads to the emission of collimated ion beams in the ion filament near the channel axis [11, 13].
In Figures 1.17 and 1.18, a summary of laser–driven acceleration mechanisms is provided and the pulse property ranges and laser–matter interaction regimes in

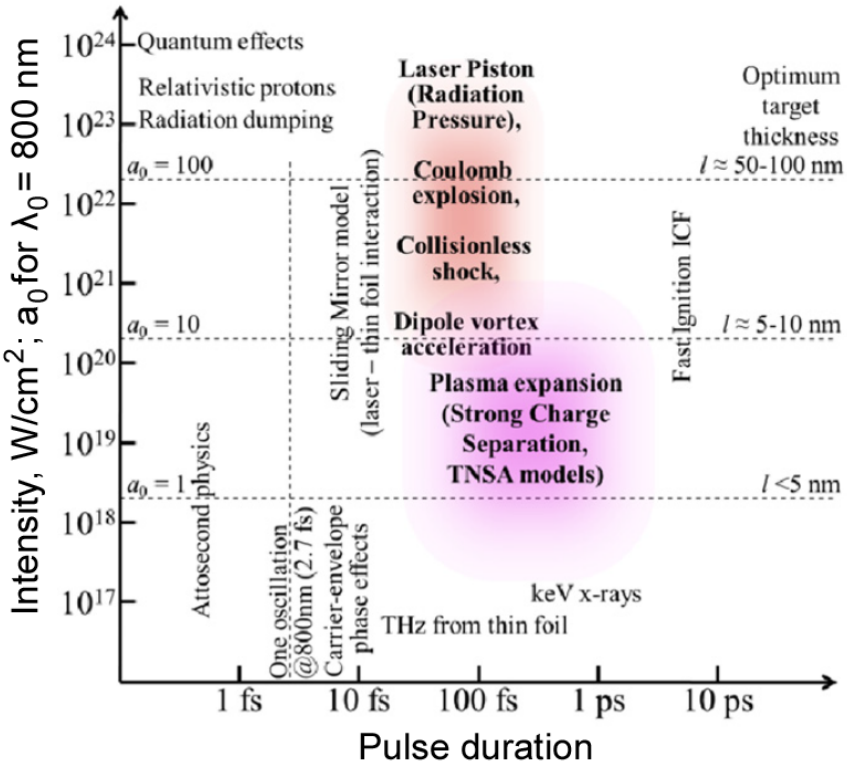


**Figure 1.17:** *Summary of possible laser–driven acceleration mechanisms in different laser–matter interaction conditions in the (intensity,pulse duration) plane. From [7].*

which each mechanism is dominant are highlighted. Due to the complexity of laser–matter interaction in the relativistic regime, it is not possible to draw sharp boundaries between different acceleration regimes: the transition between different acceleration mechanisms is gradual, thus many effects can contribute to the acceleration process.

### 1.2.2 Applications

The possibility of inducing nuclear reactions and the sensitivity to density gradients and electromagnetic fields make accelerated ions, and especially protons, very interesting in view of possible applications. In particular, one of the most relevant features of proton and ion beams is the highly localized energy deposition in materials, due to the peculiarity of their interaction with dense matter. While other kinds of radiation such as electrons, X and $\gamma$ rays release their energy gradually as they propagate in a medium, the profile of energy deposition for proton and carbon ions shows that these particles release most of their energy in a localized region at the end of their path, in the so called Bragg peak [103, 104]. This difference is evident from Figure 1.19, in which the relative dose (i.e the energy absorbed per unit mass) released in matter by protons, carbon ions, electrons and ionizing electromagnetic radiation (X and $\gamma$ rays) is plotted as a function of the travelled depth. The presence of a sharp peak at the end of the absorbed dose curve of hadrons is related to the Coulomb collisions which cause most of the

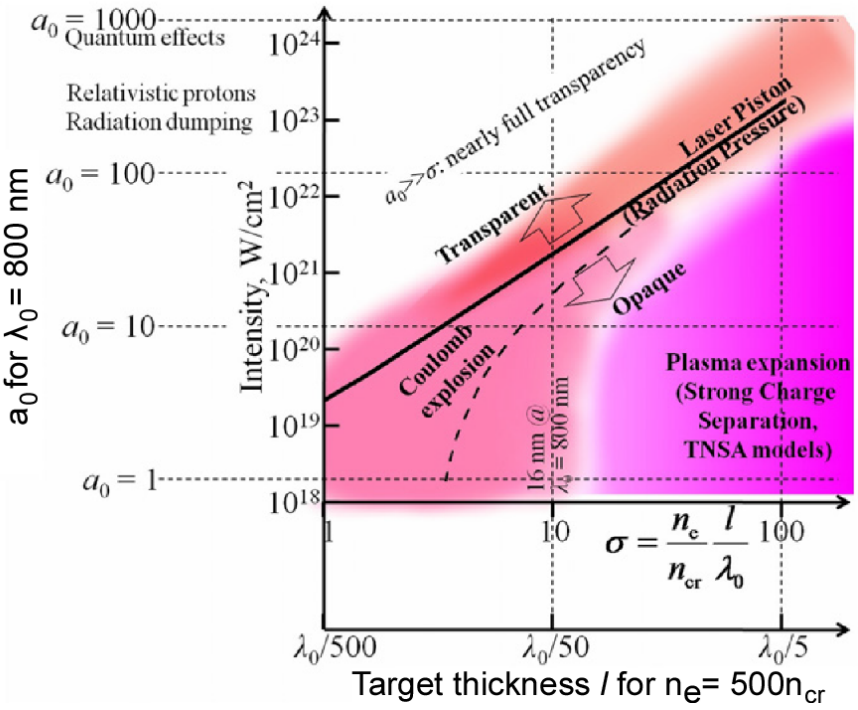


**Figure 1.18:** *Summary of possible laser–driven acceleration mechanisms in different laser–matter interaction conditions in the (intensity,areal density) plane. From [7].*

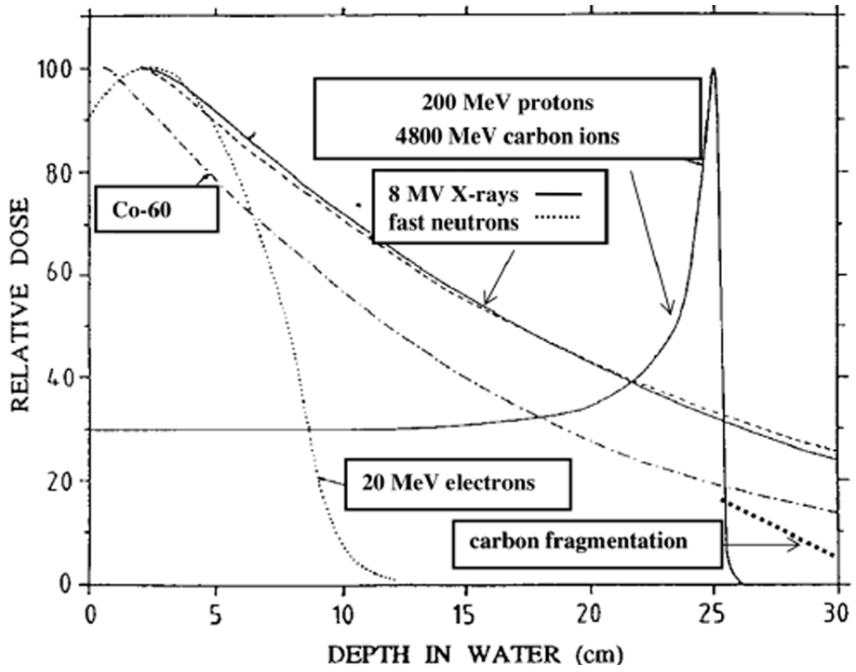


**Figure 1.19:** *Example of the energy deposition profile for protons and carbon ions in water, compared to those of X–rays, $\gamma$ rays and electrons. From [103].*

energy loss and whose cross section is strongly increased for low energy. Therefore due to their energy release profile, protons and other ions are very appealing for applications in which highly localized and/or tunable energy deposition is re-

quired.
As a consequence, one of the main reasons of the great interest raised by laser–driven ion acceleration is the possibility of producing ps collimated bunches of ions, containing $10^{11}$ to $10^{12}$ ions per bunch, with energy of several 10s MeV and extremely low emittance, with a relatively compact and cheap experimental apparatus [2–4].
One of the most interesting current applications of laser–driven ion sources is proton probing. Collimated proton bunches are particularly suitable as probe beams for material characterization and plasma diagnostics, thanks to their high sensitivity to areal density variations (affecting the proton distribution in the transverse plane due to differential absorption and scattering) and to electric and magnetic fields (deflecting charged particles during their propagation). The high degree of laminarity and small emittance allow to resolve details with spatial dimension down to a few $\mu$m. In addition, being emitted from a point–like source with a characteristic divergence, laser–driven ion sources provide intrinsically a magnification factor that depends on the probing geometry. The ps duration of proton bunches allows to investigate fast dynamical phenomena with good time resolution and the characteristic energy dispersion of TNSA protons provides intrinsic multi–frame capabilities, since protons with different energies reach the object under analysis at different times. Thus, if the proton signal is collected with a radiochromic film stack recording for each film layer the signal due to protons with energy in a given range, the layers directly provide a description of the probed system at different times. This approach allows to span time intervals up to 100 ps and was employed, for example, by Romagnani *et al* [58] to detect the structure of the accelerating sheath field produced by hot electrons in TNSA (see Figure 1.8). In general, the interpretation of proton probing results are supported by iterative particle tracing codes simulating the propagation of protons through space and time dependent systems.
Proton probing can be exploited to detect density variations: in this case it is referred to as proton radiography. This technique has an interesting possible application in Inertial Confinement Fusion (ICF), even though 50–100 MeV would be required to probe actual compressed ICF targets, and has been tested in a preliminary study of the compression of empty CH spherical shells induced by several low intensity ($10^{13}\,\mathrm{W/cm^2}$) laser beams [105] shown in figure 1.20.

Laser–driven proton probing paved the way for a completely new diagnostics for fast dynamics in plasmas, which had previously been prevented by the high costs, technical difficulties and poor temporal resolution of conventional accelerated particle sources. Two approaches have been adopted so far to apply proton probing to the investigation of plasma fields: proton imaging, based simply on the backlighting projection of the sample, and proton deflectometry, in which a mesh is introduced between the beam source and the plasma to be probed to divide the beam itself into beamlets and detect the deflection of single beamlets. In Figure 1.21 an example of proton imaging application is reported: proton imaging allows to observe the formation of a channel in the interaction of an intense laser pulse with an under–dense plasma, the filamentation of the propagating laser beam and the channel wall modulations [106]. Figure 1.22 shows an example of proton

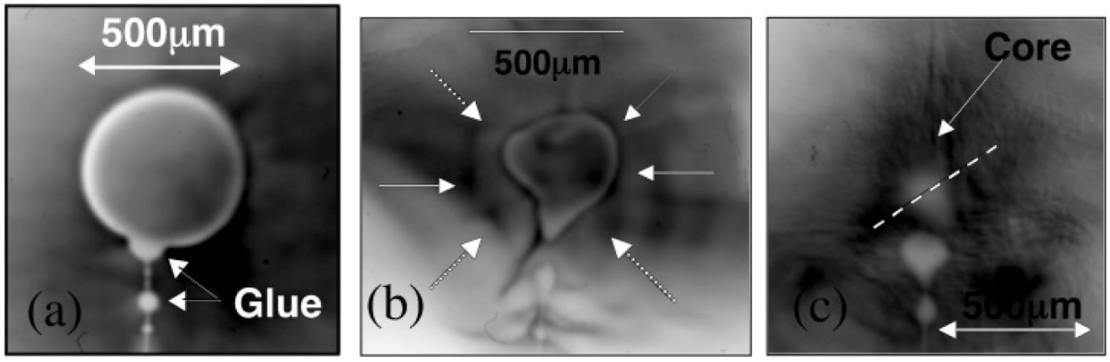


**Figure 1.20:** *7 MeV proton radiographs of (a) undriven shell with diameter 500 μm and wall thickness 7 μm; (b) highly asymmetric implosion due to bad synchronization of the laser pulses; (c) compressed microballoon with 500 μm diameter and 3 μm thick wall. From [105].*

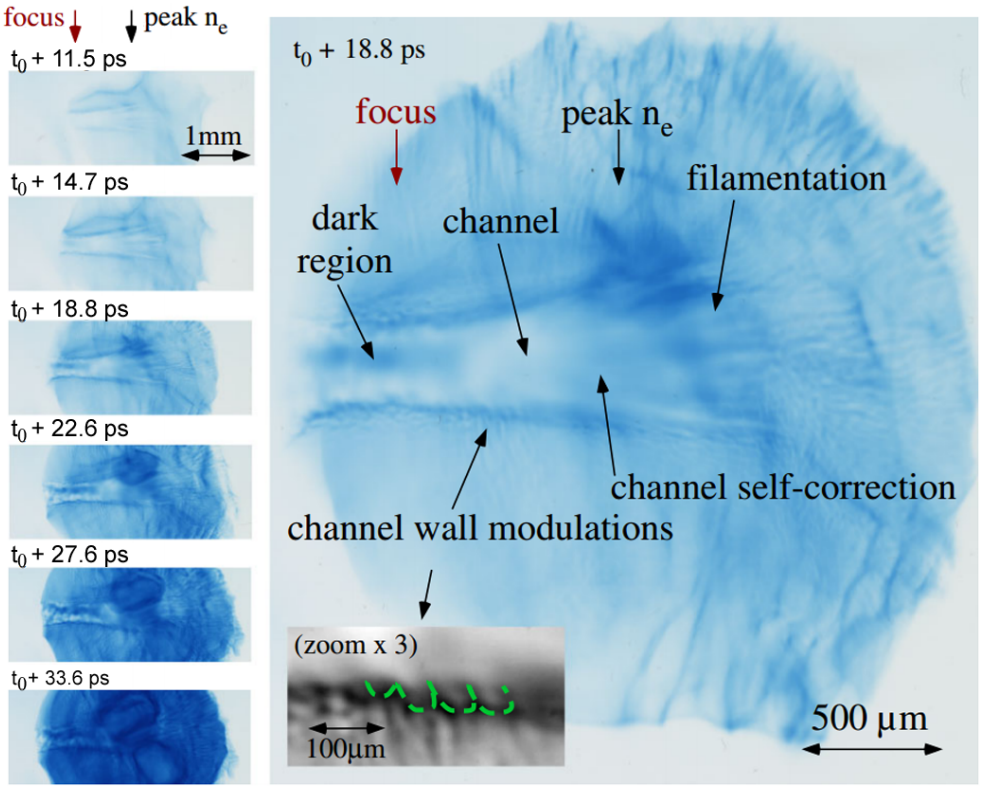


**Figure 1.21:** *Sequence of proton probing images showing the formation of a channel into a CH plasma plume with peak density* $0.05n_c$ *(left). On the right a blowup of an image is shown, with an inset illustrating a region of the channel wall. From [106].*

deflectometry applied to the study of magnetic fields produced in the interaction between a long (ns) pulse with moderate intensity ($10^{15}$ W/cm$^2$) and a 6 $\mu$m–thick Al foil [107]. A tracing code was employed to support the deflectogram interpretation: the inversion of the deflection pattern observed for proton beams incoming from the two sides of the foil was attributed to the presence of a toroidal magnetic field.

A second application of laser–driven ion sources, requiring single bunches of

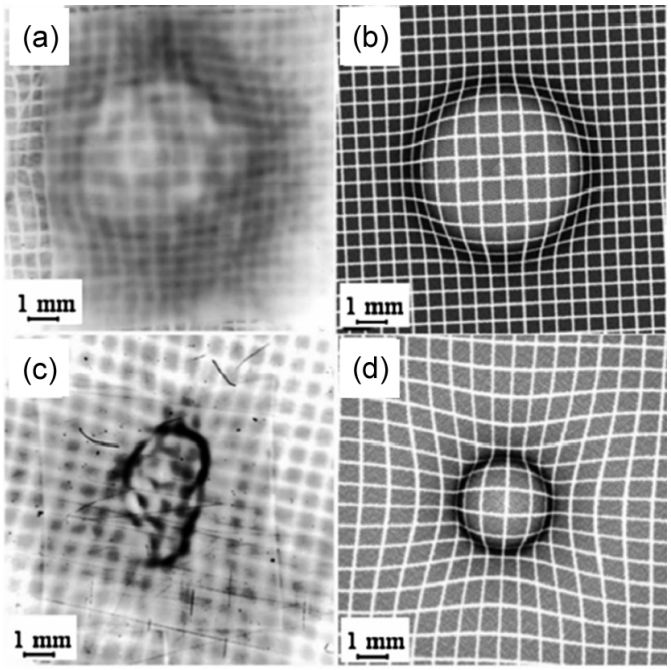


**Figure 1.22:** *Proton deflectometry of magnetic fields in laser–irradiated 6 $\mu$m–thick Al foils (ns pulse, $10^{15}$ W/cm$^3$): probing deflectrograms with proton beam entering from the non–irradiated (a) and from the irradiated side (c); corresponding simulated proton transverse distributions (b),(d). From [107].*

ions with short duration and high energy flux, is proton heating and in particular isochoric heating. This is the heating of a material to high–temperature plasma states while keeping its volume constant, to produce so–called Warm Dense Matter (WDM) states, characterized by density between 0.01 g/cm$^3$ and 100 g/cm$^3$ and temperatures of a few eV (up to 100 eV) and of high interest for fundamental physics, but also for planetary and stellar astrophysics and material studies [108]. A desirable condition in studying the fundamental properties of WDM is the uniform heating of large volumes, which makes WDM properties easier to diagnose and prevents the formation of strong gradients in the sample. Therefore, heating should occur on very short timescale, before the hydrodynamic expansion of the heated sample. The application of ultrashort–pulse proton beams to isochoric heating was demonstrated for the first time by Patel *et al.* [109]. Here, 10 $\mu$m–thick Al foils were heated to 4 eV and 20 eV at solid density on a few ps timescale by protons produced in the interaction of an incoming laser pulse and a flat or hemispherical target, respectively. The experimental configuration adopted in this study and the resulting target heating detected via time and space resolved rear surface emission are reported in figure 1.23. It is worth noticing how the adoption of an hemispherical target allowed to produce a focused proton beam and, as a consequence, to heat a reduced sample area to higher temperatures.

Besides being currently exploited for proton probing and warm dense matter studies, laser–driven ion sources are appealing for a number of possible applications requiring an enhancement of acceleration performances in terms of accelerated charge (i.e. average ion current), cut–off energy or spectral properties. The

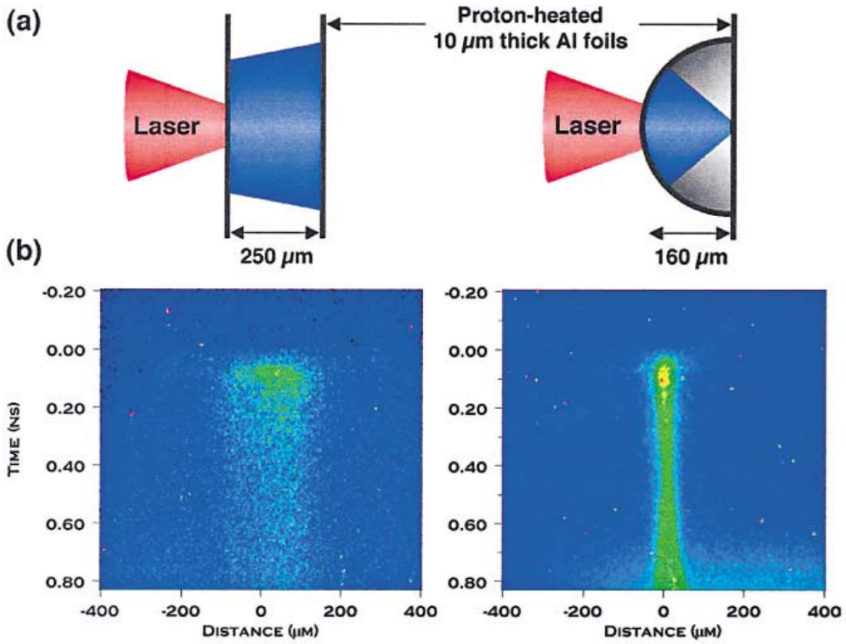


**Figure 1.23:** *Experimental setup for isochoric heating of Al foils in the flat and hemispherical geometries (a). Corresponding streak camera images showing time and space resolved thermal emission at 570 nm from the rear side of the heated foils (b). From [109].*

possibility of achieving high average ion currents is related to the availability of high repetition rate lasers and target positioning systems, thus mainly technological issues need to be solved for the effective application of laser–driven ion sources. The maximum repetition rate of laser systems, at present, is usually around 10 Hz, while several kHz would be required to achieve an average current comparable to radiofrequency–wave based accelerators. If such repetition rates were available, laser–driven proton beams could be exploited, for instance, to induce nuclear reactions (for example for the production of specific radioisotopes), to test components simulating extreme environments or for material processing and characterization. On the other hand, applications requiring also enhanced maximum ion energy or monochromatic ion beams demand the development of enhanced or novel acceleration schemes. This is the case of fast ignition of targets for inertial fusion or oncological hadrontherapy.
Protons with energy of 10s MeV can be exploited to induce nuclear reactions with the aim of producing short lived radioisotopes for nuclear medical diagnostic techniques, as Positron Emission Tomography, PET, ($^{18}$F, $^{11}$C, $^{82}$Rb or $^{68}$Ga) and scintigraphy ($^{99}$Tc). The main requirements to successfully employ laser–driven proton sources for the production of radioisotopes are the possibility of achieving an appropriate proton yield per unit time and proton energy at least above the reaction threshold (or better around the reaction maximum cross section) to produce activities of $\sim 1$ GBq. For example, the most widespread compound for PET diagnostics, $^{18}$F, is produced exploiting the $^{18}\mathrm{O}(\mathrm{p},\mathrm{n})^{18}\mathrm{F}$ reaction, whose energy threshold is 2.4 MeV and has maximum cross section around 5 MeV. Many

hospitals are equipped with their own cyclotrons for the production of radioisotopes for medical diagnostics. These machines have diameters of a few meters and deliver 100s $\mu$A currents of 10–30 MeV protons. The main drawbacks of hospital cyclotrons, besides the large size and relevant costs, are radioprotection issues, and in particular the activation of structural materials (especially around the target) and the requirement of an appropriate shielding. Feasibility studies demonstrated the possibility of applying laser–driven ion sources to the production of radioisotopes for both relatively long and energetic pulses (100 J, 1 ps) [110] and short, tight focused pulses with lower energy (30 fs) [111]. The repetition rate requirements calculated extrapolating the results of these proof–of–concept investigations are 10 Hz for 1ps pulses and 1 kHz for 30 fs pulses.
A number of possible applications of laser–driven ion sources (also on industrial scale) have been proposed for material irradiation for processing, characterization and testing.
One of the possible industrial applications of laser–driven ion sources is ion implantation. Since laser driven ion acceleration can provide high charge states (resulting in deeper ion implantation), many kinds of ion species and the ion source can easily be positively biased. The feasibility study of laser–driven ion implantation was performed by Torrisi *et al.* [112]. According to this study, however, the average current values achieved with laser–driven ion acceleration are still too low: to achieve the required fluence ($10^{13} - 10^{17}\,\mathrm{ions/cm^2}$) for protons with average energy $\sim$0.5 MeV, 0.1 J pulses with repetition rate 1 kHz would be required for a process duration of 17 minutes, provided an energy conversion efficiency from laser radiation to ions around 10%.
The possibility of exploiting proton beams for the production of radioactive isotopes, for example, can be applied to the evaluation of the wear or consumption of machine components through the activation of elements as Fe, Ti or Cr in a thin surface layer of the component to be tested. The variation of the surface activity due to usage allows to assess the amount of material lost by the component. This technique is known as Thin Layer Activation (TLA). Ogura *et al* studied the feasibility of TLA of boron nitride with proton bunches accelerated in the interaction of 30 fs 1 J pulses with a polymide tape target [113]. The reaction exploited for boron activation ($^{11}\mathrm{B(p,n)}^{11}\mathrm{C}$) had threshold around 2.76 MeV. The activity achieved in 60 shots was evaluated from the annihilation of positron produced by decaying $^{11}$C isotopes and was around 11 Bq. The activation achievable in 10 minutes with 1.7 J 34 fs pulses at repetition rate around 10 Hz, extrapolated from these results, would be sufficiently high for typical TLA application.
In addition, laser–driven ion sources can be employed to investigate radiation damage in materials. This possibility is of particular interest to test components for fission nuclear reactors, nuclear fusion machines or spacecrafts by simulating the environment in which they should operate. Low energy laser–driven protons ($<$ 1 MeV) with broad spectrum emitted with X–rays and electrons in the MeV range can also be extremely interesting to test the damage induced by cosmic radiation in solar cells, provided that an accurate characterization of laser–driven radiation emission is available.
The interaction of laser–driven accelerated ions with matter can be exploited to

perform nuclear physics experiments in laser facilities. For example, McKenna *et al.* investigated the production of compound nuclei in the interaction of high Z accelerated ions with matter and their de–excitation through the evaporation of protons, nucleons and $\alpha$ particles [114–116]. Moreover, laser–driven proton beams with broad energy spectrum can simulate the secondary radiation produced by spallation reactions due to the incidence of high energy protons (1 GeV) with thick high Z materials: in this kind of system, 10s MeV protons and neutrons produced in the intranuclear cascade and through evaporation lead to the production of residual nuclides through secondary reactions [117]. However, the application of laser–generated ions to particle physics would require a significant enhancement in the energy of accelerated particles, since energies $\sim$ 1 GeV/nucleon would be required to reach a relativistic regime. The production of pions by high energy protons beams accelerated by ultra–high intensity pulses ($> 10^{21}$ W/cm$^2$) could allow to achieve pion fluxes much higher than those achieved with other techniques [118]. Protons accelerated by pulses with intensity around $10^{23}$ W/cm$^2$ could produce pulses of 20 MeV muon neutrinos [119]. A more foreseeable application is the production of neutron beams in the interaction of laser–driven protons and secondary targets [120]. The possibility of achieving laser–driven neutron sources has great applicative potential and several advantages with respect to neutrons produced in conventional acceleration facilities or extracted from nuclear reactors due to the short bunch duration, high brightness, but also in terms of compactness and costs of the experimental apparatus.
An interesting and widely investigated application of laser–driven proton or ion bunches is the fast ignition of nuclear fusion targets [118, 121]. The conventional approach for energy production by nuclear fusion in the inertial confinement approach is based on the implosion of a pellet of thermonuclear fuel, composed by a deuterium–tritium mixture [122]. The compression, driven by ns laser pulses, produces a core plasma with suitable density and temperature conditions to have nuclear fusion reactions (ignition) between deuterium and tritium nuclei in a central hot spot of the fuel pellet. However, an extremely high degree of symmetry is required to achieve ignition and the process is strongly quenched by hydrodynamic instabilities. The fast ignition scheme allows to relax the requirements on system symmetry by separating the compression and ignition stages: the ignition is induced in the compressed pellet by an external trigger [123]. The highly localized energy deposition of heavy charged particles (see Figure 1.19), the low emittance and the beam focusability make laser–driven protons particularly suitable as fast ignition triggers in the fast ignition scheme [121]. According to detailed calculations performed by Atzeni, Temporal and Honrubia [124, 125], the quasi–thermal energy distribution of TNSA protons could favour energy deposition in the compressed fuel pellet, since the heating produced by higher energy protons leads to an enhancement of the energy deposition of lower energy protons, reaching the hot spot with some delay. On the basis of these simulations, the energy required to trigger the ignition process could be reduced by decreasing the distance between the proton source and the fuel pellet, provided that the target is suitably shielded to prevent damage and preheating due to external radiation. An example of target configuration adopted to investigate TNSA–based fast ignition is

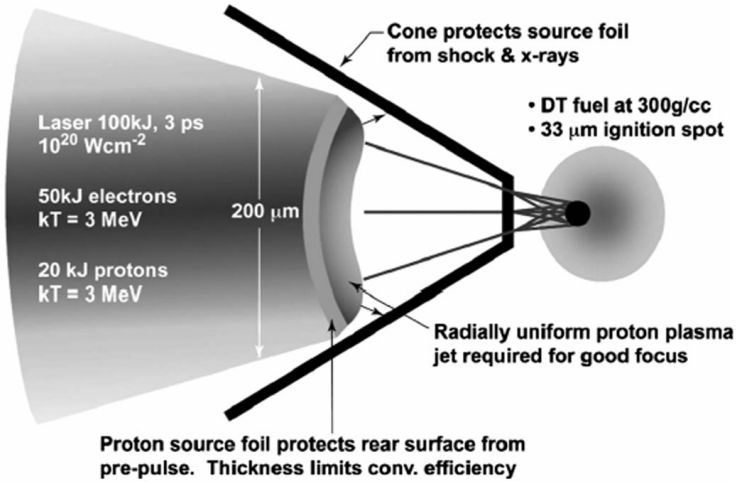


**Figure 1.24:** *Concept of proton–driven fast ignition in the TNSA–based fast ignition of inertial fusion targets. From [126].*

reported in Figure 1.24 [126]. The possibility of using ions with $Z > 1$ has been widely studied due to the higher stopping power of heavier ions with respect to protons [118]. In this case narrow energy spectra would be required to reduce the ignition threshold, thus ions accelerated via RPA or BOA would be more suitable than quasi–thermal beams produced by TNSA and the condition on the source–pellet distance would be removed. According to calculations performed by Honrubia *et al.* the conditions for fast ignition for beam of C ions are 400–500 MeV/nucleon and $\delta\mathcal{E}/\mathcal{E} < 0.2$ [127].
The localized energy deposition of protons and ions characterized by the Bragg peak makes heavy charged particles particularly suitable for oncological radiotherapy, since the peculiar shape of the hadron energy deposition profile in matter allows to irradiate tumour tissues and to prevent radiation damage in surrounding healthy tissues. Oncological hadrontherapy is based on the extremely precise irradiation of the tumour region both in the transverse plane and in the longitudinal direction, by properly tuning ion energy distribution to spread out the Bragg peak. The high ballistic precision of hadrontherapy makes it particularly suitable for tumours which couldn't be surgically removed or are located in proximity of vital organs (such as for example eye cancer). At present, hadrontherapy is commonly employed in several facilities equipped with synchrotrons, cyclotrons or linac accelerators and with suitable beam delivery systems, including large, massive and costly gantries (magnetic steering systems employed for multidirectional irradiation). In this frame, laser–driven ion acceleration systems could offer several advantages, in terms of compactness, costs, minimization of ion beam delivery issues [128, 129]. However, the energy required for therapy (60–250 MeV for protons, up to 400 MeV/nucleon for $C^+$), the narrow energy spectrum ($\delta\mathcal{E}/\mathcal{E} < 10^{-2}$), the average current (10 nA for protons, 1.2 for $C^+$) and the high reliability level required for medical application demand a significant enhancement of the acceleration performances achieved so far for laser–driven ion sources [130]. Several studies have been performed to design possible ion delivery systems [131], to obtain

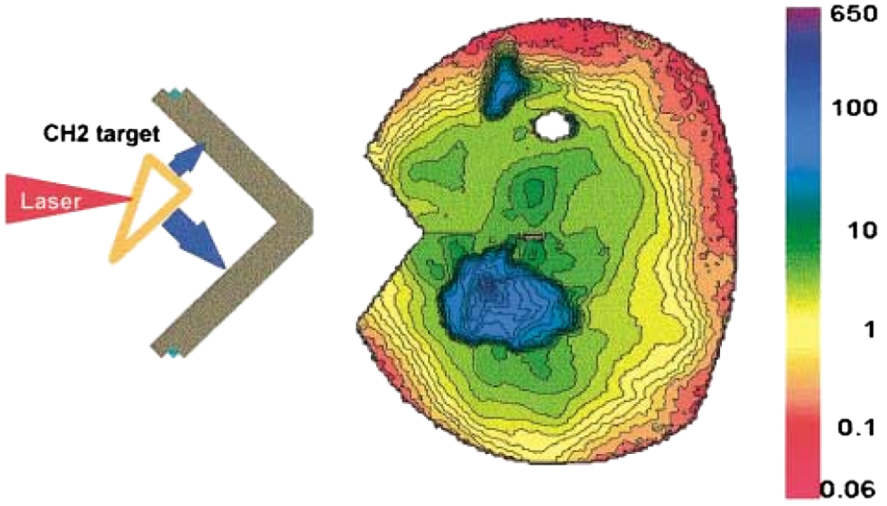


**Figure 1.25:** *Proton emission from a wedge target (dose contour plot): the presence of two separate spots provides experimental evidence that the ions are emitted from the rear target surfaces. From [4].*

suitable energy spectra distributions from the typical TNSA spectra [132] and to investigate the peculiar biological effects of pulsed, ultra–short proton beams [133] also in unexplored non–linear regimes of radiobiology [134].

## 1.3 Advanced target configurations

As mentioned in the previous section, the properties of accelerated protons and ions in the interaction of ultra–intense ultra–short laser pulses with matter are strongly dependent on the experimental conditions, i.e. on the pulse parameters and the target properties. In particular, the effect of target properties on acceleration mechanisms has been extensively studied in literature, especially as regards TNSA, to achieve a deeper insight in the physics of laser–driven ion acceleration and to tailor the properties of accelerated ions for applications. A peculiar target configuration was exploited in the first studies on TNSA to identify the ion emission region: wedge targets provided evidence that the emission of accelerated ions in the direction orthogonal to the rear target surface (Figure 1.25). Moreover, engineered targets with microgrooves on the rear target surface were used to achieve a precise evaluation of the TNSA proton beam transverse emittance through the observation of the transverse distribution of accelerated ions [9], as shown in Figure 1.9.
In general, the design of advanced targets is a promising strategy to optimize the laser–matter interaction phase, to select a particular acceleration scheme and to control the properties of accelerated ions. In this frame, many possible target configurations have been proposed to tailor the performances of laser–driven ion acceleration and in particular of TNSA, which is the most frequently observed acceleration mechanism in presently available experimental conditions. A few examples of target configurations proposed in literature to tailor TNSA perfor-

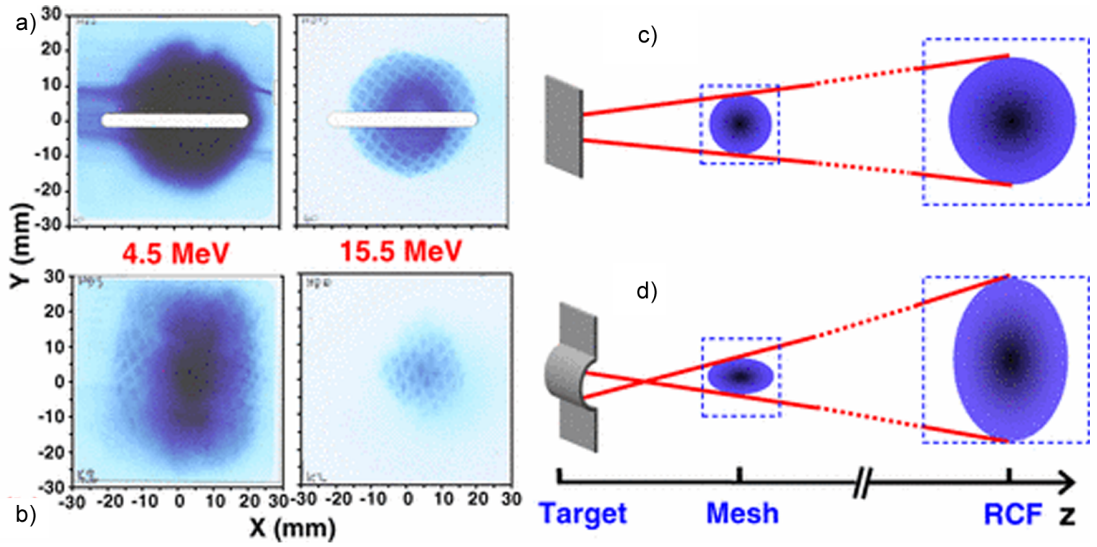


**Figure 1.26:** *Hemicylindrical targets for ion focusing. Experimental proton beam profiles for a reference flat foil (a) and an hemicylindrical target (b) for two different energies and sketch of the proton beam longitudinal envelope and observed beam transverse profiles at different planes for flat foil (c) and hemicylindrical targets (d). From [135].*

mances are illustrated in Subsection 1.3.1). In Subsections 1.3.2 and 1.3.3, two microstructured target configurations considered in my PhD thesis are described, namely *foam–attached targets*, exploiting the enhanced laser absorption in near–critical plasma, and *grating targets*, enhancing laser energy absorption through the resonant excitation of plasmonic surface waves.

### 1.3.1 State of the art

A number of different target configurations have been proposed so far to tailor the properties of laser–driven ion sources, especially TNSA, in view of specific applications. The possibility of enhancing the beam spatial quality, to achieve monoenergetic ion beams, to enhance the cut–off energy and the number of accelerated ions have been widely investigated.
The spatial quality of accelerated ion beams, for example, can be tailored exploiting the structure of the rear target surface, as in the case of the above mentioned wedge targets [4] and targets with modulated rear surface [9]. In 2001, Wilks *et al.* performed PIC simulations on an ion lens configuration showing that thin solid targets with bent rear surface should allow to focus accelerated ions to a point [5]. This target configuration was experimentally investigated by Kar *et al.* [135] using thick hemicylindrical targets with 250 $\mu$m thickness and 350 $\mu$m radius of curvature. As a result, the proton beam was focused at $\sim$ 1 mm from the rear target surface, as shown in Figure 1.26. In 2012 Bartal *et al.* proposed a more complex target configuration, in which an hemispherical target was coupled with a conic structure to achieve a compact proton focusing device [136].
The design of innovative targets can be also exploited to manipulate the spectrum of accelerated ions achieving, for example, narrow energy peaks. In 2002,

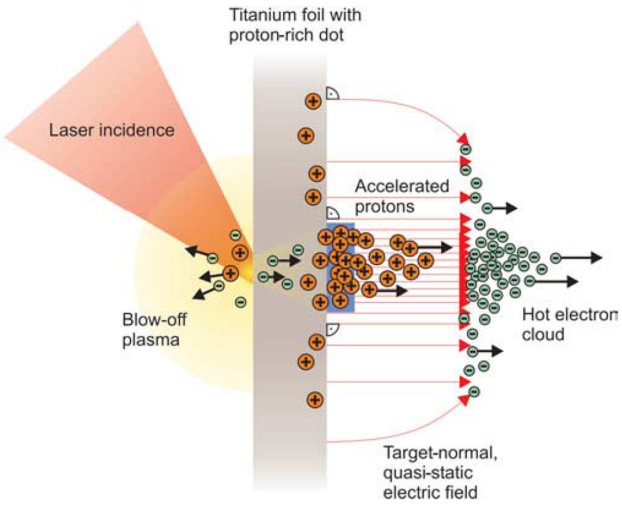


**Figure 1.27:** *Sketch of laser–driven acceleration of protons from the rear side of a structured target with PMMA micro–dots. From [138].*

Esirkepov *et al.* proposed double–layer targets composed by a high Z layer on the front side (i.e. a metallic foil) and a low Z thin coating on the non illuminated side (i.e. a hydrogenous coating) with transverse size lower than the laser focal spot area [137]. This configuration was experimentally tested in 2006 by Schwoerer *et al.* using 5 $\mu$m thick Ti foils with PMMA (poly-methyl methacrilate) dots (thickness $\sim 0.5\,\mu$m, transverse size 20 $\mu$m $\times$ 20 $\mu$m) [138]. This target design, shown in Figure 1.27, allowed to produce of proton bunches with narrow energy spectrum, since the presence of a small hydrogen rich dot on the rear surface enhanced the proton yield in the central part of the electron sheath at the rear target surface, where an approximately homogeneous accelerating field was expected. Moreover, the number of protons present in the dot was not sufficient to significantly reduce the accelerating field, thus the accelerating field was almost the same for all the emitted protons. Another strategy proposed to achieve better ion spectrum quality was based on the removal of hydrogen contaminants from the target surface and the formation of an ultra–thin graphite layer by catalytic decomposition of adsorbed hydrocarbon impurities on the surface of a 20 $\mu$m thick palladium foil [139]. Due to the extremely small thickness of the graphite layer at the rear surface, carbon ions, and especially $C^{5+}$, were accelerated at once by the sheath field, resulting in a reduced energy spread ($\sim 17\%$).
One of the main goals in the design of targets for TNSA is the enhancement of the energy of accelerated ions, since some of the foreseen applications of this technique (see Section 1.2.2) require ion energy up to several hundreds of MeV per nucleon, much higher than the maximum energy of particle beams currently produced by laser–driven ion sources. As mentioned before, the first parametric studies on the effect of target thickness on the properties of accelerated ions showed an enhancement of the cut–off energy for decreasing target thickness in the $\mu$m range [55]. However, Kaluza *et al.* observed that the scaling of proton cut–off energy with thickness was strongly dependent by laser contrast (see Figure 1.28): the existence of an optimum thickness value for experimental configurations with ordinary con-

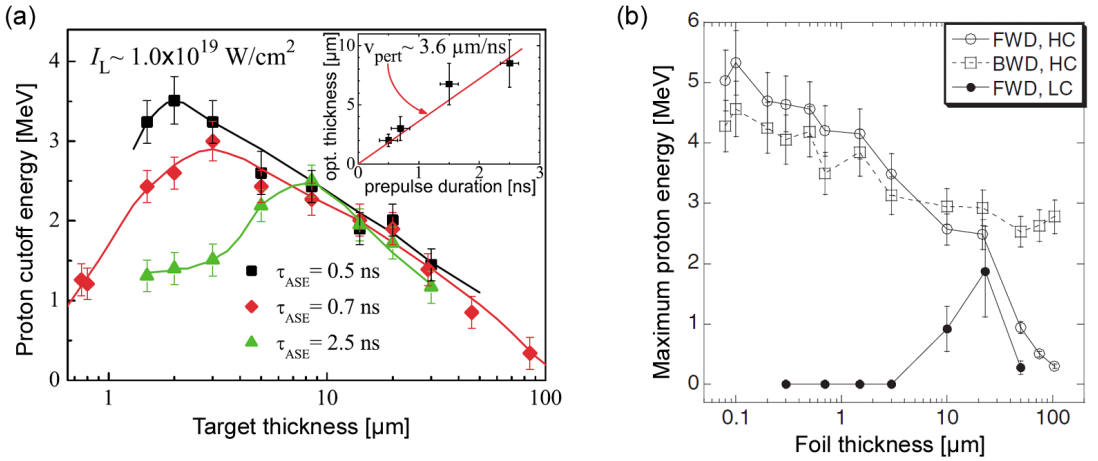


**Figure 1.28:** *Proton cut–off energies as a function of target thickness (a) for different prepulse durations, at* $10^{19}$ W/cm$^2$*, from [140], and (b) for high (*$10^{10}$*) and low contrast (*$10^6$*) at intensity* $5\times10^{18}$ W/cm$^2$ *and* $10^{19}$ W/cm$^2$*, respectively, in the forward and backward direction, from [143].*

trast values ($10^7$) was observed and the dependence of the optimum thickness value on the prepulse duration was explored [140]. These results suggest that the effective suppression of the prepulse, i.e. the adoption of higher contrast configurations, should allow to reduce the target thickness to the sub–$\mu$m range since in this case the target integrity is maintained until the main pulse incidence and, consequently, to achieve higher proton cut–off energy. Experimental campaigns performed in ultra–high contrast configuration ($> 10^{10}$) provided the evidence of the significant enhancement of the maximum ion energy with ultra–thin targets (down to 20 nm) Figure 1.28 [141–143].

Ultra–thin solid foils represent a relatively simple example of target design for TNSA cut–off energy enhancement, but a number of other possibilities have been considered. For example, in 2001 Badziak *et al.* reported an increase in the proton number and energy with double layer targets composed by a high Z front layer and a low Z rear layer [144]. In 2008, Psikal *et al.* proposed the so–called reduced–mass targets, thin solid foils of limited transverse extent (down to tens of $\mu$m) [145]. In this configuration, the transverse electron reflux due to electron reflection at the target edges should allow to maintain a hotter, denser and more homogeneous electron sheath around the target for a longer time. Buffechoux *et al.* demonstrated a twofold (up to threefold) enhancement of the maximum proton energy with 2 $\mu$m thick Au targets with surface area around $2 \times 10^3\,\mu$m$^2$ [146]. Gaillard *et al.* reported the observation of protons with energy cut–off about 67.5 MeV with a more complex geometry combining a classic thin foil target and a micro–cone structure to form a flat–top microcone [147]. The cut–off energy enhancement with respect to the conventional thin foil configuration was about 35%. The proton energy increase in this case is due to the enhanced production of hot electrons through a laser–light–pressure electron acceleration mechanism which takes place in the inner micro–cone wall [148].

Some target configurations proposed in the last few years exploit the presence of

nano or micro–structures on the directly irradiated surface of a solid foil to achieve a better control of the laser–matter interaction phase and to enhance the coupling between laser and plasma. These targets configurations exploit different physical processes to enhance the production of hot electrons and, as a consequence, the maximum energy of ions produced by TNSA. In 2011 Zigler *et al.* proposed sapphire foil targets covered with snow nanowires (i.e. nanometer size $H_2O$ frozen droplets) [149]. This configuration allowed to observe 5.5–7.5 MeV protons with moderate intensity ($5 \times 10^{17}\,\mathrm{W/cm^2}$), for which TNSA is usually quenched, due to the interaction of the laser pulse with the nanoplasma columns generated by the prepulse interacting with the nanowires on the target surface. In 2012 Margarone *et al.* investigated ion acceleration from plastic targets covered with a single layer of microspheres [150]. The optimum target configuration allowed to produce protons with maximum energy around 8.4 MeV with $5 \times 10^{19}\,\mathrm{W/cm^2}$, achieving an enhancement around 60% with respect to the reference thin foil target. The number of accelerated protons was enhanced by a factor of 5. The laser energy absorption enhancement was partly due to the larger interaction surface, thanks to which a higher number of particles could interact with the laser field. Moreover, the presence of nanospheres screened the incident laser wave. As a consequence, electrons propagating in the spheres were out of the laser wave phase, thus gaining energy more efficiently along the longitudinal direction. This mechanism was quite similar to the multipass stochastic heathing suggested by Breizman *et al.* for laser absorption in clusters [151].

### 1.3.2 Foam–attached targets

In general, the interaction of the laser prepulse with a solid foil produces a plasma with an exponential density profile. As mentioned in Subsection 1.1.2, the interaction of the main pulse with this non–uniform plasma can be very effective around the near–critical surface, but the near–critical region of the expanding plasma can have a reduced extension and the density gradient length–scale is out of complete experimental control. The enhanced laser absorption in near–critical plasma due to the coexistence of volume and surface absorption mechanisms, as well as additional absorption phenomena, can be exploited by positioning a near–critical uniform volume in front of the target surface, to optimize the pulse absorption. On the basis of these considerations, multilayer targets composed by a thin solid foil with a low–density layer (*foam*) on the directly illuminated target surface have been recently investigated through PIC simulations by Nakamura *et al.* [13] and Sgattoni *et al.* [14].
The targets considered by Nakamura *et al.* in [13] were composed by an uniform $SiO_2$ foam layer with thickness 3 $\mu$m and density 4.5 $\mathrm{mg/cm^3}$ and a 1 $\mu$m thick Al foil and the acceleration process was driven by a 40 fs laser pulse propagating in the positive $x$ direction, with intensity $10^{19}\,\mathrm{W/cm^2}$, wavelength 1 $\mu$m and no prepulse. In Figure 1.29, the simulated time evolution of ion charge density and the transverse electric field distributions are illustrated. After 50 fs a weak modulation of the charge density could be observed along the laser propagation direction. The reflection of the laser radiation at the foam–foil interface produced an electro-

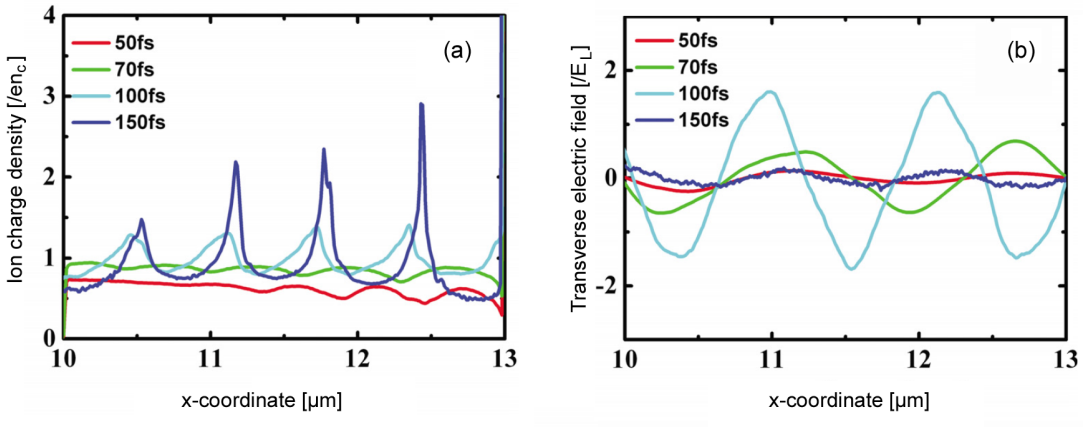


**Figure 1.29:** *Simulated time evolution of ion charge density (a) and laser field (b) distributions during the irradiation of a foam–attached target. From [13].*

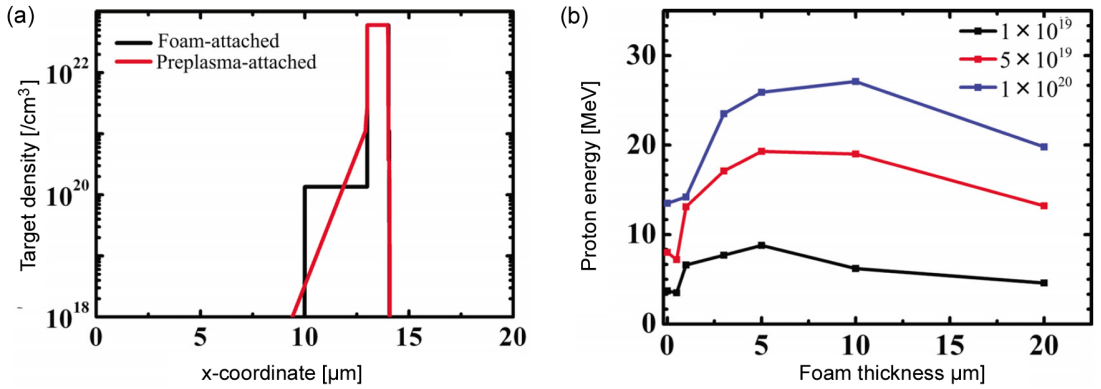


**Figure 1.30:** *Comparison between foam–attached and pre–plasma attached targets: (a) initial density profile; (b) maximum proton energy plotted as a function of foam thickness for different intensities. Foam density is* $\rho = 4.5\,\mathrm{mg/cm^3}$. *From [13].*

static wave field, which amplified the ion density modulation (70–100 fs). Then, the charge density evolved in a periodic spike structure in which under–dense regions were enclosed in high–density spikes (120–150 fs). The periodic structure of the charge density was induced by an initial spatial modulation in the ionization distribution and was much less pronounced when the ionization process was not taken into account. In Figure 1.30, the simulated maximum proton energy for foam–attached targets with foam density of 4.5 mg/cm$^3$ and thickness 0.5–20 *mu*m and solid foils with an expanding pre–plasma on the front surface (shown in figure in correspondence with $L = 0\,\mu$m) are compared. A gain factor up to $\sim 2.5$ was observed for foam–attached targets with respect to the pre–plasma attached configuration for optimized foam thickness.
Laser–driven ion acceleration with C foam–attached Al solid foils was extensively investigated by Sgattoni *et al.* [14]. In this study, both 3D and 2D PIC simulations were performed for 30 fs laser pulses with 3 $\mu$ focal spot and dimensionless intensity $a_0 = 8.5 \times 10^{-10}\lambda[\mu\mathrm{m}]I^{1/2}[W/cm^2]$ between 3 and 10. 3D simulations were performed to quantitatively assess the proton energy cut–off enhancement

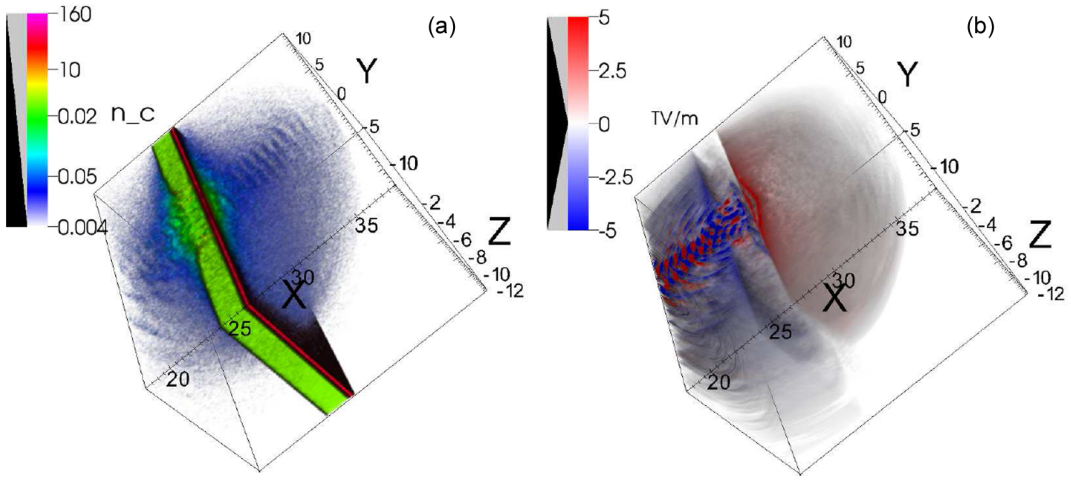


**Figure 1.31:** *Volume rendering of simulated electron density (a) and longitudinal electric field (b) at t=166 fs for a target composed by a C foam layer (3 $\mu$m, $2n_c$) on an Al foil (0.5 $\mu$m, $40n_c$) for $a_0 = 10$. From [14].*

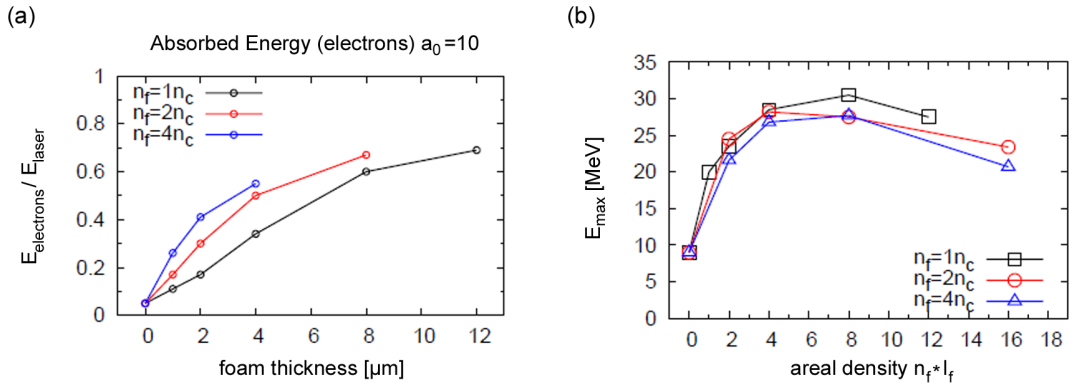


**Figure 1.32:** *Simulated (a) proton energy spectra and (b) proton cut–off energy as a function of areal density for different foam thickness and density values for $a_0 = 10$. From [14].*

produced by the presence of a low density conversion layer: for $a_0 = 10$, the maximum energy of accelerated ions in presence of a 2 $\mu$m thick carbon foam with $n = 2n_c$ on a 0.5 $\mu$m thick Al foil was 14 MeV, more than double than the cut–off value achieved for a bare Al foil (6 MeV). The electron density and the longitudinal electric field observed in the foam–attached target are illustrated in Figure 1.31. The laser pulse formed a channel in the foam layer reaching the Al foil and accelerated foam electrons. The hot electrons bunches produced by the pulse expanded beyond the rear target surface for 10 $\mu$m with a roughly spherical symmetry producing a longitudinal sheath field exceeding 5 TV/m. Figure 1.32 summarizes the results of a 2D parametric study on the effect of the foam properties on the acceleration process: according to PIC simulations the presence of a foam layer led to enhanced acceleration performances in terms of number of accelerated ions and proton cut–off energy. In addition, an optimum foam areal density range was observed for fixed laser parameters for which an increase of a 2–4 factor in the maximum energy of accelerated protons was achieved, confirm-

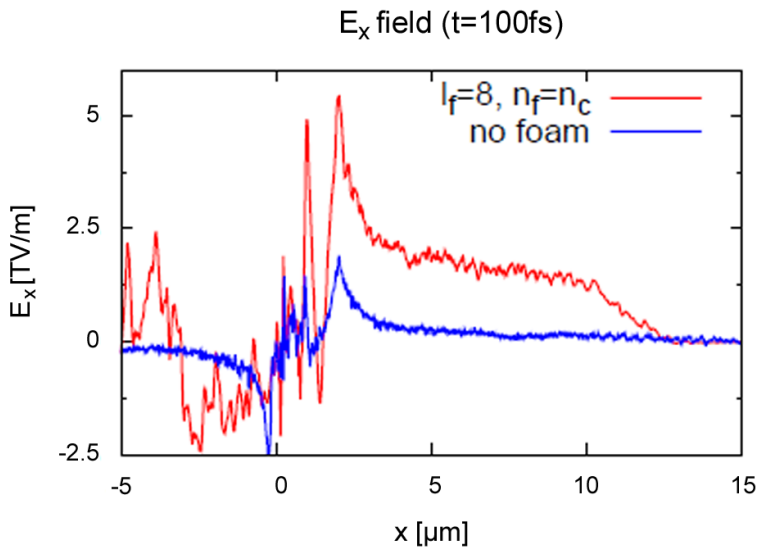


**Figure 1.33:** *Simulated longitudinal electric field on the pulse propagation axis for foam attached (8 μm thick near–critical foam) and planar targets for* $a_0 = 10$. *From [14].*

ing the results of simulations reported in [13]. According to Sgattoni *et al.* the expected energy cut–off enhancement was related to the enhanced production of hot electrons in the nearcritical plasma, leading to the onset of a stronger longitudinal electric field for foam–attached targets with respect to the case of bare thin foils, and the presence of a nearly uniform electric field for several microns from the rear target surface, which was superimposed to the exponential decreasing field typical of ordinary TNSA as shown in Figure 1.33. The investigation of the effect of the laser polarization provided indications of a strong contribution of the transverse electric field, since for normal incidence the energy cut–off enhancement was favoured for p–polarization with respect to s–polarization. This observation suggested a physical interpretation similar to the mechanism proposed for electron heating in flat–top micro–cone targets: during the laser pulse channelling in the low density plasma, a direct laser–light–pressure acceleration of electrons took place at the channel walls. Thus the p component of the electric field extracted electrons from the channel walls and the ponderomotive force accelerated them. Thus, a higher number of electrons with higher temperature is produced, leading to enhanced accelerating sheath field at the rear target surface.
Results of the simulations reported by Sgattoni *et al.* (and in particular data illustrated in Figure 1.32) were considered as a guideline for the design and production of foam–attached targets considered in this thesis, even though 2D simulations only allow to infer the qualitative behaviour of the system and often fail to provide quantitatively reliable results. From these data, a rough evaluation of optimal carbon foam properties can be inferred: the ranges of interest for the foam thickness and density are $5 - 15\,\mu$m and $3 - 10\,\mathrm{mg/cm^3}$, respectively, since the near–critical density corresponds to a $3 - 6\,\mathrm{mg/cm^3}$ for near–infrared laser wavelengths.

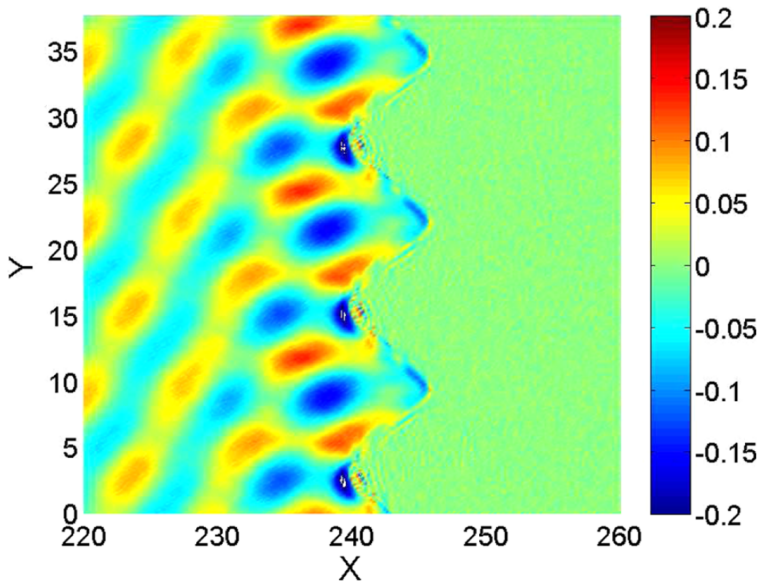


**Figure 1.34:** *Longitudinal component of the electric field of the incoming laser and the surface plasmon excited by the pulse on a modulated solid surface (left: vacuum, right: plasma, modulated surface at* $\sim 240$*). From [155].*

### 1.3.3 Grating targets

The grating target configuration was proposed by Bigongiari *et al.* [152] and Ceccotti *et al.* [153] to exploit the enhanced production of hot electrons due to the resonant excitation of electromagnetic surface waves by ultra–intense laser pulses incident with a resonance angle on a modulated surface with a periodic groove (see Subsection 1.1.2). Since a non–linear analytical description of surface plasmons is not available yet, numerical studies have been recently performed to investigate relativistic surface plasmons [154, 155].
An extensive numerical investigation on the laser–plasma coupling efficiency via surface plasma waves in a wide pulse intensity range ($10^{15} - 10^{20}\,\mathrm{Wcm^{-2}}\mu\mathrm{m}^2$) was performed by Bigongiari *et al.* [155]. Simulations were performed considering an overdense target ($n_e = 25n_c$), with surface modulation periodicity $2\lambda$ along the $y$ direction and depth $\lambda/2$ and an incidence angle of $\theta = 30°$ (laser pulse propagation along the $z$ axis). The structure of the surface plasmon electric field along the $x$ direction (shown in Figure 1.34) had the same features for all the intensity values considered. However, the maximum field amplitude was reached later for high intensity pulses. In Figure 1.35, the laser absorption ratio and the amplification factor $\eta = E_{pl}/E_x$ ($E_{pl}$ and $E_x$ electric field of the surface wave and of the incident pulse along the $x$ direction, respectively) are plotted as a function of the adimensional pulse amplitude $a_0$. From the trends reported in Figure for plane and grating targets, an enhancement in the laser absorption up to a factor $\sim 3$ is visible for the latter target configuration. The maximum absorption fraction was $\sim 77\%$ for grating targets and $\sim 40\%$ for plane targets. Moreover, a slope variation in the absorption fraction trend was observed for irradiance values around $10^{17}\,\mathrm{Wcm^{-2}}\mu\mathrm{m}^2$ for both target configurations. For plane targets, the

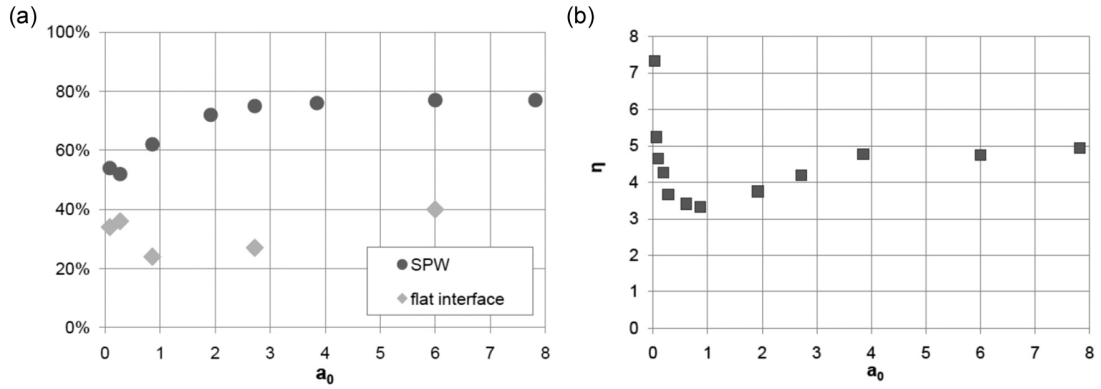


**Figure 1.35:** *Simulated laser absorption ratio for plane and grating targets (a) and plasmon field amplification factor for a modulated target(b) as a function of the adimensional pulse amplitude. From [155].*

slope variation was attributed to a transition from a regime in with dominant resonant absorption to the relativistic regime in which $\mathbf{J} \times \mathbf{B}$ and vacuum heating became dominant. The presence of a minimum in the absorption trend in the boundary regime was related to the effect of the ponderomotive force, which steepened the plasma density profile and significantly reduced the resonant absorption effectiveness. In the case of grating targets, the absorption mechanisms in the two regimes was inferred considering the amplification factor trend. For moderate laser intensities, the growth of the surface plasmon was not inhibited by the electron damping. In this regime, the electron oscillation spacescale was smaller than the extension of electromagnetic fields close to the target surface, thus electron acceleration was mainly due to the effect of the ponderomotive force and damping occurred in relatively long timescales. In the boundary regime, a minimum in the amplification factor was observed, due to an effective damping of the surface wave which could be attributed to Landau damping, electron acceleration or radiation emission. In particular, in this intensity regime, the typical electron oscillation spacescale became comparable with the spatial extension of the electromagnetic fields (or larger), thus vacuum heating process became dominant. This absorption mechanism was enhanced by the presence of the surface plasmon wave due to the plasmon electric field orthogonal to the surface wave. For higher intensities, this mechanisms became less efficient, leading to a saturation both in the absorption ratio and in the amplification factor trends. In addition, due to the conservation of the light wave momentum, electrons could acquire a non–null velocity component along the along the $y$ direction. In this case, if $v_y$ is close to the plasmon phase velocity (possible only for relativistic electrons), electrons can be accelerated along the target surface.
The effect of the enhanced hot electrons production due to surface plasmon waves on laser driven ion acceleration has recently been investigated in numerical and experimental studies [152] and [153]. The results of ad hoc PIC simulations performed by Bigongiari *et al.* [152] are illustrated in Figure 1.36. The simulation parameters were similar to the configuration adopted in [155] and described above, with p–plarized laser pulses with irradiance in the $10^{19} - 10^{20}\,\mathrm{Wcm^{-2}}\mu\mathrm{m}^2$ range.

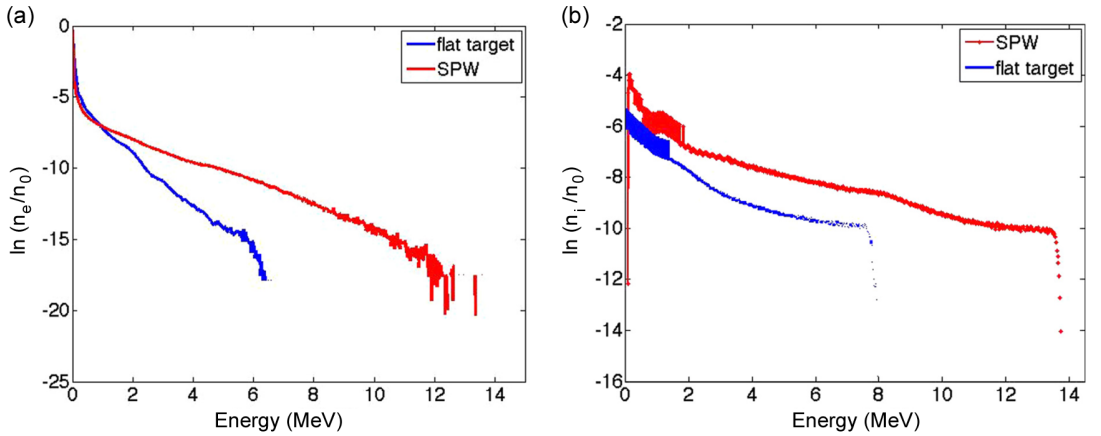


**Figure 1.36:** *Simulated spectra of accelerated protons for grating and planar targets. From [152].*

From electron spectra, reported in Figure 1.36 for plane and grating targets, an enhancement of electron number and maximum energy was observed in presence of a periodic surface modulation. Moreover, the fraction of electrons with energy higher than 1 MeV, $\sim 1\%$ for planar targets, increased to $\sim 5\%$ for grating targets and their temperature increased of a factor $\sim 4$. As a consequence, the maximum energy of the accelerated protons was enhanced of a factor $\sim 2$ for grating targets with respect to planar targets and an enhancement in the number of accelerated ions was observed. In addition, the fraction of ions in the MeV range increased from 18% (planar target) to 40% (grating).

Experimental results reported by Ceccotti *et al.* [153] confirmed these results (see Figure 1.37). In this experimental campaign, planar and grating targets were irradiated with 25 fs p–polarized laser pulses with intensity higher than $10^{19}\,\mathrm{W/cm^2}$ and ultra–high contrast ($10^{12}$), which was required to preserve the target structure until the interaction with the main pulse. Mylar targets with periodical modulation (period $d = 2\lambda$, groove depth 0.3–0.5 $\mu$) produced by thermal embossing were employed. The incidence angle was varied in a wide interval around the grating resonance angle (30°). In Figure 1.37, a comparison between 20 $\mu$m thick planar Mylar foils and 23 $\mu$m thick grating targets is illustrated. The maximum energy of protons accelerated using planar targets were well fitted by a $\sin^2\theta/\cos\theta$ function (due to the combined effect of the variation of the normal component of the electric field $\propto \sin\theta$ and of the focal spot $\cos\theta$). For grating targets, the proton energy had a broad maximum around the resonance angle. Accordingly, the laser radiation reflection was strongly reduced for incident angles around 30° for grating targets. The existence of a clear resonance provided strong evidence that the enhancement of hot electron production and, as a consequence, of the acceleration process was to be attributed to the resonant excitation of surface waves rather than to the increased target roughness, which instead was probably the origin of the maximum proton energy enhancement observed for grating targets at small angles. In addition, the angular distribution of the radiation collected by radiochromic films (RCF) suggested the emission of collimated electrons along the target surface, which was interpreted as a signature of electron acceleration

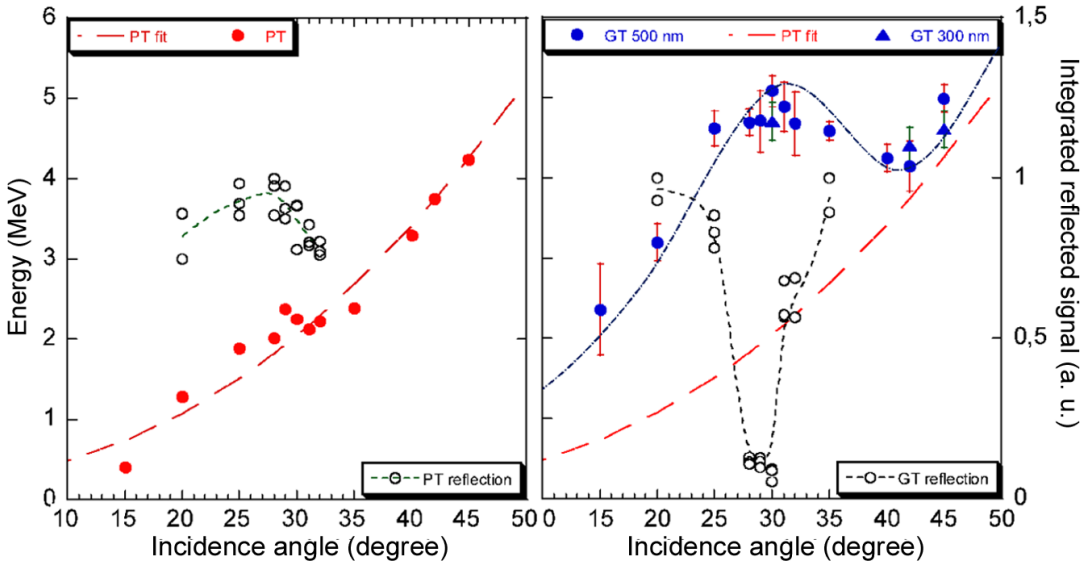


**Figure 1.37:** *Experimental proton cut–off energy and reflected light signal for planar and grating targets as a function of the incidence angle. From [153].*

produced by the excitation of surface plasmonic waves.
Besides the possibility of exploiting grating targets to achieve enhanced laser–driven acceleration performances, the experimental results reported by Ceccotti *et al.* have a fundamental interest, since they showed for the first time the possibility of exciting surface plasmonic waves in the relativistic regime (*high field plasmonics*), in which a detailed theory of surface waves is not available and highly non–linear effects of uncertain origin can contribute to collective surface excitations.

# 2

# Production and characterization of low density thin films

In light of the aspects discussed in Chapter 1, a crucial goal of this thesis project is to achieve a reliable and reproducible process for the production of few $\mu$m–thick low density carbon films with satisfactory uniformity and complete substrate coverage for enhanced TNSA targets. The possibility of producing low density carbon foams with thickness up to 100s $\mu$m is of interest for the investigation of other acceleration mechanisms, as HB–RPA or CSA (see Section 1.2.1). Moreover, suitable techniques for an exhaustive characterization of this material are required, since the film thickness and density, as well as the film microstructure, strongly affect the laser–matter interaction phase and, as a consequence, the emission of accelerated ions. However, the production and characterization of carbon foams for laser–driven ion acceleration is not straightforward, due to the extremely low density values required to optimize the laser–target interaction phase: as mentioned before, in the hypothesis of fully ionized carbon ($C^{6+}$), the near–critical density corresponds to a few mg/cm$^3$ for near–infrared waveleghts ($\sim 1\,\mu$m).
In this chapter, the main issues related to the production and characterization techniques considered in this thesis will be discussed. In particular, previous works on the production of carbon foams by Pulsed Laser Deposition (PLD) are illustrated in section 2.1, while the application of Energy Dispersive X–Ray Spectroscopy (EDS) to the evaluation of thin foam layers is introduced in section 2.2.

## 2.1 Production of low density thin films

From the material science point of view, foams are ultra–low density materials ($\rho < 100\,\mathrm{mg/cm^2}$) and belong to the class of nanoporous materials, which also includes aerogels ($\rho > 100\,\mathrm{mg/cm^2}$). Nanoporous materials have been widely studied due to their unconventional physical properties related to the presence of nanometer size voids (pores): the high specific surface area enhances the absorption, adsorption and catalytic properties of the material. In addition, they gener-

ally are effective thermal and sound insulators. These properties make nanoporous materials suitable for many applications, among which gas sensors, filters for environmental decontamination, drug delivery implants. They also find applications in the investigation of antimatter bound states [156, 157] and astrophysics, for example, for the collection of cometary and interstellar dust [158]. Foams, in addition, show black–body attitude [159], unconventional magnetic properties [160], increased gas and liquid storage capability [161] and enhanced absorption of intense laser pulses, as discussed in Section 1.1.3. A number of techniques have been proposed so far for the production of foams, such as: sol–gel polymerization [162]; polymerization of the continuous phase of high internal phase emulsions [163]; foaming with blowing agents such as carbon dioxide [164–166] or aluminium nitrate [167]; laser ablation [168].
In this frame, Pulsed Laser Deposition (PLD) represents an interesting possibility to grow carbon foam layers with tunable density, controlled thickness and a good adhesion to a solid substrate. PLD is a widespread and flexible material production technique which allows to produce films with a remarkable variety of morphologies thanks to a broad range of tunable process parameters. This technique is briefly described in subsection 2.1.1, with particular attention to the production of cluster assembled films. In subsection 2.1.2, the approach proposed by Zani *et al.* [15] and adopted in this thesis for carbon foam production is illustrated.

### 2.1.1 Pulsed Laser Deposition (PLD)

Pulsed Laser Deposition is a plasma assisted Physical Vapour Deposition (PVD) technique, in which the evaporated phase is produced by laser ablation of a solid target. The process takes place in a vacuum chamber with controlled atmosphere and can be subdivided into three stages: (i) the target surface, irradiated with a laser pulse in the $10^9 - 10^{13}\,\mathrm{W/cm^2}$ intensity regime, melts and ablates producing a cloud of vaporized species (atoms, molecules, ions, electrons and clusters); (ii) the ablated species expand in the deposition chamber (which can be filled with a buffer gas) assuming a *plume* shape; (iii) the ablated species reach the solid substrate on which they are deposited producing a thin film. The PLD equipment exploited for this PhD thesis is sketched in Figure 2.1. The properties of the deposited film are strongly dependent on the deposition conditions, which affects the plasma plume formation and propagation and the production of aggregates (molecules, nanoparticles and clusters) in the plume. A number of variables can affect the deposition process, such as the deposition geometry (substrate position and movement), the substrate temperature, the target material and the presence of a buffer gas in the deposition chamber. Also the laser properties influence the PLD process: for example, the laser wavelength and fluence affect the energy deposited in the target volume unit, the plume ionization degree and the energy of ejected species. Thus, the growth process is highly flexible and can be tuned by choosing appropriate deposition conditions to produce films with a great variety of morphologies, in wide density and thickness ranges, with controlled composition. In addition, virtually every kind of material can be adopted for both target and substrate and the congruent target ablation allows the conservation of the

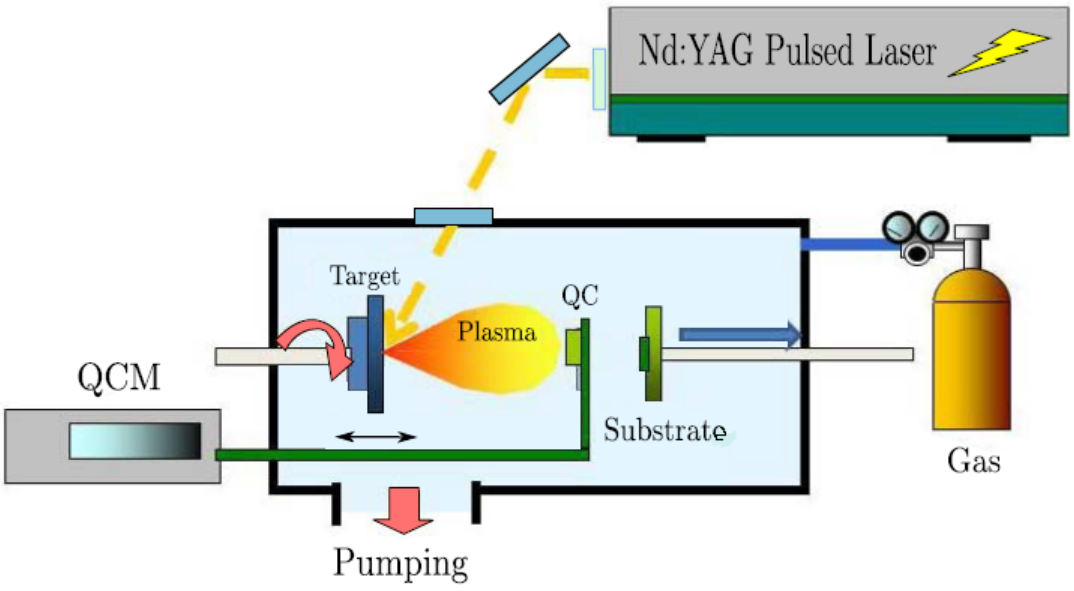


**Figure 2.1:** *Sketch of the PLD equipment in use at the NanoLab, Department of Energy, Politecnico di Milano.*

target stoichiometry in the plasma plume and (if no reactive gas is present) in the deposited film. On the other hand, the large number of variables affecting the deposition conditions can result, in particular conditions, in a poor process reproducibility. The main drawbacks of the PLD technique are the impossibility of achieving an uniform coverage on areas larger than a few $cm^2$ due to the approximately Gaussian shape of the film thickness profile and the strong influence of shadow effects which only allows to coat planar substrates. The production of particulate and droplets from the melted target region due to the recoil pressure of the ablated material can reduce the quality of the deposited film, especially when targets with low melting temperature are selected.
Hereinafter, the main stages of the PLD process are briefly described. A thorough dissertation on this subject can be found in [169].

#### Target ablation

The typical laser intensity in PLD systems ($10^9 - 10^{13}\,W/cm^2$) is much lower than the super–high intensity values which produce the interaction mechanisms discussed in section 1.1. In this low intensity regime, the exposition of the target to the incoming laser radiation produces non–thermal absorption processes (mainly electron and phonon excitation) in tens of fs. The excitation is transferred to the target lattice on the ps timescale through electron–electron and electron–phonon collisions, restoring the material thermal equilibrium. The emission of ablated species can be produced by different mechanisms, depending on the interaction conditions. An important role in the target ablation is played by the dimensions of the laser–target interaction region (i.e. the laser penetration length in the target) and by the target thermal conductivity, since these factors strongly affect

the temperature reached by the material in the region involved in the ablation process. For highly conductive materials, the energy deposited by the laser pulse in the interaction region is promptly transported in the target through thermal diffusion, thus the dominant emission mechanism is a thermal evaporation of the material surface. On the contrary, for insulators, the absorbed energy is confined in the interaction region (i.e. in a thin surface layer). This can lead to an explosive ablation phenomenon due to non–equilibrium thermal processes such as phase explosion. For fluence values above a threshold value depending on the target material, the incoming laser pulse can directly ionize the target surface producing a plasma plume. In general, the cloud of ablatied material is formed in 100 ps timescales, hence for nanosecond incoming pulses the plume absorbs a part of the incoming pulse energy via inverse bremsstrahlung, shielding the target, and is further ionized.

#### Plume propagation

In general, after the thermalization of ablated species in the so–called *Knudsen layer*, the propagation of the plasma plume towards the solid substrate can be described as the adiabatic expansion of a gas. Large temperature and pressure gradients along the target normal direction characterize the first stages of the propagation, thus the plume expansion is strongly directional. In vacuum, the effect of collisions between particles in the ablated material cloud is negligible, thus the plasma plume maintains a strong directionality and the propagation of ejected material only depends on the initial velocity of emitted particles. In presence of an ambient gas, the gas pressure and composition strongly affect the propagation of the plasma plume and, as a consequence, the spatial distribution and kinetic energy of the ablated species and the deposition rate (see Figure 2.2). In this case, two distinct plume expansion regimes can be observed depending on the gas pressure [170]. In the low pressure regime, the plume expansion is directional, since the propagation of ablated particles is not strongly affected by collisions with gas atoms. In this regime, as in vacuum, the radiative de–excitation of ablated species in the plume core produces a weak fluorescence. For high pressure, the supersonic propagation of the ablated species scatters off the background gas atoms, producing a highly compressed region at the plasma–gas interface and eventually a shock wave [171, 172]. As the pressure in the plume drops due to the expansion, the shock wave front propagation slows down and stops at a characteristic distance which depends on the gas pressure and composition. Then, the ablated material diffuses in the background gas. In this regime, the plume expansion becomes less directional, due to the effect of collisions with the ambient gas, and the fluorescence emission is strongly increased. Moreover, the plasma plume is confined by the background gas and its longitudinal extension is strongly reduced, while the transversal size increases: depending on the gas pressure, the plume takes a spherical or hemispherical shape.

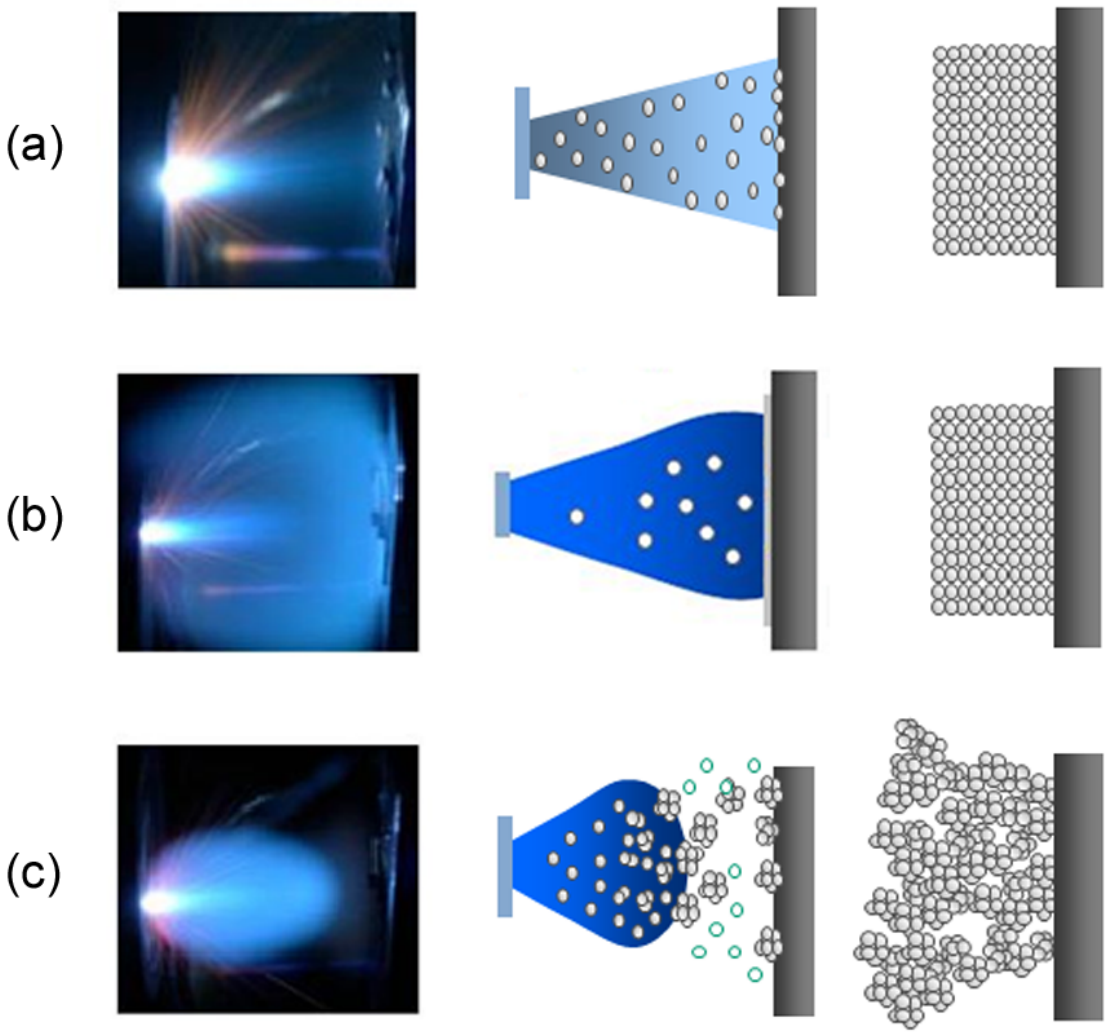


**Figure 2.2:** *Effect of gas pressure on the deposition process: typical ablation plumes of tungsten either in vacuum (a) or in He atmosphere at low (b) and high (c) pressure and sketch of the corresponding deposition mechanism. From [173].*

#### Deposition

Depending on the dynamics of the plasma plume expansion in the deposition chamber, two kinds of growth mechanisms can be identified (as shown in Figure 2.2). In the low pressure regime, the ablated species reach the substrate with high kinetic energy, since their propagation is not affected by a buffer gas and deposited films are compact. On the contrary, in the high pressure regime, the film is grown by cluster assembling. In this regime, clusters and aggregates are formed in the confined plasma plume and the propagating species lose a large part of their kinetic energy in their diffusion through the buffer gas. The structure depends on the kinetic energy that these clusters have when they reach the surface: the lower the kinetic energy, the more porous the deposited film. The film growth mechanism can be affected by the substrate temperature: heated substrates can

favour the diffusion of deposited species on the surface and the re–organization of atoms in more stable (crystalline) structures. Another parameter to be taken into account to achieve a good control of the film morphology is the ratio between the target–to–substrate distance and the extension of the plasma plume (which depends on the gas pressure). If the target–to–substrate distance is lower than the plume length, the ablated species reach the substrate while propagating in a super–sonic regime and an atom–by–atom deposition mechanism takes place, since the propagating species have high kinetic energy and high mobility once they reach the substrate surface. Films produced in these conditions have compact and smooth structure. On the contrary if the target–to–substrate distance is comparable or higher than the plume length, the film growth is due to a cluster assembling mechanism. In particular, if the target–to–substrate distance is larger than the plume extension, effective energy loss in the diffusion regime leads to the production of porous films, while if the two scale–lengths are comparable, the high energy of the material which reaches the substrate determines the production of compact columnar structures.

### 2.1.2 Growth of carbon foams by PLD

The growth of carbon nanofoams by PLD in the ps regime has been reported in 1999–2000 by Gamaly *et al.* and Rode *et al.* [174–177]. The basic idea was to exploit the presence of an ambient gas (Ar) and the high collision frequency between carbon atoms and ions in the plasma plume and Ar atoms of the ambient gas, resulting in an enhancement of the diffusion–limited aggregation of C atoms into fractal clusters. The resulting material had ultra–low density (2–10 mg/cm$^3$), a significant fraction of $sp^3$ bondings and a fractal self–similar foam morphology, shown in Figure 2.3. In these studies an unconventional set of deposition parame-

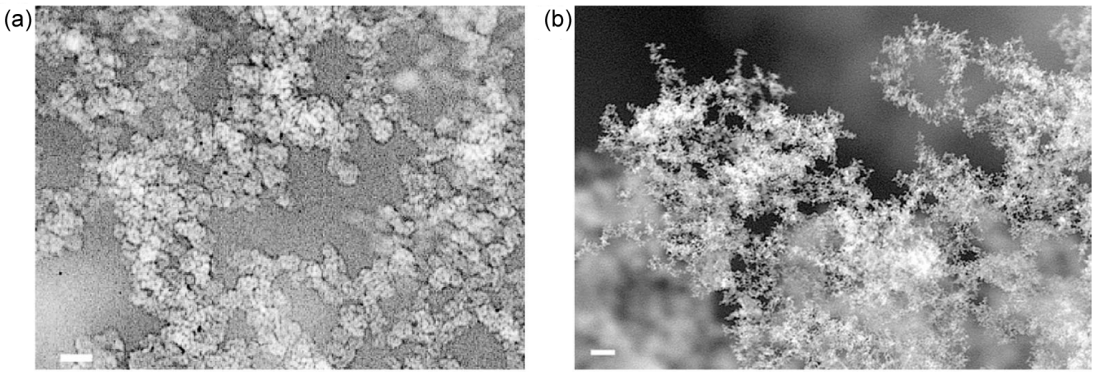


**Figure 2.3:** *Carbon foam produced by PLD in the ps regime: (a) transmission electron micrograph showing characteristic clusters (10 nm scale bar); (b) Scanning electron micrograph showing the web–like foam at lower magnification (100 nm scale bar). From [176].*

ters was considered: short laser pulses (tens of ps) with high repetition rate (kHz) were adopted in order to achieve a continuum flux of matter from the ablated target to the substrate, high fluence (120 J/cm$^2$) and Ar pressure around 100 Pa. However, the production of carbon films by PLD in ordinary experimental condi-

tions has been extensively investigated in literature in the past decades [178,179]. For example, the possibility of controlling the morphology of cluster assembled carbon films by properly selecting the composition and the pressure of the buffer gas in the deposition chamber was explored in [180,181]. Here, films were grown at room temperature on Si substrates with laser pulses in the ns regime in He with pressure from 0.6 Pa to 2 kPa. Films in a wide range of microstructures were deposited: from diamond–like carbon to cluster–assembled porous films with prevalent $sp^2$ bonding and disordered structure (see Figure 2.4). The production

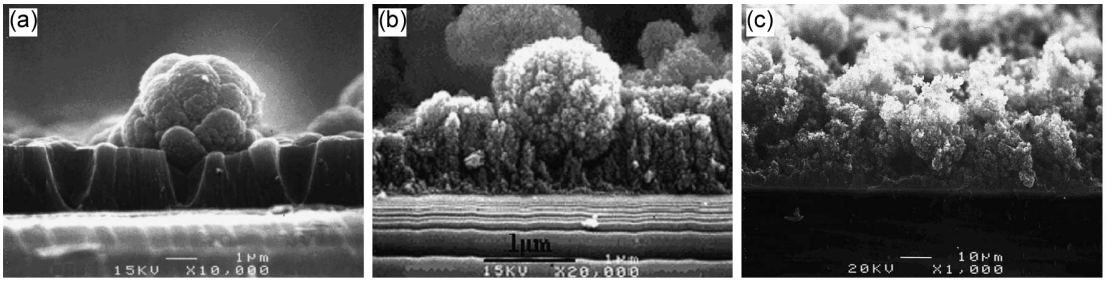


**Figure 2.4:** *Cross sectional SEM micrographs of cluster assembled carbon films deposited in He atmosphere with different gas pressures and power density on target: (a) 60 Pa and 16* MW/mm$^2$*; (b) 250 Pa and 8.5* MW/mm$^2$*; (c) 2 kPa and 16* MW/mm$^2$*.From [180].*

of nanoporous carbon films with density in the 100–1000 mg/cm$^3$ range was reported in a similar study by Siegal *et al.* [182]. A KrF excimer laser ($\lambda$ = 248 nm, fluence $\sim$ 6 J/cm$^2$, pulse duration in the ns regime) was exploited. Once again, the control of the deposition energetics (and as a consequence morphology, density and porosity) was achieved by properly selecting the pressure of the ambient gas in the deposition chamber, namely Ar between 23 Pa and 40 Pa and by considering a relatively high target–to–substrate distance (5 cm).
The PLD configuration chosen in this thesis work exploits a general approach developed by Zani *et al.* [15]. Here, a pyrolitic graphite target was ablated by the second harmonic ($\lambda$ = 532 nm) of a Nd:YAG laser (with pulse duration 5–7 ns, repetition rate 10 Hz) in a chamber filled with Ar or He as buffer gas. The gas pressure (30–1000 Pa), the laser fluence (0.8 J/cm$^2$) and the target–substrate distance (8.5 cm) were chosen to set an out–of–plume deposition regime resulting in a substantial reduction of the kinetic energy of expanding species, in the formation of clusters and nanoparticles in the plasma plume and in the production of nanoparticle–assembled films with a porous morphology. In particular, the laser fluence selected in this investigation, achieved by combining low pulse energy (100 mJ) and defocused spot on target (12.5 mm$^2$), was well below the values adopted in literature to achieve porous carbon film. The film morphology and density were controlled by properly selecting the gas pressure in the deposition chamber, covering a three orders of magnitude density range. A longitudinal gas flow between 1 sccm (0.03 mg/cm$^3$) and 100 sccm (3 mg/cm$^3$) was adopted with the aim to reduce the foam non–homogeneity scale. In Figures 2.5 and 2.6, SEM images of carbon foams deposited in He and Ar atmosphere with pressure ranging from 30 Pa to 500 Pa are shown. More and more porous foam mesoscale morphologies were achieved for increasing gas pressure, in particular around 100

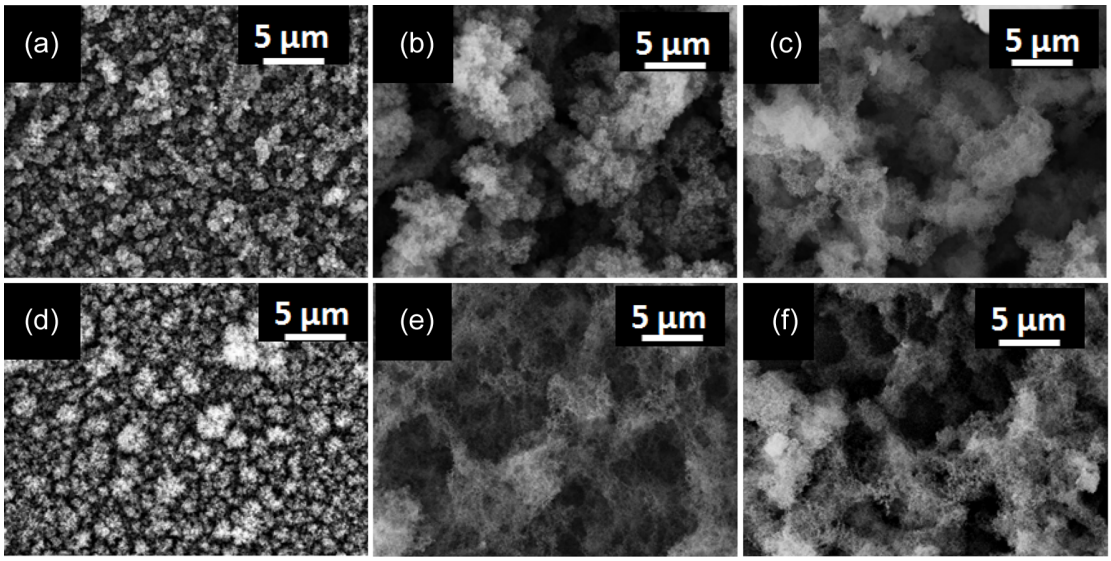


**Figure 2.5:** *Top–view SEM images of carbon foams grown in He (top) and Ar (bottom) at different pressures: (a) and (d) 30 Pa; (b) and (e) 100 Pa; (c) and (f) 500 Pa. From [15].*

Pa a transition from a cauliflower–like morphology to an isotropic porous structure was observed. Also for foams grown in Ar an enhanced porosity was observed as the gas pressure increased and a sharp transition from a directional deposition process (resulting in tree–like structures) to an isotropic foam structure occurred around 30 Pa. This trend is even more evident from cross–sectional SEM images (see Figure 2.6). A morphological difference between films produced in He and

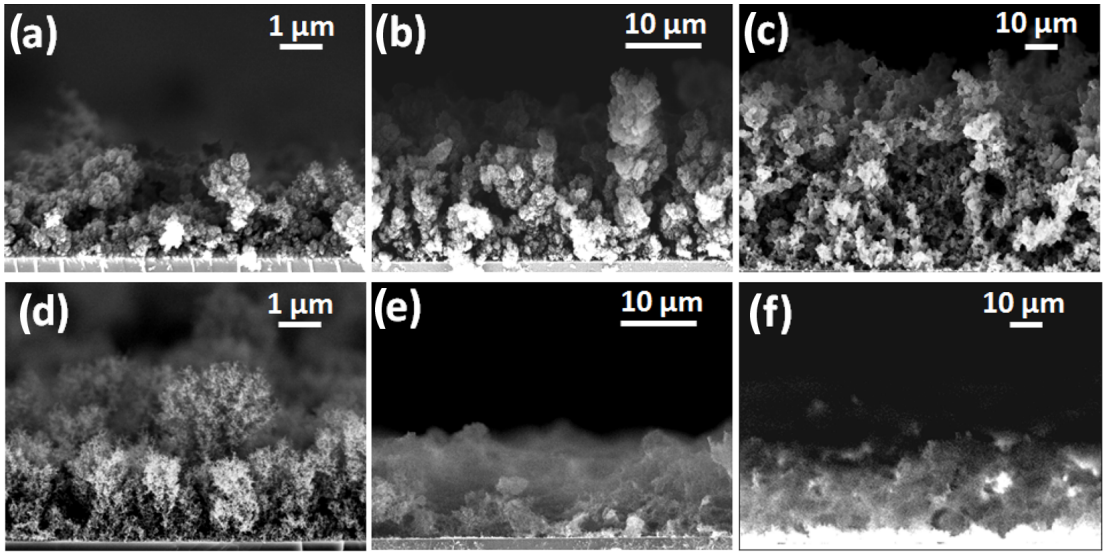


**Figure 2.6:** *Cross–sectional SEM images of carbon foams grown in He (top) and Ar (bottom) at different pressures: (a) and (d) 30 Pa; (b) and (e) 100 Pa; (c) and (f) 500 Pa. From [15].*

Ar is evident from SEM images. This difference was attributed to the different aggregation mechanisms of elementary consituents (nanoparticles with diameter $\sim$ 20 nm) in He and Ar. According to Zani *et al.*, in He these elementary con-

stituents aggregated in larger particles whose assembly produces the porous film and the mesoscale transition at 100 Pa could be attributed to the different structure of these aggregates, which became more porous and void–rich for increasing gas pressure. On the other hand, random chains were formed in Ar by the aggregation of elementary nanoparticles resulting in a self–similar structure repeated till the mesoscale. According to Raman spectroscopy in both cases the deposited material is composed by a nearly pure $sp^2$ network of topologically disordered domains, containing odd membered rings and few chain–like structures. The density of porous carbon foams was evaluated using a Quartz Crystal Microbalance (QCM) and ranged from $\sim 0.6\,\mathrm{mg/cm^3}$ to the density of bulk graphite. However, the extremely low density values achieved by QCM were certainly affected by a loss of sensibility due to the high porosity of the material, therefore the minimum density of carbon foams was assumed to be a few $\mathrm{mg/cm^3}$.

## 2.2 Characterization of low density thin films

The application of carbon foams to the production of targets for laser–driven ion acceleration requires an exhaustive characterization of the material, especially as regards the morphological analysis and the evaluation of foam thickness and density, since these properties strongly affect the laser–matter interaction processes. Nevertheless, foam characterization is a rather complex issue because of the extremely low density and porous morphology of this material.
The evaluation of foam thickness through cross–sectional SEM images is not straightforward due to the irregular morphology and the low conductivity of the film, which reduce the measurement reliability. In addition, particular attention should be paid to the sample alignment, since the thickness evaluation can be strongly affected also by a slight sample tilt. However, issues related to the thickness evaluation can be easily addressed by adopting simple measurement protocols.
On the contrary, the evaluation of foam density, which is crucial as this parameter defines the laser–matter interaction regime, is a rather complex issue. It's worth to point out that, since the material is non–continuous and non–homogeneous, foam density is defined as average mass in a macroscopic volume divided by the volume itself, i.e. as an average value over a scale larger than the inhomogeneity scale. The density of thin films produced by physical vapour deposition techniques is commonly evaluated by combining the film thickness inferred from cross–sectional SEM images or by Transmission Electron Microscopy (TEM), depending on the order of magnitude, and the film areal density measured by Quartz Crystal Microbalance (QCM). This approach was adopted for the evaluation of carbon foam density in previous work [15] and allows to measure the average areal density of a film directly deposited on its quartz crystal surface in conditions simulating the growth configuration of the film under analysis, thus providing an indirect measurement of the film areal density.
The considerable spread of the QCM technique, proposed by Sauerbrey in 1957 [183], is due to the simplicity of the required instrument: the device is composed by

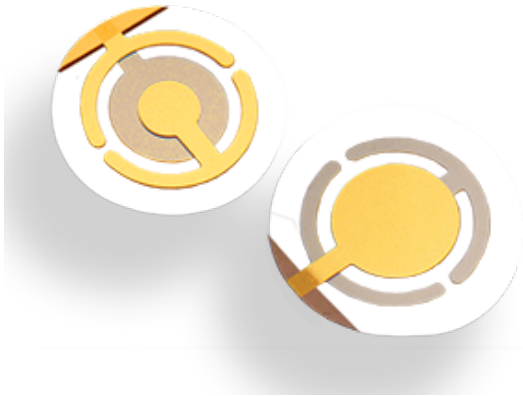

**Figure 2.7:** *AT–cut quartz crystal for QCM sensors. From [184].*

a quartz crystal disc connected to a simple electric circuit through two deposited golden electrodes. Due to an inverse piezoelectric effect, a periodic electrical stimulation of the quartz crystal generates acoustic waves in the crystal itself, which behaves as a quasi–harmonic oscillator with a characteristic frequency, $\nu_0$. The crystal resonance frequency depends on the shape and size of the crystal and on the manufacturing process. In the case of an AT–cut quartz crystal (quartz disc with 8 mm diameter and thickness lower than 1 mm, shown in Figure 2.7), the electrical stimulation at the resonance frequency produces undamped sinusoidal shear strain waves which propagate along the direction orthogonal to the crystal surface. If a thin compact film is deposited on the crystal surface with good adhesion, the deposited mass ($\Delta m$) results in a shift of the resonance frequency ($\Delta\nu$). Hence, if placed in the same position as the substrate, the QCM provides an indirect measurement on the mass deposition rate on a well defined surface and, therefore, a mean areal density value. If $\Delta m << m$, the relation between the deposited mass and the frequency shift is linear and can be expressed as $\Delta\nu/\nu_0 = -\Delta m/m$ (where $m$ is the mass of the unloaded crystal). However, this relation is not valid for thick films for which the frequency shift exceeds 2%: in this case a nonlinear correction is required [185, 186].
As mentioned before, this device was adopted for the evaluation of carbon foam density in previous work [15]. However, the steep decrease of foam density to unrealistic values well below $1\,\mathrm{mg/cm^3}$, shown in Figure 2.8 (a), clearly indicates that QCM is not reliable for ultra–low density materials. This loss of sensibility can be attributed to a deterioration of the coupling between elastic shear waves propagating in the quartz crystal and the shear waves propagating in foams, due to the low acoustic impedance of the material [187]. Moreover, for extremely porous films, the crystal vibrations could blow off part of the deposited mass, resulting in an equilibrium state in which the mass deposited on the crystal in a time interval $\mathrm{d}t$ is equal to the mass lost due to vibrations in $\mathrm{d}t$. As a result, a saturation effect in the QCM response is observed for porous films as the deposition time increases (as shown in Figure 2.8(b)). Therefore, this method is not reliable for very low density materials (below a $\sim 30$ of $\mathrm{mg/cm^3}$).
As a consequence, the evaluation of the foam layer density requires a more re-

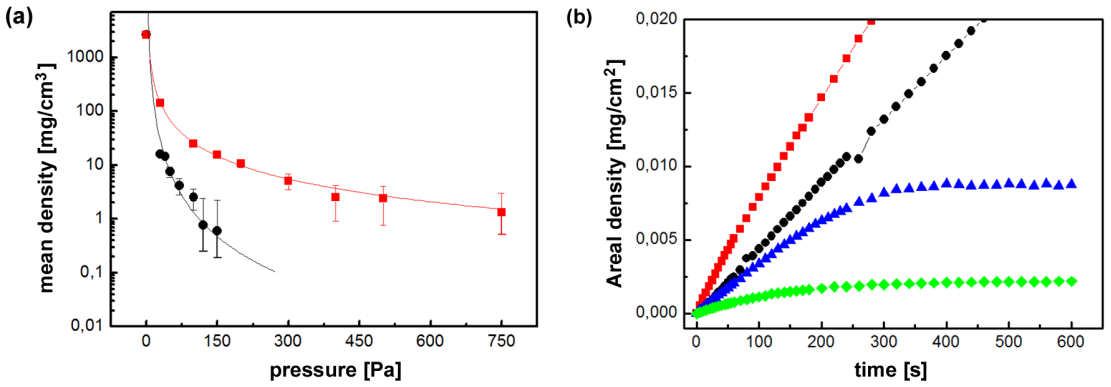


**Figure 2.8:** *(a) mean foam density measured as a function of He (red squares) and Ar (black circles) pressure; (b) QCM measurement of foam areal density at different deposition times for different working He pressures (red squares refer to the vacuum case, black circles to 30 Pa, blue triangles to 100 Pa and green diamonds to 500 Pa). From [15].*

fined technique for the assessment of the film areal density to be combined with thickness values inferred from cross sectional SEM images. In general, an ideal technique for thin film density measurement should be reliable in a wide density range (from the density of solid to a few mg/cm$^3$) and for a large variety of materials and morphologies. It should allow to evaluate the density of non-homogeneous films with a good spatial resolution. It should also be non–destructive and fast and require a simple and cheap experimental apparatus.
A possible strategy consists of studying the effect of an incoming particle beam on the film under analysis, which in general depends on the number of interaction centers, i.e. from the areal density of the material. This approach is adopted in many commonly used nuclear based techniques for film areal density evaluation, such as Rutherford Backscattering Spectroscopy (RBS), Elastic Recoil Detection Analysis (ERDA) and Nuclear Reaction Analysis (NRA). These techniques allow to achieve accurate areal density measurements with a spatial resolution on the order of 1 $\mu$m. Nevertheless, the choice of ions as probe particles requires a complex and expensive experimental equipment, i.e. linear accelerators to produce MeV ion beams.
In this context, an attractive technique satisfying most of the ideal requirements listed above exploits Energy Dispersive X–ray Spectroscopy (EDS) and is based the analysis of the spectrum of characteristic X–rays produced in matter by an electron probe beam. The energy and intensity of characteristic X–rays produced in a multilayer sample by an incident electron beam are related to the atomic number of the emitting element and to the composition and areal density of the interrogated layer, respectively. The penetration depth of electrons in matter is a function of the electron accelerating voltage and ranges approximately from 0.1 $\mu$m to several $\mu$m for standard electron probe beams (2–50 keV). As a consequence, an appropriate selection of the electron accelerating voltage allows to characterize a surface layer of the sample under investigation, i.e. a thin coating deposited on the sample surface. The application of EDS to the evaluation of the thickness of compact films with known density was proposed by Sweeney *et al.* in

the 1960s [188]. However, the parameter this technique is directly sensitive to is the film areal density. The application of EDS based methods to the evaluation of carbon foam density was proposed by Zani in his PhD thesis [16]. The main advantage of this technique is that the microanalysis equipment required for EDS is relatively simple and it is often integrated in SEM devices which are commonly used in material science laboratories. Thus, the evaluation of film areal density and thickness can be achieved using the same instrument. Moreover, this technique is non destructive and provides local density values, allowing to characterize non-homogeneous films, while QCM only provides an indirect average areal density measurement.
Hereinafter, an introduction on EDS–based methods for thickness evaluation is provided (paragraph 2.2.1) and the most relevant theoretical aspects available in the literature about areal density evaluation are described in paragraph 2.2.2.

### 2.2.1 Energy Dispersive X–ray Spectroscopy (EDS) for film thickness evaluation

The application of EDS to coating thickness evaluation has been widely explored since 1960s. To this aim, a number of methods have been employed in literature. For example, thickness evaluation was achieved by measuring the minimum accelerating voltage required to probe the whole film thickness [189] or the accelerating voltage for which a given fraction of the X–ray intensity produced by a reference standard is emitted by the sample [190]. Here, we discuss the application of two methods proposed by Sweeney, Seebold and Birks in 1960 [188] and by Cockett and Davis in 1963 [191], because of their relevance to this thesis.
These approaches, respectively known as *coating method* and *substrate method*,

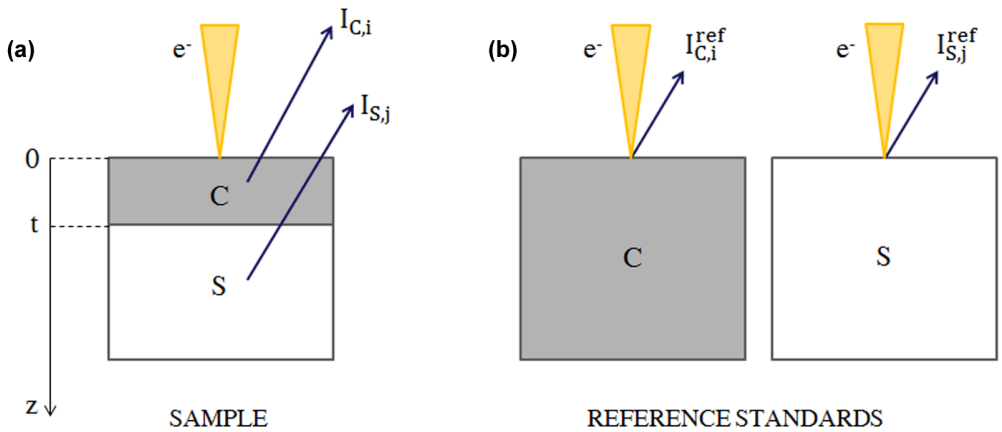


**Figure 2.9:** *Sketch of EDS based film thickness measurement methods. a) X-ray emission from the coating (thickness $t$ and density $\rho$) and from the substrate of a multilayer sample due to the incident electron beam. b) X-ray emission from reference standards for the coating method and the substrate method.*

were developed for multilayer samples composed by a known substrate and a coating with unknown thickness. In these methods, the coating layer thickness $t$ is calculated from the intensity of X–rays ($I_{sample}$) produced either in the sample

coating or substrate by an incoming electron beam with appropriate initial energy, provided that the intensity of X–rays produced by a bulk reference standard ($I_{ref}$) is known (see Figure 2.9). The main difference between the coating method and the substrate method lies in the choice of the reference standard: the reference standard must contain an emitting element present only in the sample coating or in the substrate, respectively. Figure 2.10 shows the original calibration curves calculated in [191] for the coating method (Cr films) and the substrate method (Zn and $TiF_4$ films).

The reliability of these methods for thickness evaluation was thoroughly in-

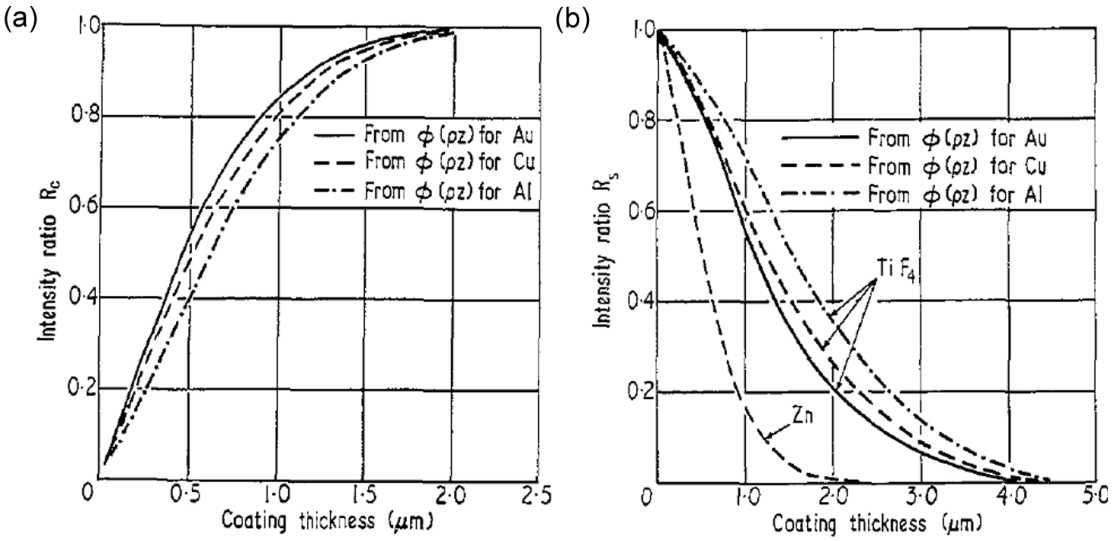


**Figure 2.10:** *Original calibration curves calculated by Cockett and Davis for (a) the coating method (Cr films) and (b) the substrate method (Zn and* $TiF_4$ *films) at 29 keV. From [191].*

vestigated in the literature. Thickness values measured employing EDS–based methods were compared to values achieved using other techniques, i.e. RBS or cross sectional SEM images. The difference between results achieved with established techniques and with EDS–based methods is generally around 15–20% [191].

### 2.2.2 EDS for film density evaluation

Although originally applied to film thickness evaluation, EDS–based methods are directly sensitive to the film areal density, since the generation of characteristic X–rays in a layer does not depend on the material thickness, $t$, or density, $\rho$, separately, but on its areal density, $\tau = \rho t$. Therefore, this technique can be adapted to density evaluation for thin films with known thickness.

The calculation of film areal density from X–ray intensity requires the knowledge of the so–called Probability Function for X–ray Production (PFXP), $\phi(\sigma)$. This function, introduced by Castaing in 1951 [192], describes the distribution in depth of the primary ionizations produced in a sample by an incoming electron (see Figure 2.11). The function argument is depth expressed in terms of areal density and is given by $\sigma = \rho z$, where $z$ is the depth measured in linear units and $\rho$ is the

mass density of the material.

The PFXP allows to calculate the X–ray intensity $\mathrm{d}I_\mathrm{l} = \phi_\mathrm{l}(\sigma)\mathrm{d}\sigma$ emitted by

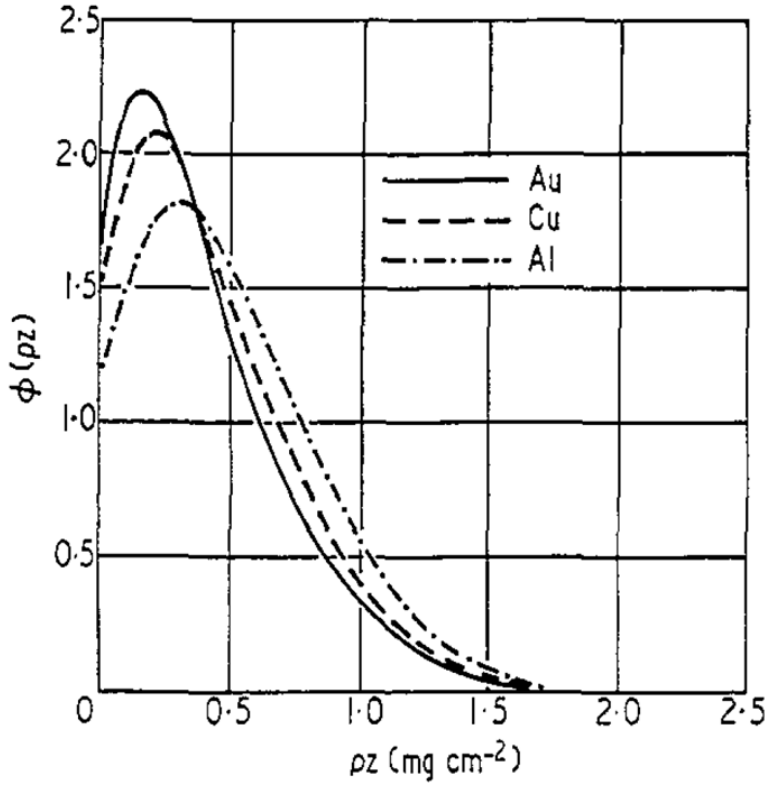


**Figure 2.11:** *The very first experimental PFXP function trends measured at for Au, Cu and Al by Castaing in 1951 [192].*

an element $Z_\mathrm{l}$ in a layer $\mathrm{d}\sigma$ at a depth $z$ below the sample surface. Thus, the intensity measured for a characteristic X–ray line emitted by $Z_\mathrm{l}$ in a layer with finite (unknown) areal density $\Delta\tau$ is

$$I_\mathrm{l} = k \int_{\Delta\tau} C_\mathrm{l}\phi_\mathrm{l}(\sigma) \exp\left(-\chi\sigma\right)\mathrm{d}(\sigma), \tag{2.1}$$

where $C_\mathrm{l}$ is the mass concentration of the element under analysis. The term $\chi = (\mu/\rho)\,\mathrm{cosec}\,\theta$ takes into account the absorption of emitted X–rays propagating to the sample surface: $\mu/\rho$ is the mass absorption coefficient and $\theta$ is the X–ray take–off angle. $k$ is a constant given by

$$k = \frac{I_\mathrm{l}^\mathrm{ref}}{\int_0^{+\infty} C_\mathrm{l}^\mathrm{ref}\phi_\mathrm{l}^\mathrm{ref}(\sigma) \exp\left(-\chi^\mathrm{ref}\sigma\right)\mathrm{d}(\sigma)}, \tag{2.2}$$

where $I_\mathrm{l}^\mathrm{ref}$ is the X–ray intensity produced by $Z_\mathrm{l}$ present in a reference standard with known composition. The *ref* superscripts in the fraction denominator indicate that the concentration of $Z_\mathrm{l}$, the PFXP and the absorption term $\chi$ refer to the reference standard. X–rays intensities must be measured under the very same conditions for the sample under analysis and the reference standard. This is a

crucial point since the intensity of detected characteristic X–rays is influenced by many factors, such as the beam current, the measurement duration and geometry. If a model for PFXP evaluation is available, the relation between the unknown coating areal density, $\tau$, and the X–ray intensity emitted by the sample can be calculated through equations 2.1 and 2.2 for both methods.
In the coating method, characteristic X–rays emitted by an element $Z_{\mathrm{i}}$ present in the sample coating are considered. The intensity of the selected X–ray line can be calculated for the sample and the reference standard from the recorded spectra by integrating the peak fitting curves. According to equations 2.1 and 2.2, the coating to reference standard intensity ratio $I_{\mathrm{C,i}}/I_{\mathrm{C,i}}^{\mathrm{ref}}$ can be expressed in terms of film areal density through the following formula

$$\frac{I_{\mathrm{C,i}}}{I_{\mathrm{C,i}}^{\mathrm{ref}}} = \frac{\int_0^{\tau} C_{\mathrm{i}}\phi_{\mathrm{C,i}}(\sigma)\exp\left(-\chi_{\mathrm{C}}\sigma\right)\mathrm{d}\sigma}{\int_0^{\infty} C_{\mathrm{i}}^{\mathrm{ref}}\phi_{\mathrm{C,i}}^{\mathrm{ref}}(\sigma)\exp\left(-\chi_{C}^{\mathrm{ref}}\sigma\right)\mathrm{d}\sigma}\,, \tag{2.3}$$

where the coefficients $\chi_{\mathrm{C}}$ and $\chi_{\mathrm{C}}^{\mathrm{ref}}$ account for the absorption of X-rays in the sample coating and in the reference standard, respectively.
In the substrate method, the intensity of a characteristic X–ray line emitted by an element $Z_{\mathrm{j}}$ contained in the sample substrate is considered. The sample substrate to reference standard X–ray intensity ratio $I_{\mathrm{S,j}}/I_{\mathrm{S,j}}^{\mathrm{ref}}$ can be expressed as a function of film areal density $\tau$ through equations 2.1 and 2.2. If X–ray absorption in the coating is taken into account, the relation between the intensity ratio and $\tau$ can be expressed as follows

$$\frac{I_{\mathrm{S,j}}}{I_{\mathrm{S,j}}^{\mathrm{ref}}} = \exp\left(-\chi_{\mathrm{C}}\tau\right)\frac{\int_{\tau}^{+\infty} C_{\mathrm{j}}\phi_{\mathrm{S,j}}(\sigma)\exp\left[-\chi_{\mathrm{S}}(\sigma-\tau)\right]\mathrm{d}(\sigma)}{\int_0^{+\infty} C_{\mathrm{j}}^{\mathrm{ref}}\phi_{\mathrm{S,j}}^{\mathrm{ref}}(\sigma)\exp\left(-\chi_{\mathrm{S}}^{\mathrm{ref}}\sigma\right)\mathrm{d}(\sigma)}\,, \tag{2.4}$$

where the coefficients $\chi_{\mathrm{C}}$, $\chi_{\mathrm{S}}$ and $\chi_{\mathrm{S}}^{\mathrm{ref}}$ introduce the effect of X–ray absorption in the sample coating and substrate and in the reference standard.
Once the X–ray intensities emitted from the sample and from an appropriate reference standard have been measured, the film areal density $\tau$ can be calculated by inversion of equation 2.3, for the coating method, or 2.4, for the substrate method.
As mentioned before, a model for PFXP evaluation is required to calculate areal density. In the first studies, PFXP was extrapolated from experimental data [188, 191] or from Monte Carlo simulations [193]. Later, many models have been proposed for PFXP approximation as a function of experimental conditions and sample properties [194]. In the 1980s Pouchou and Pichoir proposed two of the most popular methods: the PAP (*Pouchou and Pichoir*) model, in which the distribution function is approximated by two smoothly joined parabolas [195], and the XPP (*extended Pouchou and Pichoir*) model, which is based on an exponential approximation of the PFXP and allows to describe an experimental configuration with obliquely incident electrons [196]. In 1981, Packwood and Brown proposed the so–called Modified Surface–centered Gaussian (MSG) model [197], which is theoretically founded on the hypothesis that electrons diffuse isotropically in the sample. However, in general this hypothesis is not valid, since a collimated electron beam with incidence normal with respect to the sample surface maintains its

collimation in the surface region. As a consequence, the electron path in a shallow layer with mass thickness $d\sigma$ is shorter than in a deeper layer with the same mass thickness, resulting in a lower probability of X–ray production in the surface region. In this model, the persistence of a directional electron propagation near the surface and the consequent deviation from a totally random walk are taken into account introducing an exponential term which vanishes rapidly with depth. The MSG expression of the PFXP function, $\phi(\sigma)$, is

$$\phi(\sigma) = \gamma \exp\left[-\alpha^2(\sigma)^2\right] \left[1 - \frac{\gamma - \phi(0)}{\gamma} e^{(-\beta\sigma)}\right] . \tag{2.5}$$

This equation contains four shape–parameters $\alpha$, $\beta$, $\gamma$ and $\phi(0)$, which depend on the electron initial energy $E_0$, on the sample composition and on the absorption edge of the peak under analysis $E_C$. The original derivation of these parameters and the resulting equations can be found in [197]. In this thesis work the model parameters introduced by Rembach and Karduck, the so–called *RE method*, will be considered [198]. The RE method generalizes the MSG model to ultra–soft X–rays emitted by low atomic number materials on the basis of a large number of experimental and numerical results by introducing new definitions of the four shape–parameters.

$\alpha$ , whose inverse describes the width of the Gaussian function, is correlated with the penetration depth of incident electrons. In the original model, this parameter was calculated by considering the distance probability distribution of a random walk in a cylindrical symmetry system after $M$ steps with length equal to the mean free path of electrons in the sample under analysis. The number of steps was calculated as the ratio between the total energy loss of a single electron and the energy lost by the electron per mean free path. In the RE model, the expression of $\alpha$ for a multicomponent sample is calculated as a weighted average of the $\alpha_l$ related to each sample component

$$\alpha^{-1} = \frac{\sum_l C_l Z_l / A_l \alpha_l^{-1}}{\sum_l C_l Z_l / A_l} , \tag{2.6}$$

where

$$\alpha_l = 2.66 \times 10^5 \frac{Z_l^{1.04}}{A_l E_0^{1.10}} \left[\frac{\ln(1.166 E_0 / J_l)}{E_0 - E_C}\right]^{0.5} . \tag{2.7}$$

$E_0$ is the initial energy of the probe electron beam (i.e the accelerating voltage in the SEM column), $E_C$ is the so–called *critical energy* (i.e. the excitation potential of the analytical line), and the *ionization potential* of each sample component, $J_l$, is given by the Ruste formula $J_l = 0.00929(Z_l + 1.287 Z_l^{0.33333})$ [199].

$\beta$ takes into account the deviation from a pure Gaussian function in the surface region. In the original model, it was calculated considering the number of collisions required to have complete randomization of the electron propagation direction. The expression proposed by Rembach and Karduck is

$$\begin{aligned} \beta &= 2.20 \times 10^5 E_0^{-1.4} \left[1 + (U_0 - 1)^{-0.77}\right] \ln(Z - 11) \quad \text{for} \quad Z > 12 \\ \beta &= 2.08 \times 10^5 E_0^{-1.4} \left[1 + (U_0 - 1)^{-0.77}\right] \ln(Z) \quad \text{for} \quad Z < 12 \end{aligned} \tag{2.8}$$

where $U_0 = E_0/E_C$ is known as *overvoltage ratio*. For multicomponent samples, $\beta$ is calculated considering an effective atomic number $Z_{\text{eff}}$, the average of the atomic numbers of the single components weighted on the mass concentrations.

$\gamma$ represents the amplitude of the Gaussian function. It can be calculated taking into account two factors: the reduced excitation probability in the shallow layers as the electron propagation loses its directionality and the progressive reduction of the excitation efficiency of the electron beam in deep layers, as electrons lose their energy in matter. In the RE model this parameter is calculated as

$$\gamma = 2.325(1 + 0.64\eta)\frac{10U_0(\ln U_0 - 10 - U_0^{-0.1})}{\ln U_0(U_0 - 1)}\,. \tag{2.9}$$

$\eta$ is the *electron backscattering coefficient*, defined as the fraction of electrons backscattered by the sample surface. This parameter can be calculated according to the following expression, introduced by Hunger and Küchler [200],

$$\begin{aligned} \eta &= E_0^x[0.19036 - 0.2236\ln Z + 0.1292(\ln Z)^2 - 0.01491(\ln Z)^3] \\ x &= 0.1382 - 0.9211Z^{-0.5}\,. \end{aligned} \tag{2.10}$$

In multicomponent samples $\eta$ can be calculated as the average of $\eta_{\text{l}}$ of the single components weighted on the mass concentrations.

$\phi(0)$ , finally, is the surface ionization, the distribution value at the surface, whose evaluation in the original model was performed considering the ionization events induced by backscattered electrons. The value of $\phi(0)$ in the RE model is given by the following equation

$$\phi(0) = 1 + (1 - \frac{1}{\sqrt{U_0}})^a b\,, \tag{2.11}$$

where the parameters $a$ and $b$ are defined as

$$\begin{aligned} a &= (1 + 0.005Z/E_C)(0.68 + 3.7/Z) \\ b &= (1 + 0.005/E_C)(-0.01 + 0.04805Z - 0.51500 \times 10^{-3}Z^2 + \\ &+ 0.20802 \times 10^{-5}Z^3). \end{aligned} \tag{2.12}$$

Again, for multicomponent samples these parameters can be calculated considering the effective sample atomic number $Z_{\text{eff}}$.

The PFXP models described so far are valid for homogeneous samples, while for multilayer samples the electron propagation and X–ray production are altered by the presence of a coating–substrate interface [201]. Thus, in principle, a modified PFXP function should be considered to take into account this effect, but, as far as we know, no analytical model is reported in the literature. As a consequence, X–ray generation distribution functions for both coating and substrate are calculated as the PFXP of an homogeneous sample with the same composition as the

layer under analysis. Since the function does not show a strong dependence on the atomic number, this working assumption does not introduce a significant error if the difference between coating and substrate atomic numbers is below 5 [191]. For higher differences, the distortion due to the presence of the coating–substrate interface could introduce an error in areal density measurement.
Moreover, in general, PFXP models should consider the emission of X–rays due to Fast Secondary Electrons (FSE) and fluorescence. In multilayer samples, these effects can be due to the composition of the layer under analysis (matrix effects), but also to the composition of the other layer. The Rehbach–Karduck model adopted in this work only takes into account the FSE matrix effect, whose contribution can be as high as 15% for low energy X–rays if the initial electron energy is much higher than the absorption edge of the peak under analysis [202]. The fluorescence and secondary emission effects due to the sample multilayer structure are not considered in the model.
In addition to the theoretical formulation described so far, a few practical aspects concerning the experimental set–up must be taken into account to achieve reliable areal density measurements.
A noteworthy issue is related to the method selection. The coating method and the substrate method are completely equivalent according to the theory, even though their equivalence still has to be experimentally proved. However, in a given experimental configuration one method could be more convenient or more reliable than the other for merely practical reasons. Thus, the availability of two methods is a resource which can be exploited to overcome practical difficulties related to specific experimental configurations. In a few cases, the choice of the method is determined by the specific properties of the sample's X–ray spectrum. For example, the deconvolution of overlapped X–ray peaks is a time–consuming process that could reduce the technique's reliability. Thus, the selection of non–resolved peaks should be avoided. Moreover, the choice of particular elements can present critical aspects. For instance, the extremely low energy of carbon K$\alpha$ peak (277 eV) could limit the maximum detectable areal density and the low X–ray production cross–section in carbon reduces the signal to noise intensity ratio. Finally, in the case of multi–elemental coatings, the substrate method can be chosen to remove the issue related to the selection of an appropriate reference standard. In principle, it is not required for the reference standard to have the same composition as the sample coating or substrate. The only requirement is that the emitting element must not be present in both layers. Nevertheless, adopting a standard with the same composition as the material under analysis should reduce the error due to modelling approximations. For multielemental coatings it is usually difficult to produce a reference standard with the very same composition as the coating, thus the substrate method should be preferred.
Another issue is related to the selection of an appropriate electron accelerating voltage, which is a crucial issue for areal density measurement since this parameter determines the methods' reliability and applicability range. A rough criterion for voltage selection can be deduced from the requirement that the electron initial energy should guarantee a significant energy loss both in the sample coating and in the substrate. Thus, electron energy must be in a range that allows to

probe the sample substrate, but in which the effect of the coating on electron propagation is not negligible. Moreover, electron energy cannot be lower than the absorption edge of the emitting element. As a consequence, the lower detection limit of the technique is given by the minimum areal density required to absorb a significant fraction of electron energy for beams with initial energy slightly above the absorption edge. On the other hand, the maximum detectable areal density is lower than the electron penetration range at the maximum available accelerating voltage. In addition, the attenuation of X–rays in the sample can reduce significantly the detected spectral intensity and, as a consequence, the higher detection limit of the technique.
As mentioned before, the application of EDS to the evaluation of thin film density was proposed by Zani in his PhD thesis [16] for carbon foams deposited on Si wafers. However, an extensive experimental study would be required to test the applicability and limitations of EDS based density evaluation methods to nanostructured films with various compositions, a large variety of mesoscale morphologies and in a large density range. Moreover, the results reported in Zani's work for carbon foams are affected by errors and approximations. For example, the dependence of the X–ray attenuation coefficients on the X–ray energy was not always considered and the X–ray intensity measurement for the sample under analysis and the reference standard were not performed in the same acquisition conditions. Finally, the data analysis software was based on a non optimized algorithm whose accuracy and correct functioning were strongly dependent on the experimental configuration.

# Part II

# Carbon foam production and characterization

# 3

# Production of foam–based targets

In this Chapter, the main advancements in the development of a suitable carbon foam production technique achieved in the frame of my PhD are discussed, as well as technical issues related to the manufacturing of targets for specific laser–driven ion acceleration experiments described in Chapter 5.
The production of foam–based targets was achieved exploiting the PLD approach developed by Zani *et al.* [15] and described in Section 2.1.2. In particular, the very same deposition configuration was adopted for the production of foam–attached targets for the first experiment performed on this kind of targets (see Section 5.1.1). Two main issues had to be addressed to achieve a reliable carbon foam deposition technique for foam–based target production. Firstly, no attempt had been made in [15] to properly control the foam thickness. In addition, the reproducibility of the deposition process was strongly affected by the gas flow and fluid dynamics effects in the deposition chamber, so that the fine tuning of the foam properties required a time–consuming optimization of the experimental configuration before each set of depositions. Thus, a first goal related to foam–based target manufacturing was the investigation of the role of process parameters, such as deposition duration and target–to–substrate distance, aimed at achieving good process reproducibility and independent control of foam thickness, density and uniformity, in particular for films with density in the $3 - 10\,\mathrm{mg/cm^3}$ range and thickness between $5\,\mu$m and $15\,\mu$m, required for foam–attached targets for TNSA experiments. In addition, a number of technical aspects had to be taken into account in the target design and fabrication phase to make possible the target handling, to avoid target damage during the transport to the laser facility and to satisfy specific technical requirements on target holders for irradiation.
Therefore, this Chapter is divided into two Sections. In Section 3.1, an extensive study on foam thickness control and process reproducibility is presented, along with a strategy for the production of relatively thin carbon foams (below $10\,\mu$m) achieving optimal substrate coverage. In Section 3.2, the deposition conditions selected for the production of foam–attached targets and the main technical issues related to target manufacturing are discussed.

## 3.1 Advancements in the production of carbon foams by PLD

The thickness of films grown by PLD is commonly controlled by tuning the duration of the deposition process (i.e. the number of laser pulses), since this parameter determines the amount of mass deposited on the substrate per unit area, namely the foam areal density[1]. In general, the thickness of compact films increases linearly with the deposition time. This is not always true for porous cluster assembled films, whose thickness can be reduced due to structural compression or mass loss effects. Therefore, an extensive study of the effect of the process duration on the foams properties was performed to achieve an appropriate foam thickness control. Process parameters similar to those described in [15] were adopted: a pyrolitic graphite target was ablated by the second harmonic ($\lambda = 532$ nm) of a Nd:YAG laser (with pulse duration 5–7 ns, repetition rate 10 Hz and fluence $0.8\,\mathrm{J/cm^2}$) in a chamber filled with Ar or He as buffer gas with target–substrate distance $\sim 8.5$. Process durations from 5 to 60 minutes were adopted. Qualitatively different results were achieved for foams deposited in He and Ar.
In Figure 3.1, the thickness of C foams deposited in He atmosphere is reported as a function of the process duration for different pressure values. The thickness increased linearly for relatively low pressure (130 Pa), while a reduced thickness growth rate was observed for higher pressures (300 Pa and 400 Pa). This effect was interpreted considering the amount of matter deposited on the substrate surface (Figure 3.2). The areal density trend for foams grown in He was approximately linear for process durations up to 60 minutes. Therefore, the reduced thickness increase was probably due to a progressive filling of empty spaces between the film mesoscale structures or to a structural compression of the film, which led to an increase of the film density for long depositions (from 4 $\mathrm{mg/cm^3}$ to 7–12 $\mathrm{mg/cm^3}$ for foams produced in Ar at 400 Pa or 300 Pa, respectively).
Also in the case of foams deposited in Ar the relationship between foam thickness and deposition time was linear for relatively low pressure (40 Pa), but an evident thickness saturation effect was evident for high pressure values (70–100 Pa), as shown in Figure 3.3. In this case, a saturation effect was observed also for the amount of deposited mass (see Figure 3.4) and the foam density was approximately constant (in the 5-10 $\mathrm{mg/cm^3}$ range), thus the thickness saturation was attributed to a dynamic equilibrium state in which the mass deposited on the top of the foam was equal to the amount of mass lost by the foam due to its extremely porous structure and to fluid dynamic effects.
As a result of this study on the role of process duration in C foam deposition, foams with thickness from 10 to 150 $\mu$m were produced by properly selecting the deposition time and the buffer gas. In principle, the upper thickness limit could be further extended, for foams produced in He, at least to the thickness saturation threshold by simply adopting longer deposition durations. On the contrary, the deposition of films thinner than $10\,\mu$m could not be achieved by reducing the number of laser pulses, since the uniformity of coatings deposited with a target–substrate

[1] Areal density values reported in this Chapter were measured by the EDS methods introduced in Section 2.2, which will be discussed in further detail in Chapter 4.

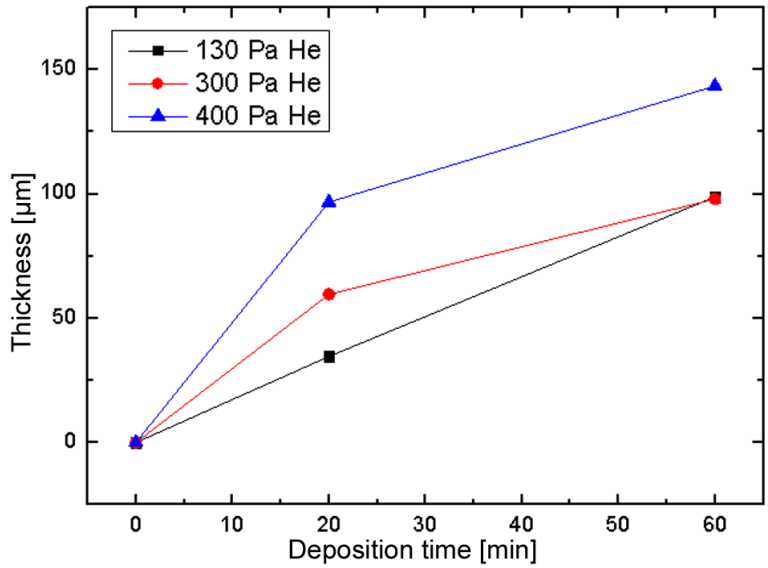


**Figure 3.1:** *Thickness of foams deposited in He with different pressures, plotted as a function of process duration.*

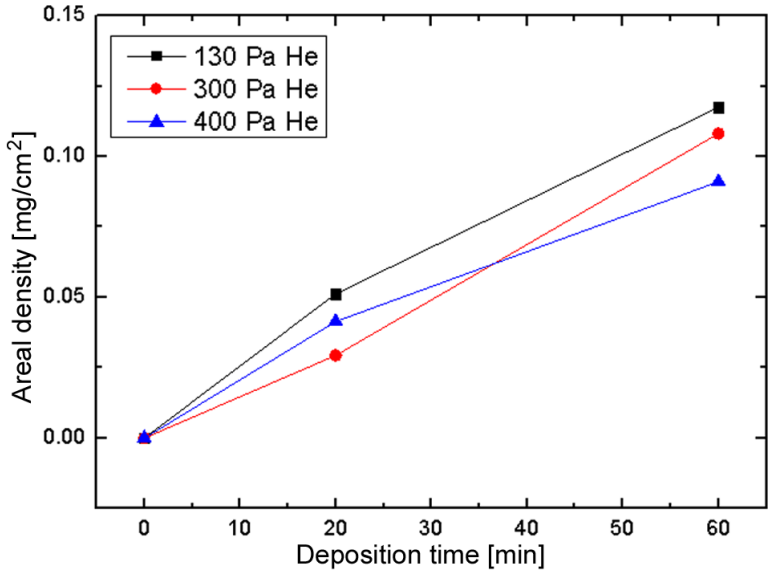


**Figure 3.2:** *Areal density of foams deposited in He with different pressures, plotted as a function of process duration.*

distance around 8.5 cm proved to be unsatisfactory for thickness below 12 $\mu$m and substrate coverage was only partial (often lower than 50%) below 10 $\mu$m, as shown in Figure 3.5. Even attempts to improve thin foam uniformity by adding a directional gas flux in the deposition chamber were unsuccessful. Thus, this deposition setting proved to be not perfectly suitable to produce films matching thickness, substrate coverage and uniformity requirements for enhanced TNSA targets for high intensity lasers.

The impossibility of growing ultra–low density films with good quality and thickness below 10 $\mu$m was intrinsically related to the deposition configuration. The

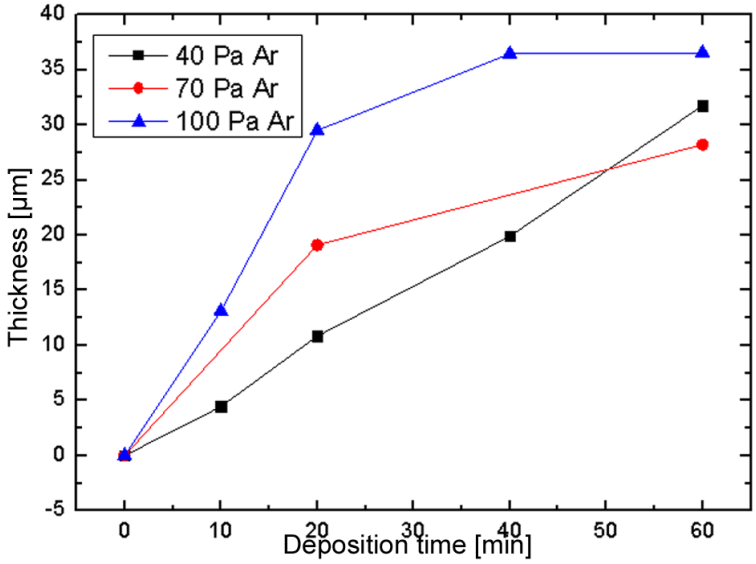


**Figure 3.3:** *Thickness of foams deposited in Ar with different pressures, plotted as a function of process duration.*

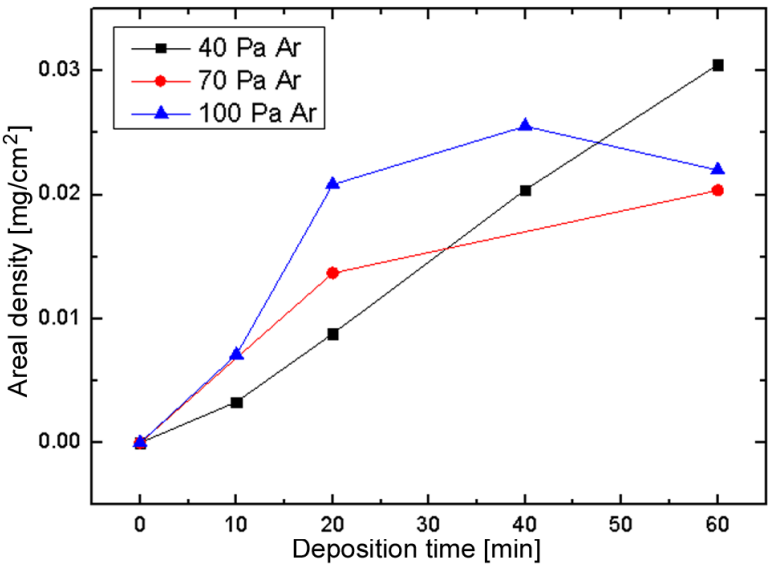


**Figure 3.4:** *Areal density of foams deposited in Ar with different pressures, plotted as a function of process duration.*

foam growth in inert gas atmosphere was achieved through the deposition of clusters and nanoparticles formed during the propagation phase and reaching the substrate with low kinetic energy. The extremely low deposition energy prevented the reorganization of the desposited material on the substrate resulting in porous structures, but also in a poor cluster packing.
As a consequence, other deposition configurations were considered to achieve good uniformity and substrate coverage for low density foams with thickness lower than 10 $\mu$m. In particular, the effect of the target–substrate distance on the deposition process and on the foam properties was investigated with the aim of exploiting

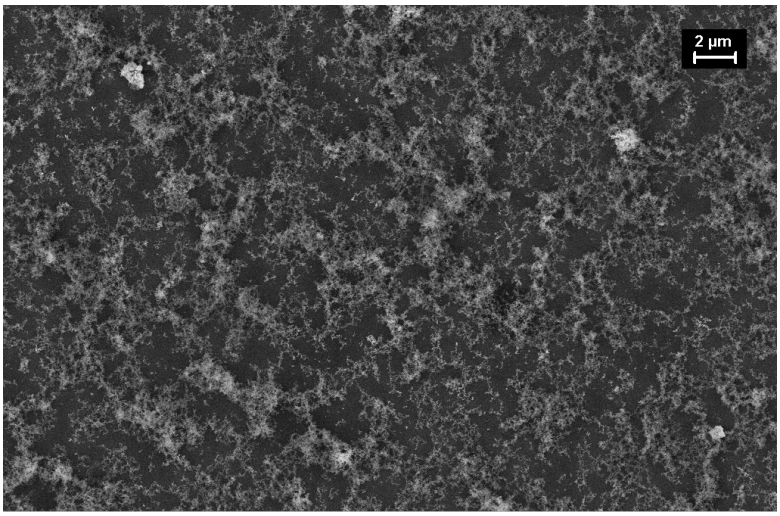


**Figure 3.5:** *Representative SEM image of carbon foam (thickness* $\sim 7.5\,\mu m$*) with incomplete substrate coverage.*

the larger solid angle intercepted by the substrate surface, the enhanced deposition rate and the higher density of particles reaching the substrate surface. This investigation was divided into two phases: at the beginning the effect of the target–to–substrate distance was studied considering the same ambient gas pressure range of previous experiments, while in a second phase higher pressure values were considered with the aim of recovering an optimal condition for the production of ultra–low density foams.
The target–substrate distance was gradually reduced from 8.5 cm down to 4.5 cm at constant pressure resulting in an enhancement of the energy of deposited particles and, as a consequence, to the production of more compact and denser structures. In Figures 3.6 and 3.7, top view SEM images of carbon foams deposited in He at 400 Pa and with target–to–substrate distance 4.5 cm and 6.5 cm are shown for two different magnifications. An evident difference between the microstructure of foams produced for different target–to–substrate distances was observed. The macroparticles produced by the aggregation of the elementary nanoparticle were very open and porous for foams deposited at 6.5 cm from the ablated particles, while they became compact as the target–to–substrate distance was reduced (see Figure 3.6), resulting in an increase of the foam density from 9.3 $mg/cm^3$ to 24.4 $mg/cm^3$ as the target–to–substrate distance was reduced from 6.5 cm to 4.5 cm. The morphological difference was less evident from SEM images with a lower magnification factor (Figure 3.7), but lower magnifications showed that the characteristic spacescale of the foam structure decreased for decreasing target–to–substrate distances. Carbon foams deposited in He at relatively low target–to–substrate distance did not satisfy the requirements for the production of foam–based targets for laser driven acceleration: besides a relatively high density, these foams showed an incomplete substrate coverage below 11 $\mu$m and a remarkable macroscopic non–uniformity (i.e. an evident Gaussian thickness profile).
A similar experiment was performed in Ar atmosphere with pressure between 40

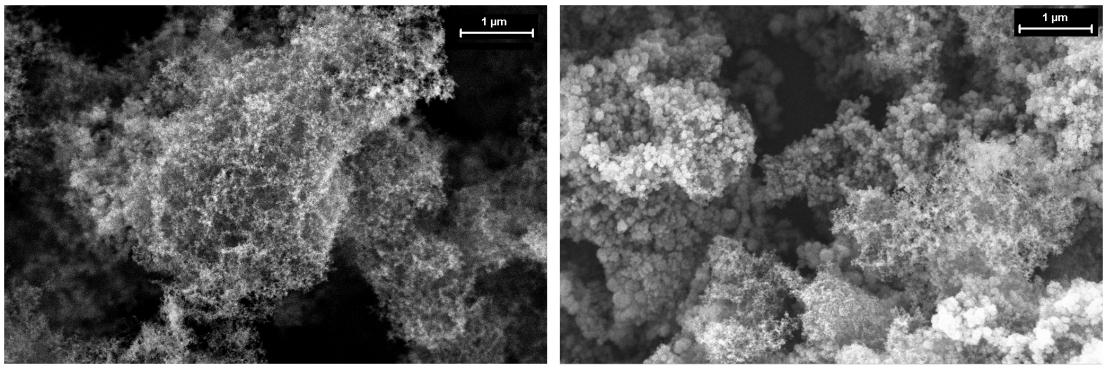


**Figure 3.6:** *High magnification top view SEM images of carbon foams deposited in He at 400 Pa with target–to–substrate distance 6.5 cm (left) and 4.5 cm (right).*

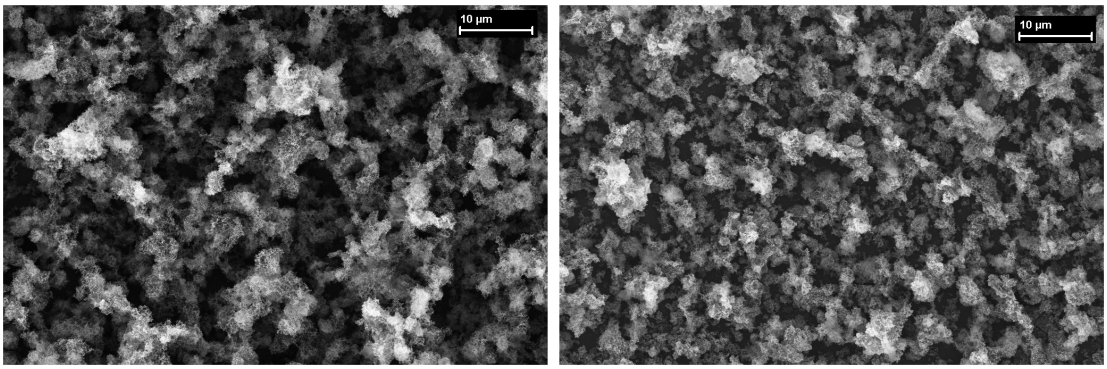


**Figure 3.7:** *Low magnification top view SEM images of carbon foams deposited in He at 400 Pa with target–to–substrate distance 6.5 cm (left) and 4.5 cm (right).*

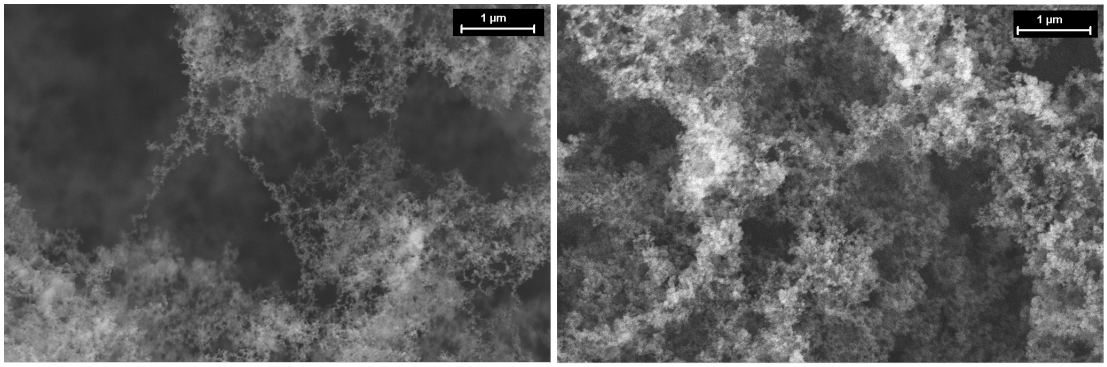


**Figure 3.8:** *Top view SEM images of carbon foams deposited in Ar at 40 Pa with target–to–substrate distance 8.5 cm (left) and 6.5 cm (right).*

Pa and 70 Pa by reducing the target–to–substrate distance from 8.5 cm to 4.5 cm. The resulting microstructures are shown in Figure 3.8. As expected, the effect on the foam structure was quite similar to the case of foams grown in He: the distance reduction led to a transition from an extremely porous morphology to a structure composed by more compact aggregates and to the production of foams with higher density. As mentioned before, this transition was to be expected since generally, for relatively low target–to–substrate distances, the diffusion of ablated

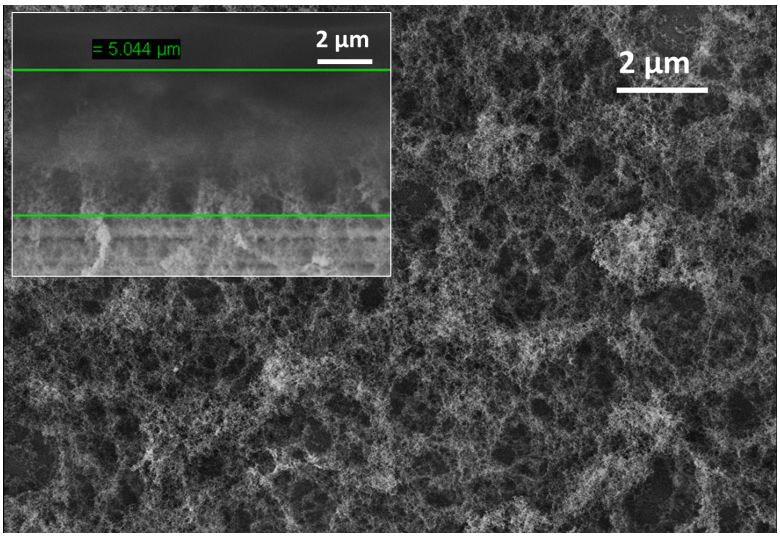


**Figure 3.9:** *Top–view and cross–sectional (inset) SEM images of a 5 µm thick foam (Ar pressure 500 Pa, process duration 60 s, target–substrate distance 4.5 cm).*

material through the ambient gas is stopped before the species lose a relevant fraction of their energy in collisions with gas atoms and more compact structures are formed. Again, a smaller characteristic foam inhomogeneity scale was observed for low target–to–substrate distance.
The possibility of achieving a better structure packing and growing foams with reduced characteristic inhomogeneity scale was crucial in the production of carbon foam layers with thickness below 10 $\mu$m, since a reduced typical length of the structure formed by macroparticles would lead to an enhanced substrate coverage even for thin foams. However, higher pressure values were required to achieve an experimental configuration suitable for the deposition of foams with extremely porous morphology and low density. Therefore, Ar pressures between 300 Pa and 700 Pa and a target–to–substrate distance of 4.5 cm were adopted. In this way, a morphology similar to the porous low density morphology demonstrated by Zani *et al.* [15] was achieved, but with a reduced foam characteristic inhomogeneity spacescale. Foams produced in this new configuration ($d_{ts} = 4.5$ cm, $P_{Ar} \sim 300 - 700$ Pa) had porous morphology (Figure 3.9), low density (down to $5\,\mathrm{mg/cm^3}$), satisfactory uniformity and substrate coverage despite their low thickness (down to $3-5\,\mu$m). Besides an increased deposition rate, in this configuration an impressive enhancement in the process reproducibility was observed since the foam growth was less affected by fluid–dynamic effects in the deposition chamber. The main drawback of this new deposition configuration was a more pronounced Gaussian–like shape in the film thickness profiles due to the low target–substrate distance, resulting in a reduction of the surface area in which the foam thickness could be considered uniform to $\sim 1\,\mathrm{cm^2}$. However, in general, this is more than enough for single laser–matter interaction targets since tight focused lasers have focal spot of a few $\mu$m).
Figure 3.10 shows a summary of the thickness and density ranges of carbon foams produced by Pulsed Laser Deposition so far. Thickness has been evaluated using

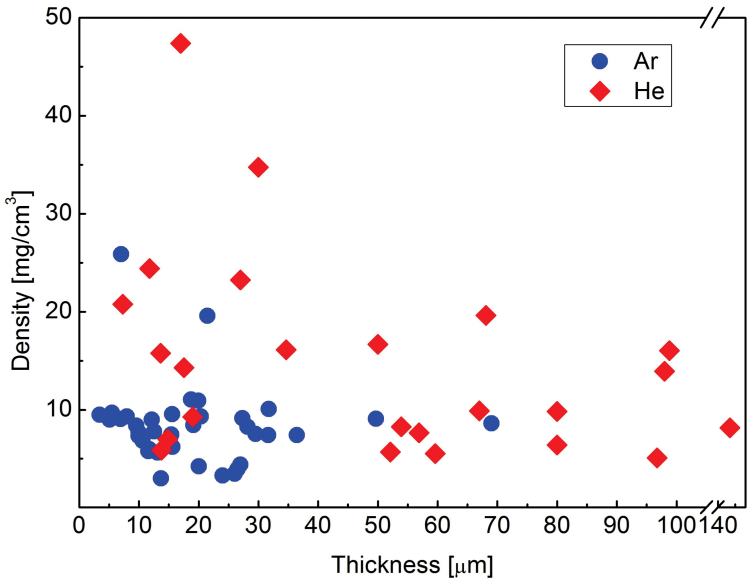


**Figure 3.10:** *Graphic representation of carbon foam thickness and density ranges achieved by PLD using Ar (blue circles) or He (red diamonds) as buffer gas.*

cross sectional SEM images, while density has been measured using an EDS based method. As shown in the figure, carbon foams with density down to 3 mg/cm$^3$ and thickness from 5 $\mu$m to 150 $\mu$m were grown by PLD tuning the target–substrate distance, the duration of the deposition process, the pressure and the composition of the buffer gas. Thus, PLD proved to be a suitable technique for the production of foam–attached targets for laser–driven ion acceleration experiments.

## 3.2 Target manufacturing

Besides the selection of appropriate conditions for the production of the carbon foam by PLD, several technical issues had to be addressed to produce targets for laser–driven ion acceleration experiments. While carbon foams produced to tune the deposition process parameters were grown on thick Si wafers which could be easily handled, the deposition of low density carbon foams on thin Al foils (0.75-10 $\mu$m) required the design of appropriate foil holders. The size and shape of these foil holders depended on the specific target holder configuration of each facility. In addition, the necessity of preserving the targets during their transport to the laser facility and the positioning in the interaction chamber had to be taken into account. Two deposition configurations and foil holder designs were considered in my thesis work for the production, transport and irradiation of foam–attached targets in two different laser systems: UHI100 at the LIDyL facility (France) and PULSER I at GIST (South Korea). Further details on the experimental configuration adopted for foam–attached target irradiation can be found in Chapter 5.

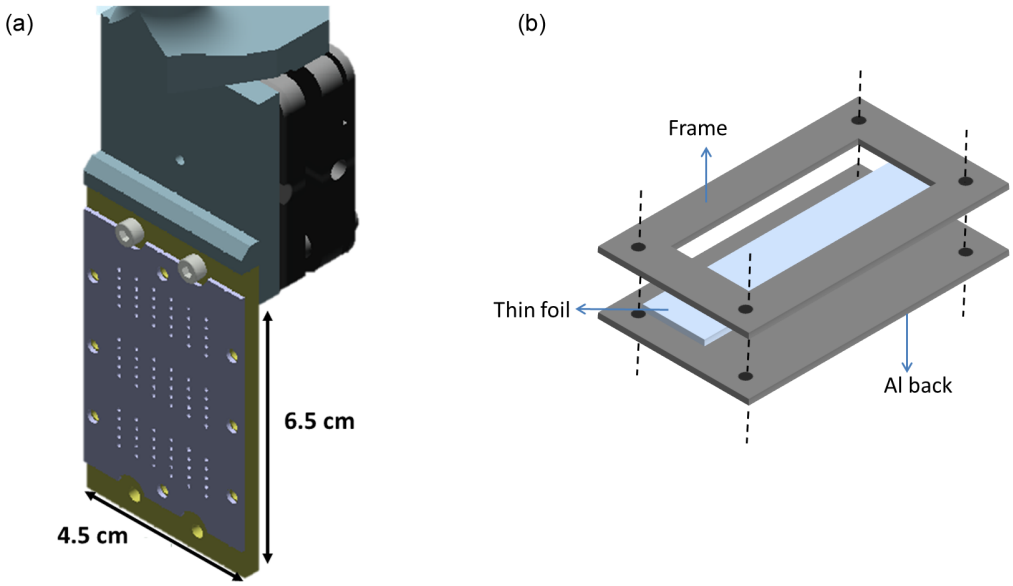


**Figure 3.11:** *Target holder in use in the interaction chamber of the UHI100 laser system at the LIDyL facility (a) and sandwich target support designed for foam–attached target manufacturing and logistic (b).*

### 3.2.1 Targets for UHI100 (LIDyL)

The first laser–driven ion acceleration experiment on foam–attached targets considered in this PhD thesis was performed in May 2012 at the UHI100 laser system of the LIDyL facility (see Section 5.1.1). The target holder in use in the interaction chamber of this laser system is illustrated in Figure 3.11(a). Here, three targets ($\sim 1.5 \times 2.5$ cm) had to be inserted between two pierced plaques. Thus, sandwich target supports were designed as shown in Figure 3.11(b). In this configuration, a commercially available Al foil ($4.5 \times 2.5$ cm) was laid down on a solid Al back and held in position by an Al frame fixed with screws. The sandwich support was then located in the deposition chamber and covered by a foam layer, before packing it for delivery. The foam–attached foil was transferred to the target holder at the laser facility before the irradiation.

Two kinds of targets were employed for this experiment, composed by a 13 $\mu$m or 23 $\mu$m thick carbon foam layer deposited onto a 1.5 $\mu$m or 10 $\mu$m thick Al foil, respectively. The PLD process parameters adopted for target manufacturing are listed below.

- Laser fluence: 0.8 J/cm$^2$.
- Ambient gas: Ar 100 Pa.
- Gas flow: 30 sccm along the target normal direction.
- Target: pyrolitic graphite.
- Target–to–substrate distance: 8.5 cm.
- Substrate: 0.5 mm thick Si wafers for foam characterization; 1.5–10 $\mu$m thick Al foils for target production.

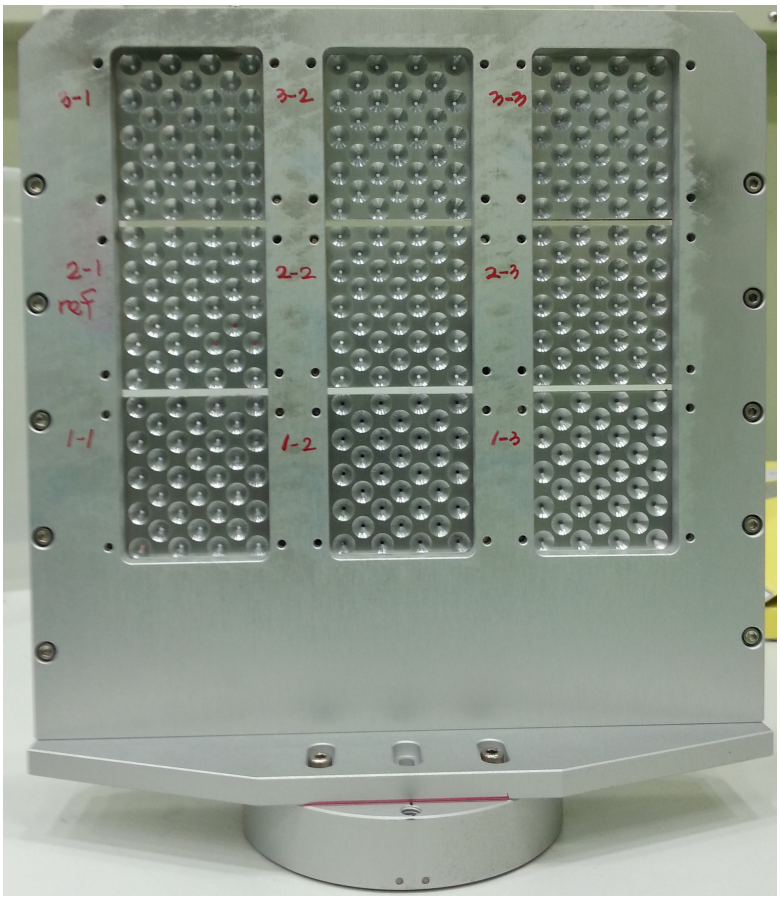


**Figure 3.12:** *Target holder in use in the interaction chamber of the PULSER I laser system at the GIST facility.*

- Process duration: 10–20 min.

### 3.2.2 Targets for PULSER I (GIST)

A second experiment on foam–attached targets was performed at the PULSER I laser system of GIST (see Section 5.1.2). In this case, the target holder placed in the interaction chamber was composed by a frame holder (Figure 3.12) containing $3 \times 3$ single target holders (Figure 3.13) with conical holes for laser focusing. In this case, an additional foil holder was designed to handle the targets from the deposition process to the irradiation experiment. This foil holder was a stainless steel plaque with holes corresponding to the apertures of the GIST single target holder. The overall assembly is shown in Figure 3.14. A spray adhesive was employed to fix the thin Al foil to the foil holder. Due to the low thickness (0.75 $\mu$m and 1.5 $\mu$m) and the large area ($\sim$ 4.5 $\times$ 5 cm) of Al foils considered in this experiment, an expedient for the correct foils positioning was contrived. A mask covering the lateral foil holder bands was employed to spray only on the central part of the plaque, producing a sharp border between the adhesive and non–adhesive regions. The edge of an Al foil, held on a paper support, was placed at the adhesive region border, which was used as a sort of hinge to rotate the

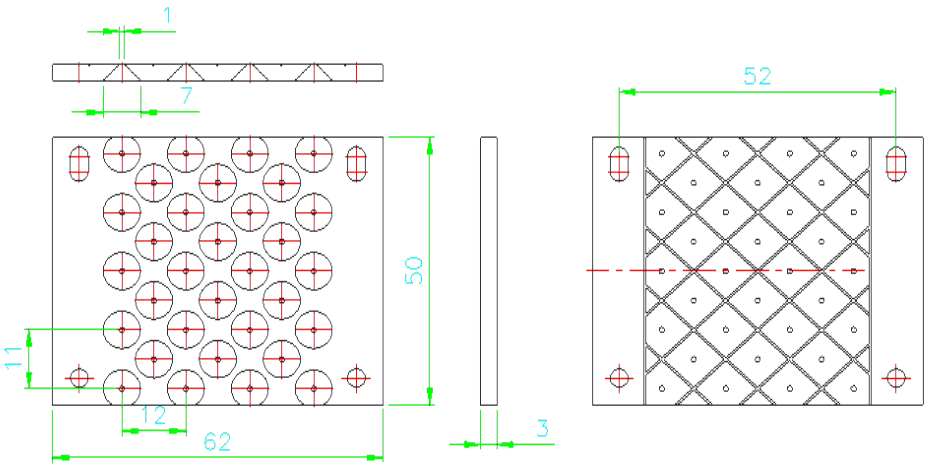


**Figure 3.13:** *Dimensioned technical drawing of the single target holder adopted at the GIST facility.*

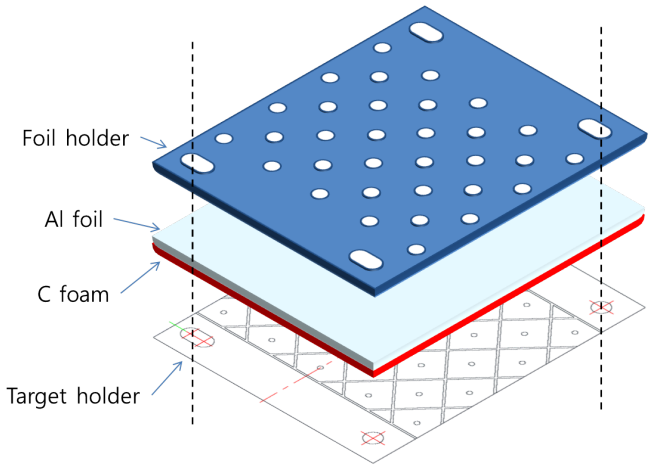


**Figure 3.14:** *Overall target assembly to be mounted in the GIST target holder frame.*

Al foil on the target support. This expedient allowed to attach the thin Al foils without producing wrinkles or breaking them. The sample was then placed in the deposition chamber and covered with carbon foam. Several targets were piled up together in bundles using spacers to prevent target damage during the transport to the laser facility. Targets were assembled at the laser facility. Due to the small diameter of the conic holes of the target holder (1 mm on the side in contact with the foam), high precision was required for this operation. The assembling phase is shown in Figure 3.15. A metallic slab with an appropriate milling was used to accurately position and fix the target holder to the foil holder. This configuration allowed to prevent any possible damage due to target assembling.
A low target–to–substrate distance deposition configuration was selected for the production of near–critical carbon foams to be employed in this experiment ($d_{ts}$ = 4.5 cm). As mentioned in Section 3.1, this deposition configuration resulted in a reduced foam uniformity area $\sim 1\,\mathrm{cm}^2$ and in a Gaussian–like thickness profile.

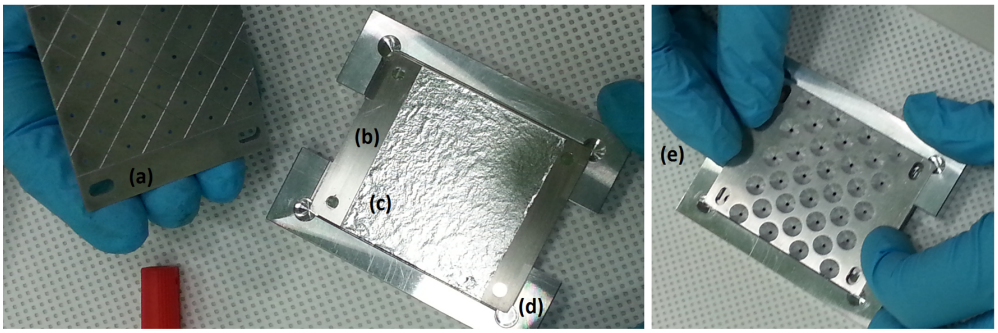


**Figure 3.15:** *Target assembling at laser facility: (a) single target holder; (b) foil holder; (c) foam–attached foil; (d) milled component; (e) target assembling.*

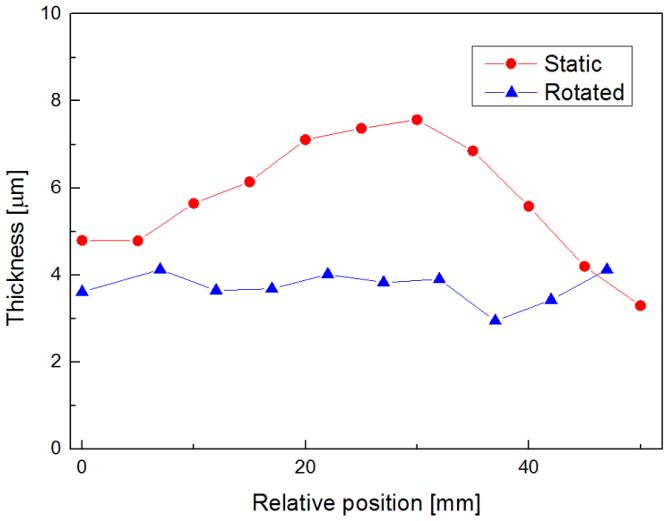


**Figure 3.16:** *Illustrative thickness profiles of films deposited on a static substrate (red circles) and on a suitably offset rotating substrate (blue triangles).*

In general, this is more than enough for single laser–matter interaction targets since tight focused lasers have focal spot of a few $\mu$m, but it is not acceptable for the large target arrays required for this experiment. This issue was addressed by suitably offsetting and rotating the substrate. This expedient allowed to produce foams with a thickness standard deviation lower than 15% on areas with diameter larger than 5 cm, as shown in Figure 3.16, even though the rotation increased to 8 $\mu$m the minimum foam thickness achievable with satisfactory coverage and microscale uniformity.

Several kinds of targets were manufactured for this experiment. Two kinds of foam with different density were considered: near–critical foams with thickness ranging from 8 $\mu$m to 36 $\mu$m and 12 $\mu$m thick slightly over–critical foams. Al foils with thickness 0.75 $\mu$m and 1.5 $\mu$m were employed. The PLD process parameters adopted to grow carbon foams for this experiment are listed below.

- Laser fluence: $\sim 1\,\mathrm{J/cm^2}$.
- Ambient gas: Ar at 500 Pa ($n_{foam} \sim 1.2\,n_c$, with $d_{ts} = 4.5$ cm); Ar 30 Pa ($4.3\ n_{foam} \sim 1.2\,n_c$, $d_{ts} = 8.5$ cm).

- Target: pyrolitic graphite.
- Target–to–substrate distance: 4.5 cm, 8.5 cm.
- Substrate: 0.5 mm thick Si wafers for foam characterization; 0.75–1.5 $\mu$m thick Al foils for target production.
- Process duration: from 6 to 23 min depending on the required thickness.

### 3.2.3 Towards high repetition rates

The solutions proposed in the previous sections for target manufacturing and handling proved suitable for the experiments performed on foam–based targets in the frame of my PhD thesis. In particular, the configuration adopted for the experiment performed at GIST was extremely easy to handle, robust enough to be safely delivered and to preserve neighbouring targets during the irradiation phase. In the GIST experimental configuration, for a single target frame (28 available targets), a number of shots between 8 and 12 was required to achieve an appropriate alignment (a procedure requiring a few minutes), leaving 16–20 available targets per frame. Therefore, this configuration would not be compatible with laser–driven ion acceleration experiments with high repetition rate. The development of acceleration systems capable of delivering ion bunches with repetition rate at least in the Hz regime is a necessary condition for most potential application of laser–driven ion sources, since in general average ion beam current values from nA to mA are required. Thus, it is interesting to discuss the possible implementation of foam–attached target configurations compatible with high repetition rate irradiation, also in the light of a comparison with other target configurations proposed so far in literature.
In principle, if suitable holders for foam deposition, transport and irradiation were available, the foam–attached target configuration would be compatible with high repetition rate experiments. According to simulations and preliminary experimental results (see Section 5.1.2), the acceleration performances shouldn't be strongly dependent on the substrate thickness, thus $\mu$m–thick foils can be employed to guarantee appropriate mechanical properties. Foils in this thickness range, for example, are robust enough to prevent damage to neighbouring targets during the irradiation. In addition, since the laser–pulse interaction in foam–attached targets takes place in the foam volume, the laser focus should be localized in the foam. Therefore, sub–micrometric precision in target alignment is not expected to be crucial for this target concept, while for solid foil targets, it is necessary to have a precise pulse focusing to provide the maximum laser intensity at the vacuum–target interface and to maximize the laser–target energy transfer. On the other hand, other advanced targets can be less robust, as for example ultra–thin targets (thickness $\sim$10s of nm), in which the incoming pulse can produce a shock propagating in the foil and damaging neighbouring targets. In addition, a high precision in target alignment is expected to be essential for ultra–thin foils, mass limited targets, flat–top microcone targets and targets with hydrogen–rich dots on the rear surface (see 1.3.1).

**Figure 3.17:** *Wheel target holder geometry of RAL High Accuracy Microtargetry System: wheel schematic (left), targets arranged in rows around the wheel circumference for each sector (center), wheel main structure (right). The holder allows to position up to 1000 targets the eight segments. From [203].*

The application of foam–attached targets to high repetition rate experiments requires planar holder geometries (tape targets, for example, would erase or at least damage the foam layer) which allow to achieve a large number of shots after the alignment stage. For example, large arrays of targets in rectangular or wheel geometry could be used if an automatic positioning system were available (see Figure 3.17). In this case, again, the thin foil could be attached to a grid or pierced plaque before the deposition stage.

Large target arrays could also be a suitable strategy for massive target production by PLD, provided that a suitable deposition configuration were adopted. In the present PLD configuration, the maximum diameter of the region in which the foam layer can be considered uniform (in terms of thickness) is $\sim 5$ cm. However, an appropriate combination of substrate spinning and traslatory movement during the deposition process should allow to achieve a satisfactory foam uniformity over larger areas.

In summary, after a preliminary evaluation, no serious drawbacks are evident as regards the possibility of employing the foam–attached target concept in high repetition rate experiments.

# 4

# Energy Dispersive X-ray Spectroscopy for thin film density evaluation

As illustrated in Chapter 2, the most complex issue related to the characterization of low density carbon foams is density measurement. In this Chapter, my activities related to the development of EDS based methods for thin film density measurement are discussed. A number of theoretical, experimental and technical issues should be taken into account to achieve reliable areal density measurements. In light of aspects illustrated in Section 2.2, the first goal of my activity was the development of a suitable software for data analysis to infer an accurate areal density evaluation from measured X–ray intensities not only for low density carbon foams deposited on Si substrates, but virtually for any possible film–substrate combination, including multicomponent films. The application of EDS based methods to thin film density evaluation, then, required an exhaustive investigation of the technique effective reliability and limitations and the availability of a suitable model for X–ray production in multilayer samples.
These issues are considered in the two first Sections of this chapter. Section 4.1 illustrates the results of an extensive validation campaign aimed at studying the applicability of the EDS based methods to nanostructured films with various compositions, a large variety of mesoscale morphologies and density ranging from the density of solid to a few $mg/cm^3$. In addition, the possibility of exploiting the spatial resolution of this technique to investigate the properties of non–homogeneous films is discussed. In the same section, critical issues related to the effect of the experimental configuration on the technique reliability are discussed, such as the selection of an appropriate electron accelerating voltage, the role of the atomic number difference between the sample coating and substrate choice of the measurement method, in order to provide useful guidelines for the application of EDS to nanostructured film density evaluation. In Section 4.2, issues related to the distortion of the PFXP function in multilayer samples are discussed and a possible approach to evaluate the distribution in the coating and substrate of multilayer samples is outlined. In Section 4.3, novel measurement approaches to extend the applicability of the technique to free–standing films and simplify the data acquisition are proposed.

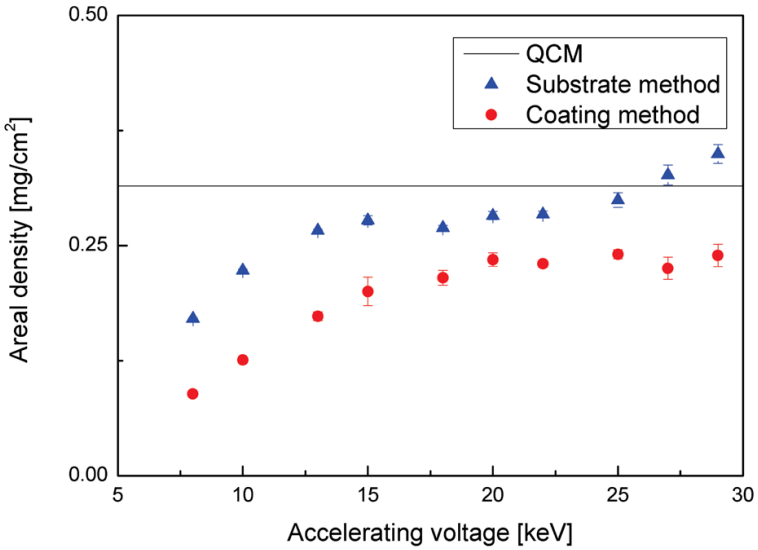


**Figure 4.1:** *Areal density of a thin Ag film on Au substrate measured as a function of the electron accelerating voltage.*

## 4.1 Experimental development of the technique

In this Section, the results of an extensive experimental campaign intended to apply EDS based methods to the evaluation of the density of nanostructured thin films with known thickness are presented. The technique validation was achieved by comparing density values measured by EDS methods and the results achieved with other well established techniques, i.e. with a high precision weighing scale or a QCM.
The first experiment aimed at the validation of the technique was performed using compact Ag films (with expected density 10.49 g/cm$^3$) deposited through thermal evaporation on a Au coated QCM resonator. In this way, EDS and QCM areal density measurements performed on the very same film were compared. The value achieved by QCM, 0.31 mg/cm$^2$, was considered as a reference, since areal density values achieved by QCM are generally very reliable for films grown by thermal evaporation. Ag and Au were chosen as coating and substrate materials, respectively, due to the high atomic number difference between these elements. As discussed in Section 2.2.2, this configuration is not optimal for EDS measurements and allows to validate the technique and quantify the error in the worst case scenario.
The coating method and the substrate method were employed to characterize the Ag film in a wide electron accelerating voltage range (8-29 kV). From the results reported in Figure 4.1, it is evident that for both methods an optimal range for the electron accelerating voltage exists, in which the areal density values are less affected by voltage variations. In this experimental configuration, for the coating method a voltage higher than 19 kV is required, while the substrate method provides stable results above 13 kV. The maximum acceptable voltage could not be determined as it is higher than the maximum value achievable with our instru-

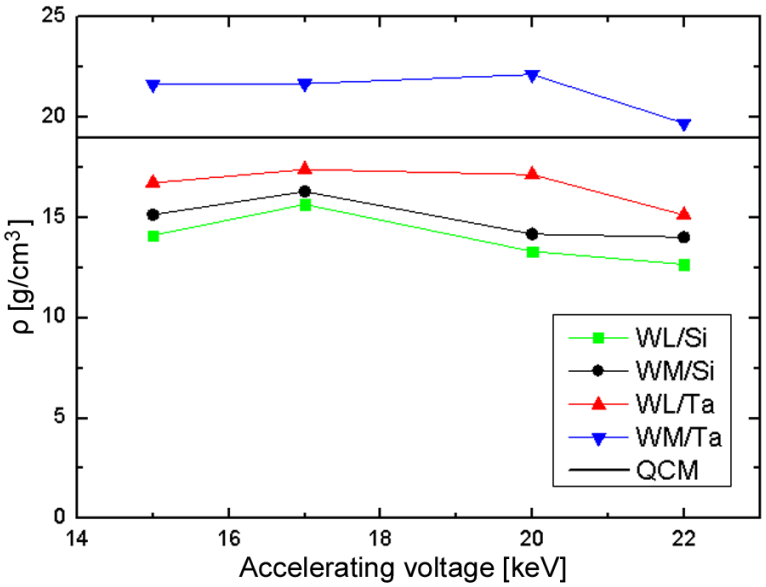


**Figure 4.2:** *Density of a thin W film on Si and Ta substrate measured as a function of the electron accelerating voltage with the coating method.*

ments. The results reported in Figure 4.1 allow to compare the accuracy of the two methods. In the optimum voltage range, the deviation from QCM measured areal density is around 10% and 25% respectively. Thus, in this case, the substrate method is more accurate than the coating method.
Amorphous–like tungsten films deposited by PLD on Si and Ta substrates [204] were exploited to investigate the main experimental issues affecting the reliability of areal density measurements: the selection of an appropriate electron accelerating voltage; the role of fluorescence effects; the role of the atomic number difference between the sample coating and substrate and the measurement approach choice. In particular, the density of W films deposited in vacuum on Si and Ta substrates was measured by a high precision weighing scale, a QCM and using both EDS methods with accelerating voltage ranging from 15 kV to 22 kV. Density values achieved by QCM are considered as a reference, even though densities achieved in PLD facilities can be affected by an error also for compact films (around 5-10% for our experimental setting) due to the difficulty of placing the sensor in the very same position as the substrate. Again, a good stability of the technique with respect to the accelerating voltage selection was observed for both methods. The effect of the atomic number difference between the sample coating and substrate on the measurement process is evident from Figure 4.2, in which density values measured with the coating method for W films deposited on Si and Ta substrates in the very same conditions are compared. Two different W peaks have been considered: W $M\alpha$ and W $L\alpha$. Two interesting observations can be inferred from these results. Firstly, the W film density measured in the case of a Ta substrate is always higher than values achieved in the case of a Si substrate. This confirms the presence of a PFXP distortion due to the sample multilayer structure. W and Ta are consecutive elements on the periodic table ($\Delta Z = 1$), thus the fraction

of electrons scattered back to the film from the Ta substrate is very close to the value which would be observed in the case of an homogeneous sample at a depth equal to the film thickness. Therefore for W films deposited on Ta substrates the adoption of a PFXP function valid for an homogeneous sample does not affect the measurement. On the contrary, the Si substrate scatters a relatively low number of electrons back to the W film, resulting in a reduction of the X–ray production in the film and in the measured density value. A second interesting observation is related to the difference between results achieved considering the W $M\alpha$ and W $L\alpha$ peaks in the case of Ta substrate. This difference is due to fluorescence effects due to the production of Ta $L\alpha$ X–rays with energy about 8.1 keV in the substrate. These X–rays can be absorbed by W atoms (the absorption edge related to the W $M\alpha$ peak is around 1.8 keV) and produce an enhancement of the intensity of the W $M\alpha$ peak, leading to an overestimation of the film density. This effect is not present if the substrate is a Si wafer because the energy of Si $K\alpha$ X–rays is not sufficient to produce fluorescence in the W film. In addition, the case of a W film deposited on a Ta substrate provides an experimental proof of the equivalence of the coating and substrate methods if no PFXP distortion effects take place: a difference lower than 3% was observed between density values measured with the substrate method and the coating method considering Ta and W $L\alpha$ peaks, whose intensity is not affected by fluorescence effects. On the contrary, in the case of W films deposited on Si substrates, the substrate method is affected by fluorescence effects due to the high energy X–rays produced in the W coating. This is evident from results of an experiment aimed at testing the reliability of EDS methods was tested for W nanostructured films grown by PLD on a Si wafer in a wide density range, reported in Figure 4.3. Here, density values measured using both EDS methods and QCM are plotted as a function of the gas pressure in the deposition chamber during the film growth process. The deviation of measured values from reference density values evaluated by QCM is around 5% for the coating method (considering the W $L\alpha$ peak), much lower than the difference observed for the substrate method, which in some cases is above 30%, except for the sample deposited in vacuum. This was attributed to a possible loss of accuracy of the thickness measurement achieved through SEM cross–section analysis, which might be affected by an error around 10% due to the low thickness of the W coating deposited in vacuum (less than 100 nm).

The effect of the substrate atomic number on density values evaluated using the coating method was further investigated in a proof–of–principle experiment performed on commercially available Al foils with known density and thickness ($2.7\mathrm{g/cm}^3$ and $750\,\mathrm{nm} \pm 30\%$). Two different experimental configurations were considered: measurements were performed on free–standing Al foils and on Al foils arranged on carbon substrates. In both cases, the foil density is systematically underestimated, but the average deviation from the nominal value is around 28% for the free–standing configuration and 20% in presence of a carbon substrate. This difference can be interpreted considering that the presence of a carbon substrate enhances the signal from the Al foil, since electrons emerging from the rear side of the Al foil are not necessarily lost by the system, but can be scattered back to the foil by C atoms. Thus, the Al PFXP approximation is more reliable

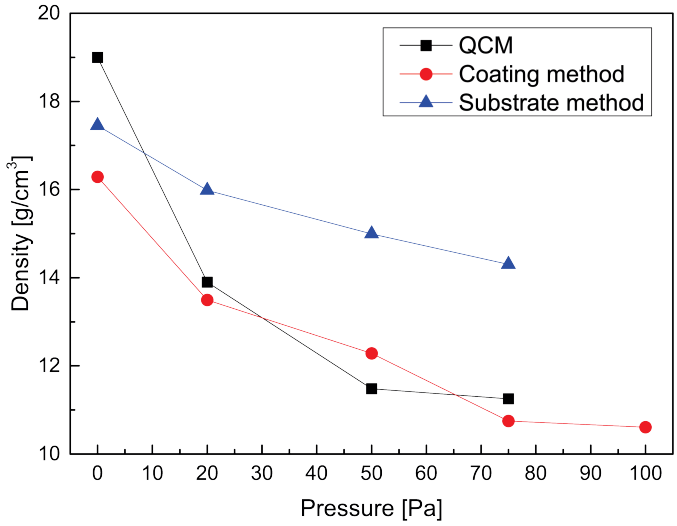


**Figure 4.3:** *Density of thin tungsten films as a function of gas pressure in deposition chamber.*

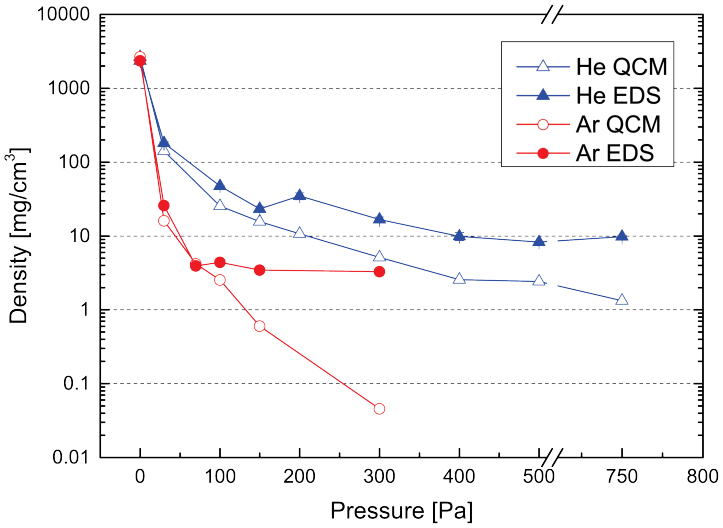


**Figure 4.4:** *Density of carbon foams as a function of gas pressure in deposition chamber.*

in presence of the C substrate than in the free–standing configuration.
As mentioned in Chapter 3, the application of the EDS methods to nanostructured films was tested exploiting carbon foam with densities down to a few mg/cm$^3$. In this case, the substrate method was selected for the reasons discussed in Section 2.2.2, namely the low energy and emission probability of C $K\alpha$ X–rays. In Figure 4.4, results for both the substrate method and QCM are shown as a function of the gas pressure in deposition chamber. The agreement between the two methods is satisfactory only for density values above 30 mg/cm$^3$. For lower densities, values

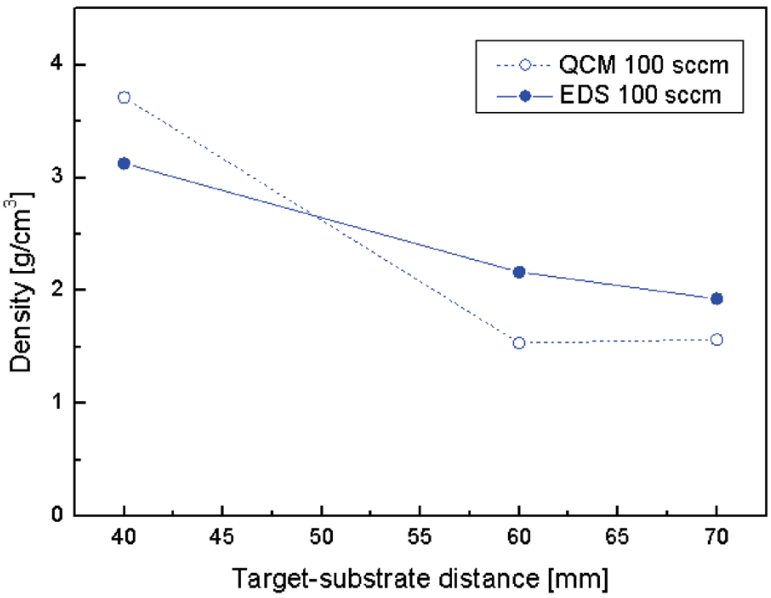


**Figure 4.5:** *Density of Al–doped ZnO films as a function of the target to substrate distance.*

measured by QCM are unrealistically low, as QCM undergoes a sensitivity loss due to the very porous foam structure which results in a decoupling between the film and the quartz crystal resonator [187]. On the contrary, the substrate method shows a more plausible density saturation for increasing gas pressure, which is typical of this kind of deposition process. From these results we can draw a fundamental conclusion: EDS–based methods can be applied for films produced by PVD for densities down to a few mg/cm$^3$, also in a density range in which QCM is not reliable.

The possibility of employing EDS for density evaluation in the case of multi–elemental coatings was tested exploiting aluminium–doped zinc oxide (AZO) nanostructured films [205]. In this case, the substrate method was chosen due to the unavailability of reference standards with the same composition as the films under analysis. In Figure 4.5, results achieved using the substrate method and QCM are shown as a function of the target to substrate distance. In this case, a strong uncertainty affects density values achieved by QCM, because the deposition configurations adopted for film growth and for QCM measurements were not equivalent. However, density trends predicted by QCM are confirmed by the substrate method. Thus, as stated in [205], a decreasing trend in the film density with the target to substrate distance is observed.

One of the most interesting characteristics of EDS is its spatial resolution, which can be exploited for the characterization of non–uniform films at a macroscopic scale, i.e. for density profile evaluation, and at a microscopic scale, for the evaluation of the characteristic inhomogeneity length of a material.

The density profiles of Rh nanocrystalline coatings were measured along a cross–section exploiting both the coating method and the substrate method. Density was calculated from areal density and thickness values measured in the very same points. The results reported in Figure 4.6 refer to a Rh film with non–uniform

thickness profile, with thickness ranging from 70 nm to 135 nm. A non–uniform

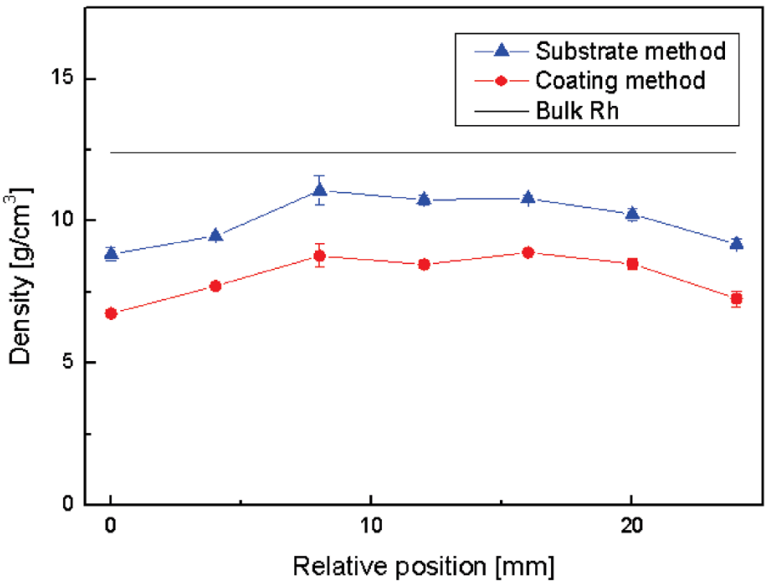


**Figure 4.6:** *Density profile of a Rh nanocrystalline film.*

density profile is evident for both methods. Film density is approximately constant in the central region of the sample, while a 15% decrement is observed in the peripheral deposit region, where the film thickness is lower than 70 nm. As the film was grown by PLD in vacuum [206], the coating density was expected to be very close to the bulk density value for Rh (12.41 g/cm$^3$). In the central region of the coated surface, film density measured by substrate method is around 10.9 g/cm$^3$, while the coating method gives a density of about 8.7 g/cm$^3$. In both cases density is underestimated with respect to the expected value. Since the results achieved with the substrate method are closer to the expected film density, the substrate method can be considered more reliable than the coating method in this case.

The application of EDS to the analysis of mesoscale inhomogeneity was investigated exploiting carbon films [15]. In general, EDS scans performed on a wide film area result in relatively low areal density standard deviation, since measured areal density values are averaged on a large surface. As the sampled region is reduced, standard deviation increases if the film presents inhomogeneities with a length scale comparable with the diameter of the sampled region. Thus, the inhomogeneity length scale can be estimated as the sampled area for which areal density standard deviation suddenly starts increasing. This approach was developed to introduce a quantitative criterion to compare films with qualitatively similar mesoscale structures and in particular carbon foams. To this aim, carbon films with different inhomogeneity lengthscales were analysed: a compact coating produced in vacuum and two foams produced using argon as buffer gas with pressures around 30 Pa and 300 Pa. These films have different mesoscale morphology (see figure 4.7) and, as a consequence, different density (2.5 g/cm$^3$, 26 mg/cm$^3$ and 4 mg/cm$^3$, respectively). Results are illustrated in Figure 4.8. The sampled

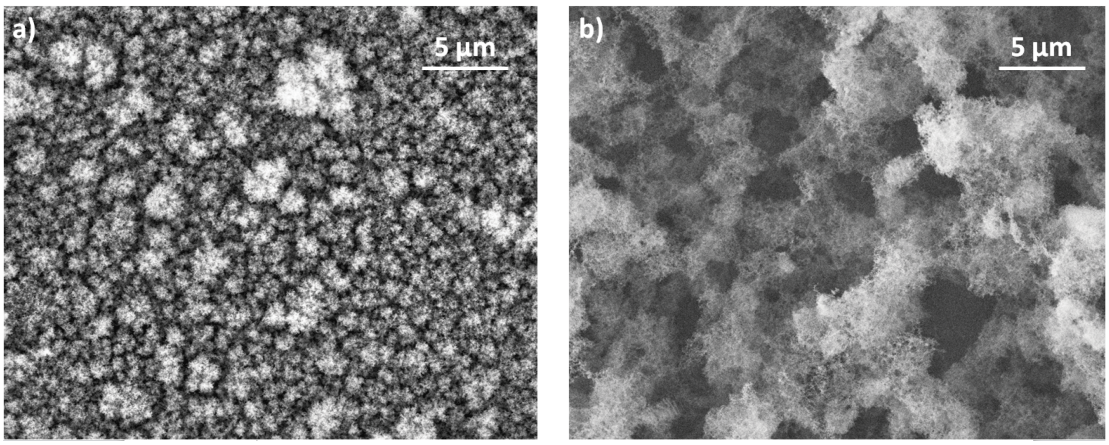


**Figure 4.7:** *SEM images of carbon films deposited in Ar at 30 Pa (a) and 300 Pa (b).*

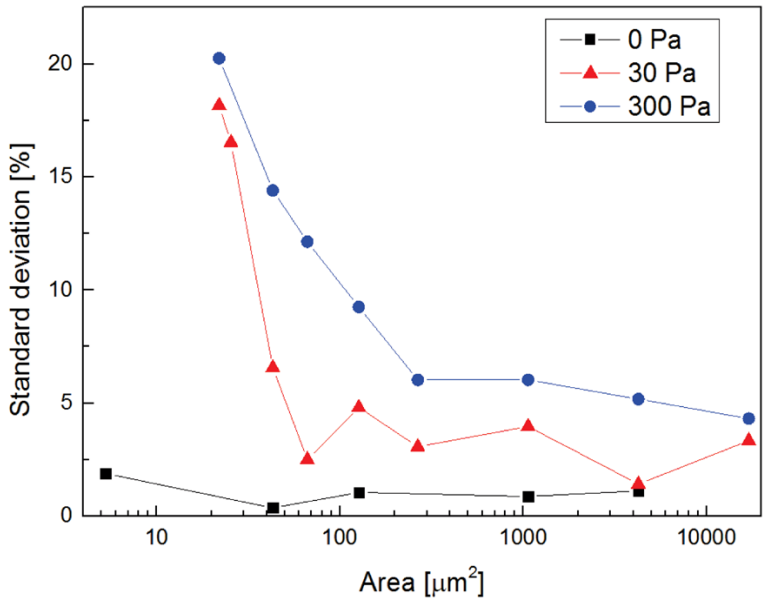


**Figure 4.8:** *Standard deviation of areal density measurement for carbon films deposited in vacuum and in argon with 30 Pa and 300 Pa.*

surface area ranged from $10\,\mu m^2$ to $10^4\,\mu m^2$. The areal density standard deviation for the compact coating was stable even for high magnifications. For carbon foam layers produced in argon at 30 and 300 Pa, a sudden increase was observed as the sampled area decreases below $65\mu m^2$ and $100\mu m^2$, respectively. Thus, the inhomogeneity length scales can be estimated as $8\,\mu m$ and $10\,\mu m$. These values confirm the morphological difference evident from SEM images and provides a quantitative criterion to compare the inhomogeneity length scale of films with similar morphology.
The experimental results reported in this Section allow to draw general conclusions regarding the application of EDS to the evaluation of nanostructured thin film density and provide useful indications regarding its practical applications for density measurements.

The first observation is related to the choice of the EDS–based method. Although the technique accuracy is strongly dependent on the specific experimental configuration and in particular on the substrate–coating combination, in general the substrate method can be considered more reliable than the coating method. This could be attributed to a lower sensitivity to PFXP distortions related to specific experimental configurations. For the substrate method, the error with respect to values measured by QCM is around 10–15%, but it can reach values up to 30% if the substrate–coating combination is particularly unfavourable, for example because of peak overlapping. Nevertheless, in a few cases (i.e. W films on Si substrates) the coating method allows to achieve very reliable measurements, with an extremely low deviation from nominal density values.
The strong dependence of the technique accuracy on the substrate–coating combination has been investigated. Apparently, this factor is the main error source in density measurements performed by EDS and the precision could be enhanced by developing an appropriate model for PFXP in multilayer samples, taking into account also fluorescence and secondary emission effects. However, the accuracy of both coating method and substrate method can be enhanced by adopting suitable conditions, namely by selecting substrates with atomic number similar to the coating atomic number and by choosing characteristic X–ray peaks not affected by fluorescence. Also the effect of the characteristic properties of the model used to evaluate the PFXP, in this case the MSG model, on the accuracy of the two methods should be considered.
The role of the electron accelerating voltage selection in areal density evaluation has been explored and the stability of the technique with respect to accelerating voltage variations has been studied from 5 kV to 30 kV for Ag films deposited on Au substrates and from 15 kV to 25 kV for W films grown on Si and Ta substrates. An empirical method to verify that the selected voltage is included in the stability voltage range consists in checking the measure repeating it with slightly higher and lower acceleration voltages for a test film. If the measured density doesn't change, the accelerating voltage falls in the optimum range.

## 4.2 Production of X–rays in multilayer samples

As mentioned in Section 2.2.2, the multilayer structure of samples can produce a distortion of the PFXP distribution (with respect to the model for homogeneous samples) due to two effects: (i) the electron diffusion can be influenced by the presence of a discontinuity at the coating–substrate interface; (ii) the intensity of X–rays produced in the layer under analysis can be enhanced by fluorescence effects due to the emission of high energy X–rays in the other layer. This section is devoted to a more detailed discussion of these issues, which can significantly affect the film areal density evaluation, and to outline possible strategies to include these effects in a suitable PFXP model.
The effect of substrate atomic number variations on electron propagation is evident from the results of Montecarlo simulations performed with CASINO [207] (Figure 4.9). The volume of interaction between the incoming electron beam and the sample and the electron energy absorption spatial distribution depend on

$\Delta Z = Z_{sub} - Z_{coat}$, resulting in a variation of the PFXP function in the coating. In particular, the number of electrons scattered by the substrate back to the coat-

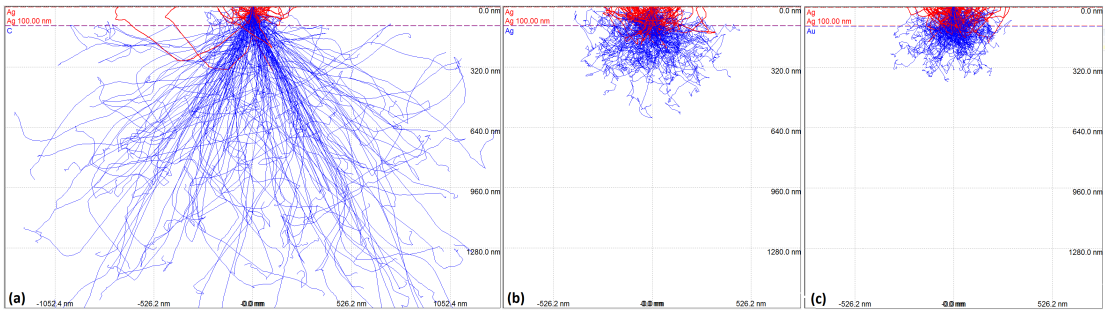


**Figure 4.9:** *Effect of the substrate atomic number in the electron propagation in a multilayer sample: (a) Ag coating on C substrate; (b) homogeneous Ag sample; (d) Ag coating on Au substrate.*

ing increases with the substrate atomic number. Thus, if $Z_{sub} < Z_{coat}$ the X–ray intensity produced in the coating is lower than the intensity calculated using the homogeneous PFXP function, reducing the film areal density evaluated by the coating method. On the contrary, if $Z_{sub} > Z_{coat}$, the production of X–rays in the coating is enhanced and the film areal density is overestimated. If coating and substrate have comparable atomic number $Z_{sub} \simeq Z_{coat}$, the electron diffusion is not affected by the multilayer structure, thus the PFXP of the homogeneous sample can be adopted without introducing a distortion in the areal density measurement. According to Cockett and Davis [191], this assumption is valid for $|\Delta Z < 5|$.
On the other hand, the coating composition can introduce a distortion in the areal density measurement of the substrate method, since the number, energy and angular distribution of electrons reaching the substrate is strongly dependent on the coating properties (see Figure 4.10). Therefore, in general, if $Z_{coat} < Z_{sub}$ the

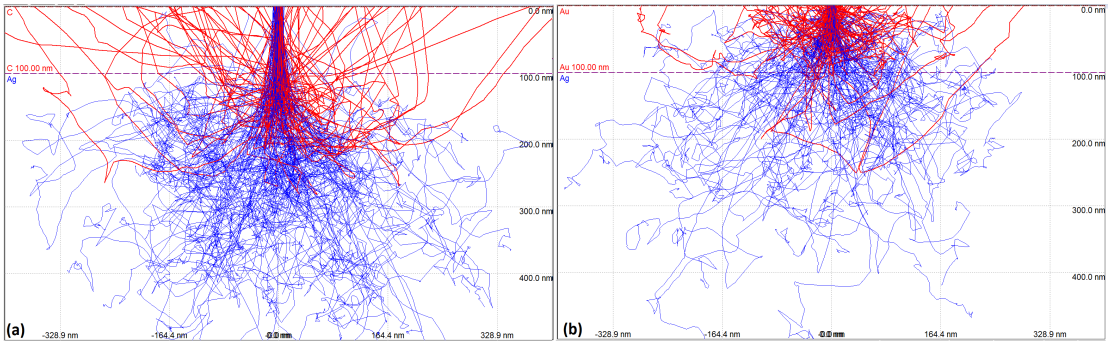


**Figure 4.10:** *Effect of the coating atomic number in the electron propagation in a multilayer sample: (a) C coating on Ag substrate; (b) Au coating on Au substrate.*

fraction of electrons crossing the coating is enhanced with respect to the fraction of electrons reaching the same depth in a homogeneous sample. In addition, electrons reaching the substrate have higher energy and directionality. Thus, in this case, the intensity of X–rays produced in the substrate is higher and the areal

density is overestimated. On the contrary, if $Z_{coat} > Z_{sub}$, the number, energy and directionality of electrons reaching the substrate is reduced, leading to an areal density underestimation. As in the case of the coating method, the areal density evaluation is not affected by the choice of an homogeneous PFXP for the substrate.
As illustrated in Section 2.2, the RE version of the MSG model includes the fluorescence effects due to the presence of high atomic number elements in the homogeneous sample. However, the PFXP function does not account for the fluorescence produced in the layer under analysis by X–rays emitted by high $Z$ elements present in the other layer. This effect can lead to an enhancement of the X–ray intensity measured for the layer under analysis and to an overestimation of the $I_{sample}/I_{ref}$ ratio. As a result, the areal density calculated exploiting the coating or substrate method can be respectively enhanced or reduced with respect to the actual value due to fluorescence effects.
These effects, which are not included in the PFXP description considered so far, can strongly reduce the technique reliability. From the experimental point of view, a possible solution consists in an appropriate selection of the substrate–coating combination and of the characteristic X–ray peak: $|\Delta Z|$ should be lower than 5 to prevent the distortion in the primary ionization distribution produced by the alteration of electron propagation in a multilayer sample and the X–ray peak should have an absorption edge energy higher than the energy of X–rays produced in the other layer (generally this is possible if Z of the element under analysis is higher than Z of elements contained in the other layer). In general, both conditions are satisfied if the atomic number of the layer under analysis is included in $[Z+1, Z+5]$, where $Z$ is the atomic number of the other layer. However, this is not always possible due to practical or technical reasons. Thus, appropriate models for the PFXP of multilayer samples are required.
Hereinafter, possible approaches for the evaluation of PFXP in the coating and the substrate are outlined. Fluorescence effects are not considered in the first part of this discussion.
The coating PFXP can be evaluated by considering the effect of the substrate on electron propagation. If the substrate acted as a perfect electron mirror ($Z_{sub} \to +\infty$), reversing the velocity of electrons reaching the coating–substrate interface (located at depth $\sigma = \tau$), the PFXP in the coating could be evaluated as the sum of the unperturbed PFXP and the PFXP of the electrons reflected by the substrate. In the perfect mirror case, the correction $\phi^{refl}(\sigma)$ could simply be calculated as the reflection of the homogeneous PFXP function for $\sigma > \tau$ with respect to the coating–substrate interface. Thus PFXP of the coating in a multilayer sample could be expressed as follows

$$\phi_{\mathrm{C,i}}^{\mathrm{ML}}(\sigma) = \phi_{\mathrm{C,i}}(\sigma) + \phi_{\mathrm{C,i}}(2\sigma_{\mathrm{C}} - \sigma)\,. \tag{4.1}$$

However, the perfect mirror case is an abstraction: in real configurations only a fraction of the electrons reaching the substrate is scattered back towards the coating. If this fraction is higher in the multilayer case than in the homogeneous sample, then the production of X–rays in the coating is enhanced, otherwise it is reduced. Thus a factor should be introduced in equation (4.1) to take this aspect into account. This factor $\zeta$ can be calculated as the difference between the fraction

of electrons scattered back by the substrate to the coating in a multilayer sample and the fraction of electrons scattered back by layers located at depth $\sigma > \tau$ to a $\tau$ thick surface layer in an homogeneous sample. These quantities can be calculated by considering the angular distribution of electrons reaching the interface and the probability for electrons to be scattered at an angle at least sufficient to enter back in the coating (or the surface layer). The parameter $\zeta$, essential for the application of this model to EDS methods for areal density evaluation, has not been calculated analytically yet. However, if $\zeta$ were known, the coating PFXP would be expressed as

$$\phi^{\mathrm{ML}}_{\mathrm{C,i}}(\sigma) = \phi_{\mathrm{C,i}}(\sigma) + \zeta\phi_{\mathrm{C,i}}(2\sigma_{\mathrm{C}} - \sigma)\,. \tag{4.2}$$

The evaluation of the substrate PFXP for a multilayer sample requires to take into account several effects. In this case, the PFXP could be approximated as a MSG function centred at the coating–substrate interface and calculated considering that the electron probe beam reaching the substrate has substantially different properties with respect to the incidence of the beam on the homogeneous sample surface. Firstly the number of electrons ($N(\tau)$) reaching the interface is lower than the initial electron number ($N_0$), thus the substrate PFXP is reduced by a factor given by the electron transmission coefficient of the coating layer $\eta_{\mathrm{T}} = N(\tau)/N_0$. In addition, the electrons reaching the substrate have lost part of their energy and collimation in crossing the coating. This should be taken into account by substituting the initial electron energy $E_0$ with the average energy of electrons reaching the substrate $E(\tau)$ in the calculation of the MSG parameters. Also the exponential factor describing the transition of the electron beam from directional propagation to diffusion in homogeneous samples ($\exp(-\beta\sigma)$ needs to be modified: since a part of the isotropization mechanism takes place in the coating an exponential factor $\exp(\beta_C\tau)$ should be introduced to describe the degree of isotropization of the electron propagation after crossing the coating. Finally, a modified backscattering coefficient $\eta_S$ should be calculated, representing the fraction of electrons scattered back by the substrate towards the coating. This parameter cannot be calculated by using equation (2.10), since electrons are not monochromatic nor collimated. As in the case of the coating PFXP model the evaluation of this parameter is still under investigation. Provided that all the parameters mentioned above are known[1], the substrate PFXP can be evaluated as follows:

$$\phi^{\mathrm{ML}}_{\mathrm{S,j}}(\sigma) = \eta^{\mathrm{C}}_{\mathrm{T}}\gamma_{\mathrm{S}}\exp[-\alpha^2_{\mathrm{S}}(\sigma-\tau)]\left\{1 - \frac{\gamma_{\mathrm{S}} - \Phi^{\mathrm{S}}_0}{\gamma_{\mathrm{S}}}\exp[-\beta_{\mathrm{S}}(\sigma-\tau)]\exp[-\beta_{\mathrm{C}}\tau]\right\}. \tag{4.3}$$

For both the coating and substrate method, fluorescence effects introduced by the multilayer structure could be taken into account by calculating the intensity of high energy X–rays produced in the substrate or coating (considering equation (2.1) and the corrected PFXP), respectively, and reaching the coating–substrate interface, $I_{CS}$. The fraction of $I_{CS}$ absorbed per unit areal density in the layer under analysis ($\mathrm{d}I_{abs}/\mathrm{d}\sigma$) can be calculated as a function of $\sigma$ using the well known

[1]Equations for the evaluation of $\eta_{\mathrm{T}}$ and $E(\tau)$ can be found for example in [208].

Lambert–Beer law. The PFXP component due to fluorescence can be then evaluated by multiplying $\mathrm{d}I_{abs}/\mathrm{d}\sigma$ by the branching ratio of X–ray emission.

## 4.3 New approaches for film density evaluation

The applicability of EDS based methods discussed so far for areal density evaluation can be extended by introducing new measurement configurations. In this section two original measurement approaches are proposed to extend the applicability of the technique to free–standing films and to simplify the data acquisition for multilayer samples removing the requirement of employing a reference standard.
The first configuration considered in this section is a variation of the coating method applied to the evaluation of the areal density of free–standing films, as shown in Figure 4.11. As for the coating method, areal density can be evaluated


**Figure 4.11:** *Sketch of EDS–based method for the evaluation of free–standing film areal density.*

using equation (2.3). Although being very simple, this approach is of great interest, for example, for the evaluation of density and uniformity of free–standing foam targets for laser–plasma experiments. However, an appropriate model for the PFXP function would be required to achieve reliable measurements, since electrons reaching the non–irradiated side of the film are definitively lost by the system producing a distortion of the PFXP and an underestimation of the film areal density. A proof–of–concept experiment was performed on commercial Al foils to test this configuration. The results, as mentioned in Section 4.1, were affected by an error of about 30%, which could be expected due to the adoption of the PFXP model for homogeneous samples. A numerical study, aimed at a possible collaboration with an external company, was performed to evaluate the feasibility of density measurements on polymeric foams ($C_{12}O_6H_{23}$) with nominal density from 20 mg/cm$^3$ to 500 mg/cm$^3$ and thickness in the 40–200 $\mu$m range. The main goal of this collaboration would have been to test the actual density and the uniformity of these foam layers, produced using a semi–automated dispensing and curing system [209]. The main result of the analytical and numerical study was the assessment of an applicability range of the EDS technique for this kind of material. This was calculated from the homogeneous PFXP model as the

areal density interval for which the film to reference standard intensity ratio was between 0.2 and 0.8. The resulting applicability range was $0.0045 - 0.6\,\mathrm{mg/cm^2}$, corresponding to densities from $1\,\mathrm{mg/cm^3}$ to $155\,\mathrm{mg/cm^3}$ for 40 $\mu$m thick foams and from $0.2\,\mathrm{mg/cm^3}$ to $30\,\mathrm{mg/cm^3}$ for 200 $\mu$m thick foams. A limitation for the technique applicability in this case was the extremely low energy of X–rays emitted by the foam constituent atoms (277 eV and 525 eV for C and O atoms respectively), leading to strong absorption of emitted X radiation by the foam itself. The reliability of the EDS based method in this specific case was tested by performing Montecarlo simulations to investigate the variation of the PFXP due to the peculiar acquisition configuration. The difference in simulated electron trajectories in the free–standing and infinite thickness configurations is illustrated in Figure 4.12. The simulated PFXPs for the two cases are compared in Figures 4.13

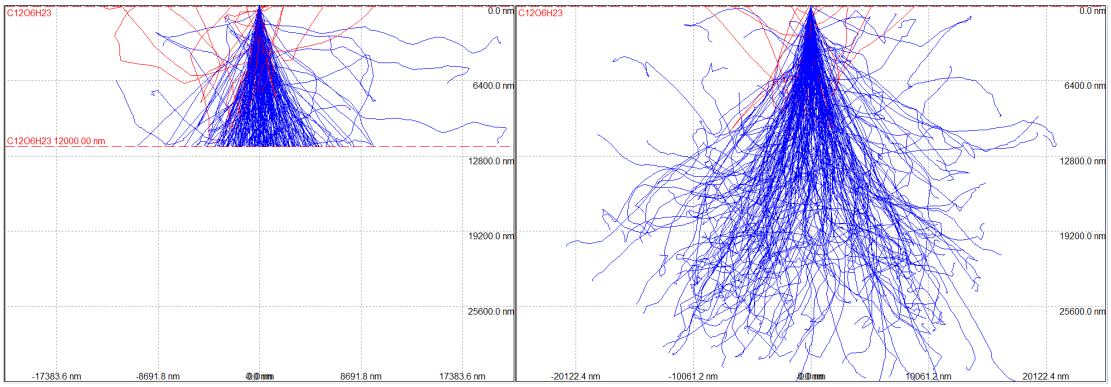


**Figure 4.12:** *Simulated electron trajectories in a 12 $\mu$m–thick free–standing foam (a) and in a sample with infinite thickness (10000 electrons with initial electron energy 30 keV, material density* $0.5\,\mathrm{g/cm^3}$*).*

and 4.14 (illustrated PFXP include absorption effects). The results reported in Figure 4.13 refer to simulation performed with 10000 electrons with acceleration voltage 30 kV (corresponding to the maximum available voltage for our experimental apparatus), for the upper limit of the technique applicability areal density range (12 $\mu$m, 0.5 mg/cm$^3$). Results illustrated in Figure 4.14 were obtained considering the lower limit of the applicability range (86 nm, 0.5 mg/cm$^3$). 10000 electron trajectories were simulated with accelerating voltage of 3 kV. The error induced by the PFXP distortion due to the adoption of a free–standing configuration was evaluated on the basis of these simulations. The expected error was between 9% and 14%, comparable with the average error observed in the experimental validation campaign illustrated in Section 4.1.
The second original measurement configuration for areal density evaluation proposed in this work is aimed at simplifying the data acquisition for multilayer samples removing the requirement of employing a reference standard. This configuration is sketched in Figure 4.15. Here, the coating areal density is calculated from the coating–to–substrate intensity ratio using the equation

$$\frac{I_{\mathrm{C,i}}}{I_{\mathrm{S,j}}} = \frac{\int_0^{\tau} C_{\mathrm{i}}\phi_{\mathrm{C,i}}(\sigma)\exp\left(-\chi_{\mathrm{C}}\sigma\right)\mathrm{d}\sigma}{\exp\left(-\chi_{\mathrm{C}}\tau\right)\int_{\tau}^{+\infty} C_{\mathrm{j}}\phi_{\mathrm{S,j}}(\sigma)\exp\left[-\chi_{\mathrm{S}}(\sigma-\tau)\right]\mathrm{d}(\sigma)}\,. \tag{4.4}$$

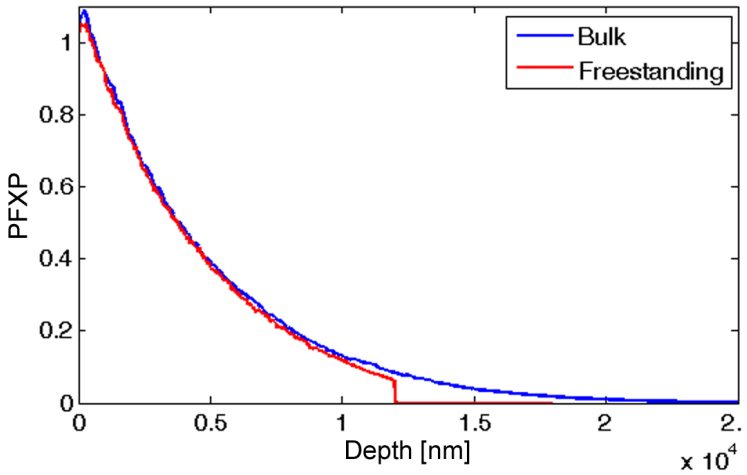


**Figure 4.13:** *Simulated PFXP for a 12 µm–thick free–standing foam and a sample with infinite thickness (10000 electrons with initial energy 30 keV, material density 0.5mg/cm3).*

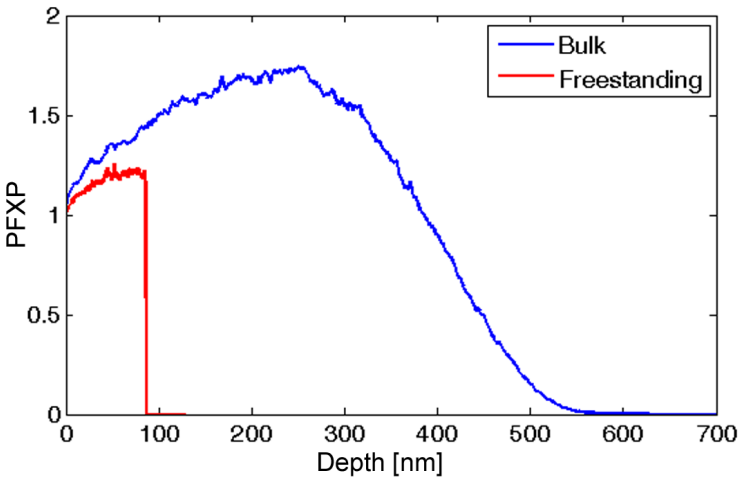


**Figure 4.14:** *Simulated PFXP for a 86 nm–thick free–standing foam and a sample with infinite thickness (10000 electrons with initial energy 3 keV, material density 0.5mg/cm3).*

The main advantage of this method would be a simpler and faster data acquisition phase, since the number of X–ray spectra to be collected would be reduced from 30% to 50% depending on the kind of sample under analysis. However, this method is more sensitive than the coating and the substrate methods to PFXP distortions due to the multilayer structure of the sample. Thus, preliminary experiments aimed at adjusting and validating this measurement technique were not successful and a rather high error was observed with respect to areal density measurements performed by QCM.

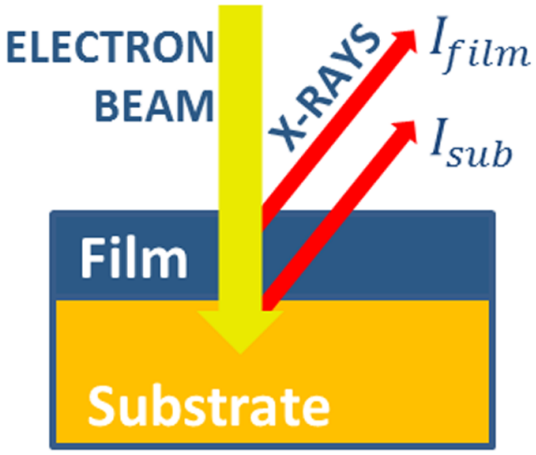


**Figure 4.15:** *Sketch of EDS–based method for coating areal density evaluation without reference standard.*

# Part III

# Laser–driven ion acceleration experiments with advanced targets

# 5

# Laser–driven ion acceleration experiments on advanced targets

This Chapter is devoted to the discussion of the results of three experimental campaigns aimed at the study of advanced target configurations for laser–driven ion acceleration. As discussed in the Introduction and in Chapter 1, one of the main goals of this thesis is the application of targets manufactured as described in Chapter 3 in laser–driven ion acceleration experiments. In particular, during my PhD, two experimental campaigns have been performed to explore the foam–attached target concept in different intensity regimes. The experimental setup and the results of these campaigns are discussed in Section 5.1. My PhD activities on structured targets for ion acceleration also include the participation to an experiment, presented in Section 5.2, aimed at investigating the excitation of surface plasmons on grating targets and its effects on the acceleration process efficiency.

## 5.1 Foam–attached targets

As illustrated in Subsection 1.3.2, the basic idea of the foam–attached target configuration is to exploit the presence of a near–critical foam layer on the directly irradiated side to enhance the laser–target coupling and the performances of the TNSA process. According to PIC simulations [13, 14], the foam layer should enhance both laser absorption efficiency and fast electron generation, resulting in an increase of the number and energy of accelerated ions. The interest in this target configuration is due to the expected possibility of producing MeV protons with moderate (sub–relativistic) intensity pulses and of combining the enhanced acceleration efficiency with the highest available laser intensities to overcome the maximum ion energies currently achievable via laser–driven ion acceleration. In addition, this solution can be more robust than other advanced target configurations, such as ultra–thin targets.
In this frame, the two main goals of the experimental campaigns on foam–attached targets were to provide a proof of the experimental feasibility of enhanced TNSA in

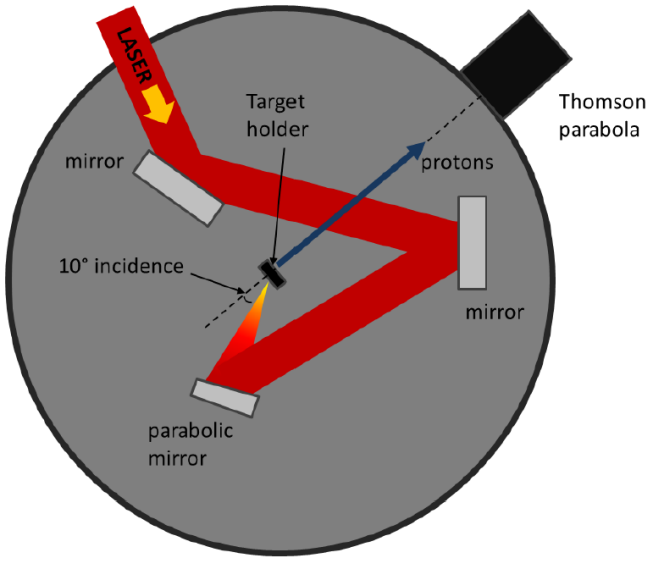


**Figure 5.1:** *Laser–driven ion acceleration experiment on foam–attached targets at moderated intensity: schematic view of the interaction chamber.*

this configuration and to investigate the dependence of the acceleration process on the target and laser properties. A first experimental campaign was performed in May 2012 at the UHI100 laser system of the Laboratoire Interactions Dynamique et Lasers (LIDyL, France) in the frame of the Laserlab–Europe programme[1]. This was a proof–of–concept experiment which provided indications on the existence of experimental conditions, in the moderate intensity regime (from $5 \times 10^{16}\,\mathrm{W/cm^2}$ to $5 \times 10^{19}\,\mathrm{W/cm^2}$), in which the foam–attached target configuration actually enhances the laser–driven acceleration performances (Subsection 5.1.1). My role in this experiment was mainly related to target manufacturing. The second experimental campaign was performed in November 2014 at the PULSER I PW laser system of the Gwangju Institute of Science and Technology (GIST, South Korea) in the frame of a bilateral collaboration[2]. In this experiment, an extensive investigation of the effects of the foam and laser properties in the high intensity regime (from $7 \times 10^{19}\,\mathrm{W/cm^2}$ to $\sim 5 \times 10^{20}\,\mathrm{W/cm^2}$) has been performed by varying foam density and thickness, substrate thickness and laser intensity and polarization. In this case, I was responsible for the target manufacturing and I directly participated to the experiment, as well as to the data analysis (which is ongoing at the moment of writing).

### 5.1.1 Moderate intensity regime

The first experimental campaign on foam–attached targets was performed at the UHI100 laser system (Ti:sapphire, 790 nm) of the LIDyL facility. A schematic view of the experimental configuration is reported in Figure 5.1. The pulse energy

[1] http//www.laserlab-europe.net

[2] Project title: *Advanced material and design of targets for laser–driven ion acceleration and high field plasmonics*, funded by Italian CNR and South Korean KRF.

after the amplification stage was about 2 J, resulting in 0.7 J energy on target (due to the losses introduced by the optical path). The laser intensity explored in this experiment ranged from $5\times10^{16}\,\mathrm{W/cm^2}$ to $5\times10^{19}\,\mathrm{W/cm^2}$, selected by tuning the laser focal spot size in the range $3.5-150\,\mu$m at fixed pulse energy 2 J and duration 25 fs. The size of the focal spot was changed by moving the target along the focusing optical axis. The intensity was evaluated by imaging the focal spot at different distances on either side of the focal plane, on a 12-bit charge-coupled device (CCD) camera through a 40× microscope objective and taking into account the laser energy included in focal area. Laser radiation was focused with a $f/2$ off–axis parabola with focal length 200 mm. A deformable mirror allowed to maintain a Gaussian–like pulse shape throughout the explored optical axis region. Two different contrast values were considered: $10^{12}$ with double plasma mirror installed (HC) and $10^7$ (LC) without any plasma mirror. The angle of incidence was 10°, chosen as a compromise between the expected optimum condition foreseen from simulations (normal incidence) [14] and the necessity of preserving the laser optics from damages due to the pulse back–reflection.
Targets with different properties were employed in correspondence of the two contrast configurations. Targets composed by a $13\,\mu$m thick carbon foam layer and by a $1.5\,\mu$m thick Al foil were irradiated at HC, while for the low contrast configuration 23 $\mu$m thick carbon foams attached on Al foils with thickness of 10 $\mu$m were considered. In both cases the foam density was $\sim 7\pm2\,\mathrm{mg/cm^3}$, which, for complete foam ionization, corresponds to a slightly over–critical density ($n_c = 5.7\,\mathrm{mg/cm^3}$ for $\lambda = 0.8\,\mu$m). Bare Al foils with the same thickness as the foam substrates (i.e. 1.5 $\mu$m and 10 $\mu$m) were used for comparison, with the aim of evaluating the effect of the foam layer.
The main diagnostics employed in this experiment was a Thomson parabola spectrometer for ion spectra detection. The spectrometer was placed along the target normal direction at a distance of about 600 mm from the target surface, with a 200 $\mu$m diameter entrance pinhole. Ions dispersed by the electric and magnetic fields in the spectrometer were detected by a two stage 40 mm diameter micro–channel plate (MCP) coupled to a phosphor screen. The image was recorded by a 12-bit CCD camera. No calibration was available for evaluation of the absolute number of accelerated particles.
In Figures 5.2 and 5.3, the maximum proton energy achieved for foam–attached targets and bare Al foils in HC and LC conditions, respectively, are plotted as a function of the laser intensity and the laser defocus. From these results, two different acceleration regimes can be identified. For moderate intensity values, from $5\times10^{16}\,\mathrm{W/cm^2}$ approximately to $10^{18}\,\mathrm{W/cm^2}$, foam attached targets allow to achieve a systematic maximum proton energy enhancement with respect to the case of Al foils, for both HC and LC configurations. In this intensity range, proton energies in excess of 1 MeV have been detected for intensities well below $10^{18}\,\mathrm{W/cm^2}$ and above the spectrometer detection limit (300 keV) even for intensities down to $10^{16}\,\mathrm{W/cm^2}$, for which the TNSA mechanism is quenched for ordinary thin targets. On the other hand, for intensity values above $10^{18}\,\mathrm{W/cm^2}$ the maximum energy of protons accelerated using foam–attached and ordinary targets are comparable.

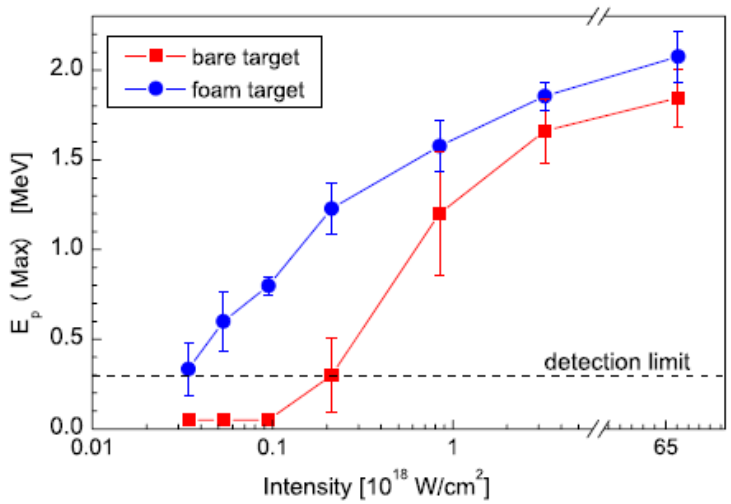


**Figure 5.2:** *Maximum proton energy as a function of laser intensity for foam–attached targets (13 μm foam on 1.5 μm thick Al foil) in high contrast configuration.*

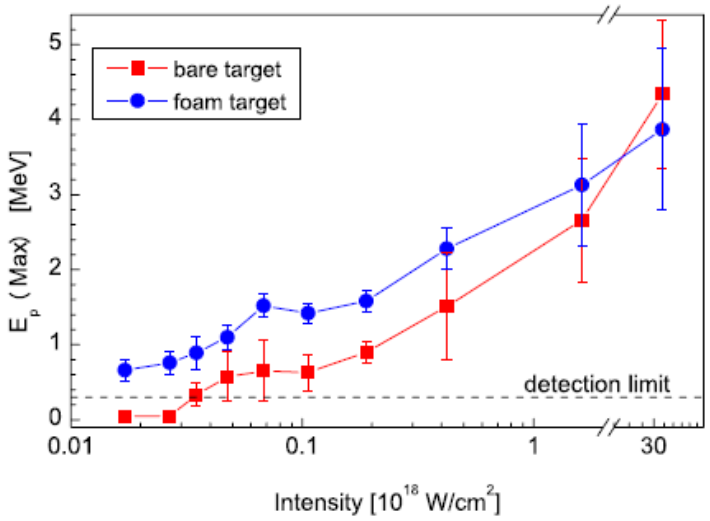


**Figure 5.3:** *Maximum proton energy as a function of laser intensity for foam–attached targets (23 μm foam attached on 10 μm thick Al foil) in low contrast configuration.*

These results were qualitatively interpreted considering that for low intensity values the foam ionization degree decreased, while the ionization was complete for laser intensities above $10^{18}\,\mathrm{W/cm^2}$. As a consequence, for intensity above $10^{18}\,\mathrm{W/cm^2}$ the irradiated foam formed a 10 $\mu$m thick slightly over–critical layer in front of the solid foil, thus the acceleration process was similar to TNSA. On the contrary, for intensities below $10^{18}\,\mathrm{W/cm^2}$, a partial foam ionization occurred, thus leading to the formation of an under–dense plasma and to an enhanced TNSA scheme.
This picture was confirmed by simulations performed with the PIC codes UMKA [210] and AlaDyn [211]. According to UMKA simulations with field ioniza-

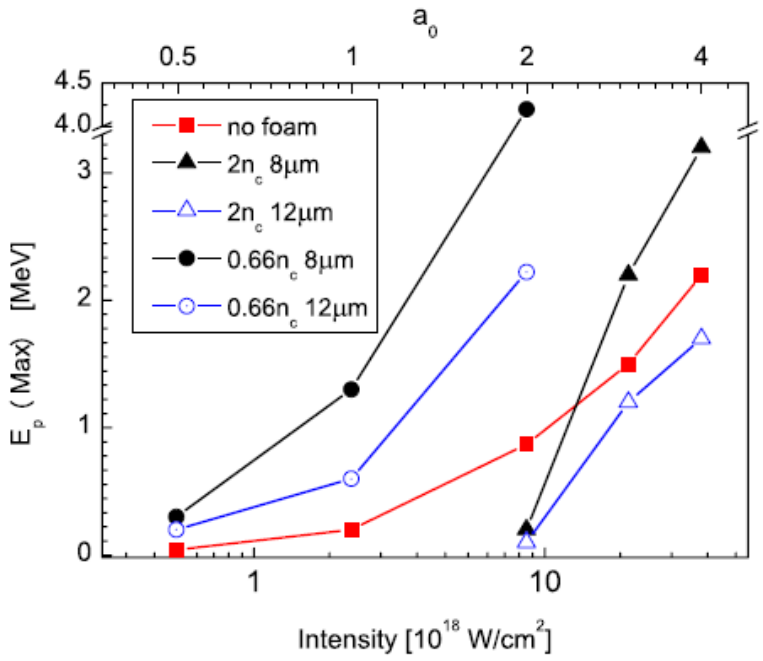


**Figure 5.4:** *2D PIC simulation results for maximum proton energy as a function of intensity, comparing the target with and without a foam layer (red squares). Foams have density $n_f = 2n_c$ (triangles) and $n_f = 0.66n_c$ (circles) for two different thickness values: 8 $\mu$m (black full symbols) and 12 $\mu$m (blue empty symbols).*

tion, the average ionization degree to be expected for a pulse with intensity $2 \times 10^{18}\,\mathrm{W/cm^2}$ was $C^{4+}$. Thus, the dominant charge states below $10^{18}\,\mathrm{W/cm^2}$ were likely $C^{2+}/C^{4+}$, corresponding to an electron density around $0.5\,n_c$ which allowed the propagation of the pulse and efficient hot electron production via volume interaction mechanisms. On the other hand, in the relativistic regime the pulse interacted with a fully–ionized over–dense and volume interaction mechanisms were quenched. On the basis of these considerations, ad hoc PIC simulations were performed with the AlaDyn code for a Gaussian pulse with $\lambda = 0.8\,\mu$m, 25 fs FWHM duration and a waist from 3 to 12 $\mu$m. The targets considered in the simulations were composed by three layers: a foam layer with thickness 8 $\mu$m and 12 $\mu$m and densities of 2 $n_c$ and 0.66 $n_c$ (for the high and moderate intensity regimes respectively); a 0.5 $\mu$m thick solid layer with density of 40 $n_c$ and a contaminant layer with thickness 50 nm and density 10 $n_c$. The simulated laser intensity ranged from $5 \times 10^{17}\,\mathrm{W/cm^2}$ to $3.5 \times 10^{19}\,\mathrm{W/cm^2}$ (corresponding to normalized vector potential values between 0.5 and 4) and the maximum proton energy was evaluated 200 fs after the beginning of the laser–plasma interaction. The simulated maximum proton energy, reported in Figure 5.4 as a function of pulse intensity, show that in the high intensity regime (in which the foam was over–dense due to the high ionization degree) the pulse couldn't propagate in the plasma and the results for bare Al foils and foam attached layers were comparable (except for $a \simeq 2$, for which very low proton cut–off was achieved for foam–attached targets). On the contrary, in the moderate density regime (in which foams were under–dense due to the lower ionization degree), the laser could propagate in the foam

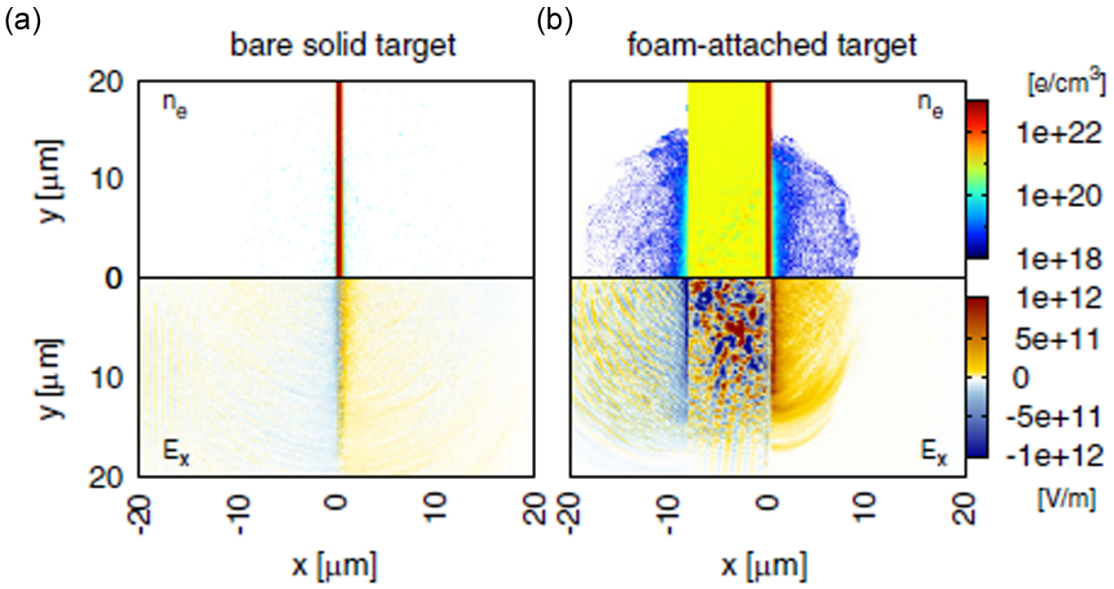


**Figure 5.5:** *Simulated electron density and longitudinal electric field for (a) a solid Al target and (b) a foam–attached target with under–dense foam (8 μm 0.66 $n_c$ foam) for $a_0 = 1$.*

and an enhanced TNSA process was achieved. This is evident, for example, from the comparison between the electron density and longitudinal electric field for a foam–attached target with under–dense foam (8 $\mu$m 0.66 $n_c$ foam) and a solid Al target, illustrated in Figure 5.5.

In conclusion, this first experiment proved the experimental feasibility of an enhanced TNSA scheme exploiting foam–attached targets. On the basis of the results discussed above and of ad hoc PIC simulations, two acceleration regimes were identified depending on foam and laser parameters. In the high intensity regime (above $\times 10^{18}$ W/cm$^2$), no clear distinction was observed between the cut–off energies of protons accelerated in ordinary and foam–attached target configurations. According to PIC simulations, in this regime either lower density or thinner foams should be considered to optimize the laser–target coupling. On the contrary, in the moderate intensity regime (below $\times 10^{18}$ W/cm$^2$) a systematic enhancement in the maximum proton energy achieved with foam attached targets was observed with respect to the bare Al target case.
These results suggest that further improvements could be achieved through an appropriate selection of target properties. In particular, foam–based targets with parameters optimized for high intensity laser pulses (above $\times 10^{19}$ W/cm$^2$) should allow to achieve maximum ion energies and laser–ion conversion efficiency suitable for specific applications.

### 5.1.2 High intensity regime

The second experimental campaign on foam–attached targets was performed at the PULSER PW laser facility of GIST (South Korea). The oscillator was a Ti:sapphire laser delivering 29 fs pulses at a central wavelength $\lambda = 805$ nm. The maximum energy before the pulse compressor was about 34 J, resulting in a 7.6

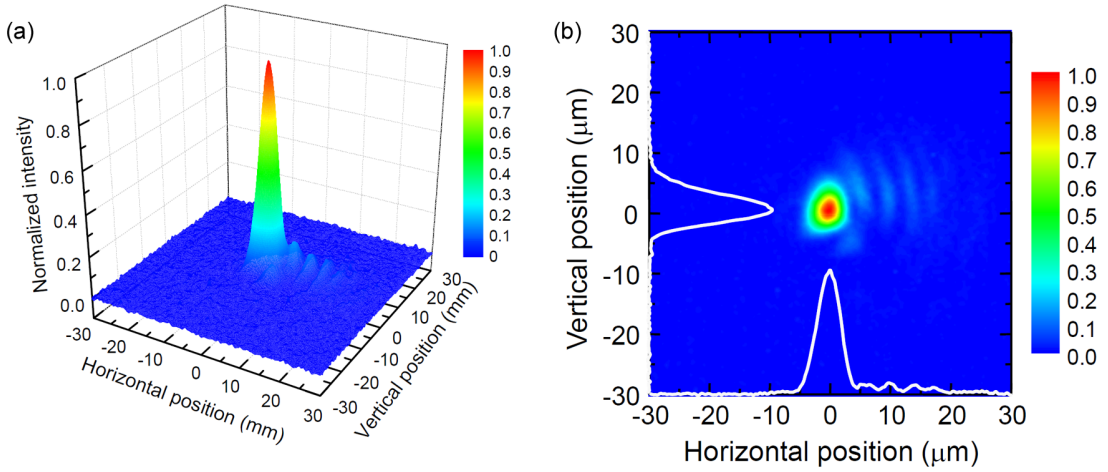


**Figure 5.6:** *PULSER I (GIST): spatial distribution of the pulse intensity on target in 3D (a) and 2D (b) rendering.*

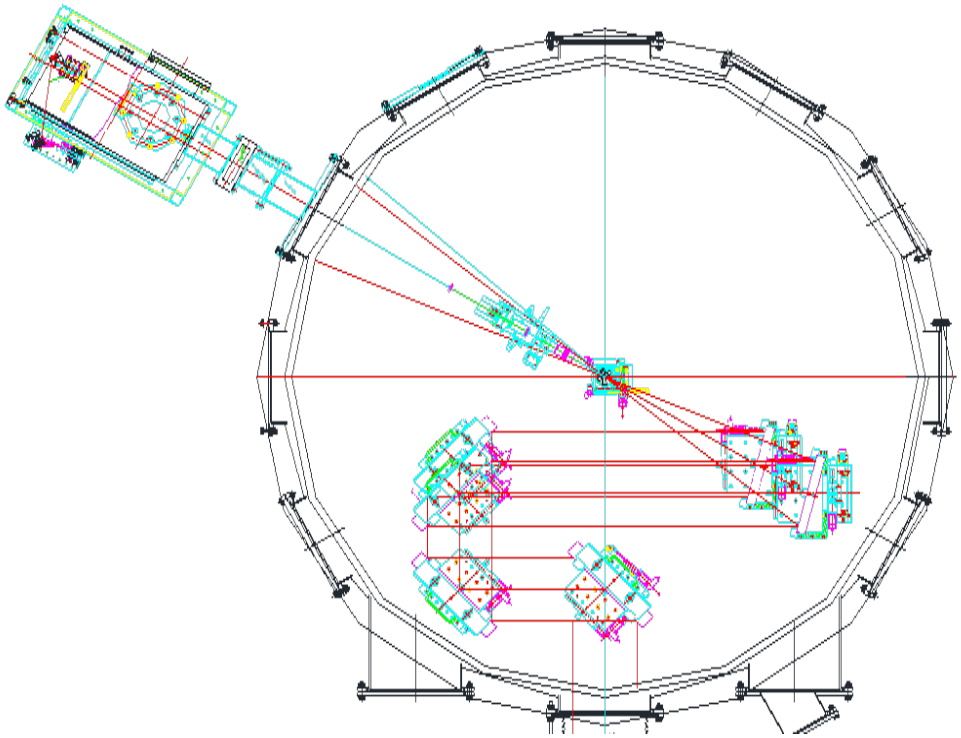

**Figure 5.7:** *Interaction chamber of the PULSER I laser system.*

J energy on target. A scan in the laser intensity from $7 \times 10^{19}\,\mathrm{W/cm^2}$ to about $5 \times 10^{20}\,\mathrm{W/cm^2}$ was performed for different target configurations by varying the pulse energy (from 1.3 J to 7.6 J) at constant duration and focal spot size $\sim 5\,\mu\mathrm{m}$, containing 22% of the total energy on target (Figure 5.6). Figure 5.7 provides an illustration of the interaction chamber. The pulse was focused on target using a $f/3$ off–axis parabola. Three different polarizations were considered: linear s and p polarization (the latter achieved through an half–wave plate with transmission

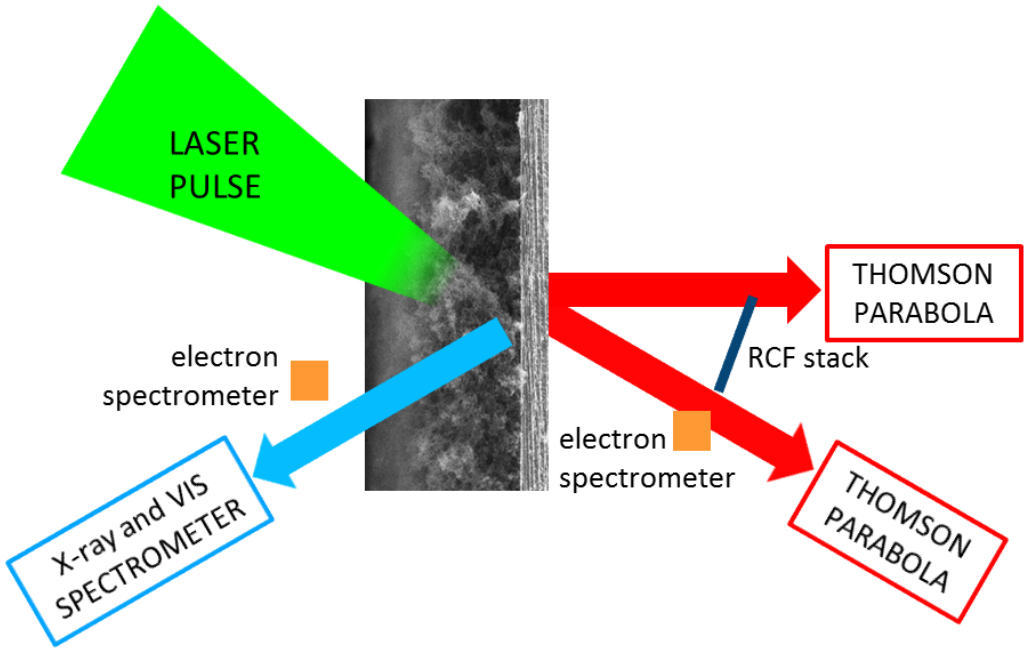


**Figure 5.8:** *Top–view sketch of the diagnostics at the PULSER I laser system.*

$\sim$ 82%) and circular polarization (achieved through a quarter–wave plate with transmission $\sim$ 87%). A contrast ratio in excess of $10^{12}$ was achieved with a double plasma mirror. The angle of incidence was 30° to prevent laser optics damage due to the pulse back–reflection.
The role of target properties in the acceleration process was investigated by considering:

- 8, 12, 18 and 36 $\mu$m–thick near–critical foams ($\rho = 6.8 \pm 10\%$, corresponding to $n = 1.2\, n_c$ for complete ionization) on 0.75 $\mu$m thick Al foils;
- 12 $\mu$m thick slightly over–critical foams ($\rho = 25 \pm 10\%$ corresponding to $n = 4.3\, n_c$ for complete ionization) on 0.75 $\mu$m thick Al foils;
- 12 and 18 $\mu$m thick near–critical foams on 1.5 thick $\mu$m Al foils.

The foam density and thickness were chosen on the basis of dedicated 3D PIC simulations. According to these simulations, the optimal thickness was expected in the 10–20 $\mu$m range for near–critical foam.
In Figure 5.8, a schematic top view of the main diagnostics positioning is reported. Two Thomson parabolas were placed along the target normal direction and the laser propagation direction for ion detection. A radiochromic film (RCF) stack was placed between the two parabolas, for a limited number of shots. An X–ray spectrometer [212] was positioned in the laser specular reflection direction, to acquire information about the carbon plasma ionization degree, in particular as regards the relative population of $C^{4+}$ and $C^{5+}$, and to estimate the electron temperature in the plasma. Finally, two electron spectrometers (with upper detection limit 10 MeV) were placed close to the laser propagation and the specular

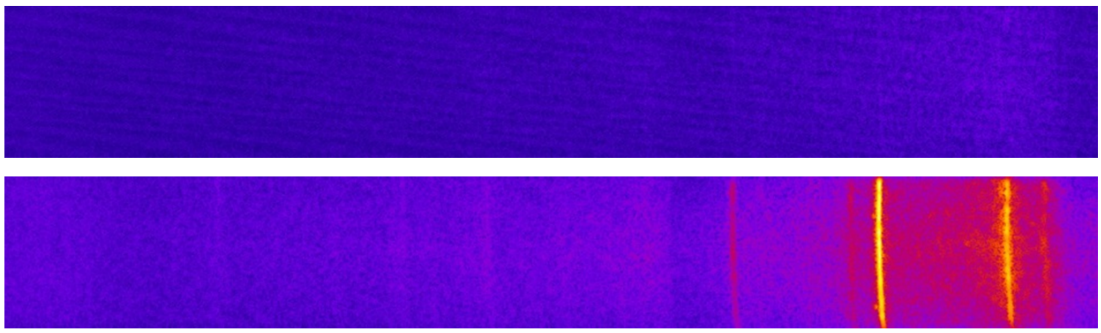

**Figure 5.9:** *Typical diffraction patterns recorded by the X–ray spectrometer for bare (top) and foam–attached (bottom) targets.*

reflection directions.
One of the main goals of this experimental campaign was an extensive investigation of the role of target properties and laser parameters in the ion acceleration process. The role of foam thickness and density and of substrate thickness was studied in the whole available intensity range and for three different polarizations. The analysis and interpretation of the acquired data are still being completed at the time of writing. Signals recorded with the Thomson parabola along the target normal direction have been extensively analysed, while ion spectra along the laser propagation direction and X–ray spectra are still under analysis. Signals recorded by RCF stacks and electron spectrometers have not been considered yet. However, hereinafter, the main preliminary results of this experimental campaign are discussed.
The effect of the thickness of near–critical foams for varying pulse intensity will be considered in the case of s–polarization first, discussing the results from the X–ray spectrometer and the two Thomson parabolas.
The interaction of the pulse with a carbon foam is evident from the row signal detected by the X–ray spectrometer, if the difference between the bare Al targets and foam attached targets is considered. Figure 5.9 shows the comparison between the typical diffraction patterns recorded by the X–ray spectrometer for bare and foam–covered targets: in presence of a foam layer X–ray peaks typical of $C^{4+}$ and $C^{5+}$ ions are evident, while they cannot be detected for bare Al foils. The relative intensity of X–ray peaks emitted by different ions can allow to evaluate the relative concentration of carbon charge states in the plasma formed in the laser–foam interaction. A preliminary analysis of X–ray spectra has been performed on data recorded for near–critical foam thickness between 8 and 36 $\mu$m deposited on 0.75 $\mu$m thick Al foils at full power with s–polarization. The ratio between the Ly–$\alpha$ peak emitted in the $1s - 2p$ transition of $C^{5+}$ and the He–$\alpha$ peak of $C^{4+}$ (corresponding to the $1s^2 - 1s2p$ transition) has been considered. From this partial analysis the ratio appears to be monotonically increasing with the thickness of the near–critical foam layer, suggesting an increase of the relative concentration of the $C^{5+}$ ionic population with respect with the $C^{4+}$ population. This could suggest an increase in the pulse absorption for thicker foams, resulting in an enhancement of the plasma ionization degree, but not necessarily in an enhancement of the ion acceleration performances (see below).

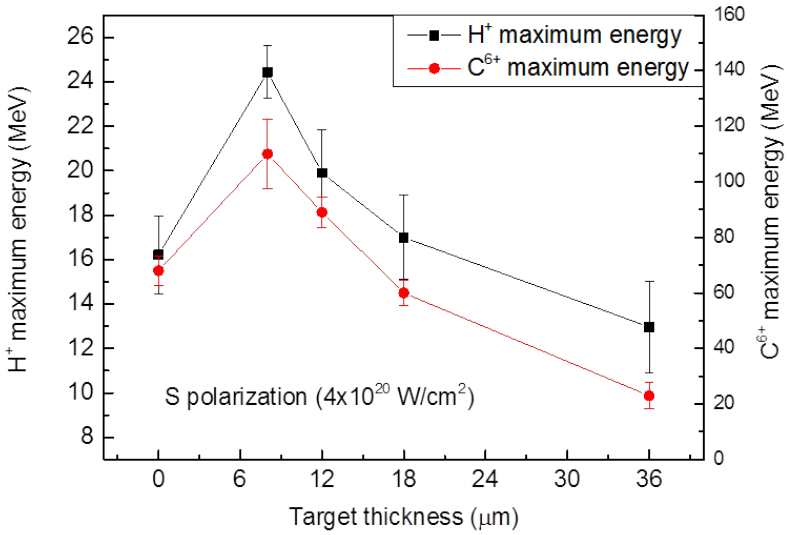


**Figure 5.10:** *Cut–off energy for protons and* $C^{6+}$ *as a function of the foam thickness at full power for s–polarization.*

The dependence of the maximum energy of accelerated protons and ions (in particular $C^{6+}$), recorded by the Thomson parabola placed along the target normal, is shown in Figure 5.10 for near–critical foam layers (8–36 $\mu$m) on 0.75 $\mu$m thick Al foils, irradiated with s–polarized pulses at maximum intensity. These results showed a clear enhancement in the proton (and $C^{6+}$) cut–off energy for targets with a 8–12 $\mu$m thick foam layer (25 MeV and 20 MeV, respectively) with respect to the case of a bare Al target (16 MeV). With thicker foams, the proton cut–off energy were comparable (18 $\mu$m, 17 MeV) or significantly lower (36 $\mu$m, 13 MeV) than values measured with bare foils. Thus, from these results, the existence of an optimal foam thickness value was evident, as far as the enhancement of proton and $C^{6+}$ ions cut–off energy was concerned. For the experimental conditions considered in this campaign, the best results for s–polarized pulses ($\sim$25 MeV for $H^+$ and $\sim$ 110 MeV $C^{6+}$) were obtained with foam thickness of about 8 $\mu$m. Analogous trends were observed for p and circular polarization. In all cases, the optimum thickness value probably falls in the thickness range $\lesssim 8\,\mu$m, suggesting the possibility of a further cut–off energy enhancement for multilayer targets with foam thickness lower than 8 $\mu$m and similar pulse properties.
The cut–off energy scaling with pulse intensity was investigated in the $7\times10^{19}$ W/cm$^2$–$5 \times 10^{20}$ W/cm$^2$ range for different near–critical foam thickness values. In Figure 5.11, the maximum energy of accelerated protons is reported as a function of the pulse intensity for targets with foam thickness from 8 to 36 $\mu$m deposited on 0.75 $\mu$m thick Al foils and for bare Al targets. The maximum proton energy increase with pulse intensity was approximately linear. The cut–off energy enhancement observed for the minimum and maximum pulse intensity values in the case of a 8 $\mu$m foam with respect to the plain Al target was $\sim$ 40% and above 50%, respectively.

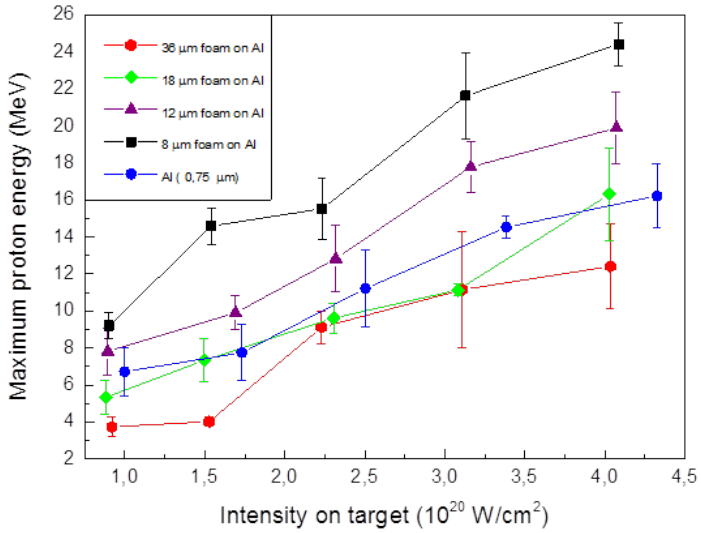


**Figure 5.11:** *Cut–off energy for protons and* $C^{6+}$ *as a function of the pulse intensity for s–polarization and several foam thickness values.*

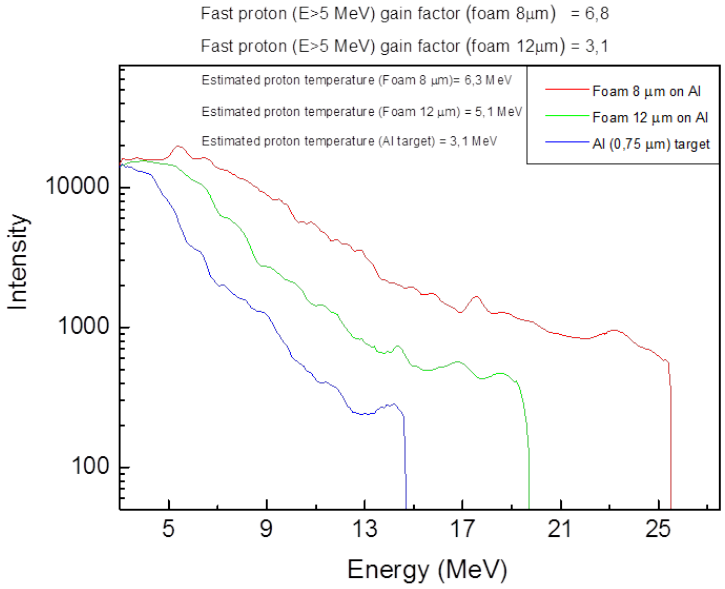


**Figure 5.12:** *Proton spectra recorded along the target normal direction for a bare Al target and foam–attached targets with near–critical foam thickness 8 and 12 µm at full power.*

The spectra of protons accelerated along the target normal direction are reported in Figure 5.12 for the case of 8 $\mu$m and 12 $\mu$m thick foams and of a bare Al foil irradiated at full power with s–polarized pulses. The Thomson parabola spectrometers used in this experiment were not calibrated, thus it was not possible to provide an evaluation of the absolute number of accelerated particles and proton spectra are shown in arbitrary units. However, from the spectra reported in

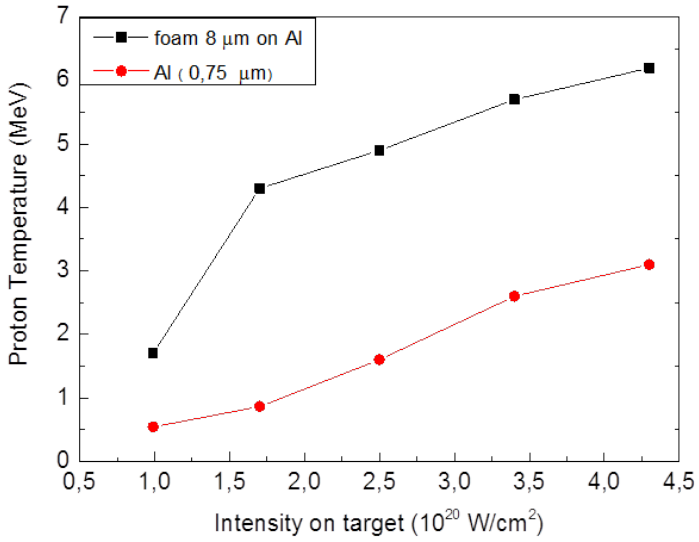


**Figure 5.13:** *Proton temperature plotted as a function of pulse intensity for bare Al targets and 8 μm–thick near–critical foam–attached targets (s–polarization).*

Figure 5.12, it was possible to observe a relative enhancement in the number of protons accelerated with foam–attached targets with respect to the case of a plain Al foil. In addition, a dependence of the number of accelerated protons on the foam thickness was observed: fast proton ($> 5$ MeV) gain factors of 6.8 and 3.1, respectively, were obtained with 8 $\mu$m and 12 $\mu$m thick foams with respect to bare Al targets. These spectra also show an enhancement in the temperature of accelerated protons (estimated considering the slope of proton spectra): again, the highest result was obtained in presence 8 $\mu$m thick foam layers (6.3 MeV), while the estimated proton temperature is $\sim$ 5 MeV for 12 $\mu$m foams and $\sim$ 3 MeV for bare Al targets. Since, in general, proton temperature provides an indirect indication also of the hot electron temperature, responsible for the generation of the accelerating sheath field (see Section 1.2.1), an enhancement in the electron temperature should be expected in presence of a 8 $\mu$m foam layers with respect to plain Al targets. The trend of proton temperature as a function of pulse intensity is reported in Figure 5.13 for 8 $\mu$m thick foams and plain Al: proton temperature increased from 1.6 MeV to 6.3 MeV and from 0.5 MeV to 3 MeV, respectively, as pulse intensity was increased from $7 \times 10^{19}$ W/cm$^2$ to $5 \times 10^{20}$ W/cm$^2$.

Proton and $C^{6+}$ ion signal detected along the laser propagation direction has not been suitably analysed yet. However, as an interesting preliminary outcome, unexpected signal was often observed with foam–attached targets and proton with cut–off energy from 10 MeV to 17 MeV were detected for full power, although with significantly lower intensity with respect to the signal acquired on the target normal direction. On the contrary, for bare Al targets no signal was detected by the Thomson parabola placed along the laser propagation direction. A systematic analysis of these data would be required to provide a physical interpretation.
Also the role of foam density was investigated in this experimental campaign. In

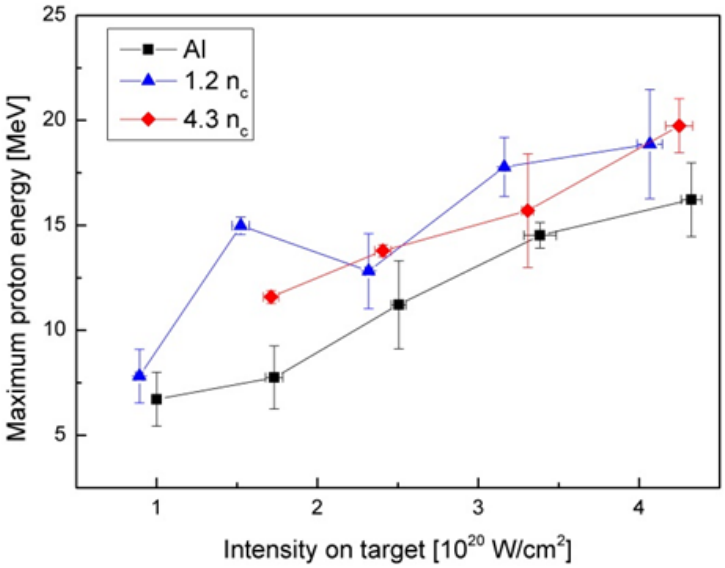


**Figure 5.14:** *Proton cut–off energy as a function of the pulse intensity for 12 $\mu$m–thick foams with density $\sim 1.2\, n_c$ and $\sim 4.3\, n_c$.*

Figure 5.14, the cut–off energy of protons accelerated with three different kinds of target irradiated with s polarization: 0.75 $\mu$m foils without foam, with a 12 $\mu$m thick near–critical foam and with a 12 $\mu$m thick slightly over–dense foam (4.3 $n_c$). Both foam–attached targets allow to achieve a proton cut–off energy enhancement with respect to the case of a bare Al target. The maximum proton energy achieved with the two foam targets are comparable.
Targets with different Al thickness (namely 0.75 $\mu$m and 1.5 $\mu$m) and 12 $\mu$m thick near–critical foam layer were considered to explore the role of the Al foil thickness in the acceleration process. From a preliminary analysis, results obtained in the two configurations were comparable, as expected from PIC simulations [14]. This suggested that the highest energy electrons were produced in volume interaction mechanisms taking place in the foam layer (if present) rather than in the Al foil. Thus the role of the foam was prevalent with respect to the role of the solid layer in the acceleration process.
The results discussed so far only refer to the case of s–polarized incoming laser radiation. The role of pulse polarization in the acceleration process was extensively studied for a variety of target properties: for almost all targets the experiment was repeated for s, p and circular polarization while keeping the same incidence angle. As an example, in Figure 5.15, the proton cut–off energies detected for bare Al foils and for targets composed by a 8 $\mu$m thick near–critical foam and a 0.75 $\mu$m thick Al foil are reported. It is interesting to observe that, while the proton cut–off was significantly different for bare targets in different polarization configurations, these differences were strongly reduced by the presence of a foam. This effect was attributed to the difference in laser–target interaction mechanisms involved for the two classes of targets. Surface laser–target interaction mecha-

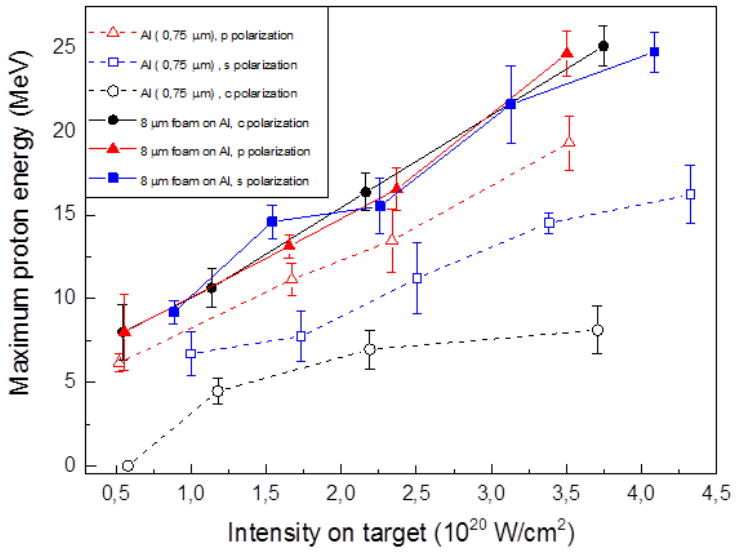


**Figure 5.15:** *Proton cut–off energy as a function of the pulse intensity for bare Al foils and targets with 8 μm–thick near–critical foams with s, p and circular polarization.*

nisms, dominant for sharp target–vacuum interfaces, are strongly influenced by pulse polarization. In this case, the production of hot electrons is almost quenched for circular polarization and much more efficient for linear polarization (in particular for p polarization). On the other hand, interaction processes typical of foam–attached targets are essentially volume interaction mechanisms and, as a consequence, they are not affected by pulse polarization. In addition, the notion of polarization for foam–attached targets is not well defined due to the extremely irregular structure of the material. As a consequence, the gain in term of proton cut–off energy due to the presence of a foam layer was strongly dependent on the pulse polarization: while for p–polarized pulses with the lowest energy the cut–off energy obtained with bare Al targets was almost comparable to the maximum proton energy observed for foam–attached targets (the gain was $\sim 25\%$), for circular polarization an increase about 300% was observed at full power.
Ad hoc 3D PIC simulations are under development to support the interpretation of experimental data discussed so far. 30 fs laser pulses with 4 $\mu$m waist and $a_0 = 18$ have been considered for s, p and circular polarization. As in the experimental campaign, the incidence angle chosen for these simulations is 30°. Foam–attached targets composed by a 0.5 $\mu$m thick Al foil with density 40 $n_c$ and a 8 $\mu$m thick foam with $n = n_c$ have been considered. A complete analysis of numerical results is not available yet. However, the first snapshot extracted from the results of a 3D PIC simulation performed considering s–polarization is reported in Figure 5.16 to give a hint of the complexity of the interaction between the ultra–intense incoming pulse and the low density foam. The image shows the foam electron density (the solid substrate has not been shown), the unperturbed electron density being marked in blu. The laser pulse comes from the bottom left. The snapshot represents the instant in which the propagating pulse reaches the solid substrate. The initial phase of the electron diffusion towards the rear target

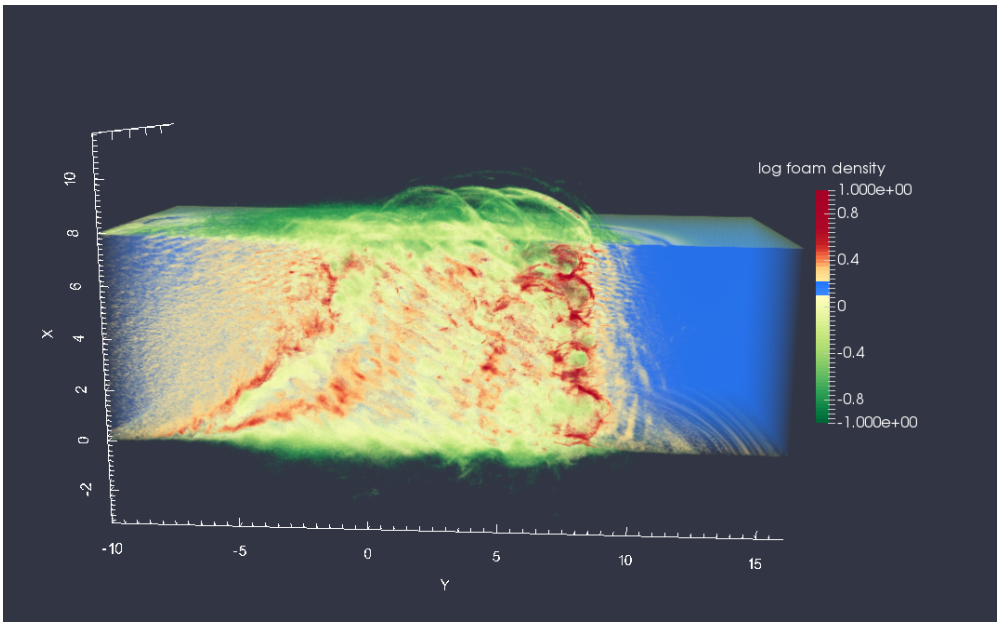


**Figure 5.16:** *Simulated foam electron density snapshot representing the instant in which the propagating pulse reaches the foam.*

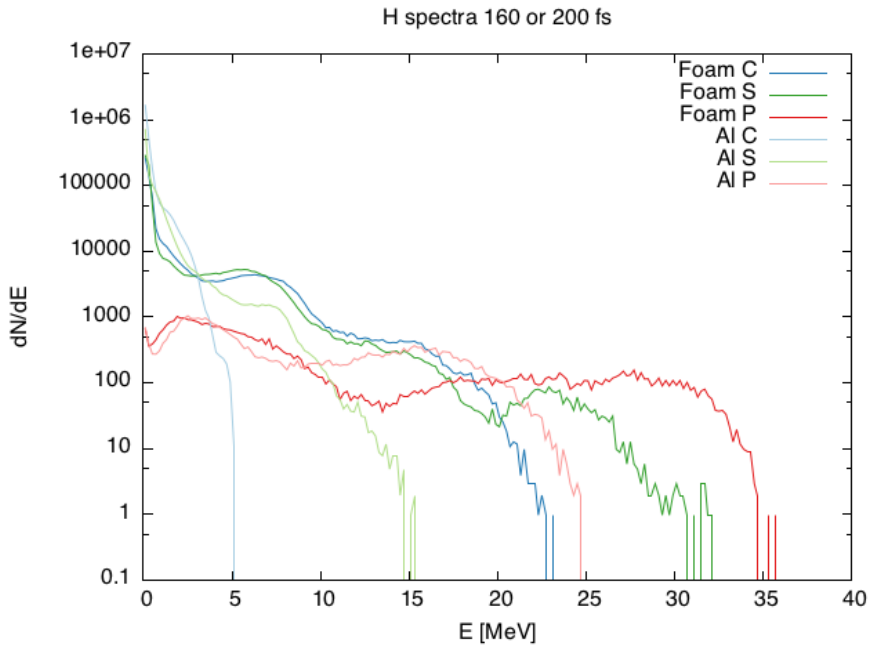


**Figure 5.17:** *Simulated proton spectra for bare Al foils and foam–attached targets shown for different polarizations.*

surface is visible as well as the propagation of electrons along the laser direction. The channel produced by the laser is characterized by strong turbulences and instabilities.

Figure 5.17 illustrates simulated spectra of protons emitted along the target normal direction for both bare Al and foam–attached targets with s, p and circularly

polarized pulses. For technical reasons, the spectrum simulated for foam attached targets with p–polarization refers to 160 fs, while other spectra refer to 200 fs. Nevertheless, this does not prevent a qualitative comparison with other spectra. In the case of bare Al targets, proton spectra confirm the experimental results, also in terms of cut–off energy order of magnitude. In all cases an enhancement of the number and maximum energy of accelerated protons is observed for foam attached targets with respect to the case of bare Al foils. However, in contrast with experimental results, spectra obtained considering circular, p and s polarized pulses show significant differences also for foam–attached targets. This could be attributed to two important differences between the real and the simulated targets. Firstly, the foam has been simulated as a low density uniform layer, while the discontinuous structure of the foam should be considered (for example, by simulating foams composed by particle aggregates). Moreover, the density of solid foils considered in the simulations is much lower than the solid density ($40\,n_c$), while their thickness is comparable. Thus, the areal density of the target substrate is not comparable with the Al foils adopted in the experiment.
In conclusion, from preliminary analysis of data collected in this experiment, a significant enhancement in the maximum energy of accelerated ions was observed for foam-attached targets with suitable foam properties with respect to the case of Al foils, reaching for example 25 MeV and 15 MeV, respectively, for s-polarized pulses at full power. The existence of an optimum near–critical foam thickness $\lesssim 8\,\mu$m maximizing the cut–off energy and number of accelerated ions suggests the possibility of a further cut–off energy enhancement by optimizing the properties of carbon foams. In addition, an enhancement of the acceleration performances is expected for lower incidence angles and higher intensity values.

### 5.1.3 Summary

As discussed in Sections 5.1.1 and 5.1.2, in this thesis work the foam–attached target concept was investigated in two experimental campaigns covering several intensity decades in two different laser facilities. Even though some important differences between the two experiments should be kept in mind, such as the incidence angle (10° at LIDyL and 30° at GIST) and the Al thickness (1.5 and 0.75 $\mu$m), the results of the two campaigns provide a coherent picture of the acceleration regimes for the foam–attached target configuration. Figure 5.18 shows a synoptic view of the experimental results achieved for p–polarized pulses and 12 $\mu$m near–critical foams in the two facilities. From data reported in Figure 5.18, three acceleration regimes can be identified. For moderate intensities ($5 \times 10^{16}\,\mathrm{W/cm^2}$–$10^{18}\,\mathrm{W/cm^2}$), the presence of a foam layer led to a systematic enhancement of the proton cut–off energy with respect to bare Al targets and allowed to detect accelerated ions also for intensities well below $10^{18}\,\mathrm{W/cm^2}$, where TNSA is generally quenched for conventional foil targets. For high pulse intensities (above $10^{19}\,\mathrm{W/cm^2}$), a relevant enhancement in the acceleration performances in terms of maximum energy and number of accelerated protons was achieved as well. In the intermediate regime ($10^{18}\,\mathrm{W/cm^2}$), the presence of a foam layer led to results comparable with the solid foil configuration (or even worse in a few cases). This behaviour was attributed to two combined effects. The acceleration per-

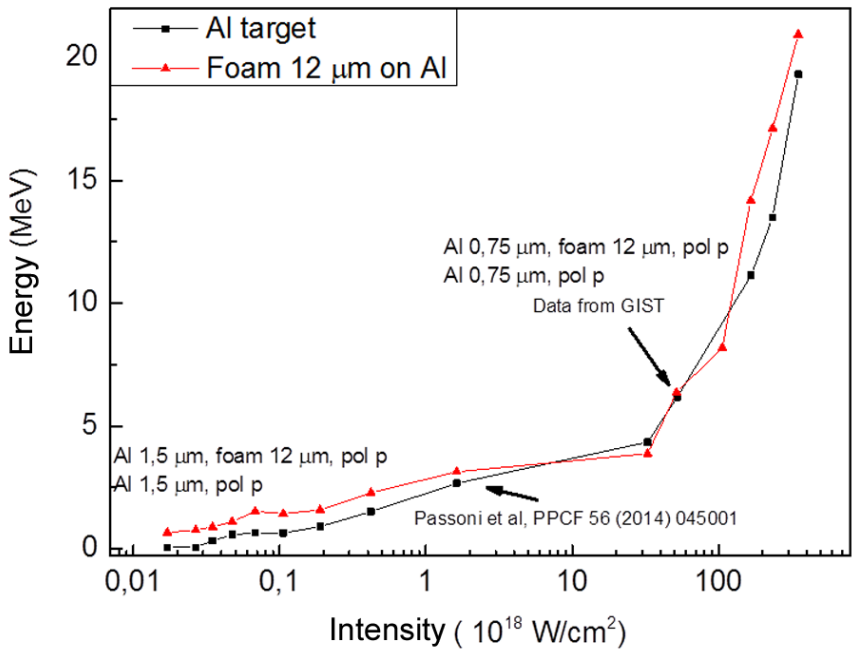


**Figure 5.18:** *Cut–off energies of proton observed in experiments performed at LIDyL and GIST (for p–polarization) plotted as a function of the pulse intensity.*

formance enhancement observed for relatively low intensities was attributed to a partial ionization produced in the foam layer by the incoming laser pulse. Thus, in this regime, the laser pulse interacted with an under–dense plasma and efficient production of hot electrons occurred in the slightly under–dense plasma due to volume interaction mechanisms. For intensity exceeding $10^{18}\,\mathrm{W/cm^2}$, however, the plasma ionization degree increased, thus the foam layer led to the production of a slightly over–dense plasma in front of the solid foil, whose thickness was higher than the optimal value expected for slightly over–dense foams. As a consequence, in this regime, the foam–attached and bare Al foil configurations resulted in comparable acceleration performances. Above $10^{19}\,\mathrm{W/cm^2}$, the pulse propagation in a slightly over–dense plasma was allowed due to the onset of a relativistic interaction regime: for high intensity, relativistic induced transparency and pulse channelling could take place leading again to enhanced acceleration performances in presence of a foam layer.
In conclusion, the results of these experiments underline the importance of an appropriate matching between foam properties and laser parameters, showing that for non optimized foam properties no acceleration performance enhancement is achieved with respect to bare Al targets. Optimum target properties (foam thickness and density) are strongly dependent on the adopted laser parameters, thus the design of foam–attached targets for a specific laser system should take into account the laser properties and the interaction conditions. The results discussed above suggest the possibility of achieving even better acceleration performances by further optimizing the target–laser coupling.
The acceleration performances achieved for foam–attached targets (especially in

the high–intensity experiment) are of interest for next future industrial applications requiring 10s MeV protons, such as the production of radioisotopes for medic diagnostics and material characterization, testing and processing. However, the acceleration of single bunches of ions is not sufficient for these applications, since they require high average currents. The reduced sensibility of the process to slight variations of target or laser properties and their robustness makes this solution suitable for high repetition rate configurations (Section 3.2), which are essential to achieve appropriate ion currents. It is interesting to consider the results discussed in this section in the frame of investigations on other advanced target configurations for laser–driven ion acceleration enhancement performed in laser facilities delivering ultra–short laser pulses with moderate energy, i.e. providing the possibility of high repetition rate operation. The proton cut–off energies achieved in this experiment for $5 \times 10^{19}\,\mathrm{W/cm^2}$ ($\sim$ 8 MeV) are slightly higher than results achieved with the same intensity using a monolayer of polystyrene nanospheres on the front surface of 1 $\mu$m thick mylar foils at the 100 TW laser system of GIST by Margarone *et al.* [150]. In addition, maximum proton energy observed for foam–attached targets (26 MeV) are higher than cut–off energies (17 MeV) reported by Zeil *et al.* for plain $\mu$m metal foil targets with high contrast ratio ($10^{10}$) at the DRACO laser system of the Dresden–Rossendorf research center (30 fs, $> 10^{21}\,\mathrm{W/cm^2}$) [75]. Despite the lower power delivered by the DRACO system (100 TW), a better focusing and the use of non destructive pulse cleaning techniques allowed to achieve pulse intensity in excess of $10^{21}\,\mathrm{W/cm^2}$, higher than the maximum intensity considered in the experiment at the 1 PW PULSER I laser system of GIST. The cut–off energy of protons detected in this experiment for intensity comparable with the maximum intensity considered at GIST (but lower energy on target) is slightly higher than 5 MeV, well below the values achieved for foam–attached targets. On the other hand, higher cut–off energies (up to 40 MeV) were recorded for simple metal targets by Ogura *et al.* at the J–KAREN laser system of the Kansai Photon Science Institute (40 fs, $\times 10^{21}\,\mathrm{W/cm^2}$, $10^{10}$ contrast ratio) [213]. However, the number of ions observed in this experiment was significantly lower than results obtained in other facilities, thus, information on the ion spectrometer detection threshold would be required to compare results in different facilities [214]. Finally, the production of 45 MeV protons form ultra–thin solid foils (10 nm) at the PULSER I laser system of GIST (29 fs, $3.3 \times 10^{20}\,\mathrm{W/cm^2}$, $10^{10}$ contrast ratio) were reported by Kim *et al.* [215], that is a result having a great intrinsic interest being the maximum proton energy ever achieved for ultra–short laser pulses. However, the foam–based target configuration discussed in this section appears more suitable to high repetition rate acceleration experiments, since ultra–thin foils are expected to pose several technical issues for operation at high repetition rates, being less robust and much more sensitive to slight variations of experimental conditions (see 3.2.3).

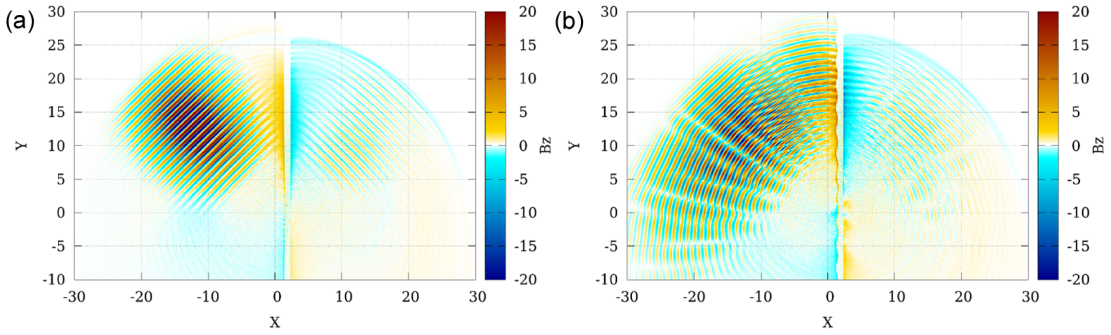


**Figure 5.19:** *2D PIC simulations: comparison between the z component of the magnetic field for a planar target (a) and a grating target with resonance* 45° *(b) for incidence at* 45°.

## 5.2 Grating targets

The grating target design exploits the enhanced production of hot electrons due to the resonant excitation of electromagnetic surface waves by ultra–intense laser pulses incident with an appropriate angle on a modulated surface with a periodic groove (see section 1.1.2). As discussed in section 1.3.3, the application of this kind of target to laser–driven ion acceleration was investigated in a first experimental campaign by Ceccotti *et al.* in 2012, showing a significant enhancement of the proton cut–off energy for grating targets around the resonant incidence angle with respect to planar targets. This behaviour was attributed to the resonant excitation of surface waves. The interest of a second experimental campaign was related to the possibility of studying the angular distribution of hot electrons produced in the laser–grating interaction and the role of target properties in the acceleration mechanism. To this aim, targets with different thickness and groove period (i.e. resonance angle) were considered. This experimental campaign was performed in October 2014 with the UHI100 laser system at the LIDyL facility in the frame of the Laserlab Europe project and my role was mainly related to the participation to the experiment.
An extensive numerical study was performed in preparation of this experiment using the *piccante* code. Solid targets ($n_e = 120 n_c$) with thickness $1\lambda$, grating depth $\lambda/4$ and groove periodicity from $1\lambda$ to $3.414\lambda$ (corresponding to resonance angles from 0° to 45°) were considered (while only $\alpha_{res} = 30°$ had been considered in previous work). Simulations were performed for pulses with p–polarization, $a_0 = 5$ (corresponding to $5 \times 10^{19}\,\mathrm{W/cm^2}$) and incidence angle from 0° to 70°. The results of these simulations confirmed the presence of a significant difference in the interaction of a laser pulse with grating and planar targets also for $\alpha_{res} \neq 30°$. The laser pulse was specularly reflected by the flat target, while a complex diffraction pattern was observed for grating targets. In particular, for resonant incidence angles, a diffraction component along the target surface with the properties of a plasmonic wave was observed, as shown in Figure 5.19 for $\theta = \theta_{res} = 45°$. Simulations also allowed to study the effect of the excitation of plasmonic waves on the ion acceleration process. As shown in Figure 5.20, the proton cut–off energy was enhanced for the grating targets with respect to the case of a planar target irradiated at the same angle due to higher absorption

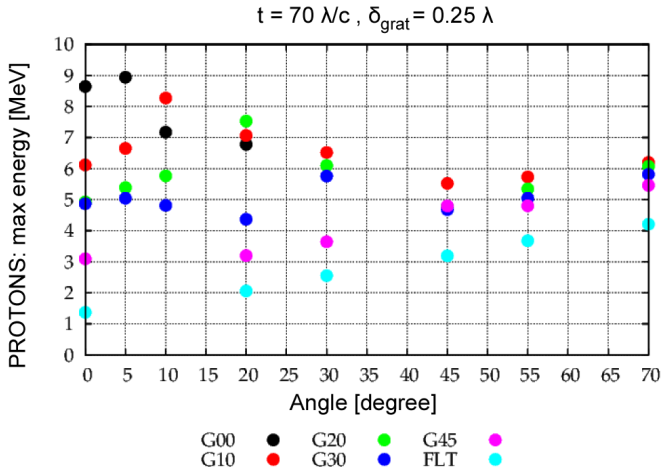


**Figure 5.20:** *Proton cut–off energies for several targets as a function of the angle of incidence.*

efficiency for rough surfaces. The resonance was present for all targets at the expected angle (except for the 0° grating) and was more pronounced for gratings designed for smaller resonance angles. Finally, the electron angular distribution was considered: a large and broad electron signal was observed along the direction parallel to the target surface in the resonance condition and the electron spectra showed significantly higher electron cut–off energy at resonance (10–20 MeV energies were expected).
The experimental campaign was performed at the UHI100 laser system of the LIDyL facility, a Ti:sapphire laser system delivering 25 fs pulses at a central wavelength of 790 ns with maximum intensity $5 \times 10^{19}$ W/cm$^2$ (already mentioned in section 5.1.1). Figure 5.21 illustrates a schematic view of the interaction chamber. A high contrast configuration ($10^{10}$) was adopted, as required to preserve the grating target structure until the interaction with the main pulse. The experimental set–up was designed to allow the irradiation of grating targets with angles from 15° to 60°: the target holder was fully motorized allowing to change the incidence angle without opening the vacuum chamber. A Thomson parabola ion spectrometer aiming at the back of the target (with a 100 $\mu$m diameter entrance pinhole) was mounted on a crescent–like rail and the position of an electron spectrometer aiming at the front face of the target could be adjusted remotely. In addition for a few shots a radiochromic film stack ring was used, to collect electron, X–ray and ion signal around the target and to have a more complete information about the particle energy spectra. The main novelty in the experimental set–up adopted in this campaign (with respect to the previous experiment [153]) was the presence of the electron spectrometer providing information on the electron spectra in different directions (in particular along the specular reflection and the target surface directions). The targets considered were 13 $\mu$m Mylar flat foils and gratings with resonance angles 30° and 45° and grating depth of 250 nm[3]. The target thickness was reduced with respect to the previous experiment with the aim of enhancing

[3]In the previous experiment, described in Section 1.3.3, 23 $\mu$m thick foils with resonance angle 30° and grating depth 300 nm and 500 nm had been considered.

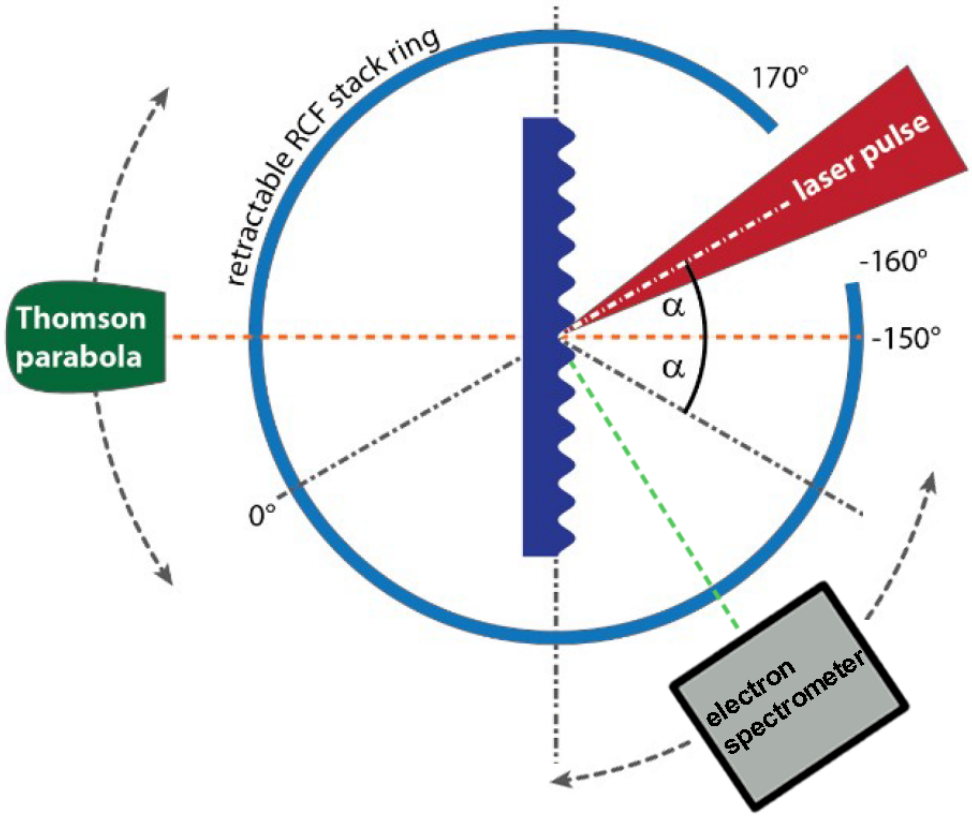


**Figure 5.21:** *Schematic view of the interaction chamber.*

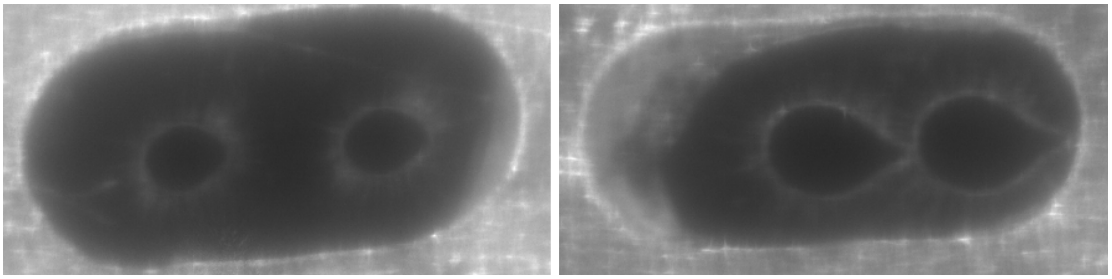

**Figure 5.22:** *Holes produced by the incident laser pulses in a flat target (left) and in a grating target at resonance (right).*

the cut–off energy of accelerated ions.
The experimental data analysis is still ongoing at the moment of writing, thus only preliminary observations are discussed in this section. A first immediate evidence of the existence of a resonance was provided by the shape of the holes produced by the incoming laser pulse, shown in Figure 5.22. In general, the hole size was much larger than the focal spot due to thermal effects. The holes observed for flat targets were approximately circular and significantly smaller than holes in grating targets, suggesting enhanced absorption in the latter case. In particular, at resonance, the holes in grating targets showed a pronounced tip in the laser propagation direction due to laser diffraction along the target surface.

The presence of the tip, not masked by thermal effects, was a first indication that the diffracted pulse can propagate along the surface for a few hundreds of $\mu$m. In addition, from a preliminary analysis of proton spectra it was inferred that the cut–off energy for grating targets at resonance ($\sim$ 6 MeV) was higher than the value recorded for planar targets for the same angle. However, it is not clear yet whether the cut–off energy detected for grating targets at resonance was also higher than cut–off energies achieved for planar targets for arbitrary incidence angle. Finally, the electron signal detected by the electron spectrometer appeared more intense for grating targets than for planar targets and for incidence angles close to the resonance angle. Also the maximum electron energy was higher in resonance conditions (reaching maximum values around 10 MeV). The observation of intense electron signal with broad angular distribution (extended for 20° from the target surface direction) was in good agreement with simulations.
These preliminary results provided evidence of an enhancement in the hot electron production along the target surface direction in resonance conditions, coherent with the excitation of plasmonic surface waves.

# 6

# Conclusions and perspectives

In this PhD thesis, advanced target configurations for ion acceleration driven by ultra–intense ($10^{18}$ W/cm$^2$) ultra–short (10–100 fs) laser pulses were investigated, through the development of suitable advanced material science techniques for target manufacturing and laser–driven ion acceleration experiments performed in external laser facilities.

As illustrated in **Part I: Chapter 1**, since it was first observed in 2000 [2–4], laser–driven ion acceleration has attracted increasing interest as a unique tool to investigate new laser–plasma interaction regimes and thanks to a number of possible application fields. The potential of this technique for scientific and technological applications is related to the possibility of producing multi–MeV protons and ions with a high degree of laminarity and low emittance with an experimental apparatus relatively compact and cheap compared to common acceleration systems [7, 8]. In particular, laser–driven ion acceleration has been employed successfully for proton imaging, for plasma diagnostics and for isochoric heating of solid–density matter on ultra–short time scales. Moreover, a number of applications requiring enhanced acceleration performances have been proposed. Oncological hadrontherapy and the fast ignition of inertial confinement fusion targets, for example, require precise and controlled beam energies in the 100s MeV/nucleon range, which are currently not available. Other interesting applications are related to the irradiation of materials for industrial or scientific purposes and to the production of isotopes for nuclear medical imaging techniques, which require lower ion energy (10s MeV/nucleon) but high average ion current (i.e. high repetition rate). Three main strategies have been considered so far to achieve an enhancement of the laser–driven ion acceleration performances: (i) theoretical investigation of the acceleration mechanisms; (ii) development of advanced laser systems; (iii) adoption of novel targets to optimize the laser–ions energy transfer. In particular, the latter approach consists of the development of engineered materials specifically designed to control the laser–matter interaction phase, to optimize the pulse–target coupling and to enhance the laser energy absorption. This strategy can lead to an enhancement in the ion acceleration performances with respect to several $\mu$m foil targets in terms of maximum ion energy, acceler-

ated charge, beam spectral or spatial quality, depending on the specific properties of the adopted target configuration. Moreover, targets providing high laser–ions energy conversion efficiency can allow to achieve acceleration performances suitable for some of the foreseen applications for laser intensities currently available with table–top lasers (up to $10^{21}\,\mathrm{W/cm^2}$). However, the major part of advanced target solutions explored so far pose experimental constraints, such as ultra–high contrast to preserve the interaction surface until the main pulse incidence, high precision positioning and control of target properties, which could prevent their application at high repetition rate.

In this frame, the main goal of my PhD thesis was the development of experimental configurations involving sufficiently robust targets to achieve enhanced acceleration performances and, at the same time, to relax the technological constraints required by most of the novel target solutions explored so far. Therefore, the most part of my PhD activities was aimed at the development of multi–layer foam–based targets composed by a solid foil with an ultra–low density foam layer on its directly irradiated surface. As discussed in Section 1.3.2, these targets were designed to exploit the enhanced laser energy absorption in near–critical matter due to peculiar interaction mechanisms occurring in this regime (i.e. pulse channeling, relativistic self–focusing and direct–light–pressure acceleration of electrons). However, foam–based target manufacturing was not straightforward due to the extremely low foam density values required (in the $\mathrm{mg/cm^3}$ regime). Thus the development and optimization of advanced material science techniques for the production and characterization of this kind of material was a necessary condition to manufacture foam–attached targets to be employed in laser–driven ion acceleration experiments, as illustrated in **Part I: Chapter 2**. An additional goal of this thesis was the participation to an experiment aimed at achieving a better understanding of electron dynamics in laser–driven ion acceleration with grating targets, of great interest also for high field plasmonics (Section 1.3.3). In this configuration, the idea was to exploit the excitation of surface plasmonic waves on a periodically modulated front surface to enhance laser energy absorption at a characteristic resonance angle and, consequently, the acceleration performances.

Therefore, the first objective of my PhD activities was the elaboration of suitable strategies for foam–based target manufacturing. These activities were discussed in **Part II**. The first part of **Chapter 3** illustrated the approach adopted for the growth of near–critical carbon foam layers by Pulsed Laser Deposition (PLD), which proved to be a flexible and reliable tool for the production of carbon foams with good uniformity, complete substrate coverage, density down to $3\,\mathrm{mg/cm^3}$ and thickness from $3\,\mu$m to $150\,\mu$m controlled by tuning the process duration, target–to–substrate distance and ambient gas pressure. In the second part of Chapter 3, technological solutions designed for foam–attached target production, transport and irradiation were discussed, along with the possibility of achieving robust target configurations for high repetition rate experiments or applications. In this frame, a natural continuation of my PhD activities would be the deposition of foams with tuned composition (for example with high hydrogen con-

tent) or density gradient and the adoption of advanced engineered configurations for target handling in the deposition, transport and irradiation phases of high repetition rate laser–driven ion acceleration experiments. In addition, a preliminary investigation was performed to verify the possibility of producing free–standing foams and foam layers on foils with nanometric thickness, of interest for hole boring radiation pressure acceleration and collisionless shock acceleration mechanisms. In principle, free–standing foams could be produced by growing the foam on a holed support until the hole is completely filled: holes with diameter around 40 $\mu$m could be filled by growing a foam directly on a grid. However, appropriate methods for the characterization of foams produced in this configuration should be developed to guarantee the target uniformity and an appropriate control of the foam density and thickness. On the other hand, foams could be grown on few nm thick substrates which shouldn't affect the properties of ions accelerated in the foam. A preliminary investigation on this possibility was performed by depositing foams on commercially available grids for Transmission Electron Microscopy (TEM) with a 3 nm thick carbon layer. Clearly, the size of the apertures of a TEM grid (20 $\mu$m) is not acceptable for laser–matter interaction experiments, since the presence of the grid would influence the acceleration process, thus a feasibility study on the possibility of depositing carbon foams on 10s nm thick SiN windows and polymeric windows will be performed.

A further objective of my PhD activities was the quantitative development and experimental validation of an innovative technique for thin film density evaluation based on Energy Dispersive X–ray Spectroscopy (EDS), as discussed in **Chapter 4**. Two EDS based methods were originally proposed for the evaluation of the density of carbon foams deposited on a Si wafer. In this thesis, a suitable data analysis software was developed to correctly calculate the foam areal density from X–ray spectra and to extend the application to films with virtually any possible composition. The applicability of this method was then demonstrated for a number of different experimental conditions: thin films with various compositions, different coating–substrate combinations, various mesoscale morphologies and with densities in an extremely wide range (few mg/cm$^3$– 20 g/cm$^3$). The effect of the atomic number difference between coating and substrate, of fluorescence induced by high energy X–rays and of the electron accelerating voltage were extensively investigated. Although the results were affected by an error up to 30% in a few unfavourable configurations, it was clear that in general this technique guarantees a reliable, fast, simple and cheap measurement process to evaluate the density of nanostructured thin films in a wide range of morphologies and compositions, exploiting a common integrated EDS–SEM equipment present in most material science laboratories. In addition, the high resolution of the electron microprobe was exploited for the analysis of coating inhomogeneity both at the macroscopic and microscopic scales. The main open issues as regards the development of EDS based methods for thin film density measurement are the development of a suitable model to take into account the distortion of the X–ray production distribution in multilayer samples and the development of a suitable data analysis software for the validation and application of the EDS based method not requiring a reference

standard.

The final goal of my PhD activities on foam–attached targets was the application of such targets in laser–driven ion acceleration experiments in external laser facilities, as discussed in **Part III: Chapter 5**. Two experiments were performed during my PhD. The first was a proof of principle experiment aimed at testing the effectiveness of this target configuration in the moderate intensity regime (from $5\times10^{16}\,\mathrm{W/cm^2}$ to $5\times10^{19}\,\mathrm{W/cm^2}$). This experiment was performed at the LIDyL facility (France) with the UHI100 laser system, a Ti:sapphire laser delivering 25 fs pulses at a central wavelength $\lambda = 790$ nm, in both high and low contrast configurations. In this experiment, the feasibility of the acceleration scheme based on foam–attached targets was demonstrated. A systematic enhancement of the maximum proton energy was observed with foam–attached targets with respect to the case of bare solid foils below $10^{18}\,\mathrm{W/cm^2}$. Protons with energies in the MeV range were produced also for moderate intensities ($10^{16}\,\mathrm{W/cm^2} - 10^{17}\,\mathrm{W/cm^2}$) much lower than the threshold value below which laser–driven ion acceleration is commonly quenched ($10^{18}\,\mathrm{W/cm^2}$). The second experiment was performed at the PULSER I laser system of GIST (South Korea), a Ti:sapphire laser producing 29 fs pulses at $\lambda = 805$ nm with intensity in the $7\times10^{19}\,\mathrm{W/cm^2} - 5\times10^{20}\,\mathrm{W/cm^2}$ range. This was an extensive investigation on the role of target properties (in particular foam thickness and density) and of laser parameters (intensity and polarization) on acceleration performances. Protons up to 26 MeV and $C^{6+}$ ions up to 120 MeV were detected for foam attached targets. A systematic enhancement by $\sim 30 - 250\%$ in the proton and $C^{6+}$ maximum energy was achieved with foam–attached targets with respect to the conventional solid foil configuration depending on the laser parameters. In addition, both the medium ion energy and the total number of high energy ions increased in presence of a foam layer, resulting in an enhancement of the acceleration process efficiency. The existence of an optimum near–critical foam thickness $\lesssim 8\mu$m was observed from comparisons between the maximum ion energy achieved in presence of foam layers with different thickness. This suggested that higher ion energies could be achieved by suitably optimizing foam properties. In addition, better acceleration performances are expected for lower incidence angles and higher pulse intensities. Results achieved so far are already interesting for some of the foreseen applications of laser–driven ion sources: 10s MeV protons can be employed, for instance, for the production of radioisotopes for medical diagnostics, for material irradiation or radiation detector testing. It is interesting to comment these results in the frame of a number of experimental studies performed with comparable intensity and ultra–short pulses to investigate advanced target configurations for laser–driven ion acceleration performance enhancement. As regards nanostructured targets, maximum proton energies around 5 MeV were achieved with 23 $\mu$m thick grating targets by Ceccotti *et al.* at UHI100 (25 fs, $> 10^{19}\,\mathrm{W/cm^2}$, $10^{12}$ contrast ratio), while 7.5 MeV protons were detected at the 100 TW laser system of GIST (30 fs, $5\times10^{19}\,\mathrm{W/cm^2}$, $5\times10^{11}$ contrast ratio) by Margarone *et al.* using 1 $\mu$m thick mylar foils with a monolayer of polystyrene nanospheres on the directly illuminated side of the target [150]. These results are comparable or lower than the cut–off

energy produced with foam–attached targets at PULSER I ($\sim$ 8 MeV) in the same intensity range. Remarkable results have been achieved for plain $\mu$m metal foil targets: protons with maximum energy of about 17 MeV were observed by Zeil *et al.* at the DRACO laser system of the Dresden–Rossendorf research center (30 fs, $> 10^{21}\,\mathrm{W/cm^2}$, $10^{10}$ contrast ratio) [75], while 40 MeV protons were detected by Ogura *et al.* at the J–KAREN laser system of the Kansai Photon Science Institute (40 fs, $\times 10^{21}\,\mathrm{W/cm^2}$, $10^{10}$ contrast ratio) [213]. However, in the latter case, the number of high energy accelerated particles was quite low with respect to other experiments [214]. Protons with energies up to 45 MeV were accelerated at the PULSER I laser of GIST (29 fs, $3.3 \times 10^{20}\,\mathrm{W/cm^2}$, $10^{10}$ contrast ratio) with ultra–thin polymeric targets (10 nm) by Kim *et al.* [215]. However, this target configuration is less robust than the foam–based configuration proposed in this thesis and it is expected to pose several issues for high repetition rate acceleration experiments.

A secondary goal of my PhD activities was the participation to a laser–driven ion acceleration experiment performed on grating targets. The experiment was performed at the above mentioned UHI100 laser system of the LIDyL facility (25 fs, $5 \times 10^{19}\,\mathrm{W/cm^2}$, $10^{10}$ contrast ratio). The main goal of this experiment was to complete a previous study performed by Ceccotti *et al.* [153] by extending the range of explored target properties (different resonance angles and different thickness values) and by analysing the angular and spectral electron distribution with the aim of achieving a deeper comprehension of high field plasmonics effects. Data analysis is still ongoing at the moment of writing, but preliminary results showed clear indications of an enhancement of the maximum energy of protons accelerated with resonant incidence angle ($\sim 6MeV$) with respect to the case of a planar target with comparable thickness. In addition, the electron signal was more intense for grating targets than for planar targets, especially for resonant incidence angles. In resonance conditions, the acceleration of electrons along the target front surface was observed consistently with the excitation of plasmonic surface waves.

In conclusion, in this thesis the possibility of exploiting novel and enhanced ultra–intense ultra–short laser driven ion acceleration schemes through the design, production and employment of engineered nanostructured targets was investigated. In general, novel target concepts exploit peculiar characteristics of structured targets, often produced with advanced material science techniques, to achieve enhanced ion acceleration performances, in terms of number or maximum energy, spectral and spatial quality of accelerated ions, and to tailor these properties for specific applications. This study draws attention to the importance of achieving a suitable coupling between target properties and laser parameters to enhance the efficiency of energy conversion from the incoming laser pulse to accelerated ions. Advanced target configurations would allow to significantly enhance the ion acceleration performances achieved with the existing laser facilities, thus relaxing the request and reducing the costs of further technology development in view of laser–driven ion sources applications and to exploit to the highest de-

gree the development of advanced ultra–intense laser facilities and pan European infrastructures (as ELI and HIBEF) to achieve unprecedented ion acceleration performances. Therefore, the development of advanced target concepts will give a decisive contribution to the worldwide efforts towards the development of advanced laser facilities for laser–driven ion acceleration.

# List of Figures

# Bibliography


[1] T. Tajima and J. M. Dawson. Laser electron accelerator. *Physical Review Letters*, 43:267–270, 1979.

[2] E. L. Clark, K. Krushelnick, J. R. Davies, M. Zepf, M. Tatarakis, F. N. Beg, A. Machacek, P. A. Norreys, M. I. K. Santala, I. Watts, and A. E. Dangor. Measurements of energetic proton transport through magnetized plasma from intense laser interactions with solids. *Physical Review Letters*, 84:670–673, 2000.

[3] A. Maksimchuk, S. Gu, K. Flippo, D. Umstadter, and V. Y. Bychenkov. Forward ion acceleration in thin films driven by a high-intensity laser. *Physical Review Letters*, 84:4108–4111, 2000.

[4] R. A. Snavely, M. H. Key, S. P. Hatchett, T. E. Cowan, M. Roth, T. W. Phillips, M. A. Stoyer, E. A. Henry, T. C. Sangster, M. S. Singh, S. C. Wilks, A. MacKinnon, A. Offenberger, D. M. Pennington, K. Yasuike, A. B. Langdon, B. F. Lasinski, J. Johnson, M. D. Perry, and E. M. Campbell. Intense high-energy proton beams from petawatt-laser irradiation of solids. *Physical Review Letters*, 85:2945–2948, 2000.

[5] S. C. Wilks, A. B. Langdon, T. E. Cowan, M. Roth, M. Singh, S. Hatchett, M. H. Key, D. Pennington, A. MacKinnon, and R. A. Snavely. Energetic proton generation in ultra-intense laser–solid interactions. *Physics of Plasmas (1994-present)*, 8(2):542–549, 2001.

[6] M. Borghesi, J. Fuchs, S. V. Bulanov, A. J. Mackinnon, P. K. Patel, and M. Roth. Fast ion generation by high-intensity laser irradiation of solid targets and applications. *Fusion Science and Technology*, 49(3):412–439, 2006.

[7] D. Hiroyuki, N. Mamiko, and S. P. Alexander. Review of laser-driven ion sources and their applications. *Reports on Progress in Physics*, 75(5):056401, 2012.

[8] A. Macchi, M. Borghesi, and M. Passoni. Ion acceleration by superintense laser-plasma interaction. *Reviews of Modern Physics*, 85(2):751, 2013.

[9] T. E. Cowan, J. Fuchs, H. Ruhl, A. Kemp, P. Audebert, M. Roth, R. Stephens, I. Barton, A. Blazevic, E. Brambrink, et al. Ultralow emittance, multi–MeV proton beams from a laser virtual–cathode plasma accelerator. *Physical Review Letters*, 92(20):204801, 2004.

[10] L. Willingale, S. R. Nagel, A. G. R. Thomas, C. Bellei, R. J. Clarke, A. E. Dangor, R. Heathcote, M. C. Kaluza, C. Kamperidis, S. Kneip, K. Krushelnick, N. Lopes, S. P. D. Mangles, W. Nazarov, P. M. Nilson, and Z. Najmudin. Characterization of high–intensity laser propagation in the relativistic transparent regime through measurements of energetic proton beams. *Physical Review Letters*, 102:125002, 2009.

[11] S. V. Bulanov and T. Z. Esirkepov. Comment on "Collimated multi-MeV ion beams from high-intensity laser interactions with underdense plasma". *Physical Review Letters*, 98(4):049503, 2007.

[12] S. S. Bulanov, V. Y. Bychenkov, V. Chvykov, G. Kalinchenko, D. W. Litzenberg, T. Matsuoka, A. G. R. Thomas, L. Willingale, V. Yanovsky, K. Krushelnick, et al. Generation of GeV protons from 1 PW laser interaction with near critical density targets. *Physics of Plasmas (1994-present)*, 17(4):043105, 2010.

[13] T. Nakamura, M. Tampo, R. Kodama, S. V. Bulanov, and M. Kando. Interaction of high contrast laser pulse with foam–attached target. *Physics of Plasmas (1994-present)*, 17(11):113107, 2010.

[14] A. Sgattoni, P. Londrillo, A. Macchi, and M. Passoni. Laser ion acceleration using a solid target coupled with a low–density layer. *Physical Review E*, 85(3):036405, 2012.

[15] A. Zani, D. Dellasega, V. Russo, and M. Passoni. Ultra–low density carbon foams produced by pulsed laser deposition. *Carbon*, 56:358–365, 2013.

[16] A. Zani. *Experimental and theoretical studies on ultraintense laser driven ion acceleration*. PhD thesis, Politecnico di Milano, Milan, Italy, 2013.

[17] S. Backus, C. G. Durfee III, M. M. Murnane, and H. C. Kapteyn. High power ultrafast lasers. *Review of Scientific Instruments*, 69(3):1207–1223, 1998.

[18] G. A. Mourou, T. Tajima, and S. V. Bulanov. Optics in the relativistic regime. *Reviews of Modern Physics*, 78(2):309, 2006.

[19] D. Strickland and G. Mourou. Compression of amplified chirped optical pulses. *Optics Communications*, 55(6):447–449, 1985.

[20] P. Maine, D. Strickland, M. Bouvier, and G. Mourou. Amplification of picosecond pulses to the terawatt level. *Optical Communications*, 55(6):447, 1985.

[21] P. Maine, D. Strickland, P. Bado, M. Pessot, and G. Mourou. Generation of ultrahigh peak power pulses by chirped pulse amplification. *Quantum electronics, IEEE Journal of*, 24(2):398–403, 1988.

[22] D. E. Spence, P. N. Kean, and W. Sibbett. 60–fsec pulse generation from a self–mode–locked Ti: sapphire laser. *Optics letters*, 16(1):42–44, 1991.

[23] W. L. Kruer. *The physics of laser plasma interactions*. Reading, MA (US); Addison-Wesley Publishing Co., 1988.

[24] P. Gibbon. Short pulse laser interaction with matter. *Imperial College Press*, 8:14–26, 2005.

[25] P. Mulser and D. Bauer. *High Power Laser-Matter Interaction*, volume 238. Springer Science & Business Media, 2010.

[26] A. Macchi. *A Superintense Laser–Plasma Interaction Theory Primer*. Springer Science & Business Media, 2013.

[27] J. M. Mikhailova, A. Buck, A. Borot, K. Schmid, C. Sears, G. D. Tsakiris, F. Krausz, and L. Veisz. Ultra–high–contrast few–cycle pulses for multipetawatt–class laser technology. *Optics Letters*, 36(16):3145–3147, 2011.

[28] A. B. Borisov, A. V. Borovskiy, O. B. Shiryaev, V. V. Korobkin, A. M. Prokhorov, J. C. Solem, T. S. Luk, K. Boyer, and C. K. Rhodes. Relativistic and charge-displacement self–channeling of intense ultrashort laser pulses in plasmas. *Physical Review A*, 45(8):5830, 1992.

[29] P. Monot, T. Auguste, P. Gibbon, F. Jakober, G. Mainfray, A. Dulieu, M. Louis-Jacquet, G. Malka, and J. L. Miquel. Experimental demonstration of relativistic self–channeling of a multiterawatt laser pulse in an underdense plasma. *Physical Review Letters*, 74(15):2953, 1995.

[30] T. M. Antonsen Jr and P. Mora. Self-focusing and Raman scattering of laser pulses in tenuous plasmas. *Physical Review Letters*, 69(15):2204, 1992.

[31] J. Krall, A. Ting, E. Esarey, and P. Sprangle. Enhanced acceleration in a self–modulated–laser wake–field accelerator. *Physical Review E*, 48(3):2157, 1993.

[32] A. I. Akhiezer and R. V. Polovin. Theory of wave motion of an electron plasma. *Soviet Physics JETP-USSR*, 3, 1956.

[33] A. Zhidkov, J. Koga, T. Hosokai, K. Kinoshita, and M. Uesaka. Effects of plasma density on relativistic self-injection for electron laser wake-field acceleration. *Physics of Plasmas (1994-present)*, 11(12):5379–5386, 2004.

[34] S. C. Wilks and W. L. Kruer. Absorption of ultrashort, ultra–intense laser light by solids and overdense plasmas. *Quantum Electronics, IEEE Journal of*, 33(11):1954–1968, 1997.

[35] F. Brunel. Anomalous absorption of high intensity subpicosecond laser pulses. *Physics of Fluids (1958–1988)*, 31(9):2714–2719, 1988.

[36] W. L. Kruer and K. Estabrook. J×B heating by very intense laser light. *Physics of Fluids (1958–1988)*, 28(1):430–432, 1985.

[37] L. Willingale, S. P. D. Mangles, P. M. Nilson, R. J. Clarke, A. E. Dangor, M. C. Kaluza, S. Karsch, K. L. Lancaster, W. B. Mori, Z. Najmudin, et al. Collimated multi–mev ion beams from high-intensity laser interactions with underdense plasma. *Physical Review Letters*, 96(24):245002, 2006.

[38] M. Borghesi, A. J. MacKinnon, L. Barringer, R. Gaillard, L. A. Gizzi, C. Meyer, O. Willi, A. Pukhov, and J. Meyer-ter Vehn. Relativistic channeling of a picosecond laser pulse in a near–critical preformed plasma. *Physical Review Letters*, 78:879–882, 1997.

[39] M. Borghesi, S. Bulanov, D. H. Campbell, R. J. Clarke, T. Z. Esirkepov, M. Galimberti, L. A. Gizzi, A. J. MacKinnon, N. M. Naumova, F. Pegoraro, et al. Macroscopic evidence of soliton formation in multiterawatt laser–plasma interaction. *Physical Review Letters*, 88(13):135002, 2002.

[40] G. A. Askar'yan, S.V. Bulanov, F. Pegoraro, and A. M. Pukhov. Magnetic interaction of self-focusing channels and fluxes of electromagnetic radiation: their coalescence, the accumulation of energy, and the effect of external magnetic fields on them. *JETP Letters*, 60(4):251–257, 1994.

[41] G. A. Askar'yan, S. V. Bulanov, F. Pegoraro, and A. M. Pukhov. Magnetic interaction of self-focused channels and magnetic wake excitation in high intensity laser pulses. *Comments on Plasma Physics and Controlled Fusion*, 17(1):35–44, 1995.

[42] S. V. Bulanov, M. Lontano, T. Z. Esirkepov, F. Pegoraro, and A. M. Pukhov. Electron vortices produced by ultraintense laser pulses. *Physical Review Letters*, 76(19):3562, 1996.

[43] T. Nakamura and K. Mima. Magnetic–dipole vortex generation by propagation of ultraintense and ultrashort laser pulses in moderate-density plasmas. *Physical Review Letters*, 100(20):205006, 2008.

[44] L. Willingale, P. M. Nilson, A. G. R. Thomas, S. S. Bulanov, A. Maksimchuk, W. Nazarov, T. C. Sangster, C. Stoeckl, and K. Krushelnick. High–power, kilojoule laser interactions with near–critical density plasmaa). *Physics of Plasmas (1994-present)*, 18(5):056706, 2011.

[45] G. Mourou, Z. Chang, A. Maksimchuk, J. Nees, S. V. Bulanov, V. Y. Bychenkov, T. Z. Esirkepov, N. M. Naumova, F. Pegoraro, and H. Ruhl. On the design of experiments for the study of relativistic nonlinear optics in the limit of single–cycle pulse duration and single–wavelength spot size. *Plasma Physics Reports*, 28(1):12–27, 2002.

[46] T. Tajima and G. Mourou. Zettawatt–exawatt lasers and their applications in ultrastrong–field physics. *Physical Review Special Topics-Accelerators and Beams*, 5(3):031301, 2002.

[47] S. J. Gitomer, R. D. Jones, F. Begay, A. W. Ehler, J. F. Kephart, and R. Kristal. Fast ions and hot electrons in the laser–plasma interaction. *Physics of Fluids (1958-1988)*, 29(8):2679–2688, 1986.

[48] K. Krushelnick, E. L. Clark, Z. Najmudin, M. Salvati, M. I. K. Santala, M. Tatarakis, A. E. Dangor, V. Malka, D. Neely, R. Allott, et al. Multi–MeV ion production from high-intensity laser interactions with underdense plasmas. *Physical Review Letters*, 83(4):737, 1999.

[49] G. S. Sarkisov, V. Y. Bychenkov, V. N. Novikov, V. T. Tikhonchuk, A. Maksimchuk, S.-Y. Chen, R. Wagner, G. Mourou, and D. Umstadter. Self–focusing, channel formation, and high–energy ion generation in interaction of an intense short laser pulse with a he jet. *Physical Review E*, 59(6):7042, 1999.

[50] T. Ditmire, J. W. G. Tisch, E. Springate, M. B. Mason, N. Hay, R. A. Smith, J. Marangos, and M. H. R. Hutchinson. High–energy ions produced in explosions of superheated atomic clusters. *Nature*, 386(6620):54–56, 1997.

[51] T. Ditmire, J. Zweiback, V. P. Yanovsky, T. E. Cowan, G. Hays, and K. B. Wharton. Nuclear fusion from explosions of femtosecond laser-heated deuterium clusters. *Nature*, 398(6727):489–492, 1999.

[52] E. L. Clark, K. Krushelnick, M. Zepf, F. N. Beg, M. Tatarakis, A. Machacek, M. I. K. Santala, I. Watts, P. A. Norreys, and A. E. Dangor. Energetic heavy–ion and proton generation from ultraintense laser-plasma interactions with solids. *Physical Review Letters*, 85(8):1654, 2000.

[53] S. P. Hatchett, C. G. Brown, T. E. Cowan, E. A. Henry, J. S. Johnson, M. H. Key, J. A. Koch, A. B. Langdon, B. F. Lasinski, R. W. Lee, et al. Electron, photon, and ion beams from the relativistic interaction of petawatt laser pulses with solid targets. *Physics of Plasmas (1994-present)*, 7(5):2076–2082, 2000.

[54] A. J. Mackinnon, M. Borghesi, S. Hatchett, M. H. Key, P. K. Patel, H. Campbell, A. Schiavi, R. Snavely, S. C. Wilks, and O. Willi. Effect of plasma scale length on multi–MeV proton production by intense laser pulses. *Physical Review Letters*, 86(9):1769, 2001.

[55] A. J. Mackinnon, Y. Sentoku, P. K. Patel, D. W. Price, S. Hatchett, M. H. Key, C. Andersen, R. Snavely, and R. R. Freeman. Enhancement of proton acceleration by hot-electron recirculation in thin foils irradiated by ultraintense laser pulses. *Physical Review Letters*, 88(21):215006, 2002.

[56] A. Fukumi, M. Nishiuchi, H. Daido, Z. Li, A. Sagisaka, K. Ogura, S. Orimo, M. Kado, Y. Hayashi, M. Mori, et al. Laser polarization dependence of proton emission from a thin foil target irradiated by a 70 fs, intense laser pulse. *Physics of Plasmas (1994-present)*, 12(10):0701, 2005.

[57] J. Fuchs, T. E. Cowan, P. Audebert, H. Ruhl, L. Gremillet, A. Kemp, M. Allen, A. Blazevic, J-C Gauthier, M. Geissel, et al. Spatial uniformity of laser-accelerated ultrahigh-current MeV electron propagation in metals and insulators. *Physical Review Letters*, 91(25):255002, 2003.

[58] L. Romagnani, J. Fuchs, M. Borghesi, P. Antici, P. Audebert, F. Ceccherini, T. Cowan, T. Grismayer, S. Kar, A. Macchi, et al. Dynamics of electric fields driving the laser acceleration of multi–MeV protons. *Physical Review Letters*, 95(19):195001, 2005.

[59] Stanley Humphries. *Charged particle beams*. Courier Corporation, 2013.

[60] M. Borghesi, A. J. Mackinnon, D. H. Campbell, D. G. Hicks, S. Kar, P. K. Patel, D. Price, L. Romagnani, A. Schiavi, and O. Willi. Multi–MeV proton source investigations in ultraintense laser–foil interactions. *Physical Review Letters*, 92(5):055003, 2004.

[61] T. Ceccotti, A. Lévy, F. Réau, H. Popescu, P. Monot, E. Lefebvre, and P. Martin. Tnsa in the ultra–high contrast regime. *Plasma Physics and Controlled Fusion*, 50(12):124006, 2008.

[62] M. Nishiuchi, H. Daido, A. Yogo, S. Orimo, K. Ogura, J. Ma, A. Sagisaka, M. Mori, A. S. Pirozhkov, H. Kiriyama, et al. Efficient production of a collimated MeV proton beam from a polyimide target driven by an intense femtosecond laser pulse. *Physics of Plasmas (1994-present)*, 15(5):053104, 2008.

[63] H. Ruhl, T. Cowan, and J. Fuchs. The generation of micro–fiducials in laser-accelerated proton flows, their imaging property of surface structures and application for the characterization of the flow. *Physics of Plasmas (1994-present)*, 11(5):L17–L20, 2004.

[64] M. Passoni and M. Lontano. Theory of light–ion acceleration driven by a strong charge separation. *Physical Review Letters*, 101(11):115001, 2008.

[65] J. Schreiber, F. Bell, F. Grüner, U. Schramm, M. Geissler, M. Schnürer, S. Ter-Avetisyan, B. M. Hegelich, J. Cobble, E. Brambrink, et al. Analytical model for ion acceleration by high-intensity laser pulses. *Physical Review Letters*, 97(4):045005, 2006.

[66] P. Mora. Plasma expansion into a vacuum. *Physical Review Letters*, 90(18):185002, 2003.

[67] P. Mora. Thin–foil expansion into a vacuum. *Physical Review E*, 72(5):056401, 2005.

[68] B. J. Albright, L. Yin, B. M. Hegelich, K. J. Bowers, T. J. T. Kwan, and J. C. Fernández. Theory of laser acceleration of light–ion beams from interaction of ultrahigh–intensity lasers with layered targets. *Physical Review Letters*, 97(11):115002, 2006.

[69] A. P. L. Robinson, A. R. Bell, and R. J. Kingham. Effect of target composition on proton energy spectra in ultraintense laser–solid interactions. *Physical Review Letters*, 96(3):035005, 2006.

[70] J. Fuchs, P. Antici, E. d'Humières, E. Lefebvre, M. Borghesi, E. Brambrink, C. A. Cecchetti, M. Kaluza, V. Malka, M. Manclossi, et al. Laser–driven proton scaling laws and new paths towards energy increase. *Nature Physics*, 2(1):48–54, 2006.

[71] L. Robson, P. T. Simpson, R. J. Clarke, K. W. D. Ledingham, F. Lindau, O. Lundh, T. McCanny, P. Mora, D. Neely, C.-G. Wahlström, et al. Scaling of proton acceleration driven by petawatt-laser–plasma interactions. *Nature Physics*, 3(1):58–62, 2007.

[72] M. Passoni, L. Bertagna, T. Ceccotti, and P. Martin. Proton maximum energy cutoff scaling laws for bulk targets. In *AIP Conference Proceedings*, volume 1153, page 159, 2009.

[73] M. Passoni, L. Bertagna, and A. Zani. Target normal sheath acceleration: theory, comparison with experiments and future perspectives. *New Journal of Physics*, 12(4):045012, 2010.

[74] A. Zani, A. Sgattoni, and M. Passoni. Parametric investigations of target normal sheath acceleration experiments. *Nuclear Instruments and Methods in Physics Research Section A: Accelerators, Spectrometers, Detectors and Associated Equipment*, 653(1):94–97, 2011.

[75] K. Zeil, S. D. Kraft, S. Bock, M. Bussmann, T. E. Cowan, T. Kluge, J. Metzkes, T. Richter, R. Sauerbrey, and U. Schramm. The scaling of proton energies in ultrashort pulse laser plasma acceleration. *New Journal of Physics*, 12(4):045015, 2010.

[76] A. Flacco, F. Sylla, M. Veltcheva, M. Carrié, R. Nuter, E. Lefebvre, D. Batani, and V. Malka. Dependence on pulse duration and foil thickness in high-contrast-laser proton acceleration. *Physical Review E*, 81(3):036405, 2010.

[77] T. Nayuki, Y. Oishi, T. Fujii, K. Takano, X. Wang, A. A. Andreev, K. Nemoto, and K. Ueda. Influence of target properties and laser fluence on energetic protons accelerated by a laser–produced plasma. *Journal of applied physics*, 100(4):043111, 2006.

[78] A. Macchi, F. Cattani, T. V. Liseykina, and F. Cornolti. Laser acceleration of ion bunches at the front surface of overdense plasmas. *Physical Review Letters*, 94(16):165003, 2005.

[79] A. Macchi, T. V. Liseikina, S. Tuveri, and S. Veghini. Theory and simulation of ion acceleration with circularly polarized laser pulses. *Comptes Rendus Physique*, 10(2):207–215, 2009.

[80] A. P. L. Robinson, P. Gibbon, M. Zepf, S. Kar, R. G. Evans, and C. Bellei. Relativistically correct hole-boring and ion acceleration by circularly polarized laser pulses. *Plasma Physics and Controlled Fusion*, 51(2):024004, 2009.

[81] C. A. J. Palmer, N. P. Dover, I. Pogorelsky, M. Babzien, G. I. Dudnikova, M. Ispiriyan, M. N. Polyanskiy, J. Schreiber, P. Shkolnikov, V. Yakimenko, et al. Monoenergetic proton beams accelerated by a radiation pressure driven shock. *Physical Review Letters*, 106(1):014801, 2011.

[82] J. Badziak, S. Głowacz, S. Jabłonski, P. Parys, J. Wołowski, and H. Hora. Production of ultrahigh-current-density ion beams by short-pulse skin-layer laser–plasma interaction. *Applied Physics Letters*, 85(15):3041–3043, 2004.

[83] K. U. Akli, S. B. Hansen, A. J. Kemp, R. R. Freeman, F. N. Beg, D. C. Clark, S. D. Chen, D. Hey, S. P. Hatchett, K. Highbarger, et al. Laser heating of solid matter by light-pressure-driven shocks at ultrarelativistic intensities. *Physical Review Letters*, 100(16):165002, 2008.

[84] A. Henig, D. Kiefer, M. Geissler, S. G. Rykovanov, R. Ramis, R. Hörlein, J. Osterhoff, Z. Major, L. Veisz, S. Karsch, et al. Laser–driven shock acceleration of ion beams from spherical mass–limited targets. *Physical Review Letters*, 102(9):095002, 2009.

[85] J. Denavit. Absorption of high–intensity subpicosecond lasers on solid density targets. *Physical Review Letters*, 69(21):3052, 1992.

[86] L. O Silva, M. Marti, J. R. Davies, R. A. Fonseca, C. Ren, F. S. Tsung, and W. B. Mori. Proton shock acceleration in laser-plasma interactions. *Physical Review Letters*, 92(1):015002, 2004.

[87] D. W. Forslund and J. P. Freidberg. Theory of laminar collisionless shocks. *Physical Review Letters*, 27(18):1189, 1971.

[88] M. Zepf, E. L. Clark, F. N. Beg, R. J. Clarke, A. E. Dangor, A. Gopal, K. Krushelnick, P. A. Norreys, M. Tatarakis, U. Wagner, et al. Proton acceleration from high-intensity laser interactions with thin foil targets. *Physical Review Letters*, 90(6):064801, 2003.

[89] G. Marx. Interstellar vehicle propelled by terrestrial laser beam. *Nature*, 211, 1966.

[90] J. F. L. Simmons and C. R. McInnes. Was Marx right? or How efficient are laser driven interstellar spacecraft? *American Journal of Physics*, 61(3):205–207, 1993.

[91] T. Esirkepov, M. Borghesi, S. V. Bulanov, G. Mourou, and T. Tajima. Highly efficient relativistic-ion generation in the laser-piston regime. *Physical Review Letters*, 92(17):175003, 2004.

[92] X. Zhang, B. Shen, X. Li, Z. Jin, and F. Wang. Multistaged acceleration of ions by circularly polarized laser pulse: Monoenergetic ion beam generation. *Physics of Plasmas (1994-present)*, 14(7):073101, 2007.

[93] O. Klimo, J. Psikal, J. Limpouch, and V. T. Tikhonchuk. Monoenergetic ion beams from ultrathin foils irradiated by ultrahigh-contrast circularly polarized laser pulses. *Physical Review Special Topics-Accelerators and Beams*, 11(3):031301, 2008.

[94] A. P. L. Robinson, M. Zepf, S. Kar, R. G. Evans, and C. Bellei. Radiation pressure acceleration of thin foils with circularly polarized laser pulses. *New journal of Physics*, 10(1):013021, 2008.

[95] S. Kar, K. F. Kakolee, B. Qiao, A. Macchi, M. Cerchez, D. Doria, M. Geissler, P. McKenna, D. Neely, J. Osterholz, et al. Ion acceleration in multispecies targets driven by intense laser radiation pressure. *Physical Review Letters*, 109(18):185006, 2012.

[96] A. Henig, S. Steinke, M. Schnürer, T. Sokollik, R. Hörlein, D. Kiefer, D. Jung, J. Schreiber, B. M. Hegelich, X. Q. Yan, et al. Radiation-pressure acceleration of ion beams driven by circularly polarized laser pulses. *Physical Review Letters*, 103(24):245003, 2009.

[97] T. Esirkepov, M. Yamagiwa, and T. Tajima. Laser ion-acceleration scaling laws seen in multiparametric particle-in-cell simulations. *Physical Review Letters*, 96(10):105001, 2006.

[98] F. Pegoraro and S. V. Bulanov. Photon bubbles and ion acceleration in a plasma dominated by the radiation pressure of an electromagnetic pulse. *Physical Review Letters*, 99(6):065002, 2007.

[99] M. Tamburini, F. Pegoraro, A. Di Piazza, C. H. Keitel, and A. Macchi. Radiation reaction effects on radiation pressure acceleration. *New Journal of Physics*, 12(12):123005, 2010.

[100] A. Henig, D. Kiefer, K. Markey, D. C. Gautier, K. A. Flippo, S. Letzring, R. P. Johnson, T. Shimada, L. Yin, B. J. Albright, et al. Enhanced laser-driven ion acceleration in the relativistic transparency regime. *Physical Review Letters*, 103(4):045002, 2009.

[101] L. Yin, B. J. Albright, B. M. Hegelich, K. J. Bowers, K. A. Flippo, T. J. T. Kwan, and J. C. Fernández. Monoenergetic and GeV ion acceleration from the laser breakout afterburner using ultrathin targets. *Physics of Plasmas (1994-present)*, 14(5):056706, 2007.

[102] B. M. Hegelich, D. Jung, B. J. Albright, M. Cheung, B. Dromey, D. C. Gautier, C. Hamilton, S. Letzring, R. Munchhausen, S. Palaniyappan, et al. 160 mev laser–accelerated protons from ch2 nano-targets for proton cancer therapy. *arXiv preprint arXiv:1310.8650*, 2013.

[103] U. Amaldi and G. Kraft. Radiotherapy with beams of carbon ions. *Reports on progress in physics*, 68(8):1861, 2005.

[104] G. F. Knoll. *Radiation detection and measurement*. John Wiley & Sons, 2010.

[105] A. J. Mackinnon, P. K. Patel, M. Borghesi, R. C. Clarke, R. R. Freeman, H. Habara, S. P. Hatchett, D. Hey, D. G. Hicks, S. Kar, et al. Proton radiography of a laser-driven implosion. *Physical Review Letters*, 97(4):045001, 2006.

[106] L. Willingale, P. M. Nilson, A. G. R. Thomas, J. Cobble, R. S. Craxton, A. Maksimchuk, P. A. Norreys, T. C. Sangster, R. H. H. Scott, C. Stoeckl, et al. High-power, kilojoule class laser channeling in millimeter-scale underdense plasma. *Physical Review Letters*, 106(10):105002, 2011.

[107] C. A. Cecchetti, M. Borghesi, J. Fuchs, G. Schurtz, S. Kar, A. Macchi, L. Romagnani, P. A. Wilson, P. Antici, R. Jung, et al. Magnetic field measurements in laser-produced plasmas via proton deflectometry. *Physics of Plasmas (1994-present)*, 16(4):43102, 2009.

[108] M. Koenig, A. Benuzzi-Mounaix, A. Ravasio, T. Vinci, N. Ozaki, S. Lepape, D. Batani, G. Huser, T. Hall, D. Hicks, et al. Progress in the study of warm dense matter. *Plasma Physics and Controlled Fusion*, 47(12B):B441, 2005.

[109] P. K. Patel, A. J. Mackinnon, M. H. Key, T. E. Cowan, M. E. Foord, M. Allen, D. F. Price, H. Ruhl, P. T. Springer, and R. Stephens. Isochoric heating of solid-density matter with an ultrafast proton beam. *Physical Review Letters*, 91(12):125004, 2003.

[110] I. Spencer, K. W. D. Ledingham, R. P. Singhal, T. McCanny, P. McKenna, E. L. Clark, K. Krushelnick, M. Zepf, F. N. Beg, M. Tatarakis, et al. Laser generation of proton beams for the production of short-lived positron emitting radioisotopes. *Nuclear Instruments and Methods in Physics Research Section B: Beam Interactions with Materials and Atoms*, 183(3):449–458, 2001.

[111] S. Fritzler, V. Malka, G. Grillon, J.-P. Rousseau, F. Burgy, E. Lefebvre, E. d'Humières, P. McKenna, and K. W. D. Ledingham. Proton beams generated with high-intensity lasers: Applications to medical isotope production. *Applied Physics Letters*, 83(15):3039–3041, 2003.

[112] L. Torrisi, S. Gammino, A. M. Mezzasalma, J. Badziak, P. Parys, J. Wolowski, E. Woryna, J. Krasa, L. Laska, M. Pfeifer, et al. Implantation of ions produced by the use of high power iodine laser. *Applied Surface Science*, 217(1):319–331, 2003.

[113] K. Ogura, T. Shizuma, T. Hayakawa, A. Yogo, M. Nishiuchi, S. Orimo, A. Sagisaka, A. Pirozhkov, M. Mori, H. Kiriyama, et al. Proton-induced nuclear reactions using compact high-contrast high-intensity laser. *Applied Physics Express*, 2(6):066001, 2009.

[114] P. McKenna, K. W. D. Ledingham, T. McCanny, R. P. Singhal, I. Spencer, E. L. Clark, F. N. Beg, K. Krushelnick, M. S. Wei, J. Galy, et al. Effect of target heating on ion-induced reactions in high-intensity laser–plasma interactions. *Applied Physics Letters*, 83(14):2763–2765, 2003.

[115] P. McKenna, K. W. D. Ledingham, T. McCanny, R. P. Singhal, I. Spencer, M. I. K. Santala, F. N. Beg, K. Krushelnick, M. Tatarakis, M. S. Wei, et al. Demonstration of fusion-evaporation and direct-interaction nuclear reactions using high-intensity laser-plasma-accelerated ion beams. *Physical Review Letters*, 91(7):075006, 2003.

[116] P. McKenna, K. W. D. Ledingham, J. M. Yang, L. Robson, T. McCanny, S. Shimizu, R. J. Clarke, D. Neely, K. Spohr, R. Chapman, et al. Characterization of proton and heavier ion acceleration in ultrahigh-intensity laser interactions with heated target foils. *Physical Review E*, 70(3):036405, 2004.

[117] P. McKenna, K. W. D. Ledingham, S. Shimizu, J. M. Yang, L. Robson, T. McCanny, J. Galy, J. Magill, R. J. Clarke, D. Neely, et al. Broad energy spectrum of laser-accelerated protons for spallation-related physics. *Physical Review Letters*, 94(8):084801, 2005.

[118] V. Y. Bychenkov, Y. Sentoku, S. V. Bulanov, K. Mima, G. Mourou, and S. V. Tolokonnikov. Pion production under the action of intense ultrashort laser pulse on a solid target. *Journal of Experimental and Theoretical Physics Letters*, 74(12):586–589, 2001.

[119] A. V. Pakhomov. Neutrino generation by high-intensity lasers. *Journal of Physics G: Nuclear and Particle Physics*, 28(6):1469, 2002.

[120] J. M. Yang, P. McKenna, K. W. D. Ledingham, T. McCanny, L. Robson, S. Shimizu, R. P. Singhal, M. S. Wei, K. Krushelnick, R. J. Clarke, et al. Neutron production by fast protons from ultraintense laser-plasma interactions. *Journal of Applied Physics*, 96(11):6912–6918, 2004.

[121] M. Roth, T. E. Cowan, M. H. Key, S. P. Hatchett, C. Brown, W. Fountain, J. Johnson, D. M. Pennington, R. A. Snavely, S. C. Wilks, et al. Fast ignition by intense laser-accelerated proton beams. *Physical Review Letters*, 86(3):436, 2001.

[122] S. Atzeni and J. Meyer-ter Vehn. *The physics of inertial fusion*. Clarendon Press, 2004.

[123] M. Tabak, J. Hammer, M. E. Glinsky, W. L. Kruer, S. C. Wilks, J. Woodworth, E. M. Campbell, M. D. Perry, and R. J. Mason. Ignition and high gain with ultrapowerful lasers. *Physics of Plasmas (1994-present)*, 1(5):1626–1634, 1994.

[124] S. Atzeni, M. Temporal, and J. J. Honrubia. A first analysis of fast ignition of precompressed icf fuel by laser-accelerated protons. *Nuclear Fusion*, 42(3):L1, 2002.

[125] M. Temporal, J. J. Honrubia, and S. Atzeni. Numerical study of fast ignition of ablatively imploded deuterium–tritium fusion capsules by ultra-intense proton beams. *Physics of Plasmas (1994-present)*, 9(7):3098–3107, 2002.

[126] M. H. Key. Status of and prospects for the fast ignition inertial fusion concepta. *Physics of Plasmas (1994-present)*, 14(5):055502, 2007.

[127] J. J. Honrubia, J. C. Fernandez, M. Temporal, B. M. Hegelich, and J. Meyerter Vehn. Fast ignition of inertial fusion targets by laser-driven carbon beams. *Physics of Plasmas (1994-present)*, 16(10):102701, 2009.

[128] S. V. Bulanov and V. S. Khoroshkov. Feasibility of using laser ion accelerators in proton therapy. *Plasma Physics Reports*, 28(5):453–456, 2002.

[129] S. V. Bulanov, T. Z. Esirkepov, F. F. Kamenets, Y. Kato, A. V. Kuznetsov, K. Nishihara, F. Pegoraro, T. Tajima, and V. S. Khoroshkov. Generation of high-quality charged particle beams during the acceleration of ions by high-power laser radiation. *Plasma Physics Reports*, 28(12):975–991, 2002.

[130] U. Linz and J. Alonso. What will it take for laser driven proton accelerators to be applied to tumor therapy? *Physical Review Special Topics-Accelerators and Beams*, 10(9):094801, 2007.

[131] C. Ma, I. Veltchev, E. Fourkal, J. Li, J. Fan, T. Lin, W. Luo, and S. Stathakis. SU-FF-T-309: Laser-accelerated proton therapy: Target chamber design and shielding requirements. *Medical Physics*, 33(6):2117–2118, 2006.

[132] E. Fourkal, I. Velchev, J. Fan, W. Luo, and C.-M. Ma. Energy optimization procedure for treatment planning with laser-accelerated protons. *Medical Physics*, 34(2):577–584, 2007.

[133] A. Yogo, K. Sato, M. Nishikino, M. Mori, T. Teshima, H. Numasaki, M. Murakami, Y. Demizu, S. Akagi, S. Nagayama, et al. Application of laser-accelerated protons to the demonstration of dna double-strand breaks in human cancer cells. *Applied Physics Letters*, 94(18):181502, 2009.

[134] D. Doria, K. F. Kakolee, S. Kar, S. K. Litt, F. Fiorini, H. Ahmed, S. Green, J. C. G. Jeynes, J. Kavanagh, D. Kirby, et al. Biological effectiveness on live cells of laser driven protons at dose rates exceeding 109Gy/s. *AIP Advances*, 2(1):011209, 2012.

[135] S. Kar, K. Markey, M. Borghesi, D. C. Carroll, P. McKenna, D. Neely, M. N. Quinn, and M. Zepf. Ballistic focusing of polyenergetic protons driven by petawatt laser pulses. *Physical Review Letters*, 106(22):225003, 2011.

[136] T. Bartal, M. E. Foord, C. Bellei, M. H. Key, K. A. Flippo, S. A. Gaillard, D. T. Offermann, P. K. Patel, L. C. Jarrott, D. P. Higginson, et al. Focusing of short–pulse high–intensity laser–accelerated proton beams. *Nature Physics*, 8(2):139–142, 2012.

[137] T. Z. Esirkepov, S. V. Bulanov, K. Nishihara, T. Tajima, F. Pegoraro, V. S. Khoroshkov, K. Mima, H. Daido, Y. Kato, Y. Kitagawa, et al. Proposed double–layer target for the generation of high–quality laser–accelerated ion beams. *Physical Review Letters*, 89(17):175003, 2002.

[138] H. Schwoerer, S. Pfotenhauer, O. Jäckel, K.-U. Amthor, B. Liesfeld, W. Ziegler, R. Sauerbrey, K. W. D. Ledingham, and T. Esirkepov. Laser–plasma acceleration of quasi–monoenergetic protons from microstructured targets. *Nature*, 439(7075):445–448, 2006.

[139] B. M. Hegelich, B. J. Albright, J. Cobble, K. Flippo, S. Letzring, M. Paffett, H. Ruhl, J. Schreiber, R. K. Schulze, and J. C. Fernández. Laser acceleration of quasi–monoenergetic MeV ion beams. *Nature*, 439(7075):441–444, 2006.

[140] M. Kaluza, J. Schreiber, M. I. K. Santala, G. D. Tsakiris, K. Eidmann, J. Meyer-ter Vehn, and Klaus J. W. Influence of the laser prepulse on proton acceleration in thin–foil experiments. *Physical Review Letters*, 93(4):045003, 2004.

[141] D. Neely, P. Foster, A. Robinson, F. Lindau, O. Lundh, A. Persson, C.-G. Wahlstrom, and P. McKenna. Enhanced proton beams from ultrathin targets driven by high contrast laser pulses. *Applied Physics Letters*, 89(2):021502–021502, 2006.

[142] P. Antici, J. Fuchs, E. d'Humières, E. Lefebvre, M. Borghesi, E. Brambrink, C. A. Cecchetti, S. Gaillard, L. Romagnani, Y. Sentoku, et al. Energetic protons generated by ultrahigh contrast laser pulses interacting with ultrathin targets. *Physics of Plasmas (1994-present)*, 14(3):030701, 2007.

[143] T. Ceccotti, A. Lévy, H. Popescu, F. Réau, P. d'Oliveira, P. Monot, J. P. Geindre, E. Lefebvre, and P. Martin. Proton acceleration with high–intensity ultrahigh–contrast laser pulses. *Physical Review Letters*, 99(18):185002, 2007.

[144] J. Badziak, E. Woryna, P. Parys, K. Y. Platonov, S. Jabłonski, L. Ryc, A. B. Vankov, and J. Wolowski. Fast proton generation from ultrashort laser pulse interaction with double–layer foil targets. *Physical Review Letters*, 87(21):215001–215001, 2001.

[145] J. Psikal, V. T. Tikhonchuk, J. Limpouch, A. A. Andreev, and A. V. Brantov. Ion acceleration by femtosecond laser pulses in small multispecies targets. *Physics of Plasmas (1994-present)*, 15(5):053102, 2008.

[146] S. Buffechoux, J. Psikal, M. Nakatsutsumi, L. Romagnani, A. Andreev, K. Zeil, M. Amin, P. Antici, T. Burris-Mog, A. Compant-La-Fontaine, et al. Hot electrons transverse refluxing in ultraintense laser–solid interactions. *Physical Review Letters*, 105(1):015005, 2010.

[147] S. A. Gaillard, T. Kluge, K. A. Flippo, M. Bussmann, B. Gall, T. Lockard, M. Geissel, D. T. Offermann, M. Schollmeier, Y. Sentoku, et al. Increased laser–accelerated proton energies via direct laser–light–pressure acceleration of electrons in microcone targets. *Physics of Plasmas (1994-present)*, 18(5):056710, 2011.

[148] K. A. Flippo, E. d'Humières, S. A. Gaillard, J. Rassuchine, D. C. Gautier, M. Schollmeier, F. Nürnberg, J. L. Kline, J. Adams, B. Albright, et al. Increased efficiency of short–pulse laser–generated proton beams from novel flat-top cone targets. *Physics of Plasmas (1994-present)*, 15(5):056709, 2008.

[149] A. Zigler, T. Palchan, N. Bruner, E. Schleifer, S. Eisenmann, M. Botton, Z. Henis, S. A. Pikuz, A. Y. Faenov Jr, D. Gordon, et al. 5.5–7.5 MeV proton

generation by a moderate-intensity ultrashort–pulse laser interaction with H2O nanowire targets. *Physical Review Letters*, 106(13):134801, 2011.

[150] D. Margarone, O. Klimo, I. J. Kim, J. Prokůpek, J. Limpouch, T. M. Jeong, T. Mocek, J. Pšikal, HT Kim, J. Proška, et al. Laser–driven proton acceleration enhancement by nanostructured foils. *Physical Review Letters*, 109(23):234801, 2012.

[151] B. N. Breizman, A. V. Arefiev, and M. V. Fomyts'kyi. Nonlinear physics of laser–irradiated microclusters. *Physics of Plasmas (1994-present)*, 12(5):056706, 2005.

[152] A. Bigongiari, M. Raynaud, C. Riconda, A. Héron, et al. Improved ion acceleration via laser surface plasma waves excitation. *Physics of Plasmas (1994-present)*, 20(5), 2013.

[153] T. Ceccotti, V. Floquet, A. Sgattoni, A. Bigongiari, O. Klimo, M. Raynaud, C. Riconda, A. Heron, F. Baffigi, L. Labate, et al. Evidence of resonant surface-wave excitation in the relativistic regime through measurements of proton acceleration from grating targets. *Physical Review Letters*, 111(18):185001, 2013.

[154] M. Raynaud, J. Kupersztych, C. Riconda, J. C. Adam, and A. Heron. Strongly enhanced laser absorption and electron acceleration via resonant excitation of surface plasma waves. *Physics of Plasmas (1994-present)*, 14(9):092702, 2007.

[155] A. Bigongiari, M. Raynaud, C. Riconda, A. Héron, and A. Macchi. Efficient laser–overdense plasma coupling via surface plasma waves and steady magnetic field generation. *Physics of Plasmas (1994-present)*, 18(10):102701, 2011.

[156] G. Consolati, R. Ferragut, A. Galarneau, F. Di Renzo, and F. Quasso. Mesoporous materials for antihydrogen production. *Chemical Society Reviews*, 42(9):3821–3832, 2013.

[157] R. Ferragut, S. Aghion, G. Tosi, G. Consolati, F. Quasso, M. Longhi, A. Galarneau, and F. Di Renzo. Positronium production in engineered porous silica. *The Journal of Physical Chemistry C*, 117(50):26703–26709, 2013.

[158] A. J. Westphal, H. A. Bechtel, F. E. Brenker, A. L. Butterworth, G. Flynn, D. R. Frank, Z. Gainsforth, J. K. Hillier, F. Postberg, A. S. Simionovici, et al. Final reports of the stardust interstellar preliminary examination. *Meteoritics & Planetary Science*, 49(9):1720–1733, 2014.

[159] V. G Shvedov, A. V. Rode, Y. V. Izdebskaya, A. S. Desyatnikov, W. Krolikowski, and Y. S. Kivshar. Giant optical manipulation. *Physical Review Letters*, 105(11):118103, 2010.

[160] A. V. Rode, E. G. Gamaly, A. G. Christy, J. G. F. Gerald, S. T. Hyde, R. G. Elliman, B. Luther-Davies, A. I. Veinger, J. Androulakis, and J. Giapintzakis. Unconventional magnetism in all-carbon nanofoam. *Physical Review B*, 70(5):054407, 2004.

[161] Q. Yue, Y. Li, M. Kong, J. Huang, X. Zhao, J. Liu, and R. E. Williford. Ultralow density, hollow silica foams produced through interfacial reaction and their exceptional properties for environmental and energy applications. *Journal of Materials Chemistry*, 21(32):12041–12046, 2011.

[162] J. W. Falconer, W. Nazarov, and C. J. Horsfield. In situ production of very low density microporous polymeric foams. *Journal of Vacuum Science & Technology A*, 13(4):1941–1944, 1995.

[163] K. L. Anderson, W. Nazarov, C. S. A. Musgrave, N. Bazin, and D. Faith. Synthesis and characterisation of low density porous polymers by reversible addition-fragmentation chain transfer (RAFT). *Journal of Radioanalytical and Nuclear Chemistry*, 299(2):969–975, 2014.

[164] S. Costeux. CO2-blown nanocellular foams. *Journal of Applied Polymer Science*, 131(23), 2014.

[165] L. J. M. Jacobs, S. A. M. Hurkens, M. F. Kemmere, and J. T. F. Keurentjes. Porous cellulose acetate butyrate foams with a tunable bimodality in foam morphology produced with supercritical carbon dioxide. *Macromolecular Materials and Engineering*, 293(4):298–302, 2008.

[166] A. Salerno, S. Iannace, and P. A. Netti. Open-pore biodegradable foams prepared via gas foaming and microparticulate templating. *Macromolecular Bioscience*, 8(7):655–664, 2008.

[167] R. Narasimman and K. Prabhakaran. Preparation of low density carbon foams by foaming molten sucrose using an aluminium nitrate blowing agent. *Carbon*, 50(5):1999–2009, 2012.

[168] E. G. Gamaly and A. V. Rode. Nanostructures created by lasers. In *Encyclopedia of Nanoscience and Nanotechnology*, volume 7, pages 783–809. American Scientific Publishers, 2004.

[169] D. B. Chrisey and G. K. Hubler. Pulsed laser deposition of thin films. *Pulsed Laser Deposition of Thin Films, by Douglas B. Chrisey (Editor), Graham K. Hubler (Editor), pp. 648. ISBN 0-471-59218-8. Wiley-VCH*, 1, 2003.

[170] D. Dellasega, A. Facibeni, F. Di Fonzo, V. Russo, C. Conti, C. Ducati, C. S. Casari, A. Li Bassi, and C. E. Bottani. Nanostructured high valence silver oxide produced by pulsed laser deposition. *Applied Surface Science*, 255(10):5248–5251, 2009.

[171] D. A. Freiwald and R. A. Axford. Approximate spherical blast theory including source mass. *Journal of Applied Physics*, 46(3):1171–1174, 1975.

[172] N. Arnold, J. Gruber, and J. Heitz. Spherical expansion of the vapor plume into ambient gas: an analytical model. *Applied Physics A*, 69(1):S87–S93, 1999.

[173] A. Uccello. *Study and development of rhodium films for production of diagnostic mirrors employed in nuclear fusion systems*. PhD thesis, Politecnico di Milano, Milan, Italy, 2014.

[174] E. G. Gamaly, A. V. Rode, and B. Luther-Davies. Ultrafast ablation with high–pulse–rate lasers. part I: Theoretical considerations. *Journal of Applied Physics*, 85(8):4213–4221, 1999.

[175] A. V. Rode, B. Luther-Davies, and E. G. Gamaly. Ultrafast ablation with high–pulse–rate lasers. part II: Experiments on laser deposition of amorphous carbon films. *Journal of Applied Physics*, 85(8):4222–4230, 1999.

[176] A. V. Rode, S. T. Hyde, E. G. Gamaly, R. G. Elliman, D. R. McKenzie, and S. Bulcock. Structural analysis of a carbon foam formed by high pulse–rate laser ablation. *Applied Physics A*, 69(1):S755–S758, 1999.

[177] A. V. Rode, E. G. Gamaly, and B. Luther-Davies. Formation of cluster-assembled carbon nano–foam by high–repetition–rate laser ablation. *Applied Physics A*, 70(2):135–144, 2000.

[178] A. A. Voevodin and M. S. Donley. Preparation of amorphous diamond-like carbon by pulsed laser deposition: a critical review. *Surface and Coatings Technology*, 82(3):199–213, 1996.

[179] M. Bonelli, A. C. Ferrari, A. Fioravanti, A. Li Bassi, A. Miotello, and P. M. Ossi. Structure and mechanical properties of low stress tetrahedral amorphous carbon films prepared by pulsed laser deposition. *The European Physical Journal B-Condensed Matter and Complex Systems*, 25(3):269–280, 2002.

[180] D. Bolgiaghi, A. Miotello, P. Mosaner, P. M. Ossi, and G. Radnoczi. Pulsed laser deposition of glass–like cluster assembled carbon films. *Carbon*, 43(10):2122–2127, 2005.

[181] P. M. Ossi, C. E. Bottani, and A. Miotello. Pulsed-laser deposition of carbon: from dlc to cluster–assembled films. *Thin Solid Films*, 482(1):2–8, 2005.

[182] M. P. Siegal, D. R. Tallant, L. J. Martinez-Miranda, J. C. Barbour, R. L. Simpson, and D. L. Overmyer. Nanostructural characterization of amorphous diamondlike carbon films. *Physical Review B*, 61(15):10451, 2000.

[183] G. Sauerbrey. Wagung dunner schichten mit schwingquarzen. In *Angewandte Chemie–International Edition*, volume 69, pages 761–761. Wiley–vch Verlag GmbH Muhlenstrasse 33–34, d–13187 Berlin, Germany, 1957.

[184] Inficon. `http://www.inficon.com/`. Accessed: 2015–02–15.

[185] C.-S. Lu and O. Lewis. Investigation of film-thickness determination by oscillating quartz resonators with large mass load. *Journal of Applied Physics*, 43(11):4385–4390, 1972.

[186] V. Mecea and R. V. Bucur. The mechanism of the interaction of thin films with resonating quartz crystal substrates: the energy transfer model. *Thin Solid Films*, 60(1):73–84, 1979.

[187] K. K. Kanazawa and J. G. Gordon. Frequency of a quartz microbalance in contact with liquid. *Analytical Chemistry*, 57(8):1770–1771, 1985.

[188] W. E. Sweeney Jr, R. E. Seebold, and L. S. Birks. Electron probe measurements of evaporated metal films. *Journal of Applied Physics*, 31(6):1061–1064, 1960.

[189] B. W. Schumacher and S. S. Mitra. Measuring thickness and composition of thin surface films by means of an electron probe. *Microelectronics Reliability*, 1(4):321–331, 1962.

[190] M. D. Bentzon, P. S. Nielsen, and S. S. Eskildsen. A simple and sensitive way to determine carbon film thickness. *Diamond and Related Materials*, 2(5):893–897, 1993.

[191] G. H. Cockett and C. D. Davis. Coating thickness measurement by electron probe microanalysis. *British Journal of Applied Physics*, 14(11):813, 1963.

[192] R. Castaing. *Application of electron probes to local chemical and crystallographic analysis*. PhD thesis, University of Paris, Paris, France, 1951.

[193] H. E. Bishop and D. M. Poole. A simple method of thin film analysis in the electron probe microanalyser. *Journal of Physics D: Applied Physics*, 6(9):1142, 1973.

[194] Y. G. Lavrent'Ev, V. N. Korolyuk, and L. V. Usova. Second generation of correction methods in electron probe X-ray microanalysis: Approximation models for emission depth distribution functions. *Journal of Analytical Chemistry*, 59(7):600–616, 2004.

[195] J. L. Pouchou and F. Pichoir. A new model for quantitative X–ray microanalysis. I.–application to the analysis of homogeneous samples. *Recherche Aerospatiale*, (3):167–192, 1984.

[196] J. L. Pouchou and F. Pichoir. Very high elements X–ray microanalysis – recent models of quantification. *Journal de Microscopie et de Spectroscopie Electroniques*, 11(4):229–250, 1986.

[197] R. H. Packwood and J. D. Brown. A gaussian expression to describe $\phi$ ($\rho$z) curves for quantitative electron probe microanalysis. *X–Ray Spectrometry*, 10(3):138–146, 1981.

[198] W. Rehbach and P. Karduck. Verification of the gaussian ($pz$) approach and determination of the limits of validity by tracer experiments and monte carlo simulations. *Microbeam Analysis 1988*, pages 285–289, 1988.

[199] J. Ruste. Mass absorption coefficients. *Journal de Microscopie et de Spectroscopie Electroniques*, 4:123, 1979.

[200] H.-J. Hunger and L. Küchler. Measurements of the electron backscattering coefficient for quantitative EPMA in the energy range of 4 to 40 keV. *Physica Status Solidi A*, 56(1):K45–K48, 1979.

[201] J.-L. Pouchou. X–ray microanalysis of stratified specimens. *Analytica Chimica Acta*, 283(1):81–97, 1993.

[202] P. Karduck and W. Rehbach. Progress in the measurement and calculation of the depth distribution of low–energy X–ray generation. *Microbeam Analysis 1988*, 1988.

[203] A. Graham and C. Spindloe. Microtarget mass production for the RAL high accuracy microtargetry system. Targetry for Laser-driven Proton (Ion) Accelerator Sources: 1st Workshop, Garching, Germany, 2013.

[204] D. Dellasega, G. Merlo, C. Conti, C. E. Bottani, and M. Passoni. Nanostructured and amorphous–like tungsten films grown by pulsed laser deposition. *Journal of Applied Physics*, 112(8):084328, 2012.

[205] P. Gondoni, V. Russo, C. E. Bottani, A. Li Bassi, and C. S. Casari. Tuning hierarchical cluster assembly in pulsed laser deposition of Al–doped ZnO. In *MRS Proceedings*, volume 1497, pages mrsf12–1497. Cambridge Univ Press, 2013.

[206] A. Uccello, D. Dellasega, S. Perissinotto, N. Lecis, and M. Passoni. Nanostructured rhodium films for advanced mirrors produced by pulsed laser deposition. *Journal of Nuclear Materials*, 432(1):261–265, 2013.

[207] D. Drouin, A. R. Couture, D. Joly, X. Tastet, V. Aimez, and R. Gauvin. CASINO V2. 42–A fast and easy–to—use modeling tool for scanning electron microscopy and microanalysis users. *Scanning*, 29(3):92–101, 2007.

[208] K. Kanaya and S. Okayama. Penetration and energy-loss theory of electrons in solid targets. *Journal of Physics D: Applied Physics*, 5(1):43, 1972.

[209] F. Hall, D. Haddock, W. Nazarov, C. Spindloe, and M. K. Tolley. Production of low density foam targets for high repetition rate laser experiments. Target Fabrication Workshop 5, St. Andrews, Scotland, 2014.

[210] T. V. Liseykina and D. Bauer. Plasma–formation dynamics in intense laser-droplet interaction. *Physical Review Letters*, 110(14):145003, 2013.

[211] C. Benedetti, A. Sgattoni, G. Turchetti, and P. Londrillo. : A high–accuracy pic code for the maxwell–vlasov equations. *Plasma Science, IEEE Transactions on*, 36(4):1790–1798, 2008.

[212] I. W. Choi, J. U. Lee, and C. H. Nam. Space–resolving flat–field extreme ultraviolet spectrograph system and its aberration analysis with wave–front aberration. *Applied Optics*, 36(7):1457–1466, 1997.

[213] K. Ogura, M. Nishiuchi, A. S. Pirozhkov, T. Tanimoto, A. Sagisaka, T. Z. Esirkepov, M. Kando, T. Shizuma, T. Hayakawa, H. Kiriyama, et al. Proton

acceleration to 40 MeV using a high intensity, high contrast optical parametric chirped-pulse amplification/Ti: sapphire hybrid laser system. *Optics Letters*, 37(14):2868–2870, 2012.

[214] A. Macchi, A. Sgattoni, S. Sinigardi, M. Borghesi, and M. Passoni. Advanced strategies for ion acceleration using high power lasers. *arXiv preprint arXiv:1306.6859*, 2013.

[215] I. J. Kim, K. H. Pae, C. M. Kim, H. T. Kim, J. H. Sung, S. K. Lee, T. J. Yu, I. W. Choi, C.-L. Lee, K. H. Nam, et al. Transition of proton energy scaling using an ultrathin target irradiated by linearly polarized femtosecond laser pulses. *Physical Review Letters*, 111(16):165003, 2013.